Collège Doctoral du Languedoc-Roussillon

THÈSE

Pour obtenir le grade de

Docteur

Délivré par **UNIVERSITE MONTPELLIER 2**

Préparée au sein de l'école doctorale **CBS2- Sciences Chimique et Biologiques pour la Santé**
Et de l'unité de recherche **Centre de Biochimie Structurale, CNRS UMR5048**

Spécialité : **Biophysique Moléculaire**

Présentée par **Linnéa Olofsson**

Mise en lumière des mécanismes d'activation des récepteurs metabotropes au glutamate par fluorescence en molécule unique

Soutenue le 28/03/2014 devant le jury composé de

Dr. Pierre-Jean Corringer	Directeur de recherche, Institut Pasteur	Président
Pr. Don Lamb	Professor Univ L-M Munich, Germany	Rapporteur
Dr. Ingo Greger	Principal Investigator, Cambridge, UK	Rapporteur
Dr. Eric Deprez	Directeur de recherche, ENS Cachan	Examinateur
Dr. Emmanuel Margeat	Directeur de recherche, CBS CNRS	Directeur de thèse
Dr. Jean-Philippe Pin	Directeur de recherche, IGF CNRS	Co-directeur de thèse
Dr. Philippe Rondard	Directeur de recherche, IGF CNRS	Co-directeur de thèse

UNIVERSITÉ MONTPELLIER 2
SCIENCES ET TECHNIQUES

"The scientist is not a person who gives the right answers; he's one who asks the right questions"

Claude Lévi-Strauss, 1964

The execution and completion of this Ph.D. thesis was made possible thanks to a grant attributed by the French Research ministry and the doctoral school "Sciences Chimiques et Biologiques pour la santé, CBS2" / Université Montpellier 2.

The research was conducted at:

Centre de biochimie Structurale
CNRS UMR 5048 - UM 1 - INSERM UMR 1054
29 rue de Navacelles 34090
MONTPELLIER Cedex - France

Under the direction of Dr. Emmanuel Margeat, in the Single Molecule Biophysics group

And

Institut de Génomique Fonctionelle
141 Rue de la Cardonille 34090
MONTPELLIER Cedex - France

in the pharmacology department, under the direction of Dr. jean-Philippe Pin and Dr. Philippe Rondard, and in collaboration with Cisbio bioassays, Codolet.

Résumé en Français:

Les récepteurs métabotropes au glutamate (mGluR) sont des Recepteurs couplés aux protéines G (RCPG) de classe C. Ils sont exprimés dans le système nerveux central où, suite à l'activation par le glutamate, ils participent à la modulation de la transmission nerveuse. En raison de leur rôle essentiel dans la régulation de l'activité synaptique, ils représentent des cibles potentielles pour le développement de médicaments contre les troubles neurologiques et psychiatriques telles que la schizophrénie, l'épilepsie, l'anxiété et la douleur. Mon projet de recherche de doctorat a porté sur l'étude du mécanisme d'activation du domaine extracellulaire de liaison au ligand du mGluR, avec un accent particulier sur ce qui différencie au niveau moléculaire un agoniste partiel d'un agoniste total. A cette fin, j'ai utilisé une méthode innovante basée sur le Transfer d'Energie par Résonance de Förster, et spécialement développée pour l'étude de la dynamique conformationnelle des molécules individuelles à l'échelle de la nanoseconde.

J'ai réussi à montrer que le domaine extracellulaire dimérique des mGluR oscille entre une conformation active et une conformation de repos sur une échelle de temps de ~100µsec et que les ligands influencent l'équilibre entre ces deux états. Pour les agonistes partiels, le déplacement d'équilibre vers la forme active est moins efficace que pour les agonistes totaux. Ces résultats sont validés par l'utilisation de mutants spécifiques et indiquent clairement que le rôle des ligands n'est pas de stabiliser une conformation donnée mais de modifier le comportement dynamique du récepteur. L'ensemble de ces résultats contribuent à une meilleure description du mécanisme d'activation des mGluRs, et ouvrent potentiellement la voie à la compréhension des RCPG en général.

Mots clés : récepteurs métabotropes au glutamate, agonisme partielle, dynamique conformationnelle, FRET en molécule unique, glutamate.

Summary in English:

Metabotropic Glutamate Receptors (mGluRs) are class C G protein coupled receptors (GPCR), expressed throughout the central nervous system. They participate in the long term modulation of neural transmission following activation by the excitatory neurotransmitter glutamate. This critical role in the regulation of synaptic activity makes them promising targets in the development of drugs for the treatment of various neurologic and psychiatric disorders such as schizophrenia, epilepsy, anxiety and pain.

My Ph.D. research project has focused on the study of the activation mechanism of the mGluR extracellular ligand binding Venus Flytrap domain (VFT), with particular emphasis on the differences between partial and full agonists on a molecular level. To this aim, I have used a state-of-the-art single molecule Förster Resonance Energy Transfer (smFRET) approach, developed for the study of conformational dynamics of single molecules on the nanosecond to millisecond timescale.

I have managed to show that the VFT dimer constantly oscillates between an active and a resting conformation on a ~100μsec timescale. I also discovered that the role of ligands is to shift the equilibrium and modulate the transition rate between these two boundary states. Moreover, partial agonists less efficiently shift the equilibrium toward the active state, with respect to full agonists. My results, supported by the use of specific mutants, clearly indicate that the role of ligands is not to stabilize a given conformation but to modify the overall dynamic of the receptor, which favors a conformational selection mechanism. Altogether, these results represent a most-valuable contribution to the better understanding of the activation mechanism of mGluRs, and potentially GPCRs in general.

Key words : metabotropic Glutamate Receptors, glutamate, Venus-Flytrap domain, partial agonism, smFRET, conformational dynamics and selection.

Acknowledgements

My most sincere and humble thanks to:

- First and foremost, my Ph.D. supervisor and friend Emmanuel Margeat for always being enthusiastic to share and teach me his knowledge and for having tirelessly guided, supported and encouraged me throughout the almost five years that I have had the good fortune to work for and with him. I could never enough stress how grateful and thankful I am that he accepted to take me under his wings.

- Jean-Philippe Pin and Philippe Rondard for enlighten me with their expertise in the vast field of G-Protein Coupled Receptors. Many thanks to Jean-Philippe for always pointing out what is relevant and important and what is not, which repeatedly helped me structure my research. As the director of the IGF, I am also thankful for having been given the opportunity to work in the institute. I would also like to thank Philippe so much for many long discussions which often stretched far beyond the realm of metabotropic glutamate receptor and which made me see and understand the bigger picture.

- Many thanks to Suren Felekyan and Claus Seidel. Thank you both for inviting me to spend some time in your laboratory and deepen my knowledge regarding the realization and analyzing of MFD experiments. I would like to express an additional acknowledgement to Suren for untiringly answering all my technical questions, and often giving me feedback within the hour.

- To my role model Catherine Royer who was also the director of the CBS for many years for having welcomed me into her lab and having opened my eyes to the world of biophysics and structural biology and for always being reassuring when the task ahead seemed overwhelming; Christian Roumestand who is the current director of the CBS for continuing carrying out the demanding task of running a research laboratory.

- I would also like to thank Marcello Nollman, Pierre-Emmanuel Milhiet, Nathalie Declerck and Francesco Pedaci for sharing their opinions regarding the progress of my work. By asking intriguing and sometimes unexpected questions during group-meetings, they motivate me to find a way to render my results more accessible to a broader audience.

- My friends Pauline Scholler and Ludovic Fabre for fruitful discussions and for helping me out with the molecular biology aspects of my project in addition to always being willing to provide me with new cells.

- Our outstanding secretary Florence Lepage and our financial director Didier Debain without whom the CBS would not function one week.

- Many thanks to Driss El-Moustaine and Etienne Doumazane for their help during the initial steps of my project. They both sacrificed a substantial amount of time to teach me the basics of cell-culture and protein purification and labeling.

- I would also like to thank Jean-Louis Banères and Bernard Mouillac for their help with the purification and the nanodisc incorporation of the 7TM.

- Thanks to Eric Deprèz for attending my thesis committee.

- Alessandro Valeri for showing me how to use the MFD software and Fred Allemand for giving me some molecular biology firsthand experiences.

- Caroline Clerte and Antoine Legall for showing me the fundamentals of building confocal microscopes; and Martin Cohen-Consaud for helping me figuring out a MSP purification protocol; and Patrice Rassam for having accepted me as a summer trainee all those years ago, we didn't work together for very long but everything he thought me has served me well on a daily basis ever since. On a more personal level, I would like to thank them all for many interesting and witty lunch discussions.

- My dear Mariya Georgieva for being my deeply cherished friend, roommate, Wikipedia (Mariyapedia) and office mate. There are so many things that I would like to thank her for but in this context I would like to highlight her valuable inputs and remarks mainly on technical issues and English grammar.

- My dear coworkers and friends Jean-Baptiste Rouget, Elodie Lemonnier, Soraya Ait-Bara-Bouhours, Nicole Lautredou, Jérôme Hottin, Ewelina Guca, Jean-Bernard Fiche, Diego Cattoni, Laura Oudjedi, Christine Doucet and Vanessa Delfosse for many laughs and pleasant moments that made going to work more than enjoyable.

- Last but not the least: my beloved husband Eric Filion for an innumerable number of things but above all for his love and immeasurable support throughout these last couple of years that unfortunately we have had to spend apart; my parents for their love and for believing in me and my capacities, always backing me up wherever my decisions carried me; Louise Lagerqvist, my precious friend, for all our deep discussions (in broken Swedish), and for helping me with English grammar and last but not least, for many girls-nights-outs making the town unsafe.

- And of course all my coworkers at the CBS and IGF, the école doctorale CBS2 and to all those strangers whose name I never got who provided me with valuable inputs and remarks during seminars.

Overview

The present dissertation, submitted to University Montpellier II for the fulfillment of the requirements for the degree of doctor of biophysics, endeavors to give its readers an extensive overview of the current scientific knowledge regarding the structural dynamics of the metabotropic glutamate receptors family (mGluRs) as well as presenting a new innovative single molecule Förster resonance energy transfer approach, implemented to determine the underlying molecular mechanism by which ligands with various efficacies modulate the degree of receptor activation.

To integrate the mGluRs in a more general context, I will begin by briefly introducing the biological functions, signaling mechanisms and molecular structures of some other well-known GPCRs, notably two class A GPCRs for which the crystal structures have been solved: rhodopsin and the β_2 adrenergic receptor. To further the understanding of the molecular basis of GPCR signaling, a thorough introduction of the mode of action of ligands with different pharmaceutical proprieties, as well as a presentation of some of the postulated activation models, is subsequently discussed.

In the 2nd part of the introduction, I will cover the basics of the biology of the different receptors belonging to the Class C family of GPCRs and then transition to focus exclusively on a single member of the Class C family: the mGluRs. I will review the current understanding of mGluR biological functions, molecular structures and their hypothesized activation mechanism. In addition, I will attempt to accentuate their importance for the pharmaceutical industry as plausible targets for the treatment of various neurological and psychiatric disorders. Furthermore, as the greater part of my research has been conducted on the extracellular ligand binding domain of the mGluR, I will lay extra emphasis on the dynamic behavior of this particular domain.

After having familiarized the readers with the biological aspects of my Ph.D. project, I will detail the background and the specific objectives of my research and describe the methodology that I have been employing to investigate the conformational changes that occur within the receptor, and how they are modulated through the action of various ligands. Throughout my three years as a Ph.D. student, I have mostly been using various *in vitro* solution based fluorescence spectroscopy approaches. In view of that, I found it necessary to provide the readers with an extensive report on the basics of fluorescence, both in terms of the underlying photophysical phenomenon that results in the emission of fluorescence on a molecular level, as well as the accurate employment of the

technique called Förster Resonance Energy Transfer (FRET). FRET is very useful technique to measure distances on a nanometer scale, and can be implemented as well on a population of molecules as on a single molecule level, the latter known as single molecule FRET (smFRET). smFRET offers the possibility to individually analyze the different subpopulations, even minor, that constitute a heterogeneous sample. This technique will therefore be explained at length and details will be provided on several of the advanced analysis procedures by which conformational dynamics can be quantified with a nanosecond time-resolution.

Up until this point of the dissertation my aim has been to provide the readers with an in depth understanding of the basis and framework of my project. The subsequent chapters will focus on my results. Firstly, I will present the technical article that was published in *Optics Express* that explains how we implemented a Supercontinuum laser for the construction of a two-color pulsed interleaved excitation time-correlated single photon counting detection setup. Secondly, the main article that summarizes my most essential findings concerning the dynamic behavior of mGluRs will be presented. In this article, I provide experimental evidence in favor of a new mGluR activation mechanism and discuss how ligands with varying efficacy modulate the degree of receptor activation. In a final results section, I will also present two related projects, focusing on the dynamic of the intracellular domain and on the development of nanobodies as mGluR ligands, which have not yet resulted in publications, but for which both the methodology and the biological results are interesting to discuss.

To conclude, I will discuss the principal points of the outcome of this study and suggest some future perspectives for the investigation of not only mGluRs, but perhaps also for other types of receptors as well.

Table of contents

Acknowledgements 7

Overview 9

CHAPTER 1. INTRODUCTION 14

1.1 G-Protein Coupled Receptors 15

1.1.1 General introduction to GPCRs 15

1.1.2 Biological functions of GPCRs 21

1.1.3 G-proteins and signaling pathways 23

1.1.4 Molecular structures of GPCRs 26

1.2 "Induced fit" or "conformational selection": that is the question! 30

1.3 Metabotropic Glutamate Receptors 34

1.3.1 Introduction to the nervous system and the synapse 34

1.3.2 General introduction to Class C GPCRs 35

1.3.3 Biological functions of mGluRs 37

1.3.4 Molecular structure of mGluRs 39

1.3.5 Suggested mGluR activation model 46

1.3.6 mGluR pharmacology and related disorders 52

CHAPTER 2. OBJECTIVES 56

CHAPTER 3. METHODOLOGY 62

3.1 Fluorescence – basic concepts and practical aspects 63

3.1.1 Theory of fluorescence 63

3.2 Förster Resonance Energy Transfer 68

3.2.1 Theory of FRET 68

3.2.2 Experimentally measuring FRET 74

3.3 Implementing FRET on a single molecule level 76

3.3.1 Technical requirements for solution based smFRET 78

3.3.2 smFRET coupled to µsALEX enables sorting of molecules of interest 85

3.3.3 Time resolved smFRET-MFD : a powerful method to analyze and display smFRET data 93

3.3.4 smFRET- Methods for analyzing fast dynamics 114

CHAPTER 4. RESULTS 134

4.1 Implementation of a supercontinuum source to perform FCCS-PIE .. 136

4.2 Illuminating the activation mechanism of mGluRs with smFRET 139

4.3 mGlu3 – a good candidate to unveil the link between glutamate affinity and dynamic behavior 148

4.4 The nanobody as a new mGluR subtype specific ligand 155

4.5 Nanodisc-incorporation as an approach to study the mobility of the C-terminus of the 7TM in solution 163

CHAPTER 5. DISCUSSION AND CONCLUSIONS 170

5.1 Result summary 171

5.2 Future perspectives 172

BIBLIOGRAPHY 178

ANNEX 189

Alternative labeling methods 189

Glossary and abbreviations 194

Chapter 1. Introduction

1.1 G-Protein Coupled Receptors

In this first chapter, I will briefly introduce the biology of G-Protein Coupled Receptors (GPCRs) and discuss the molecular structure and activation mechanisms of a couple of well-studied members of this protein family.

1.1.1 General introduction to GPCRs

G-Protein Coupled Receptors constitute the most abundant family of proteins in mammalian genomes. In humans, there are in total approximately 20 000 genes and it has been estimated that about 800 of them (4%) code for the different members of the GPCR superfamily. (Fredriksson *et al.*, 2003)

GPCRs play fundamental roles in transmembrane signal transduction. They are involved in the mediation of various extracellular signals, including photons, hormones, amino acids and peptides, and ensure subsequent appropriate intracellular responses. Despite their structural similarities, they participate in a wide range of physical processes, spanning from vision, smell and taste-recognition to endocrine, neurological and reproductive functions (Rosenbaum *et al.*, 2009; Katritch *et al.*, 2012). An important consequence of this broad diversity of biological functions is that approximately 25-30% of all drugs currently available on the market target GPCRs, (**Figure 1.1.a**) and extensive therapeutic research is conducted by pharmaceutical companies all around the world to expand the panoply of medications even further (Lagerström and Schiöth, 2008).

GPCRs are subdivided into five major families

All GPCRs share the same topology, with a heptahelical transmembrane domain (7TM) as the most characteristic common structural feature. The seven helices are linked via three extracellular loops and three intracellular loops which separate the extracellular N-terminus from the intracellular C-terminus. The C-terminus is frequently preceded by an 8th amphipathic helix which is often subject to post-translational modifications (Audet and Bouvier, 2012; Granier and Kobilka, 2012). In spite of their resemblances, the different members of the GPCR superfamily are generally subdivided into five major families, regrouped as follows based on structural- and sequence- similarities: "Class A" (Rhodopsin-like), "Class B" (Secretin-like), "Class C" (Glutamate-like), "Adhesion" and "Frizzled/Taste2" (**Figure 1.1.b**) (Foord *et al.*, 2005).

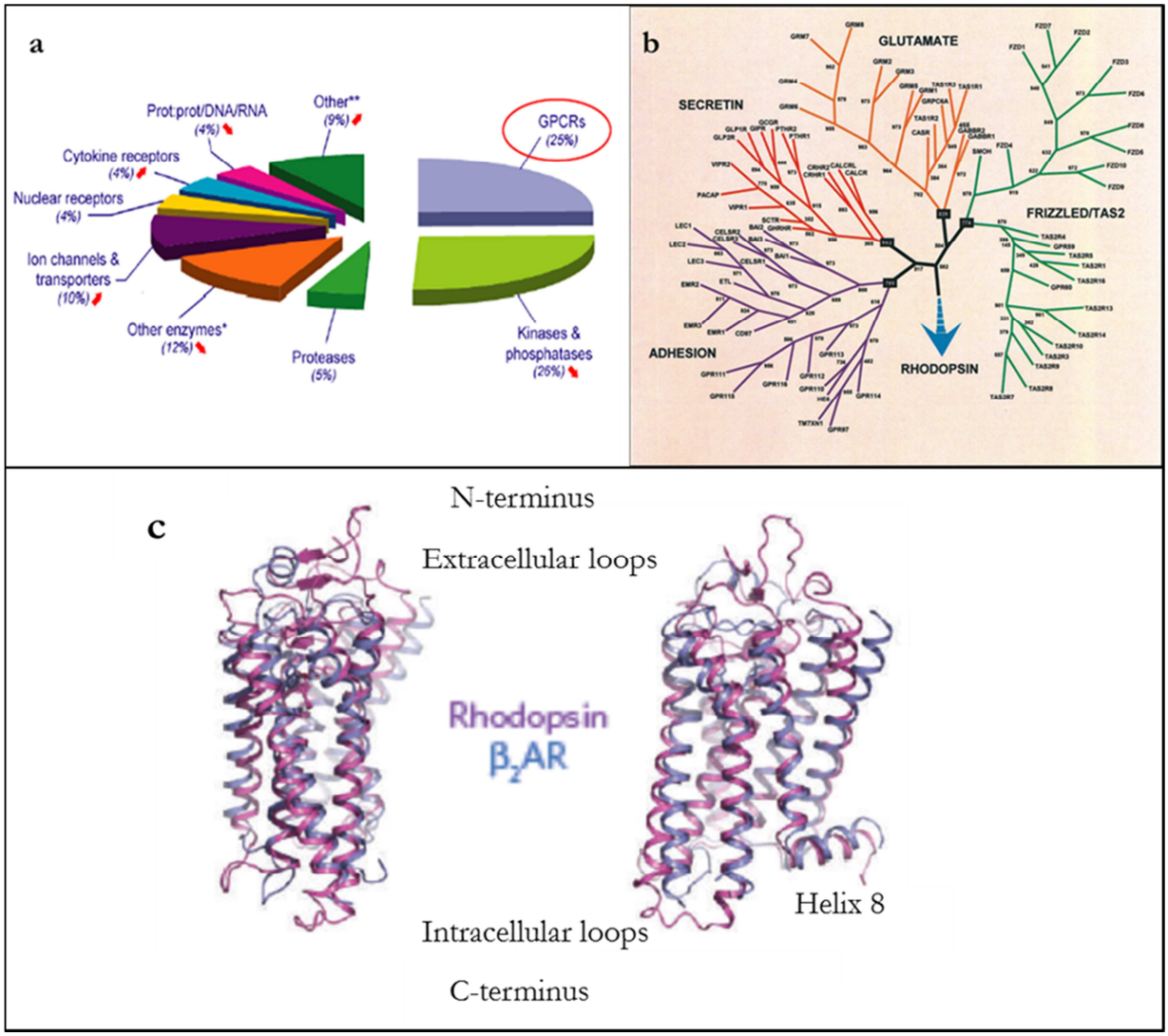

Figure 1.1 *(**a**) Pie-chart showing the major groups of molecules targeted by pharmaceutical drugs currently available on the market (Lagerström and Schiöth, 2008). Approximately 25% of these are GPCRs. (**b**) Phylogenetic tree representing the GPCR superfamily, which is subdivided into five major families based on sequence- and structural- similarities. Class A rhodopsin is the most abundant family and is therefore only represented with an arrow. The other four family-members are: Class B (secretin-like), Class C (glutamate-like), Adhesion and Frizzled/Taste2 (Lagerström and Schiöth, 2008). (**c**) Overlay of the molecular structures of rhodopsin (purple) and the β2-adrenergic receptor (β2AR) (blue).The right figure is rotated along the vertical axes by 90°. A similar heptahelical topology is observed for both receptors* (Rosenbaum *et al.*, 2009).

The pharmacological nature of a ligand determines the biological response

In order to understand how a specific intracellular response is generated by a given GPCR, the concept of "pharmacological characteristics of ligands" has to be invoked. In fact, the molecules that specifically modulate the activity of a receptor upon binding in the orthosteric (primary) binding site are classified based on the effect that they generate : an **agonist** is responsible for the full activation of the receptor ; a **partial agonist** gives rise to an intermediate degree of activation, often expressed as a fraction of the maximal response generated by the full agonist ; an **antagonist** prevents the binding of other ligands without suppressing the basal activity of the receptor ; and an **inverse agonist** which, in contrast to an antagonist, prevents both the binding of other ligands and inhibits the basal activity (**Figure 1.2.a**). In practice, this classification is somewhat oversimplified, as some ligands are known to regulate several distinct downstream signaling pathways, but to different extents (Kenakin, 2003).

The biological response generated by a given ligand might be further modulated by allosteric interactions. Indeed, positive and negative allosteric modulators (PAMs and NAMs), which bind the receptor elsewhere than in the orthosteric binding site are capable of potentiating, in the case of a PAM, or limit in the case of a NAM, the biological response stimulated by the orthosteric ligand. In other words, this means that the binding of a PAM will increase the affinity and/or the efficacy for the orthosteric ligand. In contrast, the binding of a NAM results in a decrease of the affinity and/or the efficacy of the same ligand.

This basic principle of allosteric modulation lies in the idea of the existence of a conformational link between the allosteric and the orthosteric binding site. Thereupon, it is postulated that the binding of a PAM or a NAM slightly alters the local conformation of the protein, and that these small variations will have conformational ramifications that (**i**) either affect the conformational rearrangements that are brought about by the orthosteric ligand, in which case the efficacy but not the affinity is modified, or (**ii**) influences the orthosteric binding pocket itself, and thereby changes the affinity (Sebag and Pantel, 2012). (N.B. The efficacy of a ligand represents the biological response brought about by that ligand whereas the affinity of a ligand stands for the binding constant of that ligand within the binding site.)

Following the binding of an allosteric modulator, the entire protein could be looked upon as a new signaling entity with unique characteristics. A consequence of this amplified complexity, as well as the emergence of broad diversity of new allosteric modulators imposed for the introduction

of a new mathematical model accounting for the cooperativity factor (α) (**Figure 1.2.b**). A value of α>1 defines a positive cooperativity, whereas α<1 indicates negative cooperativity (Sebag and Pantel, 2012). It is, however, crucial to point out that the cooperativity factor only reflects the modulation of the affinity for the endogenous ligand in the orthosteric binding site, and therefore, does not inform on the outcome in terms of biological activity. In reality, it might even be that an allosteric modulator acts as PAM on one signaling pathway, but as a NAM on another. Consequently, a thorough examination of both the binding constant and the intracellular response is required to fully understand the effect of a PAM or a NAM.

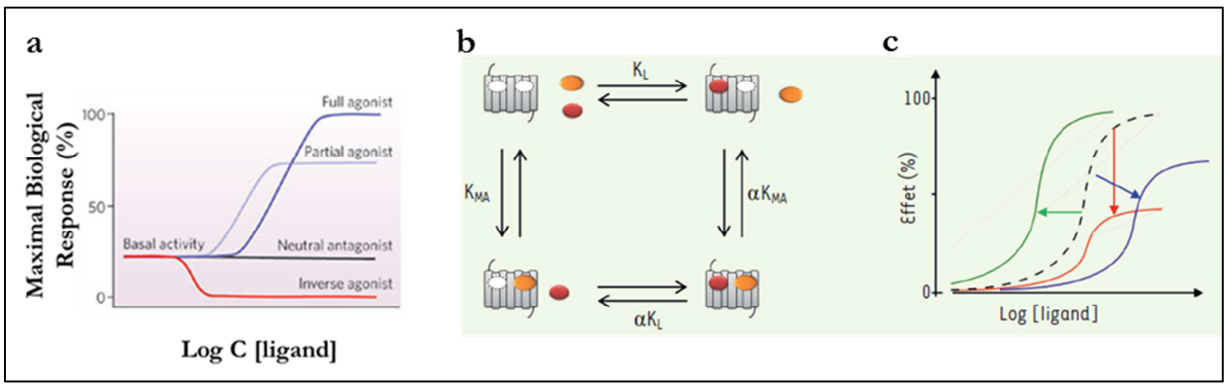

Figure 1.2. *(**a**) Theoretic titration curves representing the biological response as a function of the drug concentration. A full agonist leads to a maximized biological response. A partial agonist activates the receptor, but the level of biological response never attains that reached with the full agonist. A neutral antagonist prevents the activation of the receptor without affecting the basal constitutive activity in contrast to an inverse agonist that simultaneously inhibits activation and suppresses the basal activity. Modified from* (Rosenbaum *et al.*, 2009) *(**b**) Illustration of the cooperativity model where the red ligand bind in the orthosteric binding site and the yellow ligand represent the allosteric modulator. K_L stands for the binding constant (affinity) of the endogenous ligand, and K_{MA} stands for the binding constant of the allosteric modulator. α<1 signifies that the affinity decreases in the presence of the allosteric modulator, whereas, α>1 implies an increased affinity. (**c**) Theoretical titration curve showing the biological effect as a function of the concentration of the agonist. The effect of a PAM that increases the affinity (in comparison with the dashed curve which represents the response in absence of allosteric modulators) is represented in green, the effect of a NAM that does not alter the affinity but reduces the biological response is highlighted in red and a NAM with an altered effect on both the affinity and the efficacy is shown in blue.*

Furthermore, the theoretical titration curves illustrated in **figure 1.3** represents the particular case where a PAM clearly increases the affinity for the full agonist in a concentration dependent

manner whereas the NAM only decreases the efficacy of the agonist without influencing the affinity. In this specific example, the term NAM can instead be replaced by that of competitive antagonist.

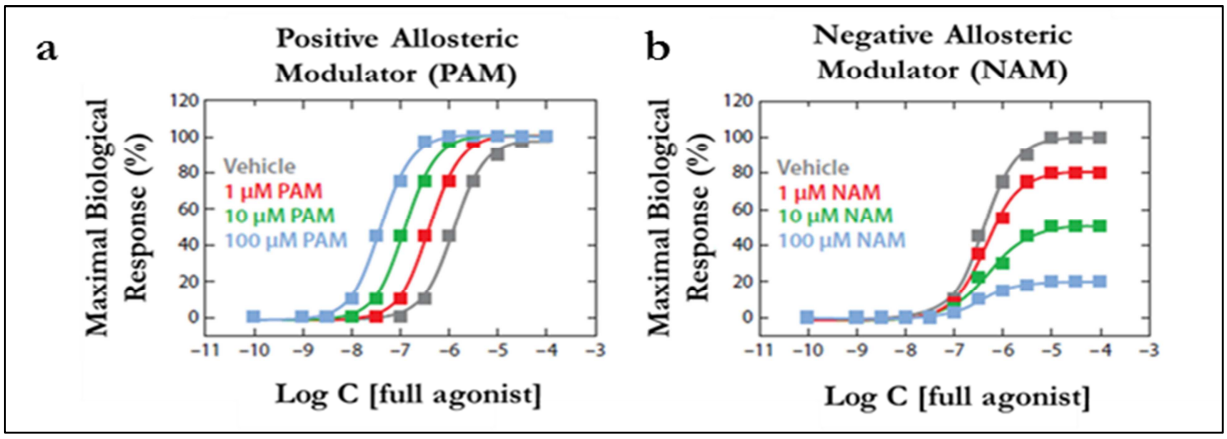

Figure 1.3. *(**a**) Theoretic titration curves representing the biological response as a function of the concentration of a full agonist for different concentrations of a positive allosteric modulator (PAM). As the concentration of the PAM increases (grey to blue lines), the efficacy of the full agonist increases, i.e. a maximal biological response is obtained at a lower concentration. (**b**) Theoretic titration curves representing the biological response as a function of the concentration of a full agonist for different concentrations of a negative allosteric modulator (NAM). As the concentration of the NAM increases (grey to blue lines), the efficacy of the full agonist decreases, i.e. even at very high concentrations, a full biological response is not reached. Modified from (Niswender and Conn, 2010)*

GPCR signaling through G-protein activation

All well-studied GPCRs have been shown to trigger intracellular signaling cascades via the direct activation of heterotrimeric G-proteins. The binding of an agonist on the extracellular side of the inactive receptor is thought to shift the conformational equilibrium of the transmembrane domain toward the active state, enabling hence the interaction with the heterotrimeric G-protein on the intracellular side of the membrane (**Figure 1.4.a**). This, in turn, induces a GDP to GTP exchange in the α–subunit of the G-protein, which undergoes a conformational change. The conformational change of the α–subunit initiates, in general, the signaling cascade by dissociating the α -subunit from the β/γ-dimer, as independently, both the α –subunit and the β/γ-dimer, are capable of triggering various 2nd messenger pathways. The inactivation of the G-protein then occurs by hydrolyzation of the GTP, and a subsequent reassembly of the α+β/γ trimer and/or in some cases, an internalization of the GPCR following β-arrestin recruitment (**Figure 1.4.b**) Depending on the receptor subtype, its localization and the bound ligand, there are numerous possible signaling

pathways that might be modulated, forming a highly complex intracellular network, essential for cellular homeostasis (Lefkowitz, 2004; Milligan and Kostenis, 2006).

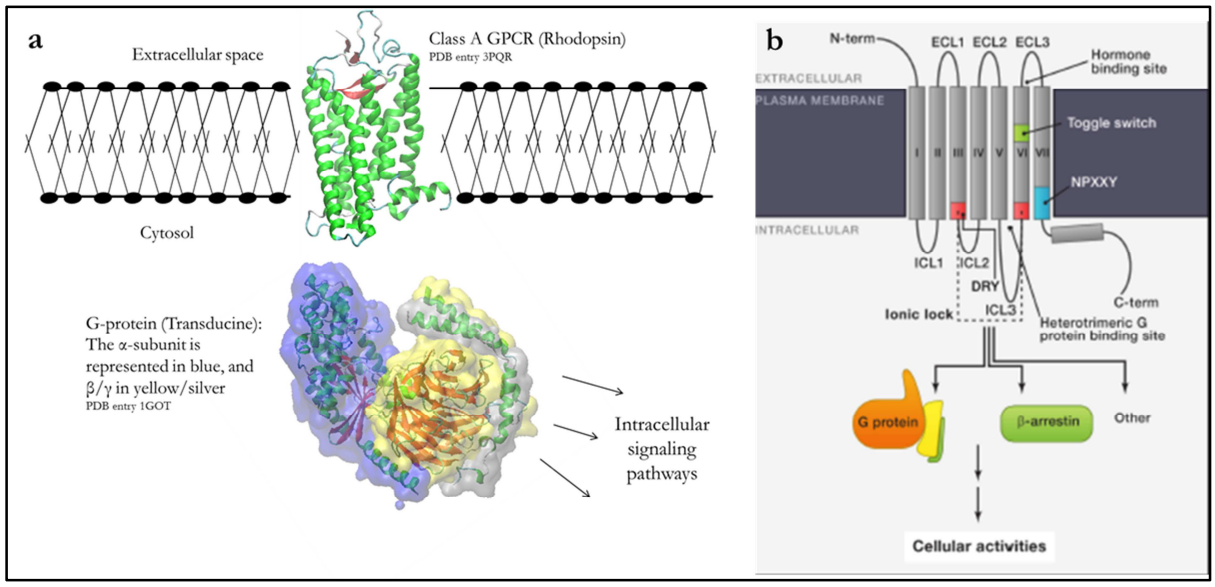

Figure 1.4. *(**a**) Crystallographic structure of the seven helices that form the transmembrane domain of the class A GPCR rhodopsin and its G-protein (transducine). The three subunits of the G-protein are shown, in blue, for α and, in yellow and silver, for β and γ respectively. Upon binding of an agonist in the orthosteric binding site on the extracellular side of the GPCR, there will be a conformational change that allows for the G-protein to bind and activate its function as a GTP exchange factor. In its GTP form, the G-protein trimer dissociates, which represent the first step of a complex intracellular signaling cascade. (Representation made with "visual molecular dynamics", (VMD 1.9.1), a software provided by the "center for the physics of living cells", university of Urbana-Champaign, Illinois) (**b**) Schematic illustration of the heptahelical topology of rhodopsin represented with some of the most important class A conserved motifs. (Toggle-switch, "NPXXY" and ionic lock" (Audet and Bouvier, 2012)*

1.1.2 Biological functions of GPCRs

Class A GPCRs

The class A Rhodopsin-like family is the most thoroughly studied group of receptors. It is also the largest family, representing almost 700 out of the 800 GPCRs found in the human genome (Fredriksson *et al.*, 2003). The most well-known members of this class of receptors are rhodopsin and the β_2 adrenergic receptor (β_2AR).

Rhodopsin is a photoreceptor found in the retina, responsible for the perception of light (Tesmer, 2010; Audet and Bouvier, 2012). It is a heteroprotein composed of the apoprotein "opsin" and the covalently bound prosthetic group "retinal", a pigment derived from vitamin-A. In the absence of light, opsin binds retinal in its cis-configuration, thus preventing the interaction with the G-protein. Upon light stimuli, retinal undergoes a cis-trans isomerization followed by a succession of conformational changes that ultimately result in the activation of the rhodopsin specific G-protein "transducin". Rhodopsin eventually returns to its inactive state after phosphorylation by the G-protein specific kinase GRK1 whose introduced phosphate-group is recognized by the specific visual arrestin (rod-arrestin) that eventually internalizes the receptor (Tesmer, 2010; Audet and Bouvier, 2012).

Thanks to the contribution of 2012 winners of the Nobel Prize in chemistry, Brian Kobilka (Stanford University) and Robert Lefkowitz (Duke University), the β_2AR has become another example of a well-studied class A GPCR. β_2ARs is found in the sympathetic nervous system, where it acts as a regulator of muscle-contraction. The β_1 and the β_2 subtype of the receptor are both involved in the indispensable response to external threats, to which the organism reacts by releasing adrenaline and noradrenaline. Likewise, the β_1 subtype acts on intracellular pathways that lead to an increase of the heart-rate, whereas the activation of the β_2 receptor leads to relaxing of smooth muscles. In parallel, β_2 increases glycolysis, which prepares the organism to decide on the appropriate response "fight or flight" (Lefkowitz, 2004; Rosenbaum *et al.*, 2009)

Class B GPCR

The topology of class B receptors differs significantly from class A receptors by the presence of a large N-terminal domain for all investigated class B members (Lagerström and Schiöth, 2008). The N-terminal domain contains three conserved disulfide bonds which are thought to be involved

in ligand binding. The 15 members of this family are necessary for the recognition of peptide hormones, of which most belong to the glucagon hormone family. Yet, the vasoactive intestinal peptide receptor, the receptors binding secretin and calcitonin, and the receptors associated with the response to parathyroid hormone also belong to this family (Lagerström and Schiöth, 2008).

Class C GPCRs

In humans, there are 22 genes coding for the receptors belonging to the class C GPCR family. They include: the metabotropic glutamate receptor, the $GABA_B$ receptor, calcium sensing receptors, pheromone receptors, as well as seven orphan receptors (Wellendorph and Bräuner-Osborne, 2009; Philippe Rondard *et al.*, 2011). Considering that chapter 1.3 of this dissertation is entirely dedicated to this class of receptors, I will not detail their characteristics at this point.

Adhesion

There are 33 known members of the human adhesion receptor family. Most of them are still considered orphans- signifying that their ligands and, for some of them, the interaction partners/transduction pathways remain to be discovered (Davenport *et al.*, 2013). They are associated with cell adhesion and migration, both of which require an interaction with the cell matrix. For this reason, they contain a large N-terminal domain known to be highly glycosylated. Another particular feature for this class of receptors is the existence of an autocatalytic site between the extracellular N-terminal domain and the transmembrane domain, which results in a receptor composed of non-covalently bound subunits (Lagerström and Schiöth, 2008).

Frizzled/Taste2

The Frizzled receptor and its interaction partners are key molecules in the Wnt/β-catenin pathway. They are, therefore, crucial factors in embryonic development and they play important roles in tumorigenesis. So far, no studies have revealed that G-protein coupling is indeed a necessary step in this signaling cascade (Lagerström and Schiöth, 2008).

In humans, the 25 different Taste2 receptors share only low sequence similarity. They are responsible for the perception of bitter taste, and the extensive genetic polymorphism of this family seems to explain the individual sensation associated with the detection of bitter ingredients in food (Lagerström and Schiöth, 2008).

1.1.3 G-proteins and signaling pathways

A large majority of the different members of the GPCR superfamily ensure their roles in signal transduction by activating heterotrimeric G-proteins (even though this has yet to be confirmed for some orphan receptors and the Frizzled receptors) (Katritch *et al.*, 2012; Davenport *et al.*, 2013).

There is a broad diversity of G-proteins. They all interact with specific partners, resulting in the activation of different intracellular signaling cascades through the participation of various effector molecules. The outcome is most commonly a modulation of transcription factors, which consequently regulate gene expression and/or have an effect on ion channels. The better understanding of this highly complex signaling network has become the aim of research groups across the globe, and it has become evident that the challenge is not trivial. Without a doubt, the task is even more complicated due to the discovery that a given receptor might interact with different G-proteins, and thereby activate divergent pathways, sometimes simultaneously (Deupi and Kobilka, 2010; Whalen *et al.*, 2011). Additionally, it seems like the degree of receptor oligomerization intervenes in regulating the resulting intracellular response (Katritch *et al.*, 2012).

Different G-proteins regulate different intracellular pathways

In humans, there are 33 estimated G-protein encoding genes: 16 for the Gα subunit, 5 for the Gβ subunit and 12 genes for the Gγ subunit (McIntire, 2009).

There are four families of G-proteins, classified based on the homology of the primary sequence of the Gα subunit and on the effector molecules they activate (**Table 1.1** and **Figure 1.5**) (Neer, 1995; Denis *et al.*, 2012).

Classes of Gα subunits	
Class	**Members**
$G\alpha_s$	α_s , α_{olf}
$G\alpha_i/\alpha_0$	$\alpha_{I\text{-}1}$, $\alpha_{i\text{-}2}$, $\alpha_{I\text{-}3}$, α_o , $\alpha_{1\text{-}1}$, $\alpha_{t\text{-}2}$, α_{gust} , α_z
$G\alpha q$	α_q , α_{11} , α_{14} , α_{15} , α_{16}
$G\alpha_{12}$	α_{12} , α_{13}

Table 1.1. *Gα subunit classification*

- $G\alpha_s$: These Gα subunits regulates Ca^{2+} ion-channels and activates the cAMP pathway- through the action of adenylyl cyclase, the 2nd messenger cyclic adenosine monophosphate (cAMP) is synthesized from ATP, which leads to a rise in the level of cytosolic cAMP. The effect is, among others, the activation of cAMP-dependent protein kinases capable of phosphorylating serine and/or threonine residues in target proteins. Subsequently, these target proteins modulate other cellular components such as ion channels, transcription factors and other enzymes. The main biological functions of these pathways consist in raising the heart rate, relaxing smooth muscles and stimulating neural activity (Denis *et al.*, 2012).

- $G\alpha_i/\alpha_o$: These Gα subunits modulates K^+ and Ca^{2+} channels and activate the phospholipase C/ phosphoinositol pathway. Phospholipase C acts by cleaving the lipid phosphatidylinositol 4,5-bisphosphate (PIP_2) into diacylglycerol (DAG) and inositol-triphosphate (IP_3), both acting as 2nd messenger molecules involved in the release of calcium from the endoplasmic reticulum. Another effect is the down-regulation of the cAMP pathway (Denis *et al.*, 2012).

- Gq: Activates the phospholipase C/phosphoinositol pathway and GPCR kinases (Denis *et al.*, 2012).

- G_{12}: Activates proteins belonging to the Rho family, which are important monomeric small GTPases involved in cell migration and angiogenesis (Denis *et al.*, 2012).

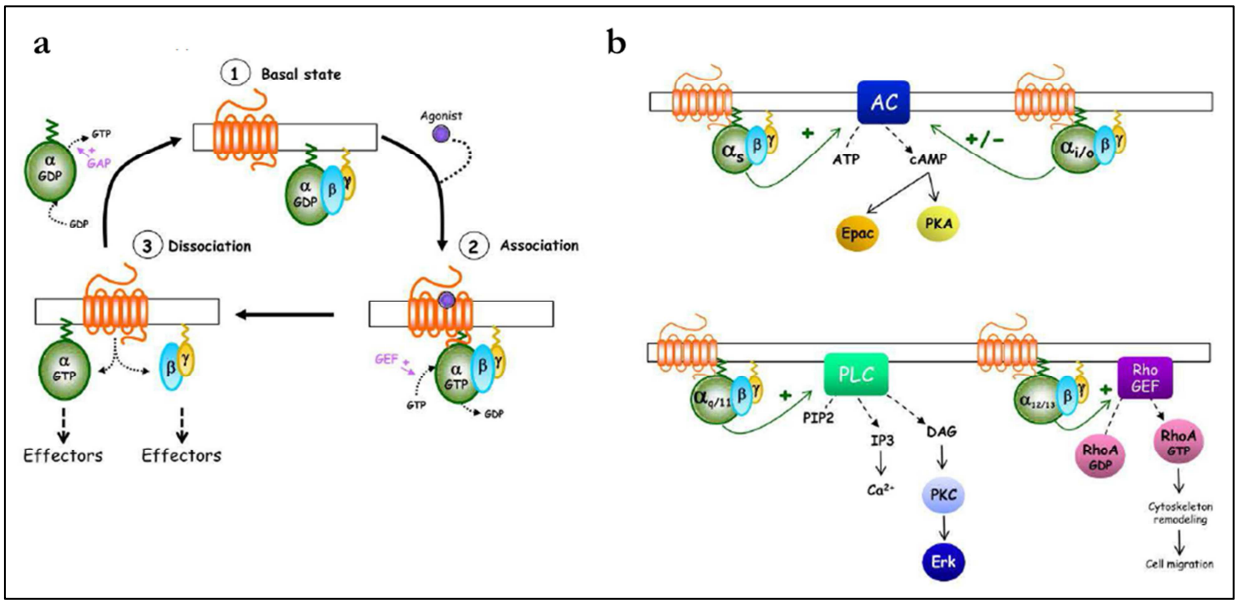

Figure 1.5. *(**a**) Cartoon illustrating the activation of the G-protein. Upon binding of an agonist, the trimeric G-protein binds to the GPCR and the GDP within the α-subunit is replaced by a GTP. This nucleotide exchange induces a conformational change that generally dissociates the α-subunit from the β/γ-dimer. The α-subunit and the β/γ-dimer subsequently initiate different intracellular signaling cascades. (**b**) Depending on the G-protein subtype, different effector molecules will be engaged. α_S and $\alpha_{i/o}$ have opposite effects on adenylyl cyclase, and therefore on the level of cytosolic cAMP. α_q upregulates the phospholipase C/phosphoinositol pathway and α_{12} modulates the activity of small GTPases such as Rho* (Denis *et al.*, 2012).

1.1.4 Molecular structures of GPCRs

Rhodopsin was the first GPCR to be crystallized in 3D (Okada *et al.*, 2000) and has over the years become a homology model for other GPCRs. Nonetheless, from a biological standpoint, rhodopsin is not a very representative GPCR. This is mainly due the particular activation mechanism of rhodopsin that does not involve diffusible ligands, contrary to most other known GPCRs. The, significant achievement of resolving the first crystal structure of β_2AR in 2007 (Rasmussen *et al.*, 2007) was, therefore, considered a major breakthrough in the field of GPCR biology, providing the first high-resolution insight into non-rhodopsin GPCR functions.

Crystallographic difficulties

There are many reasons to why GPCR crystallization is such a complicated task. Most GPCRs show low expression levels and the purified receptor is greatly biochemically instable in detergents (Granier and Kobilka, 2012). Furthermore, the crystallization is complicated by the lack of polar residues that have to interact to form the crystal lattice, and by a significant structural flexibility of the protein, which results in a highly heterogenic sample (Granier and Kobilka, 2012). Fortunately, some of these impediments are nowadays possible to overcome thanks to recent technical and biochemical developments. Many mutagenesis approaches aim to increase the stability of a given state (thermostabilization) and thereby decrease the heterogeneity of the sample and/or introduce polar residues to increase the polar surface in the crystal lattice (Lebon et al. 2011; Rasmussen et al. 2011; Rasmussen et al. 2011). Additionally, some receptors require the use of specific antibodies or fusion proteins to promote crystallization. (Rasmussen et al. 2011) Another noteworthy technical improvement to overcome the low solubility of many GPCRs in short chain detergents, which are the lipids required for the commonly used diffusion strategy, is the implementation of lipid mesophase crystallography (Khelashvili *et al.*, 2012).

First structure of a GPCR bound to its G-protein

The latest triumph in GPCR crystallography is the structure of β_2AR coupled to its G-protein (Gs) (Rasmussen et al. 2011) (**Figure 1.6**). In order to accomplish this challenge, the authors had to fuse the unstructured N-terminus of β_2AR with the T4 lysozyme, which facilitated crystal lattice contacts by increasing the number of polar residues. Moreover, the replacement of GDP with the pyrophosphate analogue phosphonoformate (foscarnet) in Gs significantly stabilized the interaction between β_2AR and Gs. Nevertheless, the complex had to be further supported to persist throughout

the purification procedure. To this aim, the authors took advantage of nanobodies, (fairly small (15kDa) heavy-chain only antibodies produced by llamas) which successfully recognized the active conformation of β_2AR at the β_2AR-Gs interface and thereby helped maintain the intact structure of the complex.

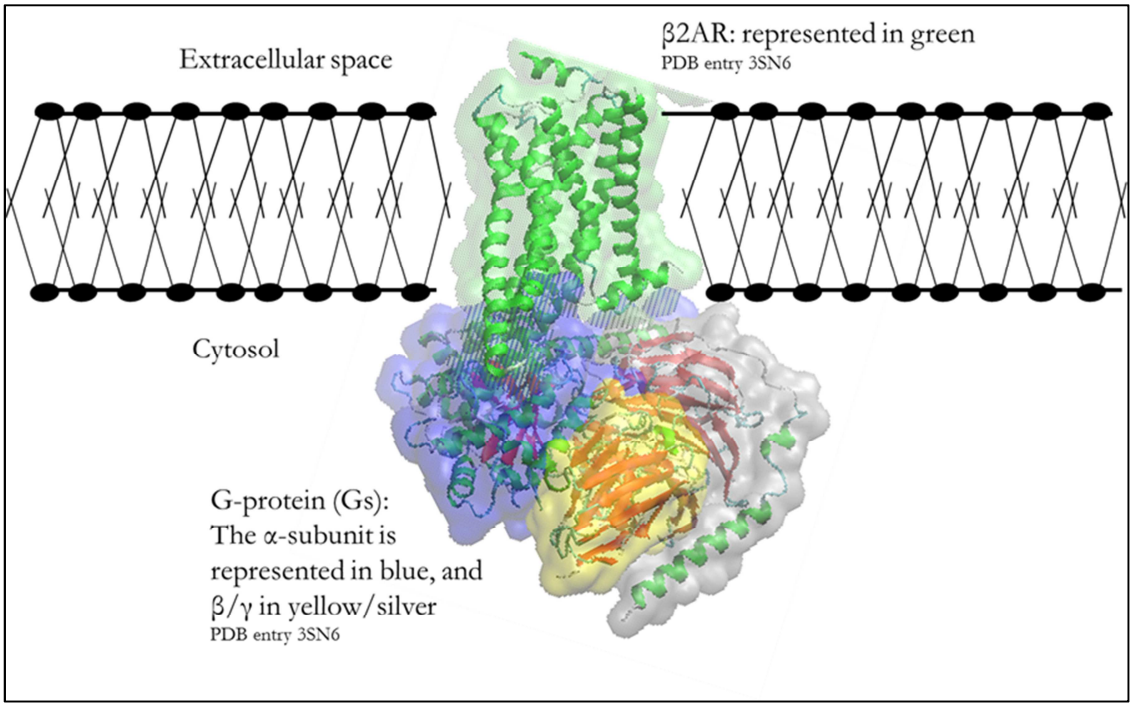

Figure 1.6. *Crystallographic structure of β2AR coupled to $G\alpha_s$. (Representation made with "visual molecular dynamics", software provided by the "center for the physics of living cells", university of Illinois)(PDB 3SN6,* (Rasmussen, DeVree, *et al.*, 2011)*)*

Comparison of active and inactive β_2AR structures

With this latest achievement, β_2AR has now been crystalized both in its inactive state bound to the antagonist carazolol (Rasmussen *et al.*, 2007), in its active state through nanobody stabilization (Rasmussen *et al.*, 2007), and its active state coupled to its G-protein Gs (Rasmussen et al. 2011). Altogether, these structures provide all the necessary information to start pinpointing the major conformational changes that seem required for activation. The most striking difference between the active and the inactive state is a 14Å outward movement of helix 6 as well as minor outward extension of helix 5 in the former. In addition, helix 3 and helix 7 show inward movements in the active state, in which also appear a previously absent α-helix in the 2nd intracellular loop and a

disordered region in the 3rd intracellular loop. (**Figure 1.7.a and b**) (Rasmussen, Choi, *et al.*, 2011; Rasmussen, DeVree, *et al.*, 2011)

For many years, as previously mentioned, the crystal structure of rhodopsin was used as a homology model to hypothesize possible activation mechanisms for other GPCRs. Several conserved motifs were highlighted as crucial in receptor regulation:(**i**) an ionic lock, represented by polar interactions between the highly conserved E/DRY motif on TM3 and a glutamate residue on TM6, believed to maintain the inactive conformation; (**ii**) a NPXXY motif in helix 7, where the proline residue distorts the α-helical shape and consequently promote hydrogen bonding with proximal side chains which further stabilizes the inactive state; and (**iii**) a so called toggle switch- the side chain of a tryptophan in the binding site shifts position upon activation which leads to the displacement of helix 6. (Rosenbaum *et al.*, 2009; Audet and Bouvier, 2012) Despite the fact that the overlay of rhodopsin and β_2AR shows an overall shared topology (**Figure 1.1.c**), no major structural differences were noticed with respect to these motifs (E/DRY, NPXXY and the toggle switch) when the inactive (Rasmussen *et al.*, 2007; Audet and Bouvier, 2012) and the active state of β_2AR were compared. This suggests a different activation scheme for rhodopsin and β_2AR. (Rasmussen, Choi, *et al.*, 2011; Rasmussen, DeVree, *et al.*, 2011; Audet and Bouvier, 2012) Given the chemical differences between the specific agonists for rhodopsin and β2AR respectively, this conclusion is not very surprising.

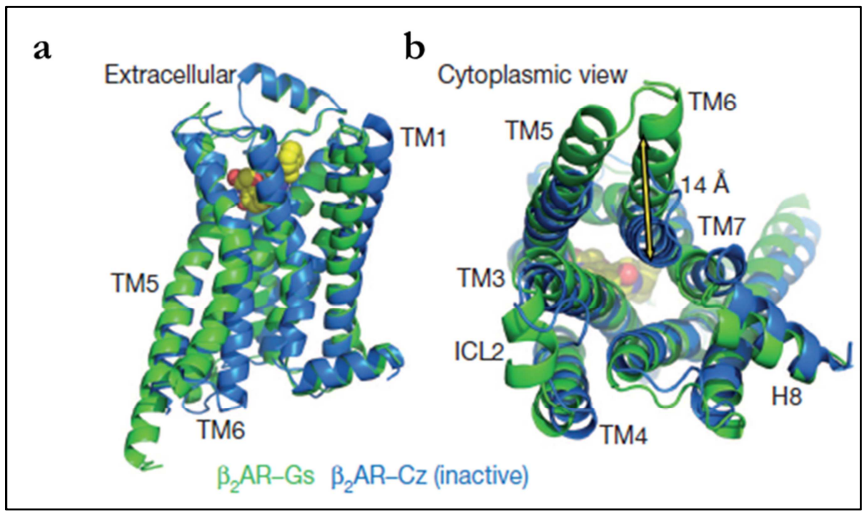

Figure 1.7. *(**a**) Side view of the overlay of the active structure (in complex with an agonist and the non-shown G-protein) and the antagonist bound inactive structure of β_2AR. (**b**) Cytoplasmic view of the same molecules as mentioned above. The main difference in the activated structure is a 14Å outward movement of helix 6 as well as minor outward extension of helix 5. In addition, helix 3 and 7 move inwards, and an α-helix is formed in the 2nd intracellular loop* (Rasmussen, DeVree, *et al.*, 2011).

Biased signaling – how one receptor regulates several pathways

As the number of available structures escalates, it becomes clear that despite topological similarities, GPCR ligand binding and signaling is vastly complex and varied. Most GPCRs have their binding pockets deep within the hydrophobic core of the protein and various factors; such as the shape, the size and the amino acid composition of this orthosteric binding site, determine which ligands are able to penetrate (Granier and Kobilka, 2012). Nonetheless, the complexity of signaling stretches far beyond the mere consequence of a single ligand triggering a predefined cascade of conformational changes. In fact, some hormones seem to activate functionally distinct receptors and depending on the nature of the ligand, a given receptor might enter either an activation- or on the contrary a repression-pathway via β-arrestin recruitment and internalization via a selection mechanism that goes under the name biased signaling (Lefkowitz and Shenoy, 2005; Hara *et al.*, 2011; Rajagopal, 2013). An example of biased signaling has been shown for β_2AR, where conformational changes of helices 7 and 8 are mandatory for the β-arrestin pathway, whereas G-protein activation involves helix 6 (Hara *et al.*, 2011).

It is also noteworthy that the C-terminus of some GPCRs contains specific phosphorylation sites for kinases. The exact role of these GPCR-kinases in the signaling process, aside their roles in β-arrestin dependent desensitization and internalization, remains to be elucidated (Lefkowitz and Shenoy, 2005; Rajagopal, 2013).

1.2 "Induced fit" or "conformational selection": that is the question!

X-ray crystallography, nuclear magnetic resonance (NMR), and other structural approaches have been proven useful to elucidate the molecular structures of receptors in various states, but these techniques do not provide any dynamic information on transitions between states. However, crystallization difficulties (Lebon *et al.*, 2011; Rasmussen, Choi, *et al.*, 2011) and biophysical data (Peleg *et al.*, 2001; Bockenhauer *et al.*, 2011) attest that GPCRs are in fact highly dynamic molecules, and several models have been put forward to account for the conformational changes that regulate receptor activation. Two main theories– the theory of conformational selection (Monod *et al.*, 1963) and the theory of the induced-fit mechanism (Pauling 1940, Koshland 1959)- have drawn a lot of attention and have been widely debated for many years.

According to the "induced-fit hypothesis", also known under the name of "the ligand driven model", ligands bind to a highly populated resting conformation of the protein. The binding of a specific ligand subsequently leads to the adjustment of the molecule as so it adopts a structurally different conformation which corresponds to the fully active state (Changeux and Edelstein, 2011; Changeux, 2012) (**Figure 1.8**).

In contrast to the induced-fit model, the conformational selection hypothesis states that the protein continually explores all possible spatial conformations even in the absence of regulatory ligands. Each conformation constituting this preformed equilibrium is defined by a specific energy directly resulting from its chemical bonds and interactions with low energy states being more populated. Therefore, the role of ligands would be to modulate the energetic barrier and shift the equilibrium toward a given state (Deupi and Kobilka, 2010). This idea constitutes the very basic principle of the generally known Monod-Wyman-Changeux (MWC) model. (Changeux Jean-Pierre and Podleski Thomas, 1968; Changeux and Edelstein, 2011; Changeux, 2012) (**Figure 1.8**).

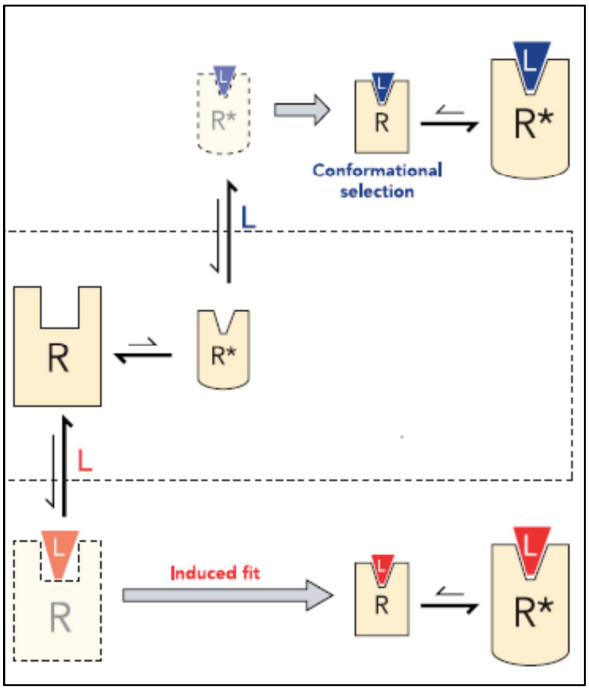

Figure 1.8. *Illustration of the two main models that describe the mechanism by which an agonist activates its target receptor. According to the conformational selection model, the receptor explores constantly all possible spatial conformations, even in absence of ligands, suggesting that the energy required to cross the energetic barrier between states is fairly low. Nonetheless, the inactive state is the lowest energy state and therefore the most populated. The effect of the agonist is to lower the energetic barrier further toward the activated state and consequently shift the equilibrium. According to the induced fit model, the receptor in its unbound form exclusively populates the inactive state. The role of the agonist is to contribute with the energy necessary to cross the energetic barrier toward the active state.*

Despite the fact that no direct evidences in favor of the theory of conformational selection have been presented for GPCRs, many observations are in line with the MWC-model. First and foremost, approximately 40% of all GPCRs exhibit constitutive basal activity, which can be further increased with point-specific mutations. This strongly argues that a fully active conformation can be reached in absence of ligands and led to the hypothesis that the level of basal activity directly reflects the degree of flexibility of the protein (Kobilka and Deupi, 2007). In addition, identical structural conformations have been solved by crystallography and X-ray diffraction with different ligands (Audet and Bouvier, 2012). In a number of cases, these ligands activate different intracellular pathways, which contradicts the model where merely inducing an active conformation would be sufficient to modulate the degree of activation and determine which signaling cascade to initiate (Changeux and Edelstein, 2011; Changeux, 2012).

Due to the broad variety of activating ligands, it is highly unlikely that all GPCRs undergo the same activation mechanism. It might be that rhodopsin indeed obeys an "induced-fit mechanism" whereas more flexible GPCRs such as β_2AR probably explores a great number of conformational states even in the absence of ligands. In fact, a recent NMR study clearly demonstrated that β_2AR constantly oscillates between a set of conformations and that an agonist alone is not sufficient to stabilize the fully active state (**Figure 1.9.a-b**) (Nygaard *et al.*, 2013). In this investigation, they demonstrated that the simultaneous presence of a high affinity agonist and a G-protein-mimicking

nanobody was necessary to entirely shift the equilibrium toward the active state, and that this fully active state was slightly different from that reached with an agonist alone. To conclude, the authors suggest that the conformational link between the orthosteric binding site and the G-protein interface is very flexible, which explains the existence of a certain degree of basal activity for the empty receptor, and that the role of the agonist is to destabilize the inactive state, which subsequently would allow β_2AR to engage in one of several alternative signaling pathways (Nygaard *et al.*, 2013) (**Figure 1.9.d**).

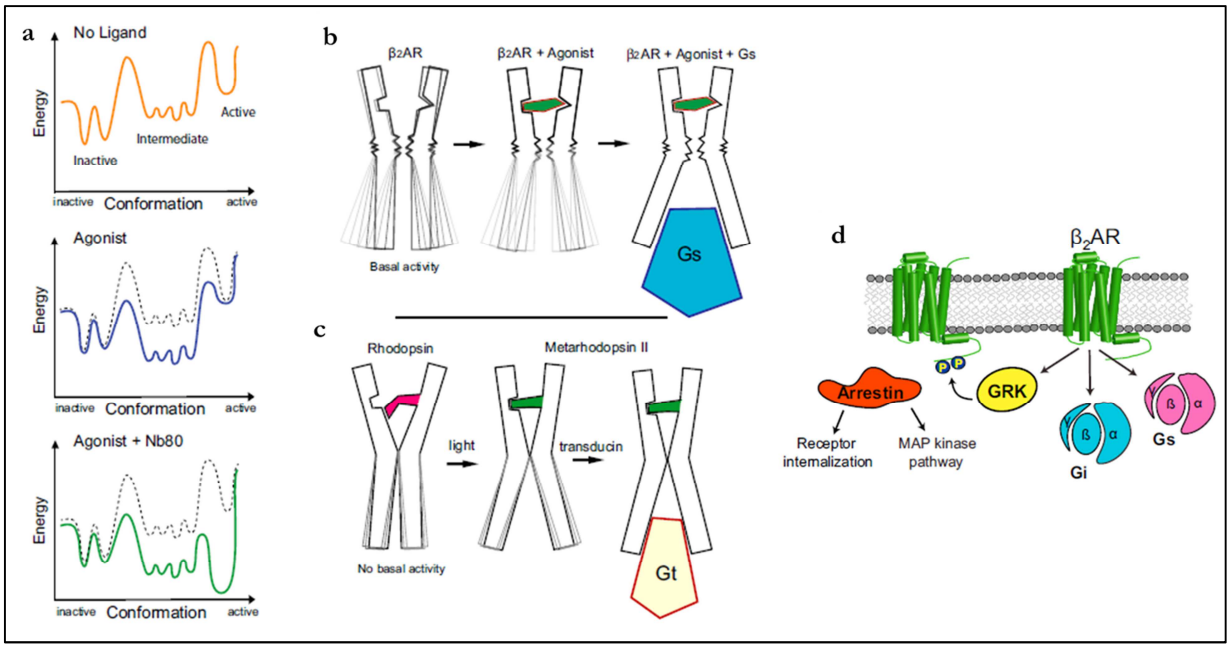

***Figure 1.9**. (**a**) Schematic illustration of β_2AR free energy landscapes along the activation pathway, in the absence of ligands (top), with an agonist (middle) and with the agonist + G-protein-mimicking nanobody (lower). The conformational link between the orthosteric binding site and the G-protein coupling interface is highly flexibly and the receptor transitions between a set of conformations with local energy minima on a sub-millisecond time scale. The effect of the agonist seems to be a destabilization of the inactive state, and, to some degree, a decrease of the energetic barrier toward the fully active state. Nonetheless, the presence of a G-protein (or G-protein-mimicking nanobody) is required to start populating this completely active state. (**b**) Illustration of the conformational dynamics of β_2AR, described by the free energy landscapes in (a). An agonist alone is not capable of stabilizing a fully active state in absence of the G-protein, but increases the overall dynamic behavior. (**c**) In the case of rhodopsin, no basal activity is detected and the agonist is assumed to be capable of inducing the fully active conformation, even in the absence of the G-protein. (**d**) The hypothesis that the agonist solely increases the dynamics instead of stabilizing the fully active state offers the possibility for the receptor to engage in one of many alternative signaling pathways.*(Nygaard *et al.*, 2013)

Keeping these activation models in mind, the question regarding the mode of action of partial agonists can now be addressed. Two main hypotheses have emerged. The first hypothesis argues that the partial agonist induces/stabilizes a conformational state that is different from the one obtained with the full agonist, and which is only sub-optimal for G-protein activation. The second hypothesis suggests that the same conformation is reached with the partial agonist as with the full agonist but with lower efficacy, resulting in less activation events despite similar affinities.

1.3 Metabotropic Glutamate Receptors

Throughout my thesis, I have focused my research on a class C member of the GPCR superfamily, namely the metabotropic glutamate receptors (mGluR). mGluRs, as well as several other members of the class C GPCR family play key roles in neural transmission. In view of this, I will begin this chapter by providing a quick overview of the nervous system, and then continue with a discussion on the structure and biological functions of mGluRs.

1.3.1 Introduction to the nervous system and the synapse

The nervous system is composed of two key components- the central nervous system (CNS) and the peripheral nervous system (PNS). Together they are responsible for the transmission of the chemical and electrical signals that regulate all our voluntary and involuntary actions. The CNS consists of the brain and the spinal cord, and the nerves of the PNS are in charge of mediating the message from the CNS to the rest of the body(Neuroscience, 3rd edition, Sinauer).

Neural transmission relies on the capacity of synapses to accurately propagate the signal from a neuron to its target cell. In fact, there are two different types of synapses: chemical and electrical. An electrical synapse works by directly conducting the electrical signal, known as the action potential, from one cell to the next via structures referred to as gap junctions. In contrast, upon stimulation, a chemical synapse releases a messenger molecule, generally known as a neurotransmitter, into the synaptic cleft. These neurotransmitters activate specific transmembrane receptors in the postsynaptic cell, and the outcome is either a modulation of the activity of one of the various ion channels, involved in depolarizing the membrane and propagate the action potential, or a regulation of gene expression via intracellular signaling pathways. Two of the main neurotransmitters are the excitatory neurotransmitter glutamate and the inhibitory neurotransmitter γ-aminobutyric acid (GABA). In fact, practically all excitatory neurons in the CNS are glutamatergic and more than 50% of all synapses in the brain release glutamate. In addition, glutamate is incapable of crossing the blood-brain barrier and has, for this reason, to be synthesized in the pre-synaptic neuron (Neuroscience, 3rd edition, Sinauer).

In addition to regulating mGluRs, glutamate also binds to postsynaptic ionotropic glutamate receptors (iGluRs). The three members of iGluRs are NMDA receptors, AMPA receptors and

kainate receptors, and they are all non-selective cation channels for Na^+, K^+ and Ca^{2+}, thereby generating excitatory responses (Neuroscience, 3rd edition, Sinauer).

To fully comprehend the present study, a more thorough introduction of glutamate is in order. In eukaryotes, the D-isoform of this non-essential (i.e. synthesized by the organism) small amino acid of 147 Da is very rare. Therefore, in the context of this thesis, whenever glutamate is mentioned, it is the L-glutamate isoform that is referred to. In addition to its role in the nervous system, glutamic acid is an important amino acid for the synthesis of proteins and is often subject to post-translational modifications. Even in its free form, glutamate is present in the entire organism and constitutes an essential component in a variety of metabolic processes.

1.3.2 General introduction to Class C GPCRs

In humans, there are 22 genes coding for the class C GPCR-family receptors. They include: the $GABA_B$ receptor, calcium sensing receptors (CaSR), pheromone receptors and the metabotropic glutamate receptors, as well as seven orphan receptors (Wellendorph and Bräuner-Osborne, 2009; Philippe Rondard *et al.*, 2011) (**Figure 1.10**).

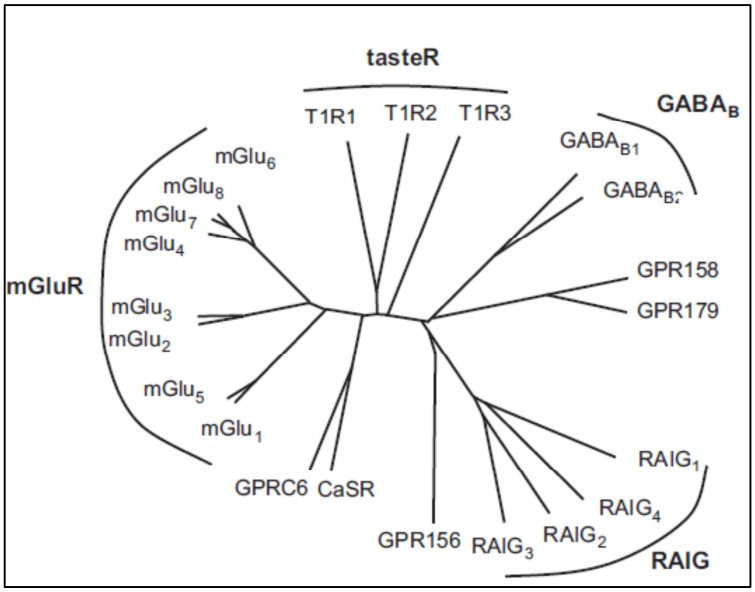

***Figure 1.10**. Phylogenetic tree of human class C GPCRs. mGluRs, the taste receptors, CaSR and GPRC6 all have a large extracellular domain composed of both a Venus flytrap domain and a cysteine-rich region, the latter being absent in $GABA_B$. For the remaining receptors: GPR156, GPR158, GPR179, and the retinoic acid-inducible receptor (RAIG), the extracellular domain has a completely different topology in comparison with the other class C members.* (P Rondard *et al.*, 2011)

Except for the orphan receptors, class C GPCRs differ from the other GPCR families by the presence of a large extracellular ligand binding domain, which will be in the focus of attention in the chapters that follow. While CaSR is critical in maintaining calcium homeostasis, (Wellendorph and Bräuner-Osborne, 2009) mGluRs and $GABA_B$ are essential in the regulation of neural transmission. $GABA_B$, the only known obligate heterodimeric GPCR, (Pin *et al.*, 2003; Padgett and Slesinger, 2010) participates in the down-regulation of neural excitability by regulating ion channels following stimulation by the main inhibitory neurotransmitter γ-aminobutyric acid (Schwenk *et al.*, 2010). mGluRs, on the other hand, are involved in the long-term modulation of neural activity upon stimulation by the excitatory neurotransmitter glutamate, and in the context of this thesis, focus will be concentrated exclusively on this group of receptors from here onward.

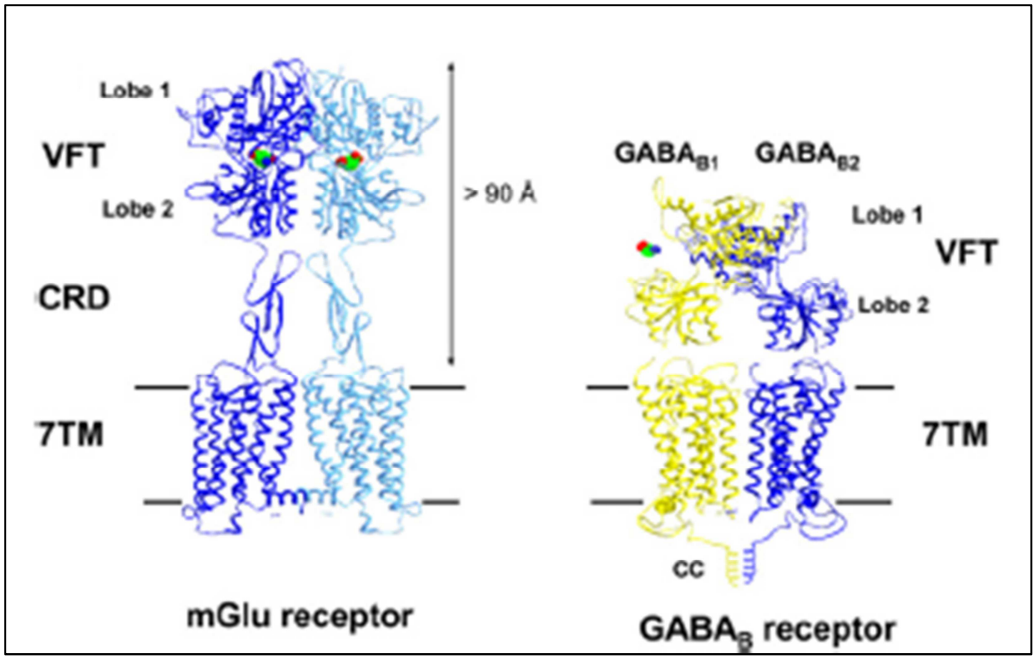

***Figure 1.11**. Illustration of the molecular structure of mGluR and $GABA_B$. They both contain a large extracellular ligand binding domain, called the venus flytrap domain (VFT) and a heptahelical transmembrane domain (7TM) responsible for G-protein activation. The main difference in the overall topology between mGluRs and $GABA_B$ is the presence of a cysteine- rich domain (CRD) that links the VFT to the 7TM in mGluRs.* (P Rondard *et al.*, 2011)

1.3.3 Biological functions of mGluRs

mGluRs are expressed throughout the central nervous system where they participate in the modulation of neural transmission through the activation of diverse second messengers pathways. In doing so, they contribute to the long-term response of regulating neural excitability (Niswender and Conn, 2010).

There are eight different subtypes of mGluRs, further subdivided into three groups based on sequence homology, the coupled G-protein and ligand selectivity. Group I comprises mGlu1 and mGlu5; Group II comprises mGlu2 and mGlu3 and Group III contains mGlu4, mGlu6, mGlu7 and mGlu8 (Conn and Pin, 1997; Bräuner-Osborne *et al.*, 2007). The sequence identity has been estimated to approximately 40-50% between groups and 60-70% within the groups (**Figure 1.12.a**) (Wellendorph and Bräuner-Osborne, 2009) and several of the subtypes also exist in different splice-variants, consequently resulting in a rich variety of possible signaling combinations. (Niswender and Conn, 2010)

The localization within the synapse varies for different subgroups. The receptors belonging to group I, mGlu1 and mGlu5 are mostly post-synaptic whereas the group III members, mGlu4, mGlu6, mGlu7 and mGlu8 are almost exclusively pre-synaptic. The group II members, mGlu2 and mGlu3, however, can be localized both in pre- and post-synaptic membranes. (**Figure 1.12.b**)

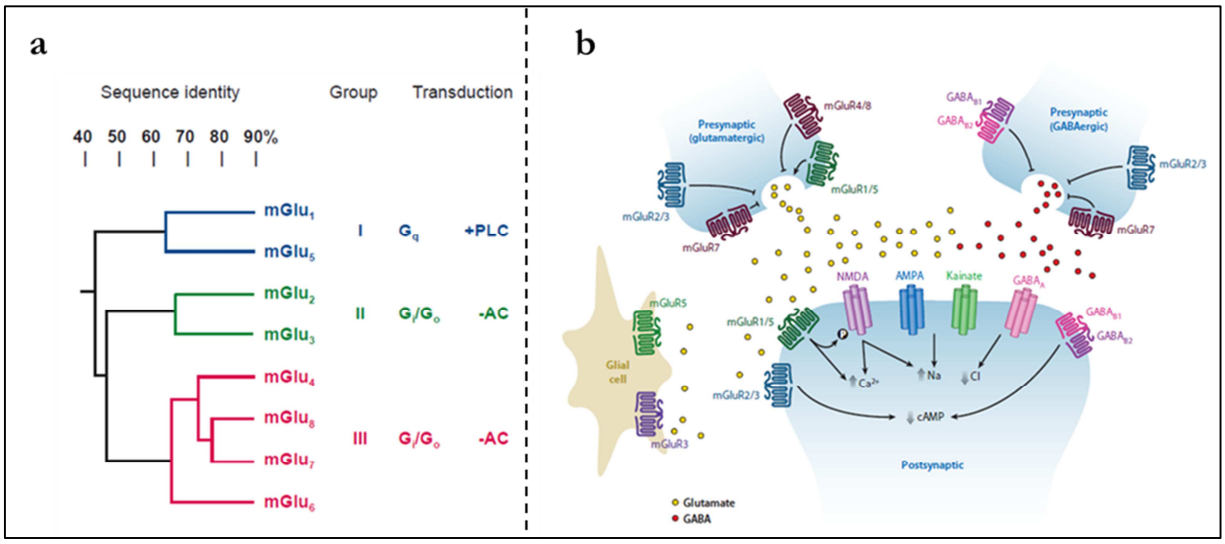

Figure 1.12. *(**a**) Phylogenetic affiliation of the mGluR family, illustrating the sequence identity between subgroups. Sequence identity is about 60-70% within subgroups and approximately 40-50% between subgroups (Tocris Bioscience Scientific Review Series). (**b**) Schematic illustration of the synaptic localization of the different mGluRs, $GABA_B$ and iGluRs. With regard to mGluRs, the group I members mGlu1 and mGlu5 are generally localized in post-synaptic neurons but they are occasionally found in pre-synaptic axons, as well. Additionally, mGlu5 is also expressed in astrocytes. The group II members, mGlu2 and mGlu3, are expressed in both pre and post-synaptic neurons whereas the group III members mGlu4, mGlu7 and mGlu8 are almost exclusively pre-synaptic. In addition, mGlu6 is exclusively expressed in the retina. The cartoon also shows the localization of the inhibitory class C GPCR member $GABA_B$ and the different ionotropic glutamate receptors, NMDA, AMPA and kainate receptors. (Niswender and Conn, 2010)*

1.3.4 Molecular structure of mGluRs

The different members of the mGluR family share the same molecular structure. They are exclusively expressed at the cell surface as homodimers, with each monomer consisting in the N-terminus of a large extracellular domain linked to the heptahelical transmembrane domain (7TM) via a cysteine-rich domain (Huang *et al.*, 2011a; Philippe Rondard *et al.*, 2011; Bruno *et al.*, 2012). (**Figure 1.13**)

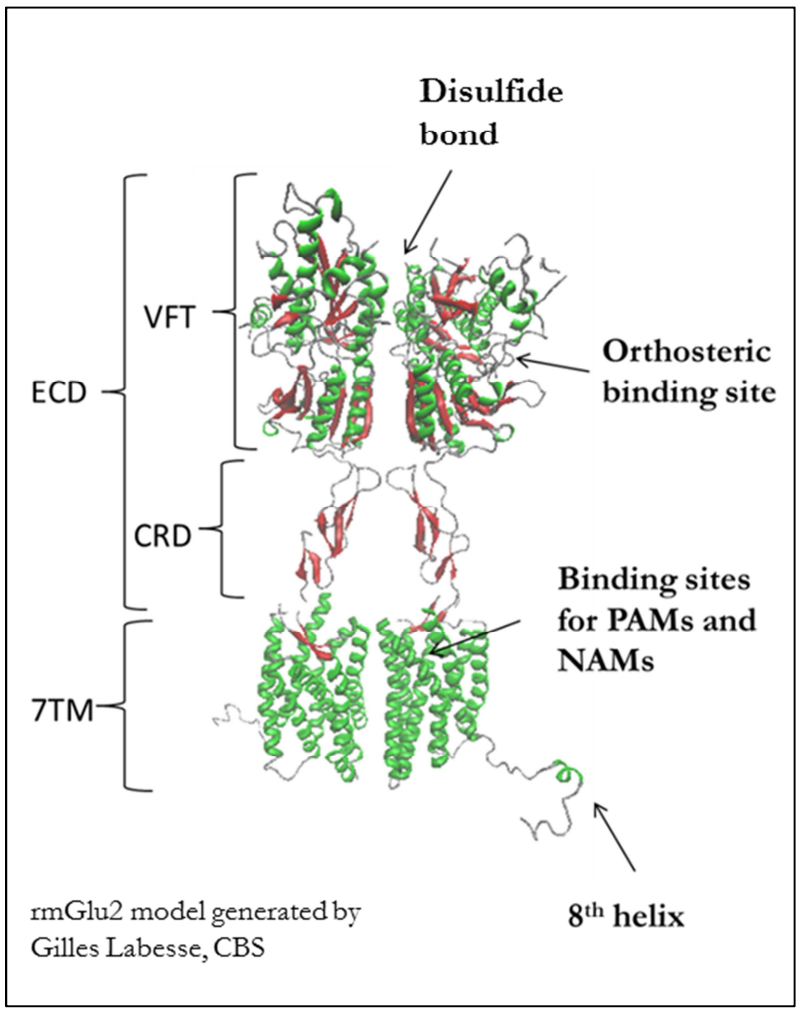

***Figure 1.13**. Molecular structure of the metabotropic glutamate receptor homodimer.*

The heptahelical trans-membrane domain is connected to the extracellular ligand binding domain (VFT), via a cysteine-rich domain (CRD). The dimeric structure is maintained by a disulfide bond between the two first lobes in each monomer, and further reinforced by hydrophobic interactions in the same region. Orthosteric ligands bind in the cleft formed between lobe 1 and lobe 2 whereas PAMs and NAMs bind within the 7TM.

Molecular structure of the extracellular domain- VFT and CRD

Several structures of the extracellular domain have been solved by crystallography and X-ray diffraction (for mGlu1, mGlu3, mGlu5 and mGlu7) (**Table 1.2**). It is constituted of about 500 amino acids and presents a clamshell-like structure composed of two lobes, both presenting an α/β topology with a central β sheet surrounded by α-helices and linked together via a flexible hinge region comprised of three β-strands (Muto *et al.*, 2007). The fact that the two lobes are positioned on top of each other results in the formation of a cleft, which has been shown to be the binding site for orthosteric endogenous ligands (Kunishima *et al.*, 2000). This particular feature is the reason why the domain is commonly referred to as "the Venus flytrap domain" (VFT) (Philippe Rondard *et al.*, 2011; Bruno *et al.*, 2012) (**Figure 1.13**).

The lobe 1 of the VFT domain also contains a strategically positioned cysteine that stabilizes the homodimeric form of the receptor (Kunishima *et al.*, 2000). The two cysteines (one on each monomer) create a disulfide bond that links the two subunits together. In addition to this covalent bond, the dimerization region is further strengthened by hydrophobic interactions (Muto *et al.*, 2007; Philippe Rondard *et al.*, 2011). This postulation was experimentally proven by the observation that isolated VFT domains are still capable of forming dimers even in the absence of the disulfide bond (Kunishima *et al.*, 2000). Consequently, the fact that only lobe 1 is engaged in maintaining the dimeric structure provides a certain degree of spatial freedom to the dimer, and this very important point is crucial for the functionality of the receptor as we will see in the next chapter.

Furthermore, the VFT domain is linked to the heptahelical transmembrane domain via a 70-amino-acid-long cysteine-rich domain (CRD) (Muto *et al.*, 2007). The structural topology of the CRD corresponds to a succession of three short β-sheets of two anti-parallel β-strands each (Muto *et al.*, 2007). Nine of the cysteines in the CRD are strictly conserved and engaged in intra-monomer disulfide bonds, four within the CRD and one with the VFT, as first shown by mutagenesis studies (Rondard *et al.*, 2006) and later confirmed with by the resolution of the X-ray structure of the ECD of mGlu3 (Muto *et al.*, 2007).

Extracellular domain – sequence alignment and evolutionary origin

To illustrate that the general topology is conserved for all mGluRs despite a sequence identity of only ~40-50% between subgroups, **Figure 1.14** shows a sequence and secondary structure alignment of the extracellular domain of all eight mGluR subtypes, classified according to their subgroup attribution. From top-to-bottom: group I, group III and group II. Amino acids with sequence homology are highlighted in yellow, and amino acids showing strict sequence identity are highlighted in pink. Accordingly, the residues in orange indicate a strict conservation within the subgroup.

Moreover, the black numbers indicate the positions and enumerate the order of the conserved disulfide bonds. The cysteine engaged in the disulfide bond between the protomers that help maintaining the dimeric structure is pointed out with a blue star.

In addition, the double arrows enclosing residues 500 to 570 designate the span of the CRD, which is composed strictly of β-strands contains most of the disulfide bonds. The number 2 label specifies the disulfide bond labeled with the VFT.

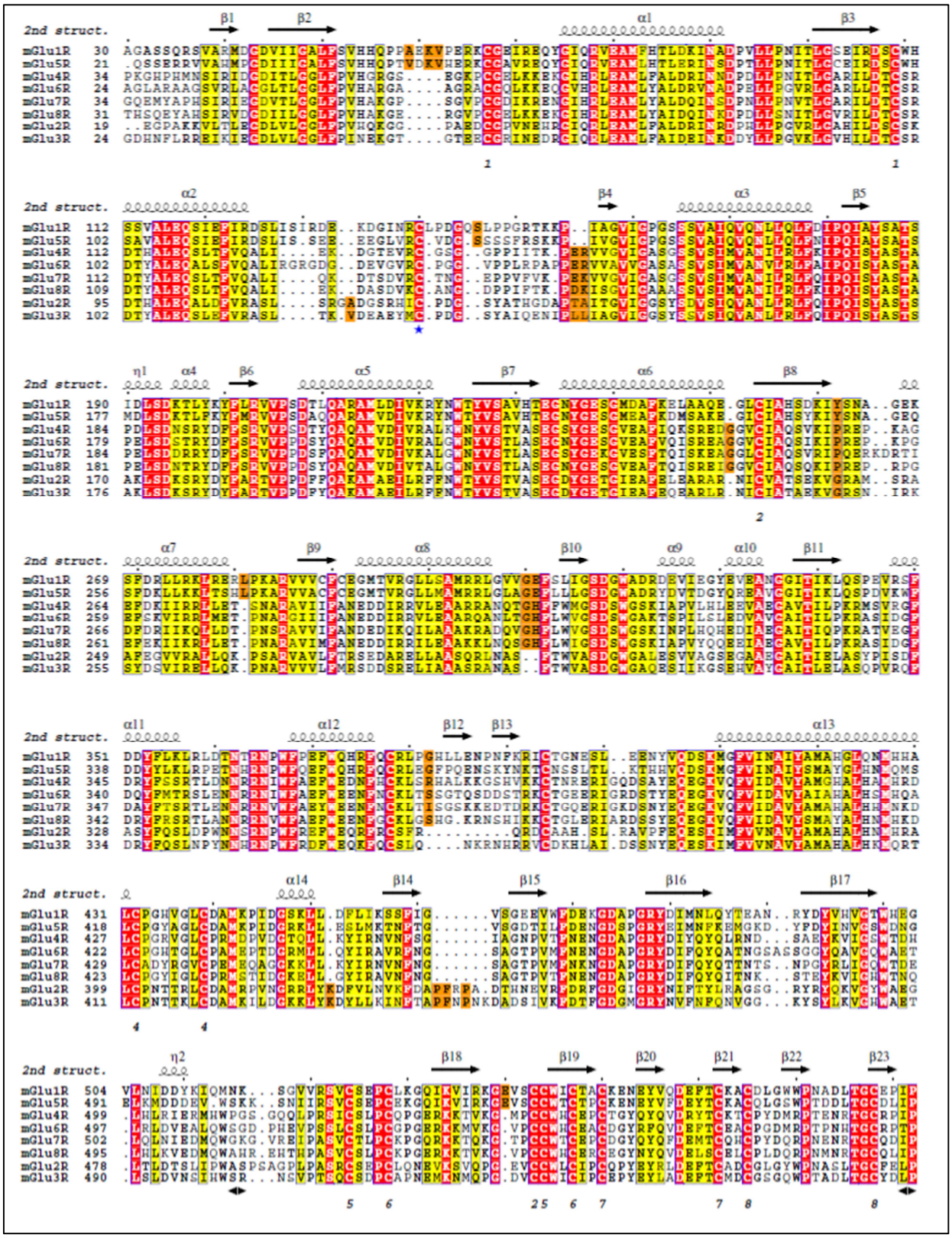

***Figure 1.14**. Sequence alignment of the extracellular domain. (espript)*

To conclude on the structural topology of the ECD of mGluRs, it is interesting to mention that the VFT domain of class C GPCRs, and the N-terminal domain of iGluRs, share structural similarities with soluble bacterial periplasmic amino acid binding proteins (PBPs), which suggest a common evolutionary origin. In addition to the presence of a transmembrane domain for class C GPCR and iGluRs, the main difference between the receptors is that PBPs are able to bind a variety of small molecules and not only one specific amino acid as in the case of mGluRs and iGluRs. Furthermore, it is thought that the evolutionary divergence emerged through three internal duplications events at the early stage of vertebrates, in parallel to a positive selection mechanism, responsible for subfamily specificities (Cao *et al.*, 2009) (**Figure 1.15**).

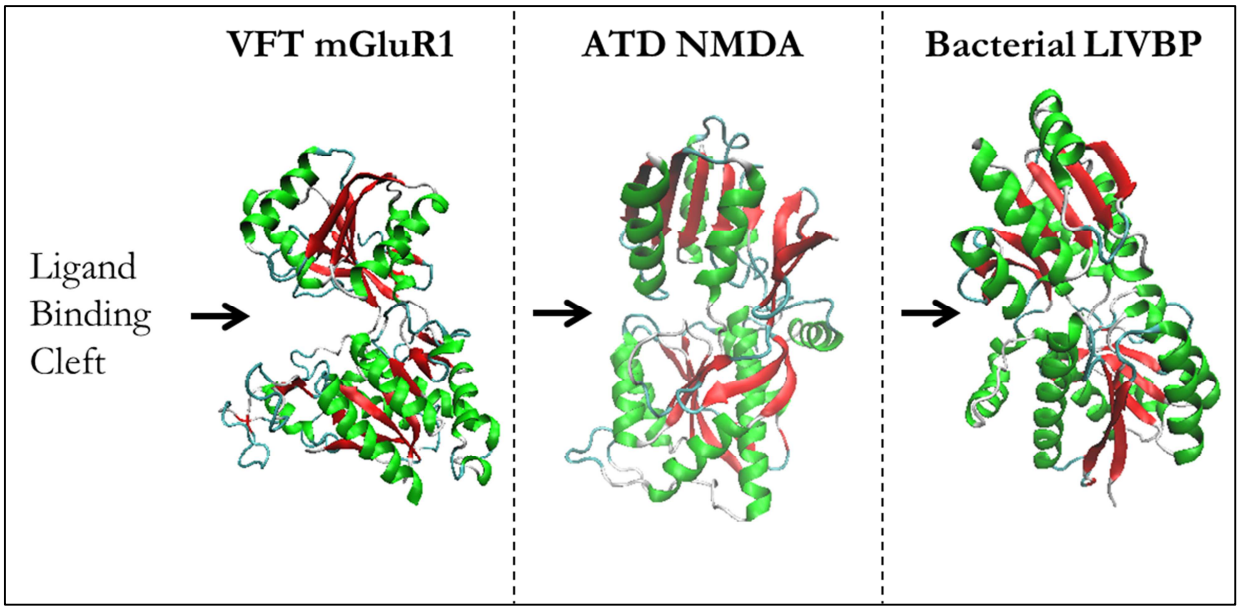

***Figure 1.15**. Crystal structures of the amino acid binding domain for, from left to right, the VFT domain of mGlu1 (PDB 1ISS), the amino terminal domain of NMDA (PDB 3HSY) and the Escherichia coli ABC leucine/isoleucine/valine transport system (PDB 1Z17). All structures present a general fold of two lobes on top of each other between which the amino acid binding cleft is formed, indicative of a common evolutionary origin. (Represented with VMD)*

Structure and sequence alignment of the heptahelical transmembrane domain

No crystal structure has yet been solved for the 7TM domain of a class C GPCR. Despite the low homology with the 7TMs of class A GPCRs (12% sequence homology with rhodopsin) (Nordström *et al.* 2011, online supp), the structural topology is very similar to the GPCR folding already described for class A GPCRs with a transmembrane domain composed of seven α-helices linked via three extracellular and three intracellular loops and an 8th helix in C-terminus.

The similar overall structure is not the only argument to suggest a related activation model for mGluRs and rhodopsin. For instance, several amino acids and motifs shown to be fundamental in class A GPCR activation have counterparts in mGluRs. Although the crystal structure is necessary to ascertain their roles in the activation process, for example, a tryptophan in TM6, which is conserved and shown to be important for the activation of class A GPCRs- is likewise found in mGluRs and involved in the recognition of positive and negative allosteric modulators (Pin *et al.*, 2003). Moreover, candidates to carry out the functions of the D/ERY and the NPxxY motifs ((xPKxY in class C GPCRs) as well as other crucial amino acids for the stabilization of the active and the inactive state are also present in class C GPCRs (Pin *et al.*, 2003; Binet *et al.*, 2007). Hence, the 2nd and the 3rd intracellular loops are most likely involved in G-protein coupling and selectivity (Granier and Kobilka, 2012; Lebon and Tate, 2012) even though, in the case of mGluRs, it seems like the 2nd intracellular loop plays the most critical role in G-protein activation as shown in mutagenesis in studies on mGlu8 where alterations of the 2nd intracellular loop strongly affect the binding and activation of the G-protein. Additionally, it was only when the 3rd intracellular loop in rhodopsin was replaced with the 2nd intracellular loop (and not the 3rd) of mGlu6 that the receptor recovered its functionality. (Yamashita *et al.*, 2001) Furthermore, the 2nd loop has also been shown to be the target for various kinases (Niswender and Conn, 2010). Nonetheless, in spite of the quite obvious role of intracellular loop 2, the existence of a conserved motif in intracellular loop 3 for all mGluRs suggests that it is also involved in G-protein regulation (Pin *et al.*, 2003).

Moreover, the 8th helix seems to be important in modulating G-protein coupling, and several studies provide evidence showing its importance as a target site for alternative splicing, phosphorylation and protein-protein interactions (Bruno *et al.*, 2012). It has also been suggested that the C-terminal domain remains stuck against the 3rd intracellular loop in absence of activation, and thereby prevents the interaction with the G-protein (Mary, 1998; Pankevych *et al.*, 2003). Consequently, it is thought that the C-terminal gains in mobility upon activation and several recent

articles investigating this possibility for closely related GPCRs seem to be in agreement with this postulation (Ghanouni *et al.*, 2001; Granier *et al.*, 2007; Yanagawa *et al.*, 2011; Rahmeh *et al.*, 2012).

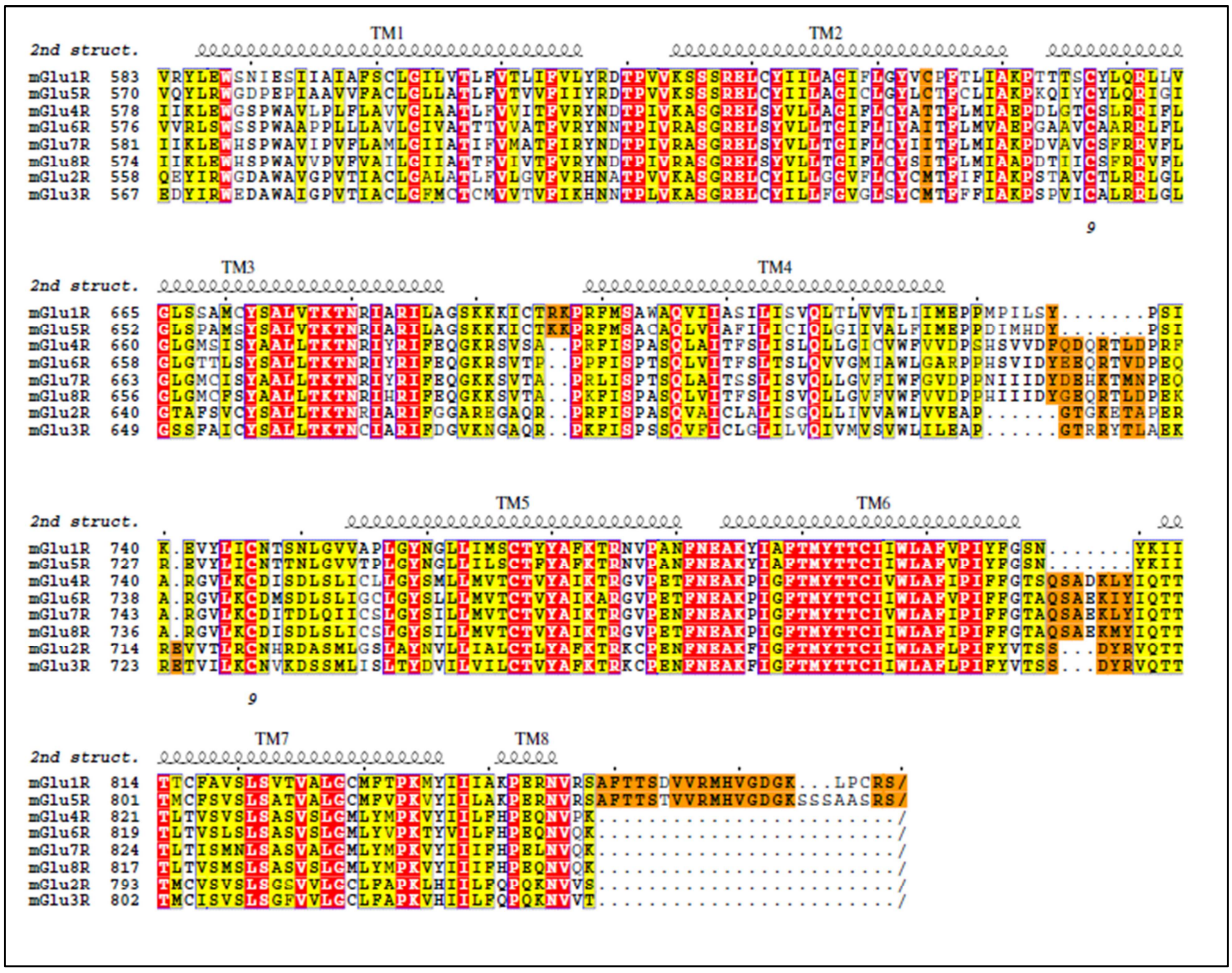

***Figure 1.16**. Structural alignment of the 7TM. The color code is the same as in Figure 1.15. It is highly interesting to point out that TM 3 and TM 6 contain a high degree of sequence conservation, due to an evolutionary pressure that probably signifies important roles in functionality.*

1.3.5 Suggested mGluR activation model

Activation of the extracellular domain

mGluRs are thought to be activated according to a model derived from the different crystal structures of the VFT domain, which exists either empty or bound by agonists or antagonists. (**Table 1.2**) The model argues that upon biding of glutamate in the VFT orthosteric binding site, there will be a stabilization of the closed cleft state (Kunishima *et al.*, 2000) (**Figure 1.17b**). In fact, evidences suggest that even though, the binding of one molecule of glutamate in one VFT monomer is sufficient for activation, the binding of two molecules of glutamate, one in each monomer, results in a more significant cellular response (Kniazeff *et al.*, 2004; Yanagawa *et al.*, 2011).

Following the closure of the binding cleft, the VFT dimer undergoes a reorientation of 70° that approaches the two CRD (Kunishima *et al.*, 2000) (**Figure 1.17.a**), and this step is crucial for the transduction of the activation signal to the 7TM. Indeed, it was recently shown that if any of the conserved cysteines in the CRD is mutated, the VFT can no longer transduce the activation signal from the VFT to the 7TM (Huang *et al.*, 2011a). Moreover, if the two CRDs are cross-linked, the receptor is constitutively active and non-responsive to ligands (Huang *et al.*, 2011a), which further demonstrates the importance of the reorientation of the VFT dimer in the activation process.

Accordingly, two major conformational changes of VFT dimer seem mandatory for receptor activation:

1. The open(O)-closed(C) transition of the binding cleft

2. The resting(R)-active(A) transition that designates the reorientation of the dimer

Consequently, the VFT dimer might adopt six possible conformations: R_{OO}, R_{CO}, R_{CC}, A_{OO}, A_{CO}, and A_{CC}, where R or A refers to relative conformation of the VFT dimer and the lower case C or O represent the state of the binding cleft for the two monomer respectively (**Figure 1.17**).

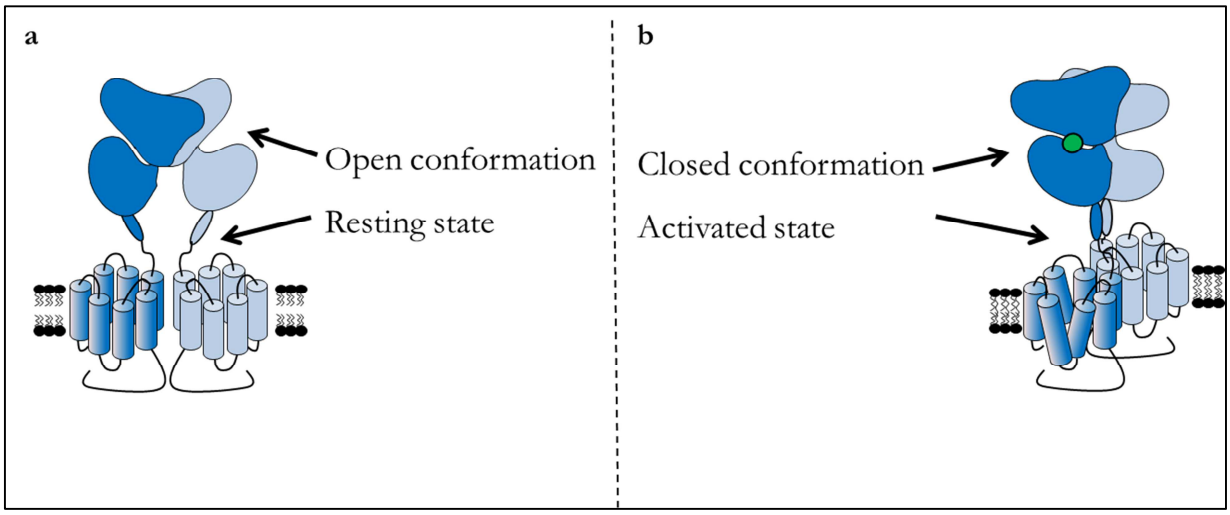

***Figure 1.17**. (**a**) Pictogram of the resting open conformation (Roo), the two CRD are far apart. (**b**) Pictogram of the active closed conformation, the dimer has undergone a 70° relative reorientation and the distance between the two CRD has now significantly decreased.*

Interestingly, as more and more crystal structures of the extracellular domain are generated, it becomes clear that not all are consistent with this formerly accepted model. For instance, several structures in presence of agonists exhibit R_{OO} conformations and others show the receptor in an A_{CC} conformation even in presence of antagonists (**Figure 1.18**). Altogether, these observations suggest a conformational selection mechanism and therefore further studies are required in order to determine the dynamics of the activation mechanism.

Year	1st author	PDB entry	mGluR	With CRD?	Ligands	Closed VFT	VFTD dimer orientation (A/R)	Code
2000	Kunishima	1EWT	mGlu1	NO	-	0/2	R	Roo
2000	Kunishima	1EWV	mGlu1	NO	-	1/2	A	Aco
2000	Kunishima	1EWK	mGlu1	NO	2 x Glu	1/2	A	Aco
2002	Tsuchiya	1ISS	mGlu1	NO	2 x MCPG	0/2	R	Roo
2002	Tsuchiya	1ISR	mGlu1	NO	2 x Glu + 1 Gd3+	2/2	A	Acc
2007	Muto	2E4Z	mGlu7	NO	-	0/2	R	Roo
2007	Muto	2E4U	mGlu3	YES	2 x Glu	2/2	R	Rcc
2007	Muto	2E4V	mGlu3	YES	2 x DCG-IV	2/2	R	Rcc
2007	Muto	2E4W	mGlu3	YES	2 x 1S,3S-ACPD	2/2	R	Rcc
2007	Muto	2E4X	mGlu3	YES	2 x 1S,3R-ACPD	2/2	R	Rcc
2007	Muto	2E4Y	mGlu3	YES	2 x 2R,4R-APDC	2/2	R	Rcc
2009	Dobrovetsky	3KS9	mGlu1	NO	2 x LY341495	0/2	A	Aoo
2010	Dobrovetsky	3LMK	mGlu5	NO	2x Glu	2/2	A	Acc

***Table 1.2**. Available crystal structures for the extracellular domain with or without the ECD and in presence of various ligands. Between 2000 and 2007, all structures were in total agreement with the hypothesized activation model (green) suggesting a closure and reorientation of the dimer upon activation (Acc) and a stabilization of the open-resting conformation in presence of antagonists (Roo). However, more recently, several new structures have been solved and they are not all consistent with the proposed activation scheme as some are presenting the "forbidden" conformations Aoo and Rcc (red)*

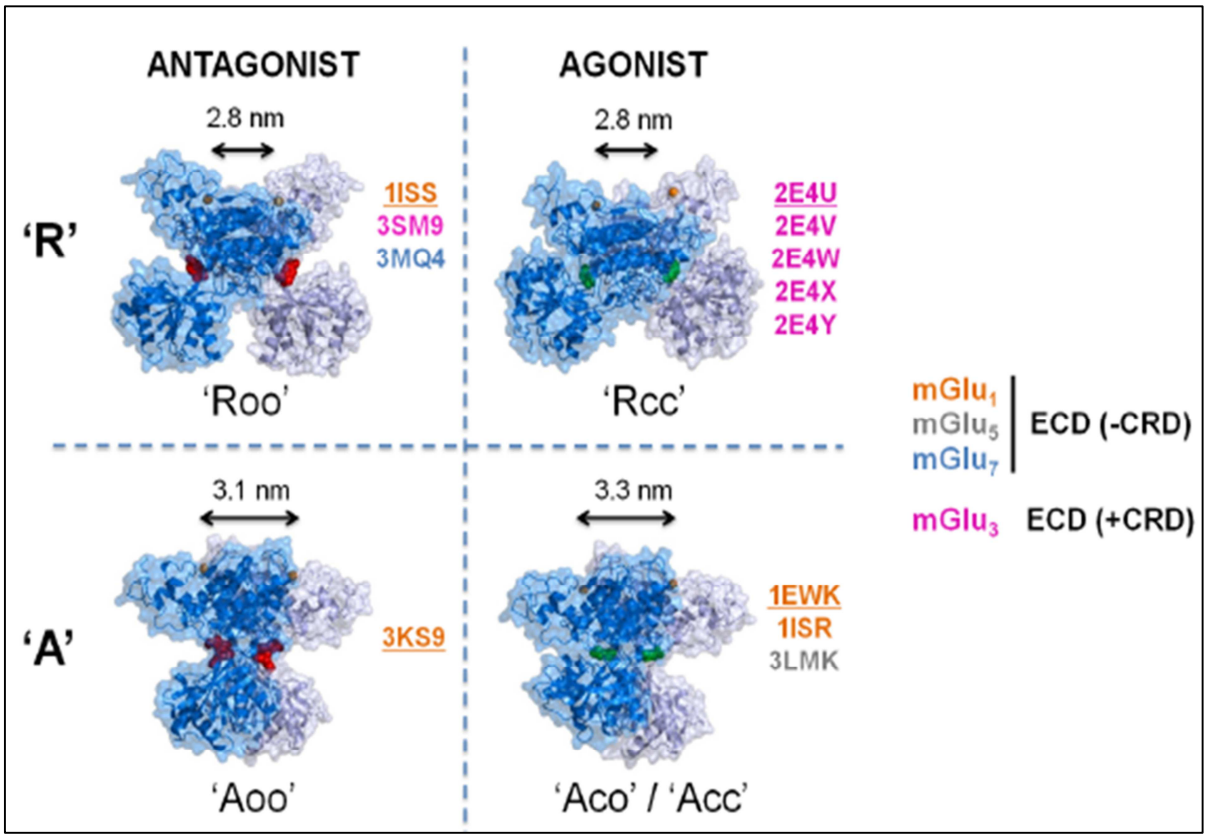

***Figure 1.18**. Crystal structures for mGluR 1, 3, 5 and 7 from **table1.2** in the resting conformation (upper) and in the active conformation (lower). Interestingly, the Rcc (upper right) conformation is observed in presence of an agonist and the Aoo (lower left) conformation is crystalized with an antagonist, neither of which is consistent with the postulated activation model.* (Doumazane *et al.*, 2013)

Activation model for the transmembrane domain

As the structure of the mGluR 7TM still remains to be solved, little is known concerning the different conformational changes occurring within this domain upon activation. Nevertheless, two major studies have provided some first experimental evidence suggesting that the conformational change that brings the two CRDs together triggers an interdomain reposition, followed by an intradomain movement within the 7TM. A first ensemble FRET examination carried out by Tateyama *et al* demonstrated that the distance between the two intracellular loops of the mGlu1 dimer decreased whereas the distance between the first intracellular loops increased upon activation, a result that can only be interpreted as a reorientation of the two subunits forming the dimer (Tateyama *et al.*, 2004). This line of investigation was then pursued by Hlavackova *et al,* who in

addition to measuring the intermolecular FRET also included the intramolecular FRET, once again within the mGlu1 dimer. In fact, by introducing fluorescent proteins (eYFP and/or eCFP) either in the 2nd intracellular loop and/or in the C-terminus, they showed that upon activation, the two subunits move closer together, resulting in an increased FRET signal. Only then does the intra-molecular conformational change takes place. The outcome of this study specified the timescale of the inter-molecular and intra-molecular movements to occur on a ~35ms and on a ~50ms timescale, respectively (Hlavackova *et al.*, 2012). The intra-molecular conformational change is most probably an increase in C-terminal mobility that enables G-protein interaction (Brock *et al.*, 2007).

Although substantial measures have to be put in place to clearly decipher the interplay between the ECD and 7TM, a recent mutagenesis study has revealed that if the VFT domain is removed, PAMs and NAMs act as full agonists and antagonists, respectively (El Moustaine *et al.*, 2012). Consequently, one might argue that the VFT domain is the dominant element in the regulation, which rather than trigger a conformational change required for activation imposes constraints on the 7TM domain and, thus, prevents it from adopting a conformation compatible with G-protein activation.

On the same note, when an ECD-only construct of mGlu1 was co-expressed in rat sympathetic neurons with the full-length monomeric construct, the two ECDs were capable of forming a dimeric receptor for which, however, the signaling was strongly reduced as shown in calcium current experiments, which, hence demonstrates the dominant negative nature of the VFT (Beqollari and Kammermeier, 2010). In view of this, it is also appealing to hypothesize that VFT only splice-variants, thought to intervene as regulators of glutamate concentrations, may additionally play a role in down-regulating the signaling response despite high concentrations of glutamate.

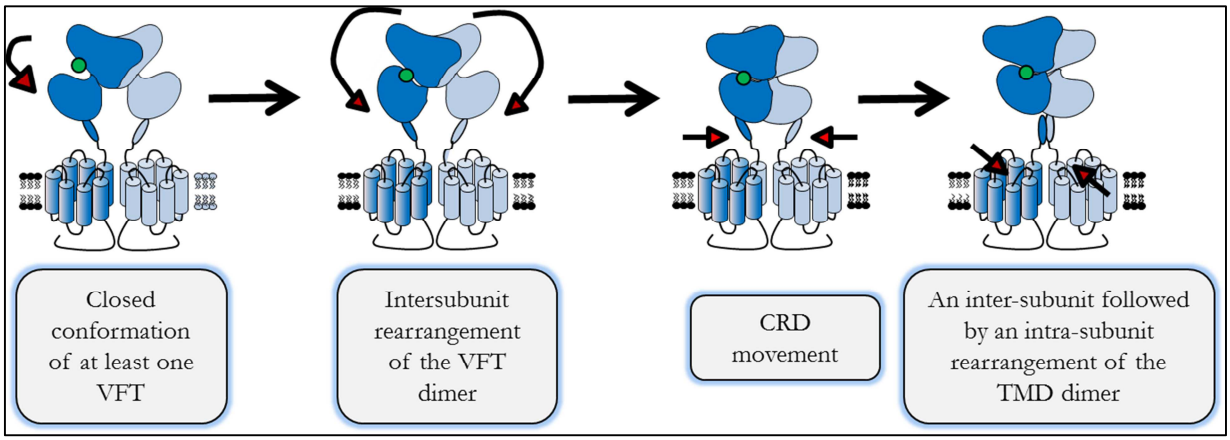
Closed conformation of at least one VFT
Intersubunit rearrangement of the VFT dimer
CRD movement
An inter-subunit followed by an intra-subunit rearrangement of the TMD dimer

***Figure 1.19**. Suggested activation model. Following activation by glutamate, at least one of the VFT closes and the VFT dimer undergoes a reorientation that brings the two CRD together. By a still unknown mechanism, the 7TM dimer goes through an intersubunit rearrangement that repositions the two protomers before at least one of them submit to an intrasubunit rearrangement that is presumed to activate the G-protein.(Adapted from the Ph.D. thesis of Etienne Doumazane)*

1.3.6 mGluR pharmacology and related disorders

A broad range of neurological and psychiatric disorders including cognitive disorders, anxiety, schizophrenia, pain, drug addiction, migraine and Parkinson's disease, are linked to mGluR expression and/or function (**Table 1.3**), and many pharmaceutical companies strive to develop new and better drugs targeting this receptor family (Yasuhara and Chaki, 2010).

Group	mGluR subtype	CNS expression	Synaptic localization	G-protein Coupling	Signaling pathways	Associated neurological disorders
Group I	mGlur1	Neurons	Generally postsynaptic	Gαq	Phospho Lipase C activation cAMP↗ MAPK	cognitive disorders, anxiety, schizophrenia ,pain
	mGluR5	Neurons Astrocytes				cognitive disorders, anxiety, schizophrenia ,pain, drug addiction, migraine, Parkinson's disease
Group II	mGluR2	Neurons	Presynaptic and postsynaptic	Gα i/o	cAMP↘ Activation K+ channels Inhibition Ca2+ channels	cognitive disorders, drug abuse, psychosis, anxiety, schizophrenia
	mGluR3	Neurons Astrocytes				schizophrenia
GroupIII	mGluR4	Neurons Cerebellum	Generally Presynaptic	Gα i/o	cAMP↘ Activation K+ channels Inhibition Ca2+ channels	anxiety/depression
	mGluR6	Retina	Postsynaptic			night blindness
	mGluR7	Neurons	Presynaptic			anxiety/depression
	mGluR8	Neurons	Generally Presynaptic			anxiety/depression

***Table 1.3**. Table summarizing the current knowledge regarding mGluR biology, in terms of subtypes, CNS expression synaptic localization, G-protein coupling, signaling pathways and the associated neurological disorders.*

It has been proven difficult to design subtype specific orthosteric drugs due to the highly conserved amino acid sequence within the VFT-binding pocket. In fact, eight residues have been shown to be directly associated with the binding of glutamate and among the 21 residues surrounding the binding pocket at a distance inferior to 6Å, nine are identical in all subfamilies (Wellendorph and Bräuner-Osborne, 2009).

The eight conserved amino acids that are involved in the binding of glutamate are distributed on both lobe 1 and 2 and stabilize the interaction via hydrogen and ionic bonds. Five of these eight amino acids interact with the amino- and carboxylic- groups of the amino acid core and three basic residues and three water molecules interact with the acid side chain (**Figure 1.20.a**) (Muto *et al.*, 2007). Their importance in the binding of glutamate is further strengthened by the fact that a mutation of any of these amino acids strongly decreases the affinity (Kniazeff *et al.*, 2004). In the case of the mGlu3 partial agonist (2S,2'R,3'R)-2-(2',3'-dicarboxycyclopropyl)glycine DCG-IV, two of the water molecules are replaced with a tyrosine to stabilize the γ-carboxyl group via wan-der-Waals interactions (**Figure 1.20.b**). In contrast, competitive antagonists generally act by binding one of the two lobes and thereby prevent by steric hindrance or electrostatic repulsions the binding of agonists (Kniazeff *et al.*, 2004).

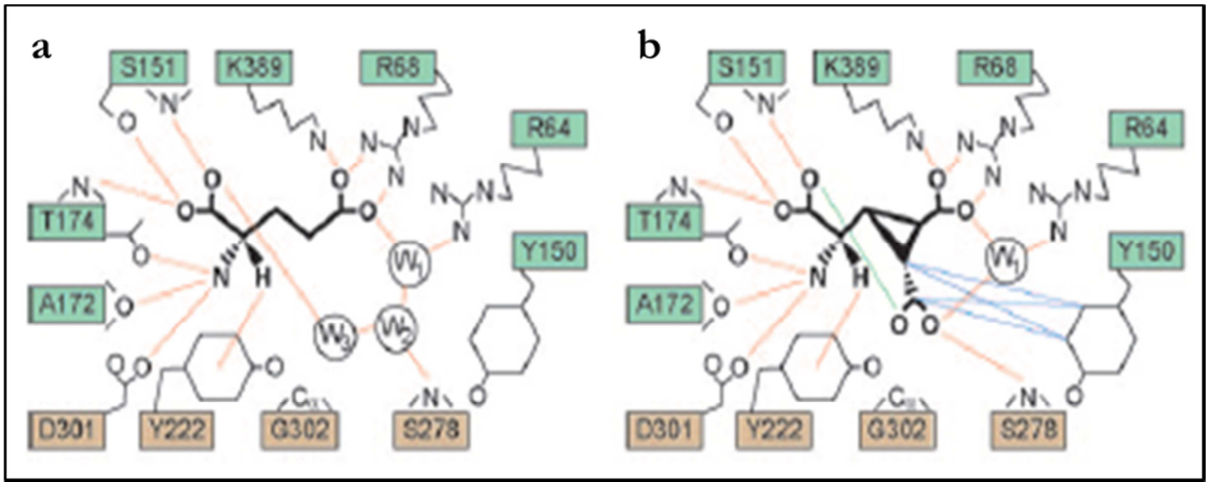

***Figure 1.20**. Illustration of the interaction between the agonist Glutamate (right) and the partial agonist DCG-II (left) in the orthosteric binding site of mGlu3.See text for details.* (Muto *et al.*, 2007)

Furthermore, crystal structures and mutagenesis studies, conducted to alter the affinity for DCG-IV showed that one of the vital residues involved in DCG-IV efficacy is not localized within the binding pocket itself but seems to play a role in the stabilization of the pocket from a distance (Muto *et al.*, 2007). Although this observation remains to be verified for mGlu2, the other mGluR group II member, it is of high importance to point out that DCG-IV has been shown to be a partial agonist on both mGlu2 and mGlu3 (Doumazane *et al.*, 2013). Therefore, not only does this observation highlight the substantial measures that will need to be put into place in order to specifically target the different members of the mGluR-family, but the fact that mGlu3 has been

crystalized in the same active conformation with a full agonist and a partial agonist is very interesting from a more general standpoint, as it agrees well with the conformational selection model.

Another difficulty intensifying the problem of finding compounds that are truly subtype-specific is their hydrophilic nature, which limits their capacity to cross the blood-brain barrier. Consequently, despite a certain number of possible candidates, not a single drug targeting the orthosteric binding site is currently on the market or in clinical trials. For this reason, the discovery of the previously mentioned positive and negative allosteric modulators is a significant development in the field of mGluR pharmacology. PAMs and NAMs are more hydrophobic in nature, which is quite logical considering that they bind within the 7TM domain, and therefore represent promising future drug candidates.

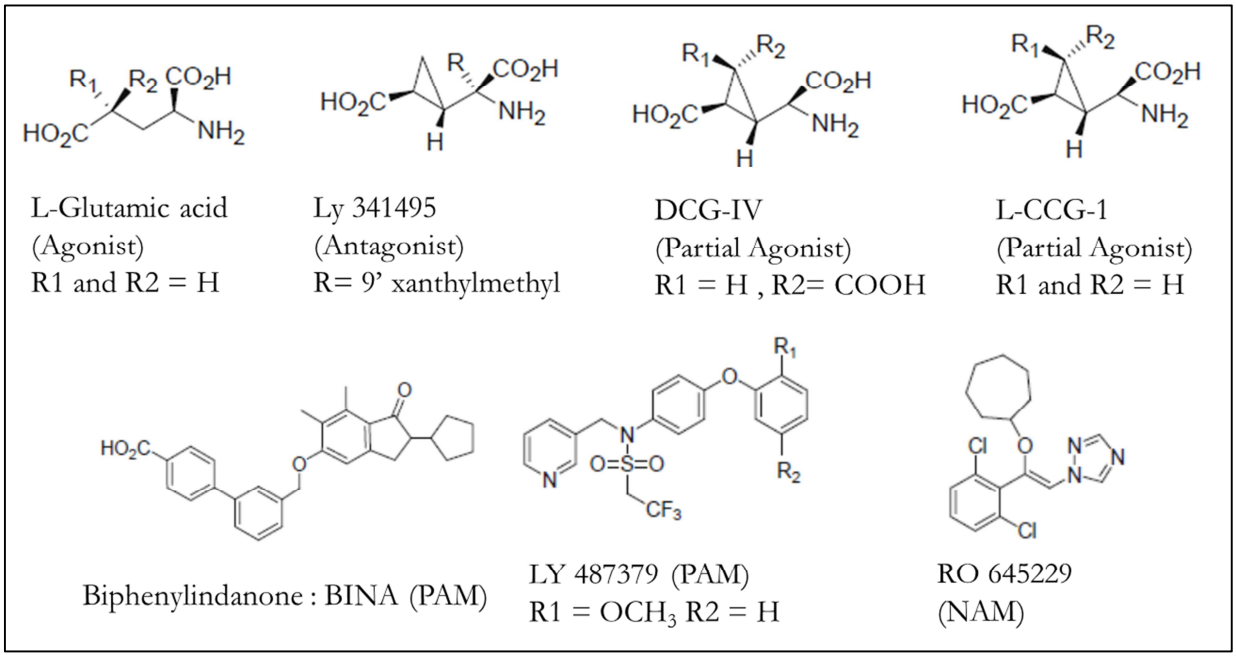

Figure 1.21. *Chemical structures of four commonly used mGlu2 ligands. Upper panel from left to right, the full endogenous agonist glutamate, the antagonist Ly34, the partial agonist DCG-IV and the partial agonist LCCG-1. Lower panel from left to right, two main positive allosteric modulators BINA and Ly48 and the negative allosteric modulator Ro64 (Tocris Bioscience Scientific Review Series).*

Chapter 2. Objectives

In order to determine whether the previously hypothesized model- where a closing and a reorientation of the two lobes of the VFT domain is required for receptor activation, the structural dynamics of the extracellular domain of the mGluRs were recently investigated by Etienne Doumazane and Pauline Scholler in the team of Jean-Philippe Pin at the Institut de Génomique Fonctionnelle. (Doumazane *et al.*, 2013)

To this aim, they established a cell surface time–resolved Forster Resonance Energy Transfer (trFRET) approach, also known as HTRF. In chapter 3, the basics of FRET and HTRF will be exhaustively detailed. In the meantime, it is only important to point out that FRET is a fluorescence-based technique that reports on the distance that separates two fluorescent dyes, referred to the as the donor and the acceptor dye. Largely simplified, the theory of FRET states that a short inter-dye distance results in a high FRET value, and that this FRET value decreases drastically as the distance becomes greater. In order to monitor variations in FRET, the molecule of interest has to be specifically labeled with fluorescent dyes at known positions, which in this study was accomplished by fusing the N-terminus of each monomer to a SNAP-tag® (Juillerat *et al.*, 2003). The SNAP-tag is a ~20kDa suicide enzyme that can be covalently labeled with benzylguanine-derived fluorescent substrates. In this particular case, the labeling with the two spectrally distinct dyes was entirely random, and therefore, the labeling concentration of each dye had to be optimized to achieve a high ratio of doubly labeled receptors (**Figure 2.1**).

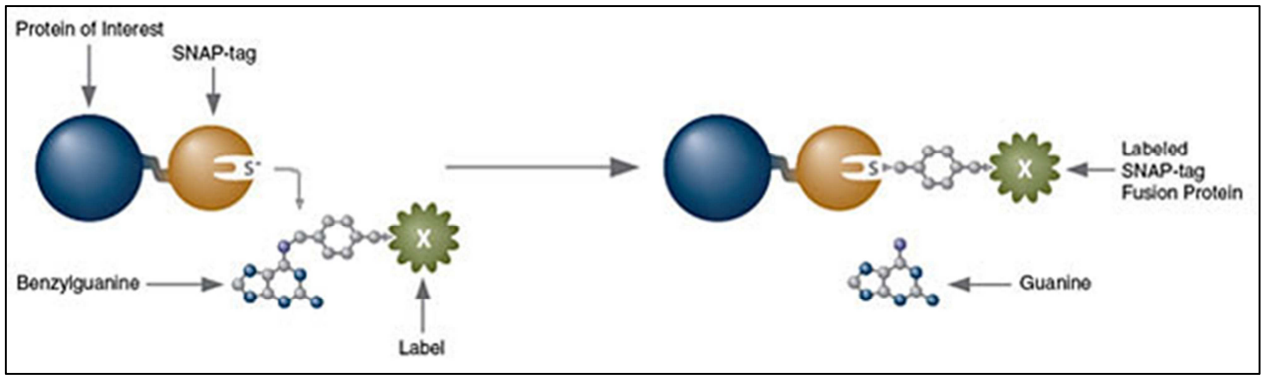

Figure 2.1. *Cartoon demonstrating the SNAP-tag® labeling strategy. The protein of interest is fused to the SNAP-tag®, which is a suicide enzyme capable of reacting with a benzylguanine group carrying the fluorescent dye. (New England Biolabs®)*

To be more precise, the experiments were performed using a steady-state HTRF approach based on the use of donor dyes derived from rare earth elements which can transmit

the energy of the excited state to organic acceptor dyes. In fact, in HTRF, the transfer efficiency is estimated through the determination of the delayed acceptor emission ratio and by variations in the donor lifetime. Hence, by employing this method on mGlu2, they observed a decrease in the averaged FRET in presence of agonists, which is in agreement with a reorientation and closure of the VFT. In addition, high affinity competitive antagonists reversed this effect and resulted in FRET values higher than those observed for the empty receptor (**Figure 2.2**).

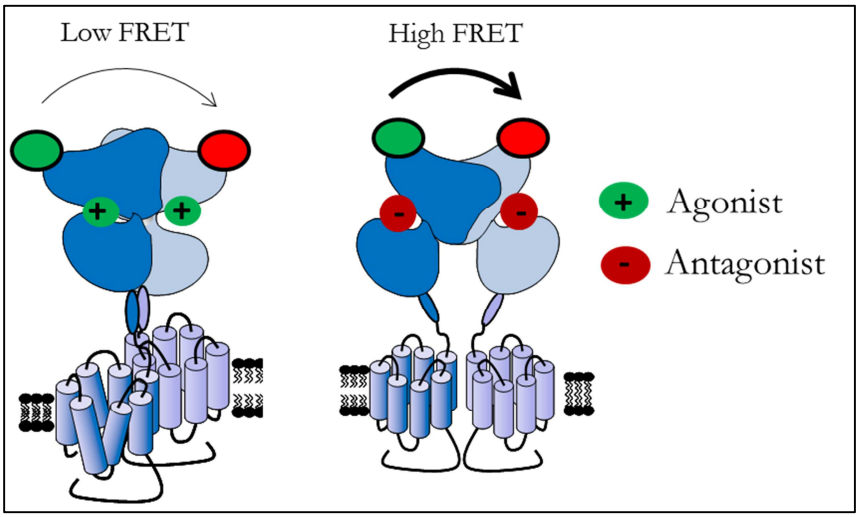

***Figure 2.2**. Principle of the FRET experiment carried out on mGlu2. Each monomer is labeled in N-terminus with a donor and an acceptor dye. Upon activation with an agonist, the FRET value decreases. This signifies that the distance between the dyes has increased, which in turn suggests a transition from the resting to the active state. In contrast, the presence of an antagonist results in a higher FRET efficiency, which implies that the receptor preferentially adopts a resting conformation.*

This study also showed that the group II specific agonists DCG-IV and L-CCG-I behave as partial agonists, revealed by the intermediate FRET obtained for these compounds. In order to confirm these results, inositol phosphate (IP) accumulation and calcium mobilization assays were conducted, and it was demonstrated that not only is the HTRF method suitable for the discovery of partial agonists, but also that the affinity measured for the various drugs is very similar to values obtained by other well-established techniques.

Interestingly, the results for mGlu2, mGlu3 and mGlu1 were comparable, which is indicative of an identical activation mechanism for all subtypes. To further strengthen the hypothesis stating that a reorientation of the dimer is mandatory for activation, two mutants were designed for mGlu2: (**i**) a constantly inactive mutant, blocked in a "resting" conformation due to a "glycan wedge" inserted between the CRDs and (**ii**) an active mutant, blocked in an

"active" conformation by a disulfide bond that crosslinks the CRDs. The FRET for the "resting" mutant was similar to the empty WT receptor with strongly impaired effects with glutamate and other full agonists. In contrast, the constantly active receptor presented a FRET value similar to the WT receptor in the presence of saturating concentrations of agonists. A minor increase in FRET was nonetheless observed upon the addition of a competitive antagonist, but the basal activity of the receptor remained unchanged.

Additionally, the HTRF sensor approach was applied to investigate the hypothesis arguing that the ECD acts as brake on the transmembrane domain (7TM) by preventing it from reaching a fully active conformation in the absence of orthosteric ligands. In fact, even though PAMs and NAMs do slightly modify the efficacies of orthosteric ligands, it was shown that a PAM or a NAM alone is neither sufficient to vary the level of activation, nor able to influence the conformation of the ECD.

In order to further support the role of the ECD as the key player in regulating receptor activation. The ECD was expressed at the cell surface linked to the membrane via a GPI anchor and subsequent HTRF experiments with this truncated construct revealed similar FRET values as those observed for the WT receptor. (Doumazane *et al.*, 2013) Moreover, the GPI anchor is cleavable with a phospholipase C enzyme (PI-PLC), and HTRF results on the cleaved construct were similar to those of the full-length receptor and the VFT GPI-anchored construct (**Figure 2.3**).

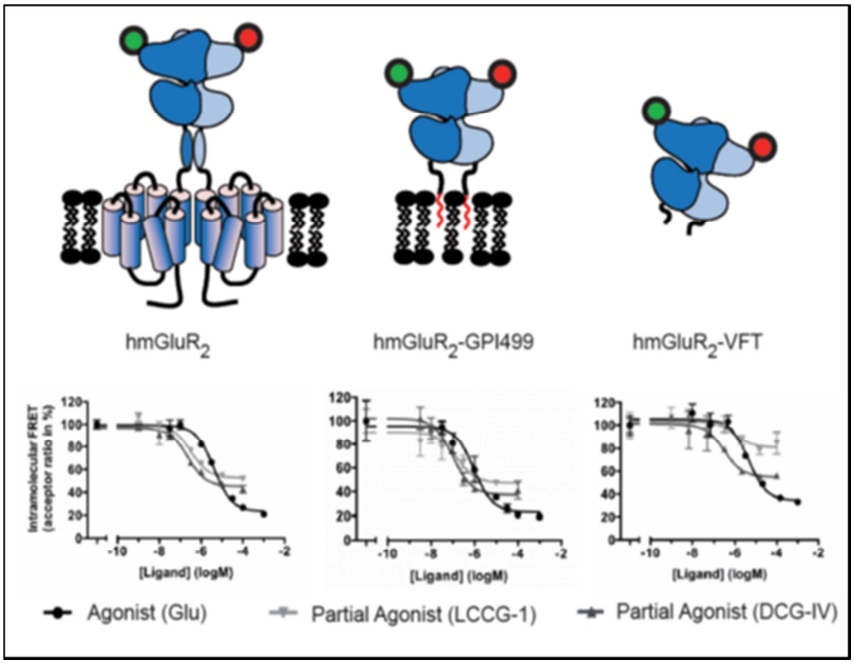

***Figure 2.3**. Ensemble HTRF changes observed within the VFT dimer on the WT full-length receptor (left), GPI-construct (center) or the soluble GPI-construct after PI-PLC cleavage (right) The HTRF signal is represented as the ratio of the acceptor-sensitized emissions and is normalized to the maximum signal. Binding of the full agonist glutamate leads to a decrease in FRET as expected for a transition from the resting to the active state, all the while the binding of the partial agonists LCCG-1 and DCG-IV also decrease the FRET but to a lower extent, indicating a partial shift of the equilibrium toward the active state, or possibly a stabilization of a partially active intermediate state.*

It is, however, important to bear in mind that the HTRF data only reflects the average behavior of all the receptors at the cell surface. Consequently, the objective of my Ph.D. thesis has been to further the understanding of the underlying activation mechanism of mGluRs by quantifying the structural dynamics of individual receptors. I have studied the VFT dimer using single molecule FRET (smFRET) to establish whether a ligand induces the stabilization of a static conformation, or if the role of ligands is more that of shifting the equilibrium and modulating the transition rates between states. In addition, I have studied the effect of partial agonists in an attempt to figure out whether the partial effect is due to the stabilization of an intermediate state or if the active state is the same as for the full agonist, but reached through altered dynamics. To this end, I have optimized a smFRET compatible labeling approach, built several smFRET adapted confocal microscopy setups and implemented advanced smFRET analyses.

Chapter 3. Methodology

In this third chapter, I will attempt a comprehensive description of some of the techniques and methods that I have employed for the completion of my Ph.D. thesis. I will, firstly, introduce some of the aspects of the phenomenon of fluorescence, which are important to understand the subsequent description of its usefulness in Förster Resonance Energy Transfer (FRET) experiments. Secondly, I will report on some of the technical requirements for the implementation of FRET at a single molecule level and present some advanced methods developed for analyzing fast dynamics.

3.1 Fluorescence – basic concepts and practical aspects

3.1.1 Theory of fluorescence

Over the years, fluorescence based methods have revolutionized the work of scientists in a variety of fields spanning from cellular and molecular imaging and DNA sequencing to forensics and medical diagnostics, just to mention a few examples.

Luminescence is the term used to describe the phenomenon of emission of a photon that occurs when an electron returns to its ground state from an electronically excited state in a conjugated system such as a fluorescent dye. The lifetime of the electron in the excited state varies considerably depending on whether the photon is emitted from the triplet excited state or the singlet state (**figure 3.1**). Consequently, two different categories of luminescence have been defined: Phosphorescence and Fluorescence.

Phosphorescence refers to the de-excitation of an electron from a triplet excited state. This transition is considered forbidden due to the spin orientation of the electron in the excited state being identical to that of the electron in the ground state, and the lifetime of the excited state is, therefore, relatively long, spanning from milliseconds to several seconds.

In contrast to phosphorescence, fluorescence is the term given to describe the phenomenon of de-excitation of an electron whose spin orientation in the excited state is opposite to the spin of the paired electron in the ground state (singlet state). This transition is, therefore, a fast process, occurring typically on a timescale of a couple of nanoseconds.

These different excitation and de-excitation pathways are presented in the Jablonski diagram (**figure 3.1**) in honor of the Polish physicist, Pr. Alexander Jablonski, acknowledging his major contribution to the improved understanding of the underlying quantum mechanics of luminescence.

By observing the simplified Jablonski diagram, it becomes clear that the emitted photon corresponds to a longer wavelength than the photon that was absorbed (**figure 3.2**), as described in **equation 1**, which states that the energy of a photon is inversely proportional to its wavelength. This phenomenon, generally referred to as "Stokes's shift", is due to the loss of small amounts of energy because of the internal transitions that lead to the relaxation of the system. Moreover, the apparent excited state lifetime of the dye (τ) depends on the rate constants of non-radiative de-excitation (k_{nr}) and radiative de-excitation (k_r) as presented in **equation 2**.

$$E_{h\nu} = \frac{hc}{\lambda} \qquad \textbf{Equation 1}$$

where $E_{h\nu}$ represents the photon energy, h is Planck's constant, c is the speed of light and λ is the wavelength.

$$\tau = \frac{1}{k_{nr}+k_r} \qquad \textbf{Equation 2}$$

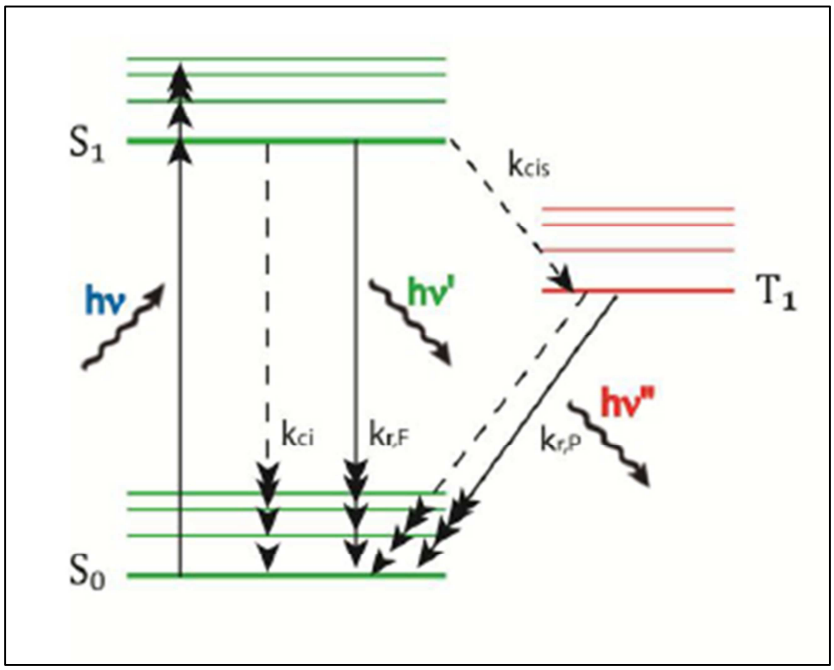

Figure 3.1*.The simplified Jablonski diagram represents the different energy transitions associated with phosphorescence and fluorescence. S_0, and S_1 correspond to the ground and the 1st electronic state, respectively. In addition to the electronic states, each state exists in several vibrational energy levels. The excitation by a photon whose energy is equivalent to the energy difference between the ground-state and the excited state (blue wavy arrow), the photon is absorbed and an electron from the S_0 energy level is excited to one of the vibrational energy levels of the excited state (S_1). By a process called internal conversion (10^{-12}sec), the excited electron relaxes to the lowest vibrational energy level of the 1st excited state from which it will then return to one of the vibrational energy levels of the ground state while emitting a photon by fluorescence (kr,F) or by a non-radiative pathway (kci). In contrast to the previously described mechanism, phosphorescence originates in a phenomenon called intersystem crossing (kcis), whereby the electron undergoes a spin conversion populating the 1st triplet state from which it will then de-excite leading to a longer lifetime in the excited state (kr,P).* (Lakowicz, n.d.)

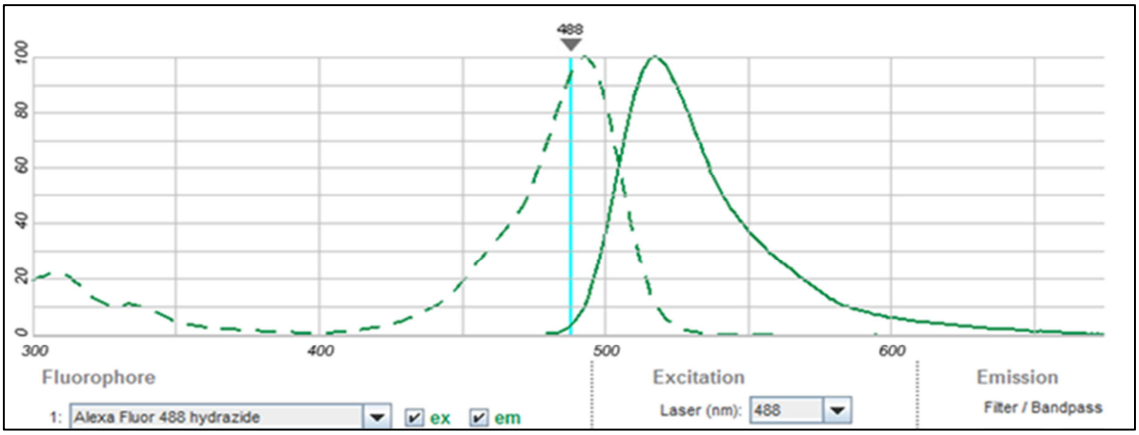

Figure 3.2*. Absorption and emission spectra for the fluorescent dye Alexa488. Due to internal transition occurring after excitation, the energy of the emitted photon is lower than the energy of the absorbed photon as represented by the amplitude versus wavelength diagram. (InvitrogenTM, fluorescence spectra viewer)*

Anisotropy – significance and implications

In order to attempt an explanation of the concept of anisotropy, let us consider a sample of free randomly oriented fluorescent dyes in solution and a polarized excitation source. At any given moment in time, the dyes with their absorption transition moments (directly linked to the dye's molecular structure) aligned with the polarized excitation beam will preferentially be excited. Consequently, the direction of emission from this mostly oriented population of excited dyes will depend on the orientation of the emission dipole and on the dyes' rotational characteristics in a specific medium, hereafter defined as the rotational correlation time (θ).

Generally, the anisotropy of the fluorescence emission is calculated by means of **equation 3**:

$$r = \frac{I_{\parallel} - gI_{\perp}}{I_{\parallel} + 2gI_{\perp}} \qquad \textbf{Equation 3}$$

where $I_{\parallel}$ is the fluorescence intensity in the parallel direction (relative to the polarization of the excitation source), $I_{\perp}$ is the fluorescence intensity in the perpendicular direction (relative to the polarization of the excitation source) and g represent the detection efficiency (a description of the G-factor is provided in an upcoming paragraph). From **equation 3**, it becomes obvious that any restrains on the dye's spatial mobility decreases the intensity detected in $I_{\perp}$ and consequently the anisotropy increases. In addition, the anisotropy is linked to rotational correlation time via the Perrin equation (Francis perrin, 1923; Berberan-Santos, 2001) (**Equation 4**):

$$r = \frac{r_0}{1 + \frac{\tau}{\theta}} \qquad \textbf{Equation 4}$$

where r is the steady state anisotropy, r_0 is the fundamental anisotropy, τ is the excited state lifetime and θ is the rotational correlation time, which strongly depends on the molecular volume (V) (for a spherical molecule) and the viscosity (η) of the medium via **equation 5**:

$$\theta = \frac{\eta V}{RT} \qquad \textbf{Equation 5}$$

where R represents the perfect gas constant and T, the temperature in Kelvin. Steady-state anisotropy measurements, thus, offer the possibility to estimate the volume and/or the weight of a macromolecule, and if the anisotropy is strongly affected by changes in shape and weight, molecular interactions might be investigated.

Moreover, to determine the volume and consequently the molecular weight using **equation 5** via the Perrin equation (**Equation 4**) the fundamental anisotropy (r_0) for the dye has to be known. The fundamental anisotropy is characterized by the angle between the excitation and the emission dipole and corresponds to the anisotropy in absence of movement, i.e. at 0°K. Because of the technical challenge to conduct experiments at 0°K, r_0 is generally estimated in a concentrated glycerol solution at 4°C and generate generally values equal or close to 0.4, for collinear excitation and emission dipoles.

At this point of the dissertation, it seems necessary to highlight the importance of distinguishing between the emitted and the detected fluorescence. The different components of a classical detection system will be discussed at length in a later section, however, it should be noted that the detection efficiency of a modern setup rarely exceeds 10%. In other words, only 10% of all emitted photons will be detected and accounted for in the calculations. For anisotropy measurements, it is critical to ascertain that the detection efficiency is identical in the parallel and the perpendicular channel. For that reason, the G-factor has been introduced to inform on any differences in detection efficiency between the channels. The G-factor is defined in **equation 6**.

$$G = \frac{\delta_{\perp}}{\delta_{\parallel}} \qquad \textbf{Equation 6}$$

where $\delta_{\perp}$ and $\delta_{\parallel}$ stand for the detection efficiency in the perpendicular and the parallel detection channels, respectively.

3.2 Förster Resonance Energy Transfer

To fully understand the photophysical phenomenon of Förster Resonance Energy Transfer (FRET) at a single molecule level, I am first going to present the theory of FRET and talk about its employment on an ensemble level. I will then move on to explain how FRET measurements are carried out to study diffusing single molecules.

3.2.1 Theory of FRET

Förster Resonance Energy Transfer, named after its discoverer, the German physical chemist Theodor Förster (1946), is the mechanism by which the energy of the electronically excited state of a fluorescent dye is transferred to another fluorescent dye whose absorption spectrum overlaps with the emission spectrum of the former. The transfer efficiency depends on the distance that separates the donor and the acceptor dye, which has to be in the range 1-10nm (**figure 3.3**).

Moreover, the transfer efficiency is inversely proportional to the sixth power of the intra-dye distance, which makes it very sensitive to small spatial variations. For this reason, FRET was first referred to as a "spectroscopic ruler" in 1978 (Stryer, 1978) and has since become a useful tool in many scientific disciplines requiring measurements on a nanometer scale.

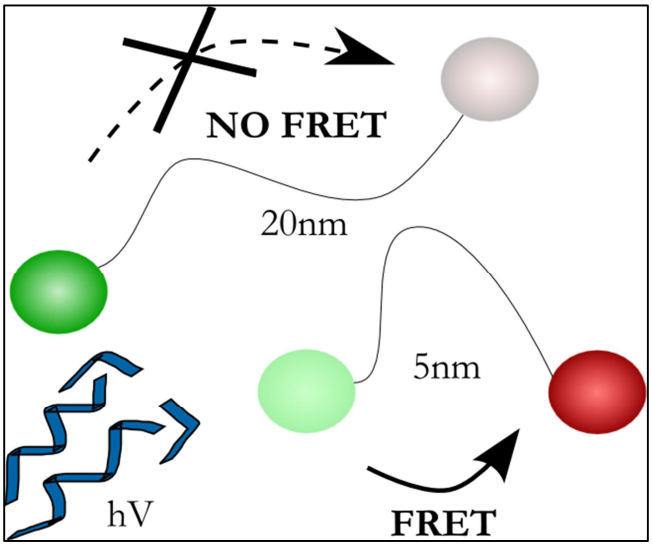

***Figure 3.3**. Cartoon illustrating the distance dependency of FRET. If the donor and acceptor dye are separated by a distance greater than approximately 1.5 R_0, no energy is transferred from the electronically excited donor. In contrast, if the dyes are separated by a distance within the valid FRET range, the acceptor may get excited and subsequently emit a photon.*

It is not uncommon that the acronym FRET is claimed to stand for Fluorescence Resonance Energy Transfer. This might however be slightly misleading as the energy transfer does not involve the emission and absorption of photons. To clarify this, let us take a look at the simplified Jablonski diagram once again, now extended to account for FRET (**Figure 3.4**). Following the absorption of a photon by the donor, the excitation energy can be transferred to the acceptor via long-range dipolar-dipolar interactions (dashed arrows and $k_{,FRET}$). The donor then returns to the ground state while the acceptor can either emit a photon by a mechanism called "acceptor sensitized emission" (red wavy arrow and $k_{r,A}$) or de-excites via a non-radiative pathway ($k_{nr,A}$) .

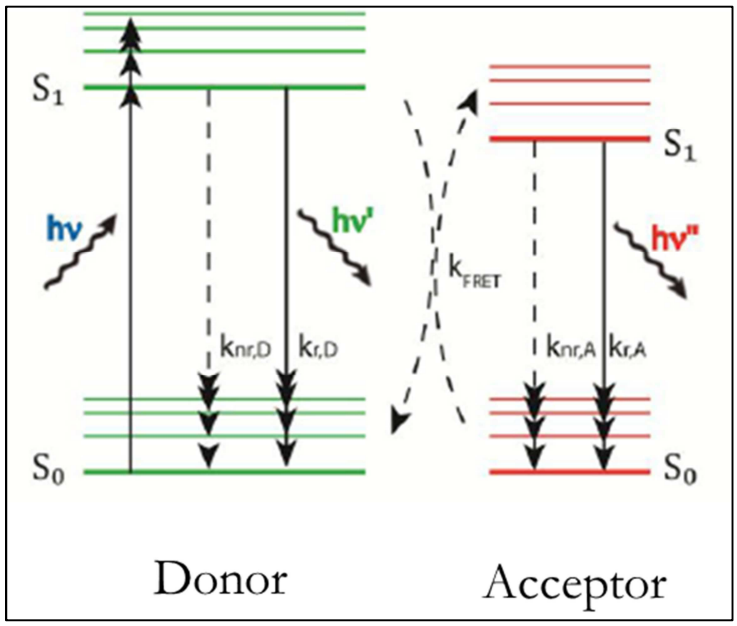

***Figure 3.4**. The simplified Jablonski diagram, extended to account for FRET represents the donor transferring the energy of the electronically excited state to the acceptor (k_{FRET}). The transfer occurs via dipolar-dipolar interactions and not by the emission and reabsorption of a photon. The de-excitation of the acceptor then occurs through either a non-radiative pathway (knr,A) or a radiative pathway (kr,A). The emission of a photon from the acceptor following donor excitation and FRET is generally called "acceptor sensitized emission"*

Furthermore, **figure 3.4** shows that an additional rate constant (k_{FRET}) has to be added for in a system involved in energy transfer, which leads to **equation 7**.

$$\tau_{D(A)} = \frac{1}{k_{nr}+k_r+k_{FRET}} \qquad \textbf{Equation 7}$$

where , τ_{DA} stands for the lifetime of the donor in the presence of an acceptor.

Thereupon, it can be concluded that an increase in k_{FRET} decreases the apparent lifetime of the donor. **Equation 7** demonstrates this influence of FRET on the donor lifetime and justifies the use of the comparison in lifetime for the donor in the presence and absence of an acceptor as a valid FRET-indicator.

From **equation 7** derives the relation between the FRET efficiency (E) and the donor lifetime as shown in **equation 8**.

$$E = \frac{k_{FRET}}{k_{nr}+k_r+k_{FRET}} = 1 - \frac{\tau_{DA}}{\tau_D} \qquad \textbf{Equation 8}$$

where E stands for the FRET efficiency, and τ_D stands for the lifetime of the donor in the absence of acceptor.

The FRET efficiency depends on the Förster distance of the dye-pair

As previously mentioned, the FRET efficiency (E) is strongly distance-dependent. The most convenient and explicit expression used to represent this distance dependence is given in **equation 9**.

$$E = \frac{R_0^6}{R_0^6+R^6} \qquad \textbf{Equation 9}$$

where R_0 stands for the Förster distance, which represents the distance for which the transfer efficiency is 50% (E=0.5), and which depends on the characteristics of the dyes in a defined environment. At this distance, the probability that the donor dyes decay by the classic radiative or non-radiative pathways is the same as the probability of the donor dyes engaging in energy transfer to the acceptor via FRET. From this equation and **Figure 3.5**, it becomes clear that variations in transfer efficiency are strongest when the distance that separates the dyes is close to the R_0 value. When the distance increases, E drops rapidly to 0 and when the distance decreases, E increases until the transfer efficiency is total and E=1 (**Figure 3.5**). It is, thus, essential to choose a dye-couple with an appropriate R_0 value, especially if the investigated system is dynamic and the goal of the study is to measure small variations in FRET.

The Förster distance is expressed in **equation 10**:

$$R_0 = 978\sqrt[6]{\phi_D.\mathrm{K}^2.\eta^{-4}.J} \text{ (in nm)} \qquad \textbf{Equation 10}$$

where ϕ_D is the quantum yield of the donor, K^2 is the dipole orientation factor, η is the refractive index and J (expressed in $M^{-1}.cm^3$) is the spectral overlap integral, all of which will be detailed in the upcoming sections.

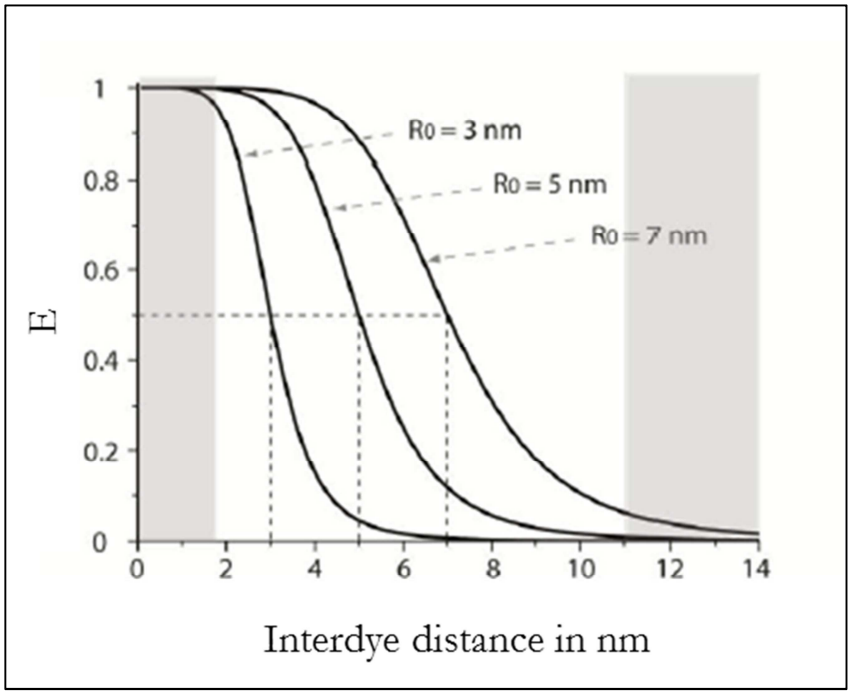

Figure 3.5. *Theoretical curve of the FRET efficiency (E) expressed as a function of the distance, in nanometers, separating the donor and the acceptor dye. Depending on the dye-pair, the R_0 value varies as shown by the three curves R_0=3, 5 or 7nm. When the distance between the dyes exceeds $2R_0$, the transfer efficiency drops to 0 and when, on the contrary, the distance is shorter than $0.5R_0$, the transfer efficiency reaches a plateau at 1, signifying that no donor emission is detectable. It is also worth mentioning that the slope is steepest when the distance is close to R_0, indicating that a slight variation in distance will result in a significant change in E.*

The dipole orientation factor informs on the dye's spatial freedom

The second parameter in the R_0 equation (**Equation 10**) is κ^2, which refers to the relative orientation of the two dipoles. Although κ^2 theoretically takes a value between 0 and 4, it is often times assumed that the dyes are freely rotating in space, which implies that the reorientational diffusion of the dyes is faster than the emission rate of the donor, hence resulting in a κ^2 approximation of 2/3. However, this assumption is sometimes incorrect because of interactions between the dye and the protein, and since κ^2 significantly influences the R_0 value, the importance of consistently verifying this parameter becomes clear. Fortunately, a time-resolved anisotropy measurement is a straightforward way to ascertain that the dyes are freely rotating, and if this criterion is not fulfilled, there are several possible methods to narrow down the possible κ^2 range (Sindbert *et al.*, 2011). Nevertheless, it is important to point out that exactly knowing the κ^2 value is only necessary if the intention is to determine exact distances. In general, an approximate estimation of the distance is enough for comparative studies, in which case the κ^2 value only has to be constant.

The quantum yield of the donor reports on the dyes' brightness

The quantum yield signifies the number of photons emitted with respect to the number of photons absorbed. The quantum yield is given by **equation 11:**

$$\phi = \frac{k_r}{k_r + k_{nr}} \qquad \textbf{Equation 11}$$

For an optimal dye, the non-radiative process is only minor, which results in a quantum yield ϕ close to 1.

Moreover, the quantum yield varies with the local environment and it is therefore necessary to measure the "true" quantum yield after labeling of the molecule of interest. This can be done by comparison with standards for which the quantum yield is known using **equation 12:**

$$\phi = \phi_R \frac{I}{I_R} \frac{OD_R}{OD} \frac{n^2}{n_R^2} \qquad \textbf{Equation 12}$$

where Φ_R is the quantum yield of the standard, I is the fluorescence intensity, OD is the optical density and n the refractive index of the medium.

The spectral overlap of the dye-pair strongly influences their R_0 value

FRET can only occur if there is a spectral overlap between the emission spectrum of the donor dye and the absorption spectrum of the acceptor dye. As previously discussed, FRET does not result from a transfer of photons but should be looked upon as two oscillating dipoles with similar resonance frequencies between which energy can be transferred. The transfer is unidirectional as the donor is excited at a shorter and thus more energetic wavelength than the acceptor. **Figure 3.6.a** represents the spectral overlap of the frequently employed dyes Cy3 and Alexa647. For this dye couple, the spectral overlap is large, which results in a R_0 value as high as approximately 55Å (assuming $\kappa^2 = {}^2/_3$).

In order to evaluate if two dyes are suitable to form a FRET pair, their spectral overlap J(ν) has to be calculated. This is generally achieved by **equation 13**

$$J(\nu) = \int_0^\infty \left(\frac{\varepsilon^A(\nu)\Phi(\nu)}{\nu^4}\right). d\nu \qquad \textbf{Equation 13}$$

where $\varepsilon^{A}(\nu)$ represents the normalized excitation spectrum of the acceptor multiplied by ε^{A}_{max} (maximum absorption coefficient for the acceptor) and $\Phi(\nu)$ represent the normalized spectral shape function. In turn, the normalized spectral shape function corresponds to the normalized emission spectrum of the donor whose integral is further normalized to 1. An attempt to clarify this is shown in **figure 3.6.b**, where the normalized emission spectrum of the donor is highlighted in pink. By normalizing the integral of the normalized emission spectrum of the donor, the normalized spectral shape function is obtained, which is here shown in green. The normalized excitation spectrum of the acceptor, here shown in blue, is then multiplied with its maximum absorption coefficient and then again multiplied with the (green) spectral shape function and divided by the wavelength to the power of 4. This procedure has to be repeated for each wavelength and summed over all wavelengths.

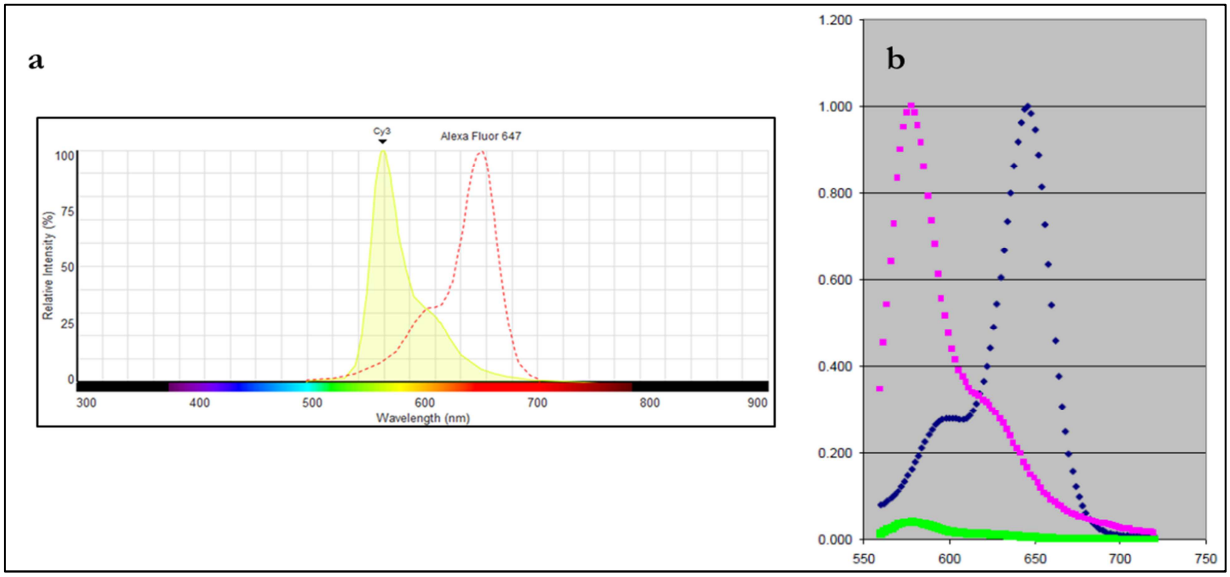

***Figure 3.6**. (**a**) Illustration of the spectral overlap for a commonly used FRET couple Cy3-Alexa647. The integral of the overlap of the green curve with the red curve gives J(v) expressed in $M^{-1}.cm^{3}$. (InvitrogenTM, fluorescence spectra viewer) (**b**) Illustration of the calculation of the spectral overlap, see text for details.*

To close the section on the accurate determination of the R_0 value and on the measurement of exact distances using FRET, it is indispensable to highlight that the exact FRET efficiency (E) is not the only way to express FRET values. As a matter of fact, various FRET indicators exist to inform on the transfer efficacy, some of which will be introduced in the chapter on single molecule FRET.

3.2.2 Experimentally measuring FRET

There are many different methods to estimate and perform FRET experiments, both *in vivo* and *in vitro*. *In vitro* measurements are generally carried out using a spectrometer, a micro-plate reader, a Total Internal Reflection Fluorescence Microscope (TIRFM) or a confocal microscope adapted for solution-based microplate measurements. In a typical experiment, the sample, labeled with a donor-acceptor FRET compatible dye-pair at known positions of the macromolecule(s), is excited at the wavelength of the donor. The FRET efficiency is then estimated either by (**i**) calculating the ratiometric value of the acceptor sensitized emission and the donor emission or (**ii**) by measuring the lifetime of the donor in the excited state, the latter being the most thorough approach, less prone to artifacts. Moreover, in the case where the acceptor is replaced by a quencher, a molecule that de-excites the donor in a distance-dependent manner without emitting a photon, the measurement of the donor lifetime is a straight-forward way to assess the FRET efficiency.

HTRF to measure FRET at the cell-surface

Time resolved FRET (trFRET), also known as homogenous time resolved fluorescence (HTRF), is a useful approach to measure FRET, notably on a cellular level where the specific fluorescent signal is difficult to extract from the auto-fluorescence of the cell itself.

The main difference between trFRET/HTRF and classical FRET lies in the use of donors belonging to the rare earth lanthanide family. In the periodic table, there are 15 lanthanides spanning the atomic numbers 57 to 71 and they have unique spectroscopic proprieties. In HTRF, the most frequently used lanthanides are europium and terbium, chelated with cryptates. In fact, upon excitation, these molecules have exceptionally long lifetimes of several milliseconds in the excited state due to complex internal electronic transitions (**Figure 3.7**) (Degorce *et al.*, 2009).

Furthermore, the emission is depolarized, which implies that κ^2 can only take values between 1/3 and 2/3, which limits the error estimation of the Förster radius to approximately 10%. The advantage of this delayed emission is that the acquisition of the specific signal can begin several milliseconds after the excitation pulse, and therefore long after the disappearance of other contamination sources of fluorescence such as autofluoresence or impurities. Moreover, both europium and terbium cryptates are compatible donors with most red-shifted organic acceptor dyes, enabling thus their use in FRET experiments. The FRET efficiency is estimated by either one of two

possibilities: (**i**) by fitting the exponential decay of the donor, or (**ii**) by measuring the sensitized emission of the acceptor (Degorce *et al.*, 2009).

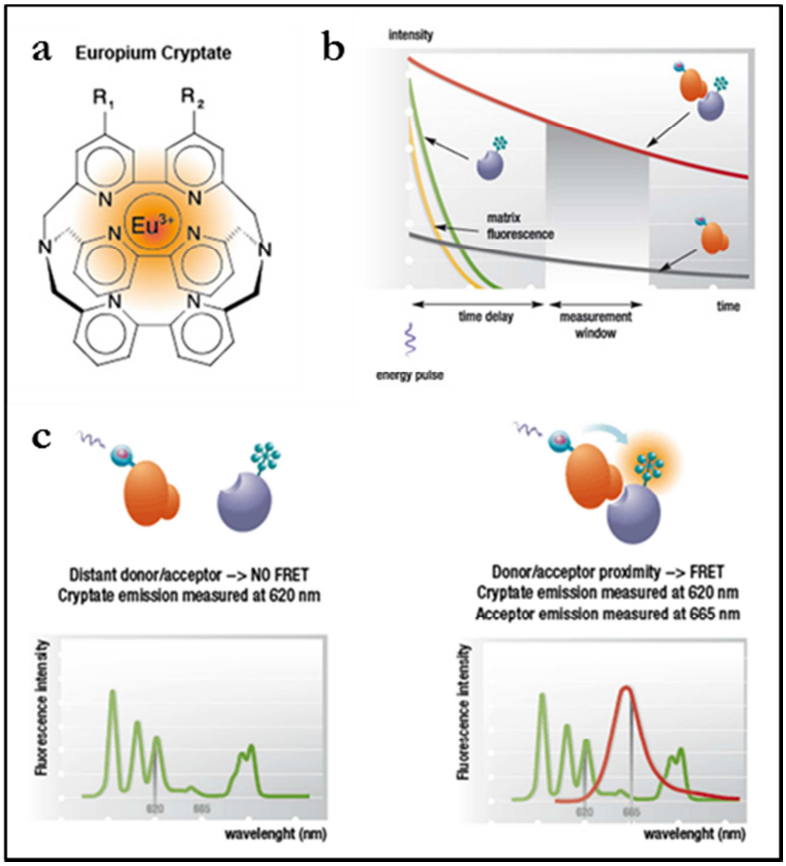

***Figure 3.7**. (**a**) Chemical structure of the HTRF donor europium cryptate. The europium ion is embedded in a molecular cage which provides the complex with unique spectroscopic proprieties. (**b**) Schematic illustration of the time delayed donor emission. The measurement window is set to begin after the disappearance of the short-lived interfering fluorescence. (**c**) In absence of FRET no emission is detected at the specific acceptor emission wavelength. If FRET occurs, a distinctive peak is observed. (CisBio Bioassays)*

3.3 Implementing FRET on a single molecule level

For many years, scientists were limited in their research to the study of biomolecules exclusively at an ensemble (or steady state) level. For this reason, the acquired data reflected the average behavior of the molecules constituting the sample. In biology, it is seldom the case that molecules act in a synchronized manner and thus, valuable information might get lost if only the mean is considered. The first break-through in the field of single molecule biology came from the implementation of single-channel conductance experiments by electrophysiologists (Erwin Neher and Bert Sakmann, "The Nobel Prize in Physiology or Medicine 1991"). These experiments consist of the measurements of the ion-flux through single open membrane ion-channels in response to specific electrochemical forces (neuroscience 3rd edition, Sinauer).

Fluorescence based techniques provide scientists with a means to detect specific signals with extremely high sensitivity and accuracy. With regard to FRET experiments, steady state measurements of heterogeneous samples lead to the estimation of mean intra and/or intermolecular distances which are sometimes difficult to interpret. However, FRET can nowadays be investigated at a single molecule level if the excitation or observation volume is confined. To this aim, a highly diluted sample can be investigated in solution by means of a confocal microscope, coupled to single photon detectors, or by immobilizing the molecules on a coverslip and observe them by TIRFM (Jaiswal and Simon, 2007; Walter *et al.*, 2008). Nonetheless, the first ever single molecule FRET experiment was carried out by near-field scanning optical microscopy (NSOM) by Taekjip Ha and coworkers under the supervision of Shimon Weiss at Berkeley National Lab in 1996 (Ha *et al.*, 1996).

The main advantage of performing single molecule FRET (smFRET) resides in the possibility to isolate and study all the different sub-populations that constitute a heterogeneous sample. In fact, in ensemble measurements, minor populations are often times hidden because of their weak contributions to the total signal, whereas in smFRET, they are not only visible but also accessible for subsequent specific analyses. For the sake of clarity, **figure 3.8** illustrates an example of a simulated two-state dynamic system composed of molecules either in a high FRET (B) or a low FRET (A) state. At too high a concentration, only the mean value of all the molecules oscillating between the two states is detectable, and it is therefore impossible to conclude whether the sample corresponds to (**i**) a static system with a single FRET efficiency, (**ii**) a mix of static molecules with

different FRET efficiencies, or, (**iii**) a dynamic sample with molecules interconverting between different states.

At an intermediate concentration, it becomes clear that sample is heterogeneous but the concentration is still too high to allow for a thorough examination of sub-states.

If the concentration is further decreased, individual molecules become discernible and it is fairly easy to draw the conclusion that the sample contains molecules belonging to different FRET states. Furthermore, the signal emitted from a single molecule can now be examined over time and the timescale of the dynamic transition between states, alongside their individual characteristics, can be measured.

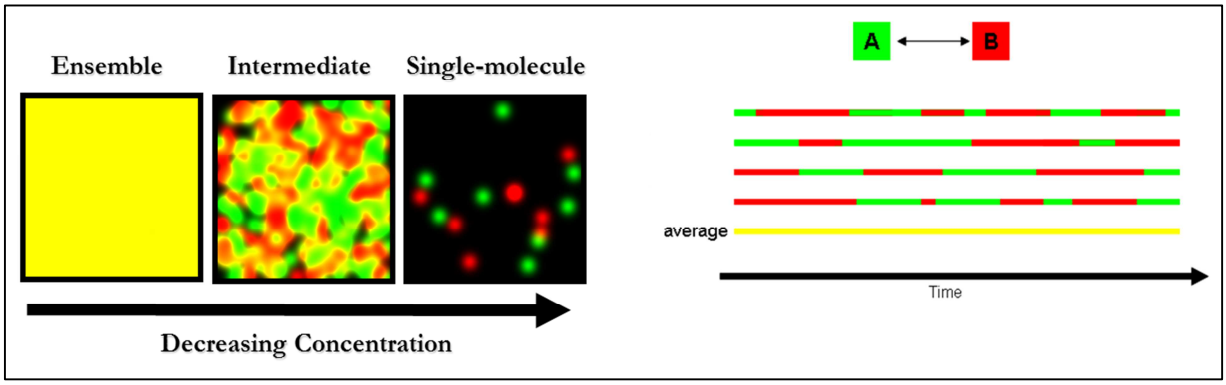

***Figure 3.8**. Representation of the evolution of the detected signal as the concentration of the sample decreases. At too high a concentration, only the mean FRET efficiency is detected and it is difficult to draw conclusions on the composition of the sample. Through successive dilutions, the existence of two sub-populations is ascertained, and the signal from single molecules is recorded over time to gain access to the timescale of the underlying dynamics.*

The usefulness of performing smFRET having now being highlighted, this dissertation endeavors from here onward to take on the question of how solution-based smFRET experiments are accomplished using a confocal microscope. In this upcoming chapter, some of the technical requirements to this aim, such as the optical setup and the criteria that the fluorescent dyes have to fulfill, are going to be presented. The smFRET acquisition and analyzing method "alternated excitation of single molecules for fluorescence aided molecule sorting" (μsALEX) will then be discussed. After having familiarized the readers with μsALEX, a powerful time-resolved smFRET technique that comes under the label multiparameter fluorescence detection (MFD), and which is useful for the study of fast dynamics, will be explained in depth.

3.3.1 Technical requirements for solution based smFRET

The very basic principle of a single molecule experiment is to limit both the excitation and the detection volume in a way that only the photons emitted from a single molecule are detected at any given moment in time. To this aim, the characteristics of a simplified confocal microscope can be exploited.

Although the sample is illuminated along the entire path of the laser beam in a confocal microscope, most out-of-focus detected light can be removed by placing a pinhole at the focal point of the lens that refocuses the light after the objective (the tube lens). Hence, the size of the observation volume, generally a couple of femtoliters, depends on the size of the pinhole even though several additional factors such as the wavelength, the numerical aperture and the magnification, contribute as well (Lakowicz 2006 Pawley, handbook of biological confocal microscopy, 2nd edition) (**Figure 3.9**).

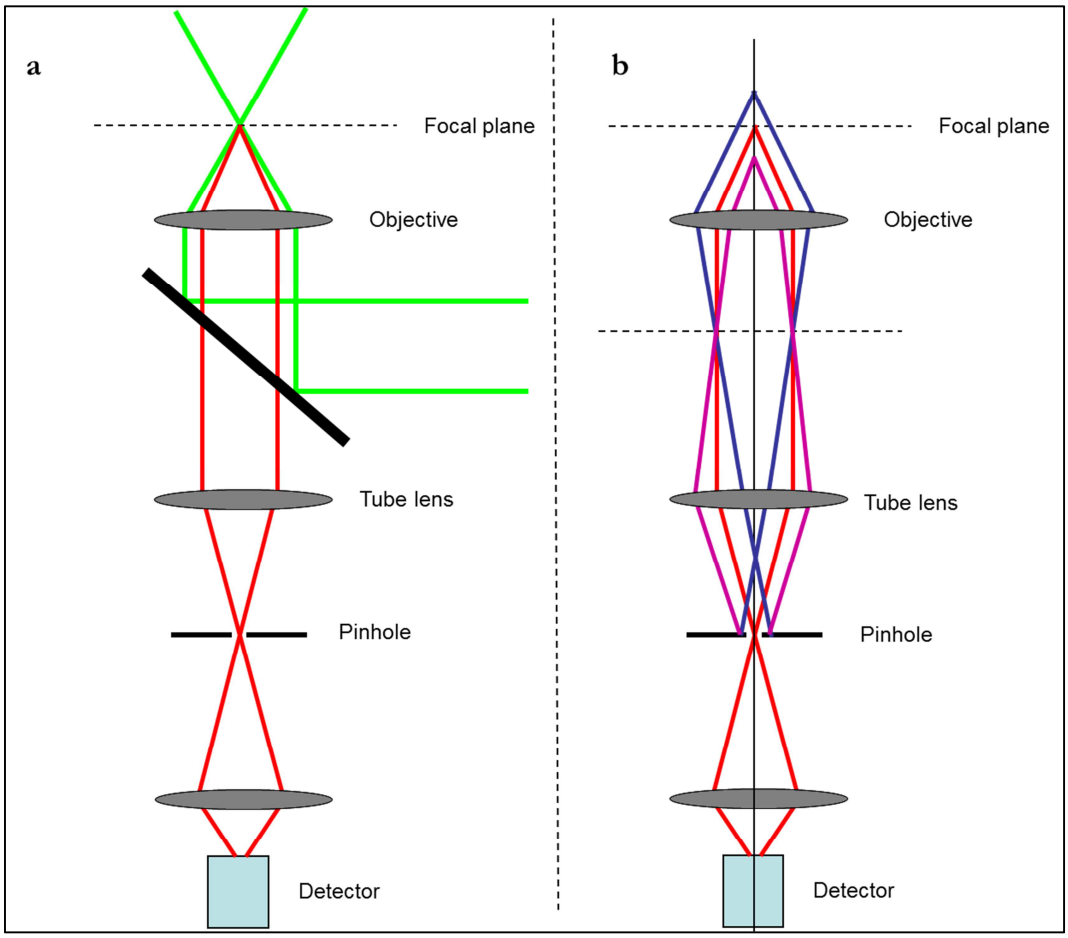

***Figure 3.9**. (**a**) Schematic representation of the optical path in a confocal microscope. The excitation beam (green) is reflected by the dichroic mirror and focused by the objective. The emitted fluorescence beam (red) is then collected by the objective and traverses the dichroic mirror before being focused into the pinhole by the tube lens. A second lens then refocuses the light onto the detection area, in the center of the detector. (**b**) Illustration showing the role of the pinhole in removing out-of-focus light. The pinhole is conjugated with the focal plane and consequently, only light emitted from this area (red beam) goes through the pinhole and is detected. Even though the sample is illuminated along the entire path of the excitation beam, it is clearly demonstrated here that neither the blue, nor the purple beam will ever reach the detector.*

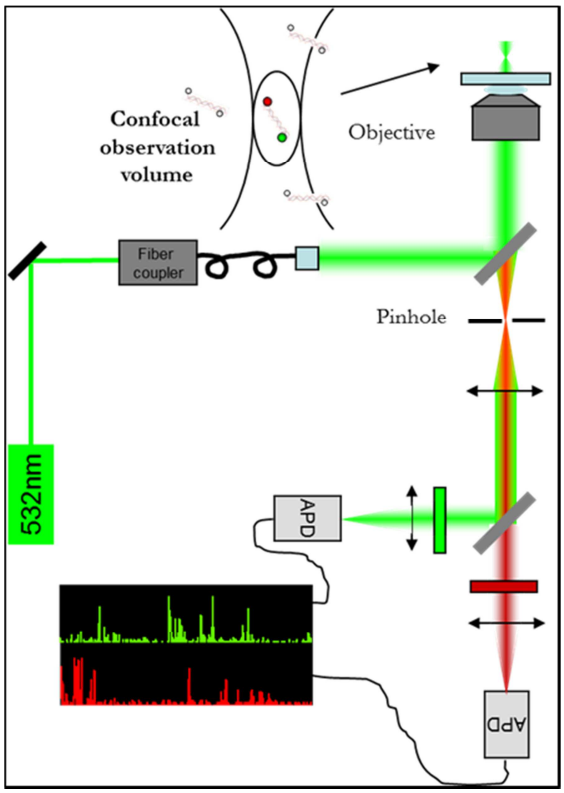

***Figure 3.10**. Schematic representation of a confocal adapted smFRET setup*

In order to respect the single molecule criterion in a femtoliter volume, the sample has to be diluted to a concentration as low as 20-50pM. At this low a concentration, statistically, there is less than one molecule in the focal volume at a time, as represented in **figure 3.10**. **Figure 3.10** also shows the basic design of a confocal microscope adapted to allow for smFRET experiments. In this example, the sample is excited at 532nm, and scattered photons originating from the laser are separated from the fluorescent signal emitted by the sample by a dichroic mirror. The fluorescent beam is then focused into the pinhole for the elimination of out-of-focus light before the spectral separation that deviates the photons emitted by the donor into the "green" detection channel and the photons predominantly emitted by the acceptor into the "red" detection channel. The recorded signal, represented as an output photon trace (black box, photon count versus time) shows the photons detected in the "green" and the "red" channel, respectively. Single molecule events are separated by time-periods, over which only background noise is recorded. The detected photons are plotted as a function of time, and all the photons detected for a single molecule define a "single molecule event" or "burst". The mean FRET efficiency for each molecule is subsequently calculated and displayed in either a 1D or 2D histogram, as will be thoroughly described in upcoming chapters.

Laser sources for single molecule microscopy

The word laser is actually an acronym standing for "light amplification by stimulated emission of radiation" and choosing the appropriate laser source is a crucial step in performing high accuracy single-molecule fluorescence spectroscopy. There are a growing number of available laser types, each one having their own characteristics and advantages. For a laser source to be considered ideal, some crucial proprieties are required: the emitted laser beam has to be quasi-monochromatic,

collinear, and bright. Depending on the intermittency of the emitted photons stream, lasers are classed into two sub-categories: pulsed or continuous-wave (CW).

CW lasers emit a constant flux of light and are the most commonly used lasers in classical fluorescence microscopy. They derive from various technologies, which in turn lead to their classification into gas lasers, dye lasers and solid state lasers (Pawley, handbook of biological confocal microscopy, 2nd edition).

Pulsed lasers are mandatory for time-resolved experiments. In the visible spectrum, most modern pulsed lasers currently in use are diode lasers. Due to their monochromaticity, it takes several individual lasers to perform multicolor excitation experiments. In order to overcome this technical limitation, our setup has been designed with a High-Power Supercontinuum laser as input source. It runs at 20MHz, and has a power density >2mW/nm over the 450-800nm range (**Figure 3.11)**, with an average pulse width of 100-150ps. The desired wavelength can be selected by using appropriate bandpass filters. A multicolor excitation scheme is easily achieved by splitting the excitation beam into two distinct optical pathways and by using different filters for each path.

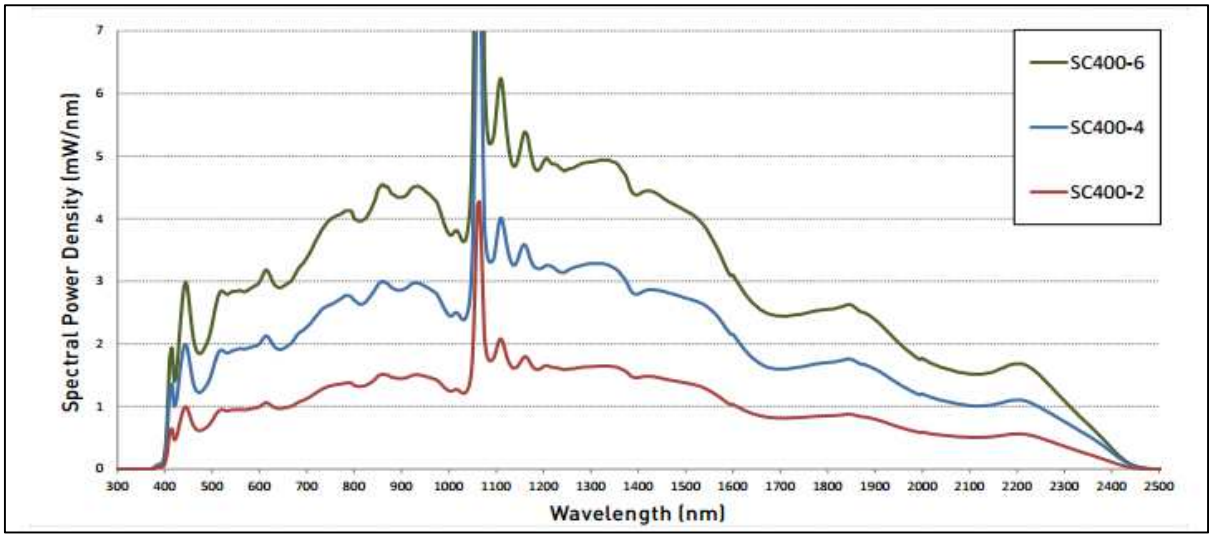

***Figure 3.11**. Supercontinuum laser spectrum. See text for details.*

A thorough description of the laser and the optical setup will be provided in chapter 4.1 and in our article "Pulsed interleaved excitation fluorescence spectroscopy with a supercontinuum source" (Olofsson and Margeat, 2013)

Single photon counting detectors

The accuracy of solution-based smFRET measurements depends on the accurate detection of single photons by highly sensitive single photon counting detectors. Currently, the detectors of choice for this purpose are Single Photon Avalanche Diodes (SPADs). Upon detection of a single photon, a SPAD triggers a burst of current which will then trigger a detection card. SPADs offer the advantage of producing a low number of dark-counts in addition to their high quantum yield. However, there are some problems associated with the use of SPADs, the main difficulty being the small detection area of less than 170μm^2. For this reason, a high degree of alignment is required and substantial efforts have to be made in order to correctly focus the emitted fluorescence in the center of the detection area (Pawley, handbook of biological confocal microscopy, 2nd edition).

In addition, developmental efforts by the photon detection brand "micro photon devices" (MPD) have managed to increase the time resolution of classical SPADs, from ~300ps to ~35ps (**Table 3.1)**, and this in combination with an improved detection efficiency at shorter wavelengths. However, the photon detection efficiency for the MPD drops significantly at wavelengths beyond 600nm. Consequently, the photon detector of choice for the red channel remains the classical SPAD.

λ	PDE (%) MPD	PDE (%) SPAD
450	35	25
500	46	43
550	49	55
600	45	60
650	37	65
700	30	65

MPD	Detector	SPAD
35ps	**Time Resolution**	300ps
0.1-3%	**Afterpulsing**	0.50%
100µm	**Active Area**	170µm
250 cps	**Dark Counts**	100cps

Table 3.1*. Detection efficiencies and characteristics of MPDs and classical SPADS. The main advantage of using a MPD for photon detection in the green channel is the increased time resolution, with respect to classical SPADs, and this in combination with a good detection efficiency at wavelengths shorter than 600nm. However, due to the significantly higher detection efficiency for SPADs at wavelengths above 600nm, SPADs are still the preferred photon detectors for the red channel.*

Characteristics of smFRET compatible fluorescent dyes

In vitro smFRET experiments typically depend on the utilization of extrinsic dyes covalently bound to the biomolecule of interest subsequent to purification. A large selection of fluorescent dyes is available both in terms of wavelength spectrum, photophysical properties and of reactive chemical groups, needed to perform specific labeling. Nonetheless, amongst the large number of commercially available fluorescent dyes, not all are optimal for smFRET experiments, which require the use of dyes respecting some basic photophysical proprieties:

Bright/High quantum yield: It is easy to understand that one strives to optimize the number of photons per dye and the brightness, therefore, represents an important criterion. An ideal fluorescent dye should have an extinction coefficient > 50,000 M^{-1} $cm^{-1}$and a high quantum yield (Roy *et al.*, 2008). Indeed, a fluorescent dye with a quantum yield of 0.8 and a mean lifetime of 4 ns, could in theory emit 200 million photons per second. Considering that an efficient optical setup detects roughly 5-10% of these photons, and that a fluorescent molecule spends a couple of milliseconds in the focal volume, several thousands of photons could, in theory, be detected per molecule.

Photostable and not subject to blinking: The major limitation in smFRET is the issue of low photostability. In fact, fluorescent dyes photobleach upon extended illumination at a rate that depends both on the laser intensity and the local environment of the dye. In general, dyes absorbing at longer wavelengths are more inclined to photobleach, which results in an underestimation of the FRET (Ha and Tinnefeld, 2012). Several strategies to improve the dye's photostability have been explored, most of them based on the removal of oxygen with a combination of glucose, glucose oxidase, and catalase (Roy *et al.*, 2008), and by adding a reducing agent such as β-mercaptoethanol or trolox (Rasnik *et al.*, 2006), a vitamin E analog. However, the chemical structure is different from one dye to another and there is hence no versatile protocol adapted to circumvent this problem for all kinds of dyes (Roy *et al.*, 2008; Ha and Tinnefeld, 2012). Moreover, some dyes periodically enter "dark states" during which no emission occurs. At a macroscopic level, the consequence of this phenomenon is a blinking behavior sometimes difficult to discern from FRET variations with biological relevance and which might broaden the FRET distribution (Ha and Tinnefeld, 2012).

Excited state lifetime: To perform accurate time-resolved measurements, it is preferable to work with fluorescent dyes with a monoexponential decay; i.e. a single excited-state lifetime. In fact,

some dyes display multiexponential decays sometimes due to isomerization transitions within the dye's chemical structure.

In addition, the excited state lifetime of the dyes employed in time-resolved smFRET experiments should be neither too long nor too short. In fact, it is important to find a good compromise between a high time resolution and the number of photons collected per molecule. On the one hand, the time-resolution is higher if the lifetime of the dye is shifted toward longer times (ideally 3-4 ns), but on the other hand, if the lifetime is short, more photons can be collected per molecule, which leads to a better signal-to-noise ratio. This is, parenthetically, also the reason why the extremely long lifetime of lanthanide-derived dyes explains why they are not well adapted for smFRET experiments, as only very few photons would be collected per time unit.

Comparison of a couple of commonly used smFRET dyes

	Dye	Excitation λ_{max} (nm)	Emission λ_{max} (nm)	Brightness[a]	Photostability (s)[b] (in Trolox or βME)
Donors	Cy3	550	565	1.0	91/50
	Atto550	554	577	1.9	72/27[c]
	Alexa555	555	567	0.8	65/35
Acceptors	Cy5	655	667	1.0	82/25
	ATTO647N	644	664	1.3	62/31
	Alexa647	650	667	1.2	58/20[c]

[a]Intensity at emission λ_{max} compared to Cy3 for donors (excitation at 532 nm) and compared to Cy5 for acceptors (excitation at 633 nm) while conjugated to DNA under same excitation power. [b]Average photobleaching time constant in 10 mM Tris-HCl (pH 8.0), 50 mM NaCl, oxygen-scavenging system with 2 mM Trolox or 142 mM βME at 200 W/cm² continuous wave incident excitation (532 nm or 633 nm) tethered to BSA-biotin surface. Corresponding dye pairs (Cy3-Cy5, R_0 = ~60 Å[35]; Atto550 - Atto647N, R_0 ~65 Å (a list of R_0 values for various Atto-dye FRET pairs is available at http://www.atto-tec.com/ATTO-TEC.com/Products/documents/R(0)-Values.pdf); Alexa555-Alexa647, R_0 = ~51 Å (Haugland, R. *Handbook of Fluorescence Probes and Research Products*, 9th edn., Molecular Probes; 2002) are labeled on duplex DNA with a 15-base-pair separation. [c]Dye displays severe dark state formation (blinking) in this solution condition.

***Table 3.2**. Comparison of several frequently employed smFRET dyes. Despite the fact that neither Cy3 nor Cy5 are very bright, their fairly large spectral separation in addition to their relatively high photostability (in trolox) have made them one of the most used dye-couple for smFRET experiments. (*(Roy *et al.*, 2008)

3.3.2 smFRET coupled to µsALEX enables sorting of molecules of interest

The general principle and some of the technical aspects enabling a correct implementation of solution based smFRET has now been introduced. In this chapter the smFRET technique called µsec ALternated EXcitation of single molecules for fluorescent aided molecule sorting (µsALEX) will be discussed. This experimental method was first developed by the group of Shimon Weiss in 2004 (Kapanidis *et al.*, 2004) and has since its introduction repeatedly proven its usefulness (Michalet *et al.*, 2006; Santoso *et al.*, 2008).

The implementation of a second laser to directly excite the acceptor makes it possible to sort out donor- and acceptor-only molecules

This method requires the use of two lasers (one emitting at the wavelength of donor excitation and the other emitting at the wavelength of acceptor excitation). An alternating excitation pattern is introduced on a microsecond timescale by use of electro-optics modulators- either an Acousto-Optical Tunable Filter (AOTF), or by directly modulating the diode lasers.

As previously mentioned, the sample has to be highly diluted to respect the single-molecule criterion. In fact, at a concentration as low as 20-50pM, statistically only one molecule is present in the focal volume at a time. Therefore, when a labeled molecule enters the focal volume, the dyes will be excited at the wavelength of the donor and at the wavelength of the acceptor, in an alternated manner. The emitted fluorescence is then detected in an identical manner as in a classical confocal smFRET setup.

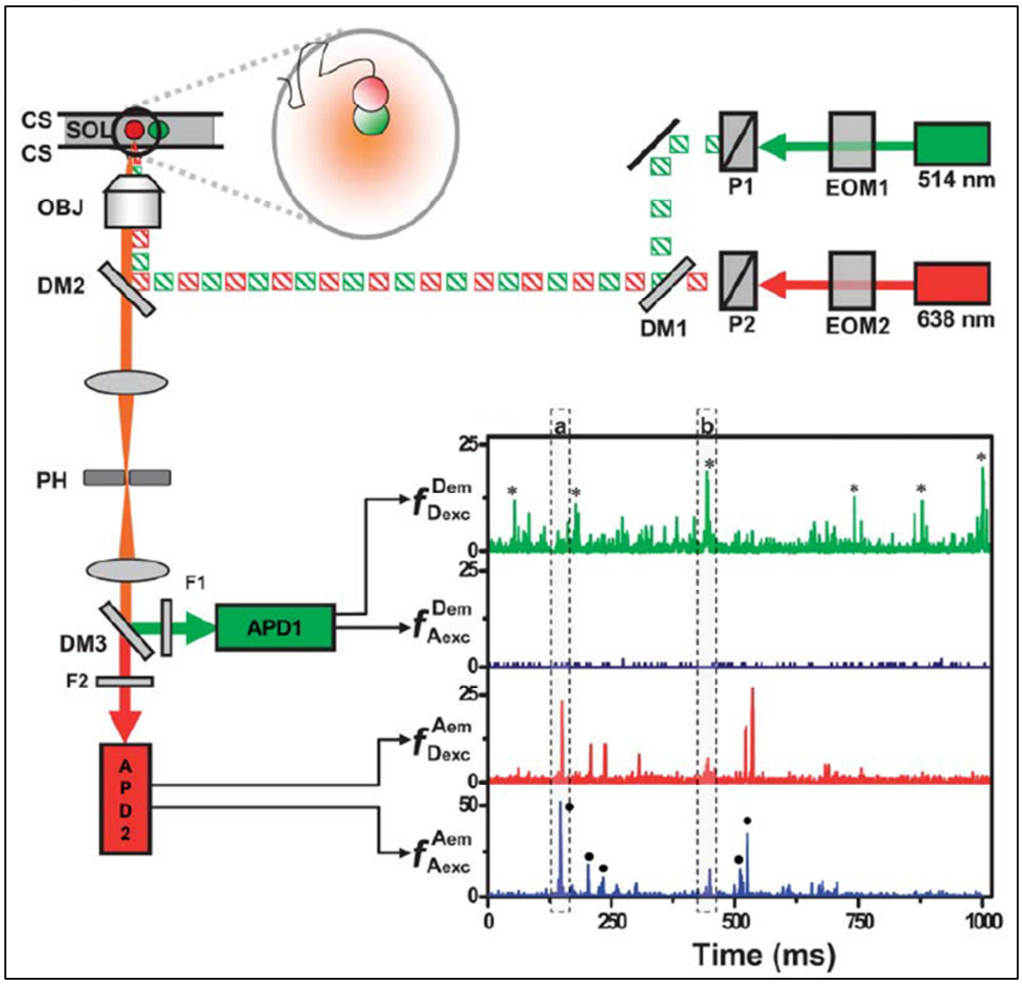

***Figure 3.12**. Schematic representation of a microsecond ALEX setup. A two-color alternated excitation beam enters the microscope and excites the sample. All the photons originating from the same molecule define a burst and it is known, for each photon, whether it was the "'green" or the "red" laser that generated it. Consequently, donor- and acceptor-only molecules can be discarded from molecules engaged in FRET (reproduced from* (Kapanidis *et al.*, 2004)*).*

Given that the alternation period is known, each photon can be attributed to originate from either the "green" (donor excitation) or the "red" (acceptor excitation) excitation, and this is precisely what gives μsALEX a major advantage over most other smFRET methods based exclusively on donor excitation. In fact, due to this alternated excitation pattern, donor- and acceptor-only labeled molecules can be distinguished from doubly labeled molecules, which is particularly helpful if the sample contains very low and/or very high FRET states. A thorough description of how to calculate these FRET-parameters will now be provided.

Calculation of the FRET efficiency

Donor excitation results in both donor emission and FRET if the acceptor dye is at a FRET compatible distance. A ratiometric calculus of the emitted fluorescence allows for the determination of the FRET efficiency (**Equation 14**).

$$E = \frac{F^{FRET}}{F^{FRET} + \gamma F_{Dexc}^{Dem}} \qquad \textbf{Equation 14}$$

where F^{FRET} stands for the acceptor emission upon donor excitation, i.e.: signal resulting from FRET, and F_{Dexc}^{Dem} stands for the donor emission upon donor excitation. γ is the detection factor that takes into consideration the quantum yield (Φ) of the dyes and the detection efficiency (δ) (**Equation 15).**

$$\Upsilon = \frac{\Phi_A \delta_A}{\Phi_D \delta_D} \qquad \textbf{Equation 15}$$

The quantum yield (Φ) depends on the local environment of the dye and the detection efficiency (δ) is directly linked to intrinsic characteristics of the detectors in addition to the various elements along the optical path such as filters and dichroic mirrors.

Shortly, a description will be given on how smFRET data is usually visualized on a 2-dimensional diagram and how this enables an accurate determination of Υ (Lee *et al.*, 2005). However, it is of high importance to stress that numerous additional factors strongly influence the calculated FRET efficiency, and that they have to be corrected for. Some of these parameters are listed below:

Bleed-through/Leakage (Lk): A certain amount of donor-emission could be detected in the acceptor channel. This bleed-through contribution is often considerable, especially when the spectral overlap between the donor emission and the acceptor excitation is very large, in which case the tail of the asymmetric distribution of the donor emission overlaps with the acceptor emission (**Figure 3.13**). Moreover, the bleed-through effect is further increased if the emission filters do not present a sufficient 0-to-100% cut-off at the desired wavelength.

Direct Excitation (Dir): Acceptor dyes sometimes get directly excited at the wavelength of the donor (**Figure 3.13**). The same reasoning is accurate vis-à-vis the direct excitation of the donor at the wavelength of the acceptor, but this contribution is negligible. Once again, this contribution becomes more significant when the dyes are spectrally similar.

Consequently, to estimate the real FRET efficiency, the leakage and the direct excitation have to be accounted for (Lee *et al.*, 2005), which brings about **equation 16.**

$$F^{FRET} = F_D^A - Lk - Dir \qquad \textbf{Equation 16}$$

where F_D^A stands for the fluorescence detected in the acceptor channel following donor excitation, and the leakage factor is defined as $Lk = \left(\frac{\delta_{Aem}^D}{\delta_{Dem}^D}\right) F_{Dexc}^{Dem}$, and the direct excitation factor is calculated as follows: $Dir = I_{D_{exc}} \sigma_{D_{exc}}^A \Phi_A \delta_{A_{em}}^A$, where $I_{D_{exc}}$ represents the donor laser intensity and $\sigma_{D_{exc}}^A$ represents the absorption cross section of the acceptor upon donor excitation.

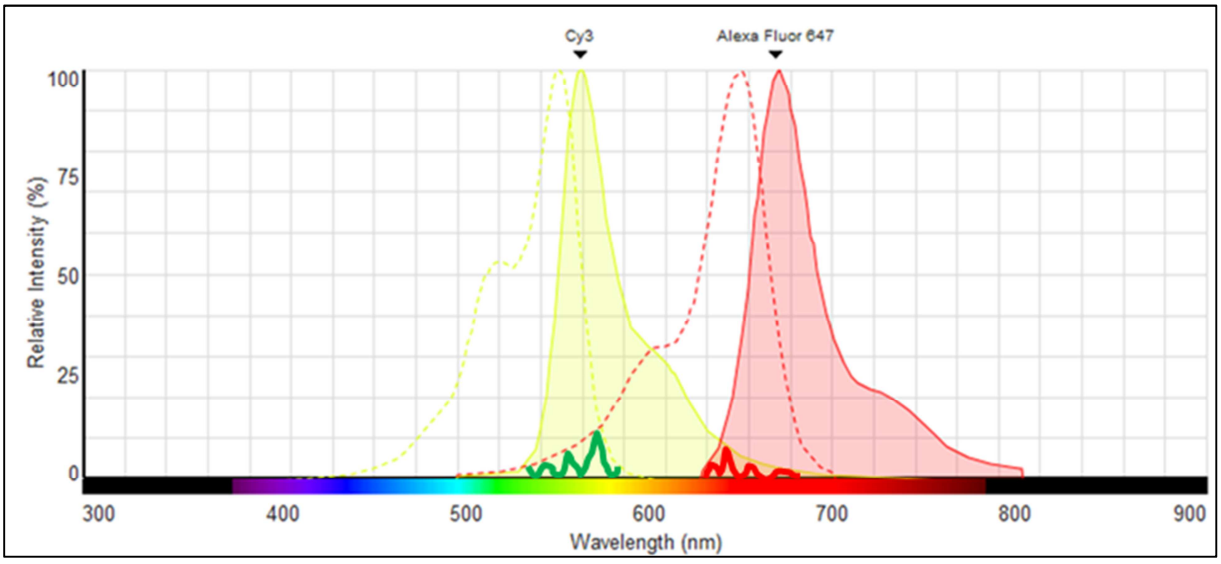

***Figure 3.13**. Absorption and excitation spectra for the dye couple Cy3 and Alexa647. The initial part of the excitation spectrum for Alexa647 overlaps with the excitation spectrum for Cy3. Consequently, a fraction of acceptor molecules are directly excited at the wavelength chosen to excite the donor. The tail of the donor emission overlaps with the emission spectrum of the acceptor leading to the detection of donor emission in the acceptor channel. (Invitrogen™, fluorescence spectra viewer)*

ALEX as a tool to sort molecules based on their stoichiometry value

As highlighted in the introduction of μsALEX, a great challenge in classical single laser smFRET experiments is to distinguish donor-only labeled molecules from molecules with a low FRET efficiency. The introduction of a second "red" laser offers the possibility to sort molecules based on their stoichiometry (S) (Kapanidis *et al.*, 2004) (**Equation 17**).

$$S = \frac{\gamma F_{D_{exc}}^{Dem} + F^{FRET}}{\gamma F_{D_{exc}}^{Dem} + F^{FRET} + F_{A_{exc}}^{Aem}} \qquad \textbf{Equation 17}$$

where $F_{A_{exc}}^{Aem}$ is the detected fluorescence in the acceptor channel following acceptor excitation.

Consequently:

For **donor only** labeled molecules: F^{FRET} and $F_{A_{exc}}^{Aem} \approx 0$, and consequently

$$\boldsymbol{S = \frac{\gamma F_{D_{exc}}^{Dem} + F^{FRET}}{\gamma F_{D_{exc}}^{Dem} + F^{FRET} + F_{A_{exc}}^{Aem}} \approx 1}$$

For **acceptor only** labeled molecules: F^{FRET} and $F_{D_{exc}}^{Dem} \approx 0$, and consequently

$$\boldsymbol{S = \frac{\gamma F_{D_{exc}}^{Dem} + F^{FRET}}{\gamma F_{D_{exc}}^{Dem} + F^{FRET} + F_{A_{exc}}^{Aem}} \approx 0}$$

By displaying the data on a 2-Dimensional E vs. S diagram, molecules of interest are easily sorted

The calculation of the FRET efficiency (E) and the stoichiometry (S) for the all molecules having individually diffused through the focal volume makes it possible to plot an E-S 2-dimensional diagram. On this 2D E-S diagram, donor only labeled molecules are displayed at a low FRET efficiency and a high stoichiometry value, whereas acceptor only molecules appear at a high FRET efficiency but low stoichiometry value. In contrast, doubly labeled molecules are seen at intermediate S-values and at the molecules respective FRET efficiencies.

The next step of the analysis consists in the estimation of the correction factors for direct excitation and leakage. To this aim, the 2D diagram is very useful. Indeed, the appropriate correction factors can be evaluated by adjusting the donor-only population to exactly correspond to an E of 0, and the acceptor-only population should be centered on a S-value of 0. Consequently, the population of doubly labeled molecules should appear with a S-value of approximately 0.5, as the exact values depends on the laser ratio, and thereby clearly separated from the simply labeled molecules (**Figure 3.14**).

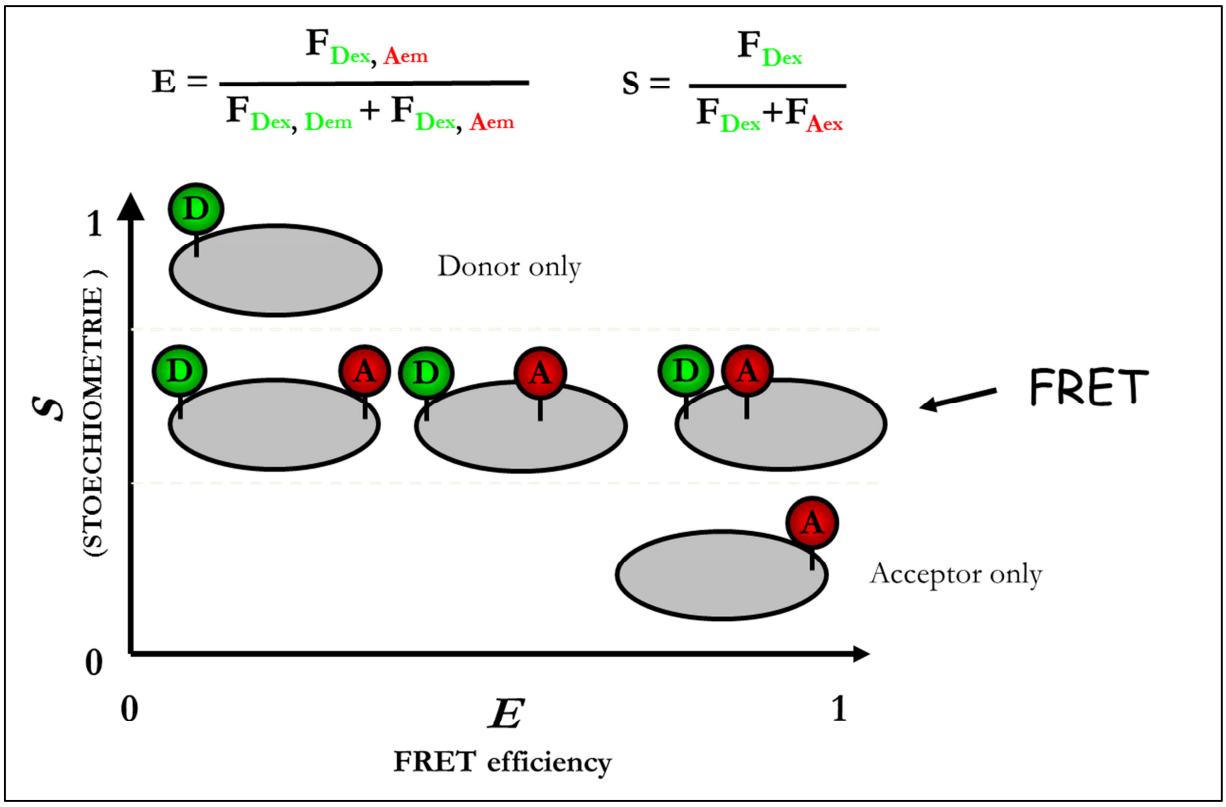

***Figure 3.14**. Stoichiometry versus FRET efficiency 2D plot for single molecules. Doubly labeled molecules result in a S-value of approximately 0.5 whereas donor only and acceptor only molecules take S-values of 1 and 0 respectively. Consequently, the different populations constituting a sample can be correctly sorted.*(Kapanidis *et al.*, 2004)

Figure 3.15.a shows an example of real data acquired with two double stranded DNAs (Kapanidis *et al.*, 2004) labeled with both a donor and an acceptor, separated by either 11 or 4 nm. After sorting of the molecules on the 2D diagram, the doubly labeled population is projected on the axes. The resulting 1D histograms are, generally, a more convenient way of representing the data. It is noteworthy to point out that, despite the difference in FRET efficiency, the doubly labeled

populations of each sample both have a stoichiometry value of 0.5 (after γ correction). **Figure 3.15.b-c** also show the usefulness of the small fraction of simply labeled molecules, as they allow for the correct estimation of the leakage and direct excitation contribution.

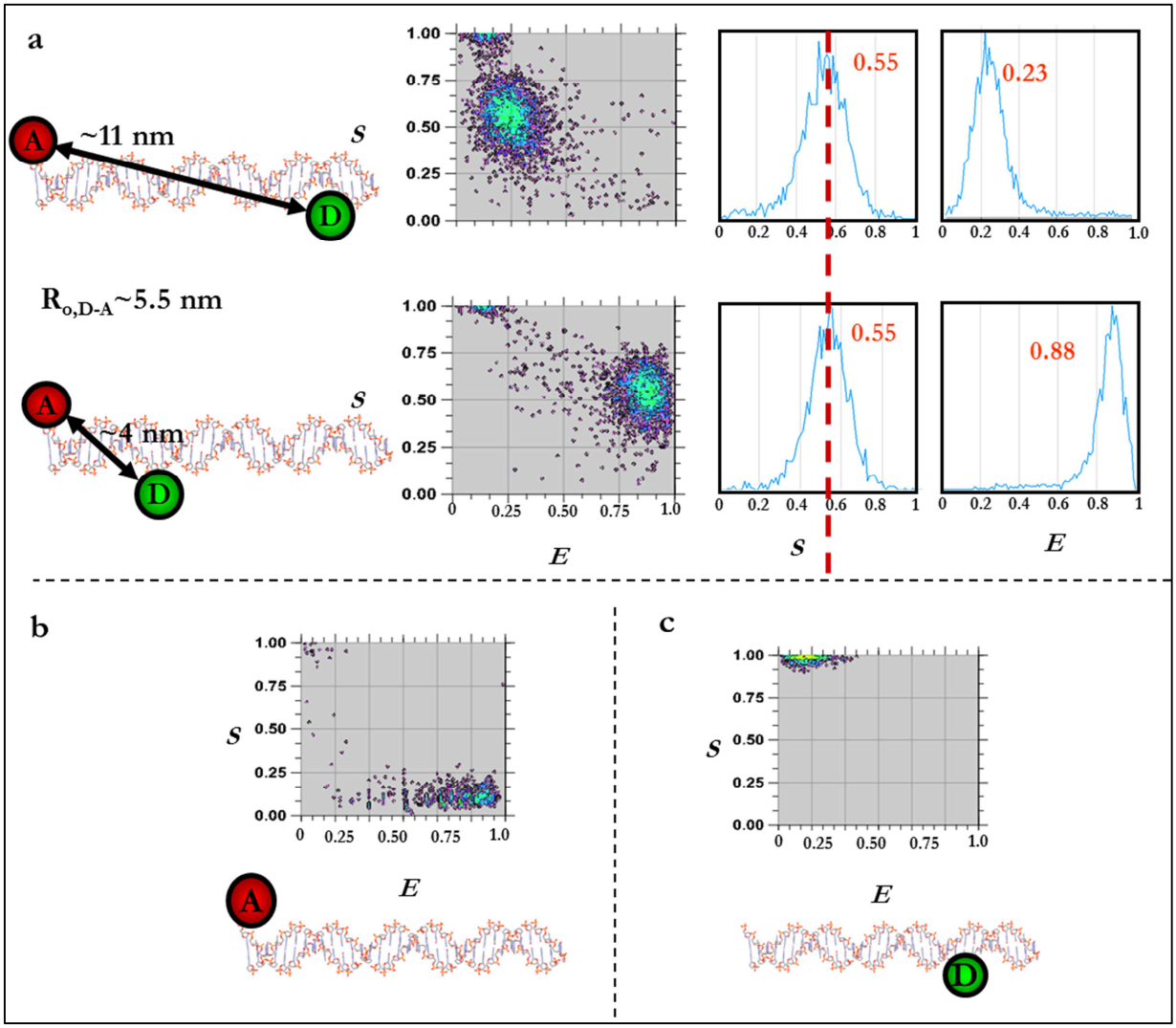

***Figure 3.15**. (**a**) Illustration of the distribution of single molecules on a 2-Dimensional E vs. S diagram for two doubly labeled DNA samples differing by the distance that separates the donor and the acceptor dye. Despite the differences in FRET efficiency, they both appear with S-values of 0.5, and are therefore well separated from the donor- and acceptor-only molecules. (**b and c**) Illustration of uncorrected acceptor (b)- and donor-only (c) molecules. This raw data clearly show that, initially, the acceptor-only molecules are not centered on a S-value of 0, and that the E value of the donor only population is slightly above 0. This is due to the contribution of leakage and direct excitation. Hence, the correction factors are adjusted until the S and E values for the donor- and acceptor-only molecules agree with the expected values for these populations.*(Kapanidis *et al.*, 2004)

Finally, to retrieve correct FRET efficiencies, the γ-factor, defined in **equation 15**, has to be estimated. Once again, this is easily done by means of the 2-dimensional diagram. In fact, there is a linear relation between E(raw) and 1/S, with E(raw) standing for the leakage and direct excitation uncorrected FRET signal. Therefore, by plotting 1/S=f(E(raw)) for two or more populations with different FRET efficiencies, the intercept $\Omega=1+\gamma\beta$ and the slope $\Sigma=\beta(1-\gamma)$. From these two values, γ is estimated and E can be correctly estimated (Lee *et al.*, 2005).

To summarize, μsALEX was the first smFRET method to introduce the use of a second laser to directly excite both the donor and the acceptor in an alternated manner. This technique has time and again proven its usefulness (see Michalet *et al.*, 2006 for a detailed review) as it offers the possibility to separate the doubly labeled molecules of interest from the simply labeled molecules that might be mistaken for low FRET or high FRET molecules as a consequence of the contribution of leakage and direct excitation. Moreover, the advantages provided by μsALEX have inspired several groups to develop the highly useful methods nsALEX (BK Müller *et al.*, 2005; Kudryavtsev *et al.*, 2012) and msALEX (Margeat *et al.*, 2006), the former being the topic of discussion in an upcoming chapter.

However, it is important to highlight that the calculated FRET efficiency (E), in μsALEX, is burst-integrated, i.e. averaged over the residence-time of the molecule in the focal volume. Consequently, in presence of a dynamic system where the molecule undergoes conformational changes at a rate faster than the residence-time, the true dynamics cannot be directly retrieved by this method. Nonetheless, if the Gaussian distribution of E is broader than the width expected to be caused only by shot-noise (Santoso *et al.*, 2010), the presence of underlying dynamics is very likely, and fortunately, other time resolved smFRET methods exist to extract this highly interesting information.

3.3.3 Time resolved smFRET-MFD : a powerful method to analyze and display smFRET data

In theory, precise distances with a spatial resolution of a couple of Ångströms, and dynamic transitions with a nanosecond temporal resolution, are obtainable through smFRET experiments. For many years this goal was way out of reach, but thanks to recent technological improvements and the development of new efficient software, we are now one step closer to this aim (Craggs and Kapanidis, 2012). In this chapter, I will therefore thoroughly describe the powerful time-resolved smFRET technique known as multiparameter fluorescence detection (MFD) and its latest extension, MFD with pulsed interleaved excitation (PIE), both of which I have employed throughout my thesis, and on which a large majority of my results are based.

MFD is a technique developed by the molecular physical chemistry group at Düsseldorf University under the direction of Pr. Claus SEIDEL. In addition to the information contained in a classical smFRET experiment, MFD also incorporates two other important parameters, namely anisotropy and excited-state lifetime. MFD therefore directly offers the possibility to investigate a system's dynamic properties, and helps estimate the contribution of diverse complicated photophysical artifacts that might be misinterpreted as biologically significant (Sisamakis *et al.*, 2010).

In order to perform time-resolved smFRET measurements, the single photon counting detectors of the confocal setup have to run in a time-correlated single photon counting (TCSPC) detection mode, by which the excited state lifetime of the dyes can be estimated. It is, thus, first necessary to introduce the concept of TCSPC prior to any attempt to explain the principle and applications of MFD.

Principle of Time-Correlated Single Photon Counting (TCSPC)

As previously mentioned, time-resolved smFRET techniques directly estimate the FRET efficiency from the lifetime of the donor dye through **equation 8**.

$$E = 1 - \frac{\tau_{DA}}{\tau_D} \qquad \textbf{Equation 8}$$

Presently, TCSPC is the only reliable way to determine the donor lifetime at the single molecule level. As a matter of fact, the principle of TCSPC detection is in itself very simple,

nonetheless, its realization requires highly sophisticated equipment and constant awareness of the many possible artifacts that might bias the data.

In very basic terms, the principle of TCSPC is to measure the time between a short laser pulse and the arrival of the photon originating from that very same pulse. Hence, by repeating this procedure many times, a histogram of arrival times can be generated, and the mean excited state lifetime of the dye can be estimated (**figure 3.17**). In the case where many detectors are in use, each and every detected photon will be assigned with three tags: channel number (spectral region and polarization), micro-time and macrotime. The micro-time corresponds to the aforementioned time-delay between excitation and emission and the macro-time is the total time from the beginning of the experiment. The macro-time is obtained by counting the number of laser pulses for which the repetition rate is known or, alternatively, has to be measured (**figure 3.17**)(Becker and Hickl TCSPC handbook).

TCSPC requires the use of a high-repetition pulsed laser, efficient single-photon counting detectors and a TCSPC reading card. The experiment begins with the excitation of the sample by a laser pulse for which the arrival time is measured with high accuracy by the constant function discriminator (CFD) (**Figure 3.16**). The CFD then instantly triggers the time-to-amplitude converter (TAC). The function of the TAC is somewhat similar to a charging condenser with the charge building up linearly over time on a pico-second time scale. When the photon originating from the molecule excited by the laser pulse that started the TAC is detected, a stop signal will be sent to the TAC. As the TAC's charging rate is known, the voltage is proportional to the time delay between the pulse and the arrival of the fluorescence photon. In order to convert the amplitude of the TAC signal into a specific time, the signal firstly has to be amplified by the programmable gain amplifier (PGA) and secondly being processed by the analog-to-digital converter (ADC) from which the numerical value will be given (Becker and Hickl TCSPC handbook).

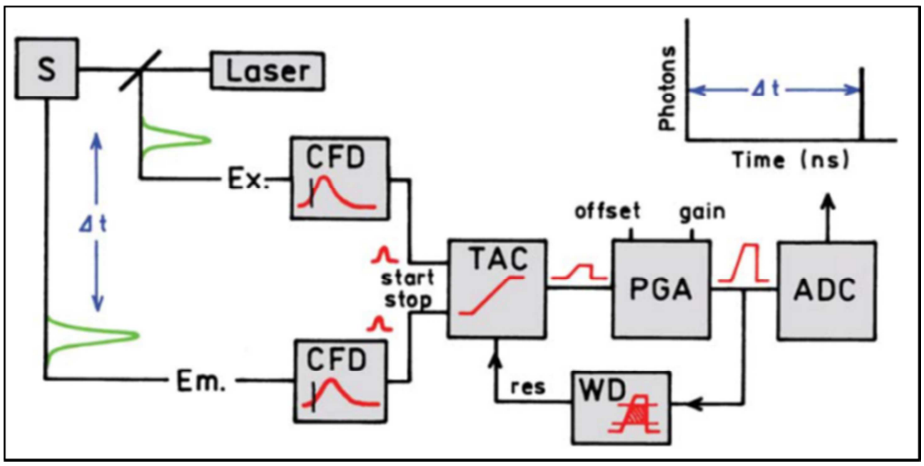

***Figure 3.16**. Scheme of the electronics used in TCSPC, see text for explanation. (TCSPC handbook, Becker and Hickl, 3rd edition, 2008)*

In reality, it is more convenient to let the arriving photon trigger the TAC and using the succeeding laser pulse to stop it, in what is called a reversed start-stop mode. The reason for this is that most laser pulses do not lead to the emission of a photon, in which case, the TAC do not receive a stop signal if the TCSPC runs in a start only mode. That aside, the principle remains the same as formerly described since the laser repetition rate is both known and constant, and consequently the desired time-delay can still be extracted (TCSPC handbook, Becker and Hickl, 3rd edition, 2008).

Moreover, if the emission rate is too high, there is risk of having a so called "pile-up effect". As the measured time-delay corresponds to the time between the pulse and the 1st photon, all photons originating from the same pulse that could hypothetically follow are not going to be accounted for, which results in a shift of the estimated lifetime toward a lower value. This is due to the fact that the TAC has to reset between each start-stop signal and even with modern technology, this takes a finite amount of time during which no further photons can be detected. This is defined as the dead-time of the TAC. Therefore, the experimental condition has to be set to make sure that only one pulse out of 100 actually produces the emission of a photon. In general, this is accomplished by either decreasing the sample concentration or the light intensity (Becker and Hickl TCSPC handbook).

The data obtained from a TCSPC experiment is hence a decay plotted in a graph illustrating the photon count as a function of time from which the average lifetime can be estimated by exponential fitting. However, the unique intrinsic characteristics of the electronics (for instance in terms of time-delays within the detectors or unwanted after-pulses) also have to be taken into consideration. In fact, the measured decay is, in reality, a convolution of the "real" fluorescent decay

and the instrumental response function (IRF). The IRF can be evaluated by measuring a non-fluorescent sample, for instance water or a clean buffer, and then in order to determine precisely the lifetime of the dye, its decay has to be deconvoluted from the detected signal (Sisamakis *et al.*, 2010).

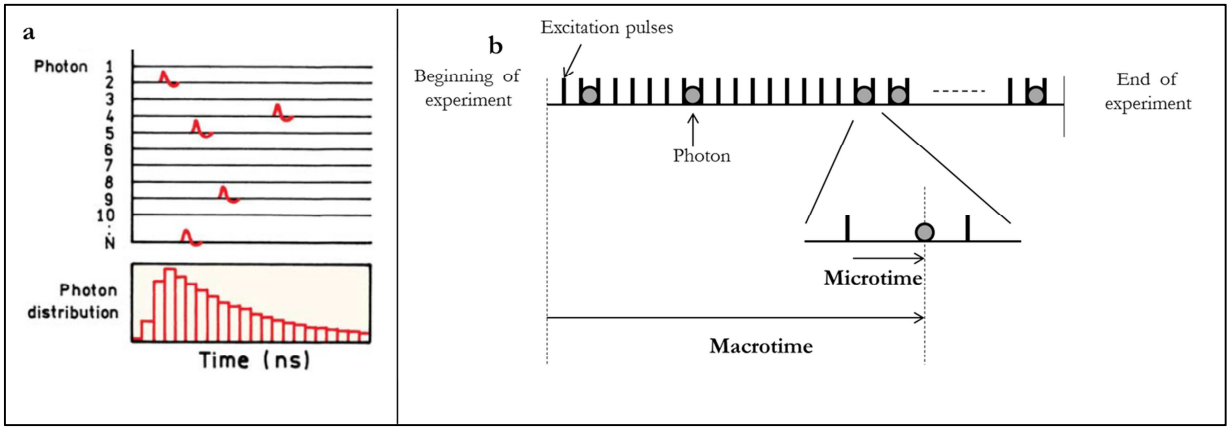

Figure 3.17. *(**a**) Illustration of how the decay from a TCSPC experiment is generated. Photon emission is a stochastic process with a given probability at each moment in time and this probability distribution can be known by measuring the arrival-time of a large number of individual photons. Consequently, as the probability of emitting a photon decreases exponentially over time, the mean lifetime of the dye can be estimated from ($\tau_{1/2}$.) (**b**) Principle of time-tagging. On average, only one pulse out of 100 leads to the emission of a photon. The microtime is defined as the timedelay between an excitation pulse and the arrival of the photon resulting from that very pulse, and the macrotime corresponds to the arrival time of the photon with respect to the beginning of the experiment. Accordingly, each and every detected photon in an experiment is assigned three tags: its microtime, its macrotime and its channel number (color and polarization) (TCSPC handbook, Becker and Hickl).*

General description of a MFD Setup

The TCSPC detection mode, which is a requirement to perform MFD experiments, has now been explained and I will move on and describe some additional necessary features concerning the design of the setup. For an in-depth description of the different components of our MFD setup, readers are directed to our article in chapter 4.1 "Pulsed interleaved excitation fluorescence spectroscopy with a supercontinuum source" (Olofsson and Margeat, 2013). The general principle is, however, represented in **figure 3.18**.

The principle of MFD is, as introduced above, based on the determination of several critical parameters: donor lifetime, polarization anisotropy and color. In order to access all this information, the confocal microscopy setup must be constructed with a picosecond pulsed polarized laser and at

least four single photon counting detectors (SPADs) coupled to a TCSPC reading card. The pulsed laser is required to engender lifetime decays by TSCPC and the four detectors must be positioned to collect photons following spectral (for FRET) and polarization (for anisotropy) separation.

Firstly, **figure 3.18** shows that the sample is excited with a horizontally polarized excitation beam, and secondly, that the resulting fluorescent signal is directed through a polarizing beamsplitter which splits the signal into its parallel and perpendicular components. The parallel and the perpendicular beams are then spectrally separated by dichroic mirrors just before the photon counting detectors. Accordingly, the four detectors are labeled: donor parallel ($D_{//}$), donor perpendicular ($D_{\perp}$), acceptor parallel ($A_{//}$) and acceptor perpendicular ($A_{\perp}$).

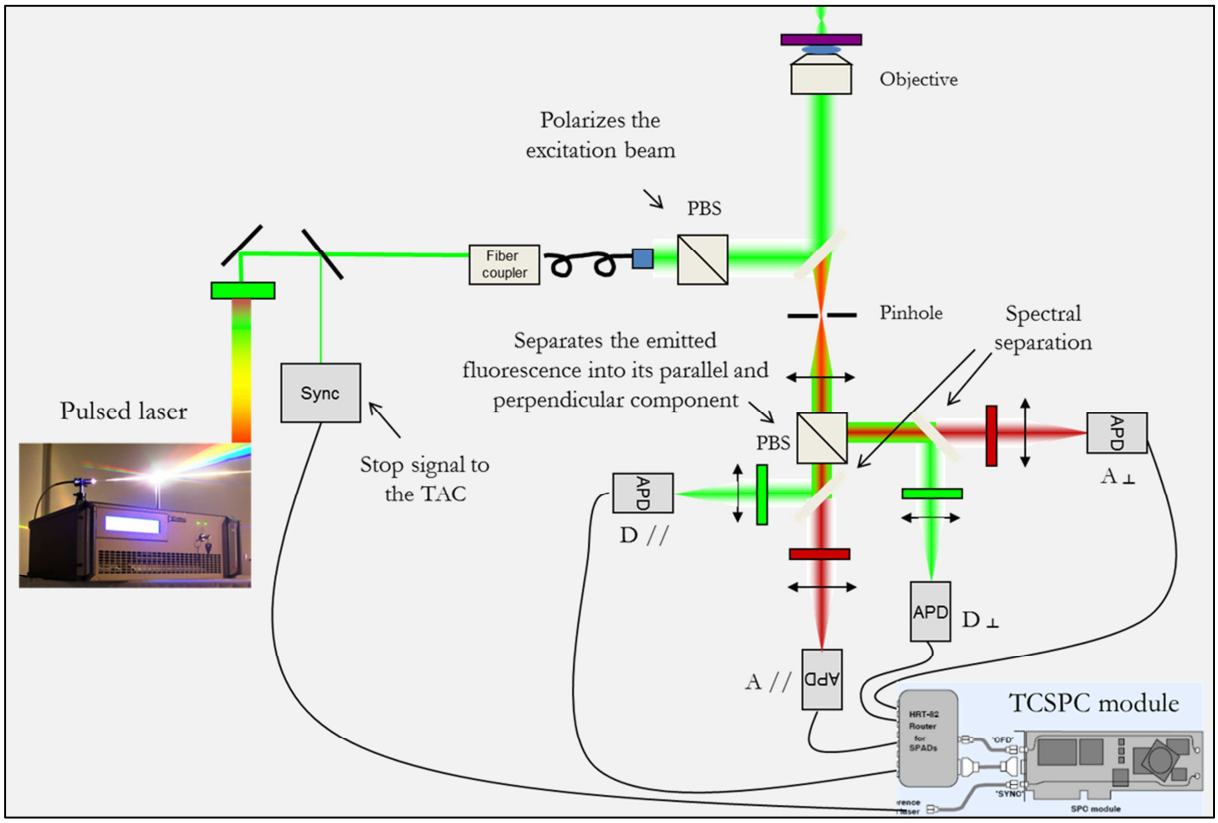

***Figure 3.18**. Example of a classical MFD Experimental setup. The sample is first excited with a polarized excitation beam and the emitted fluorescence is directed through the pinhole for the removal of out-of-focus light. The fluorescent signal is then separated into its parallel and perpendicular components by a polarizing beamsplitter prior to the spectral separation by the dichroic mirrors. Accordingly, the setup is equipped with in total four SPADs labeled: donor parallel ($D_{//}$), donor perpendicular ($D_{\perp}$), acceptor parallel ($A_{//}$) and acceptor perpendicular ($A_{\perp}$), which are all coupled to the TCSPC reading card.*

Principle of MFD data acquisition and analysis

Having now explained the more technical aspects of the MFD setup, I will explain how a MFD experiment is carried out experimentally, and how the data is analyzed. It was previously briefly mentioned that MFD experiments can be performed by using either a single monochromatic excitation, or combined with a second excitation pulse that directly excites the acceptor, the latter referred to as the "Pulsed Interleaved Excitation" (PIE) mode (Kudryavtsev *et al.*, 2012; Hendrix and Lamb, 2013). I will begin by focusing exclusively on the analysis of data acquired using a single excitation wavelength and then, later on, I will detail the interest of using the PIE mode.

In a classical MFD experiment realized in our lab, the laser runs at 40MHz, and as the molecule spends on average 4ms in the focal volume, each molecule could theoretically be excited up to 10^5 times. However, we know that in an ideal TCSPC measurement, only 1% of the laser pulses really lead to the emission of a photon, (to prevent creating pile-up effects that would bias the estimated lifetime toward a lower value) and that the detection efficiency is assumed to be approximately 5-10%. In practice, this still means that a few hundreds of photons are theoretically collected per molecule, which is sufficient for smFRET experiments. To each and every one of these detected photons, the single photon counting module assigns the three tags that were mentioned in the earlier description of TCSPC (microtime, macrotime and channel number, and which report on color and polarization).

The first step of the analysis generally consists of a reconstruction of the entire photon trace from the beginning of the experiment. From this photon trace, the fluorescence originating from the molecules of interest has to be extracted from the non-negligible contribution of scattered photons and other sources of background noise. This task is performed using a "burst search algorithm" or a "time-window analysis" (Sisamakis et al. 2010):

Burst search algorithm: By applying a maximum allowed interphoton-time filter on the reconstructed photon trace, the high emission rate of fluorescent dyes enables the sorting out of fluorescent molecules from the background (**Figure 3.19.a-b**). The emitted photons from single molecule events can now be analyzed separately. If an event contains enough photons (typically more than 20), the decay histogram for the donor is generated. From the reconstructed decay, the donor excited state lifetime in presence of an acceptor ($\tau_{D(A)}$) is determined, and this for each molecule. (**Figure 3.20**). In a similar manner, the anisotropy of the donor as well as the ratiometric

FRET parameters can easily be calculated. Nevertheless, it is important to point out that the calculated FRET as well as the anisotropy are burst-integrated, i.e. averaged over the dwell time of the molecule in the focal volume (Sisamakis et al. 2010).

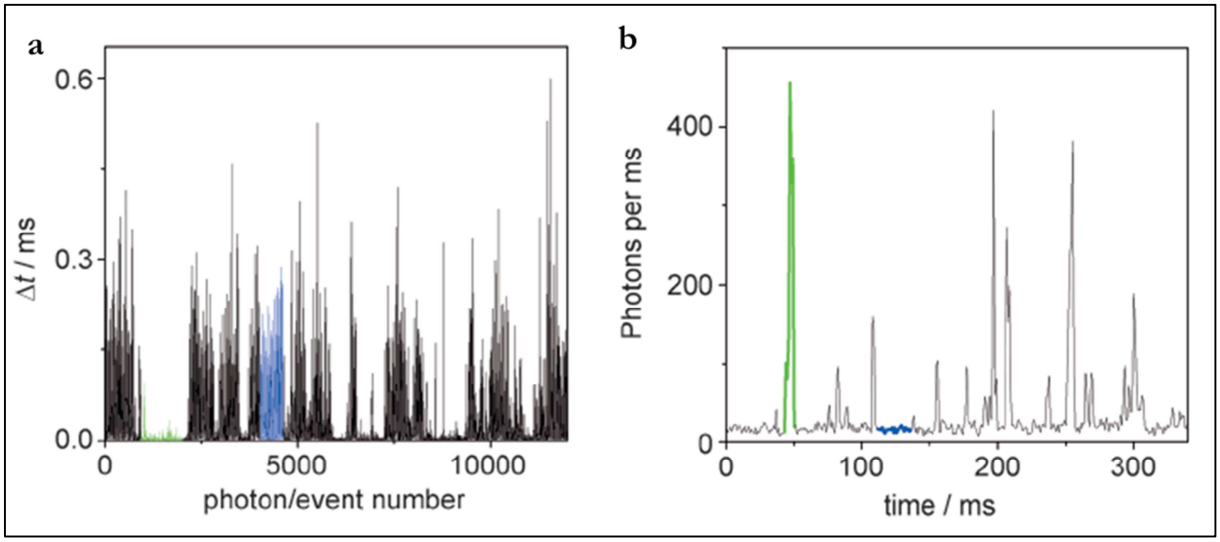

***Figure 3.19**. Principle of the maximum allowed interphoton-time burst-search algorithm. (**a**) The detected photons are represented on the x-axis and the "time between photons" is represented as on the y-axis. The background is mostly due to scatter photons and "dim" impurities for which the time period between two successive photons is long (blue selection). Consequently, by applying a short maximum allowed interphoton-time filter, only photons emitted at a high rate will be selected (green selection). (**b**) Photon count vs. time for the same photons as in (a). This representation clearly shows that the green selection corresponds to a labeled molecule that emitted a significant number of photons while in the focal volume whereas the photons selected in blue contribute to the background noise.* (Kudryavtsev *et al.*, 2012)

Time-window analysis: Instead of performing a burst-search, the entire photon-trace can be divided into time-frames of equal length, possibly as short as 250μsec. The subsequent analysis is carried out in an identical manner as described above where the decay is generated and fitted for the time-windows which contain more than 20 photons in the green channel (**Figure 3.20**), and the ratiometric FRET and the anisotropy are calculated for the time-windows that respect the short inter-photon time criterion. Performing a time-window analysis can be proven useful if dynamic phenomena occur on a timescale similar to the chosen timeframe. For instance, if a molecule undergoes constant conformational changes between two states, only the mean value for E, τ and r will be obtained if a burst-search approach is implemented. By applying a time-window analysis and progressively decreasing the length of the timeframes on the same data, E will not remain constant,

indicating that more than one conformation is required to accurately describe the system. (Sisamakis et al. 2010). Yet, it is nearly impossible to quantitatively study conformational changes faster than 250µsec with this method due to a too low a number of photons per timeframe (Kalinin *et al.*, 2010a). Fortunately, other strategies are available to overcome this limitation. Some of these methods, including "the photon (or probability) distribution analysis method", "Fluorescence Cross Correlation Spectroscopy" and its extension "Species Filtered Cross Correlation", will be explained at length in an upcoming chapter.

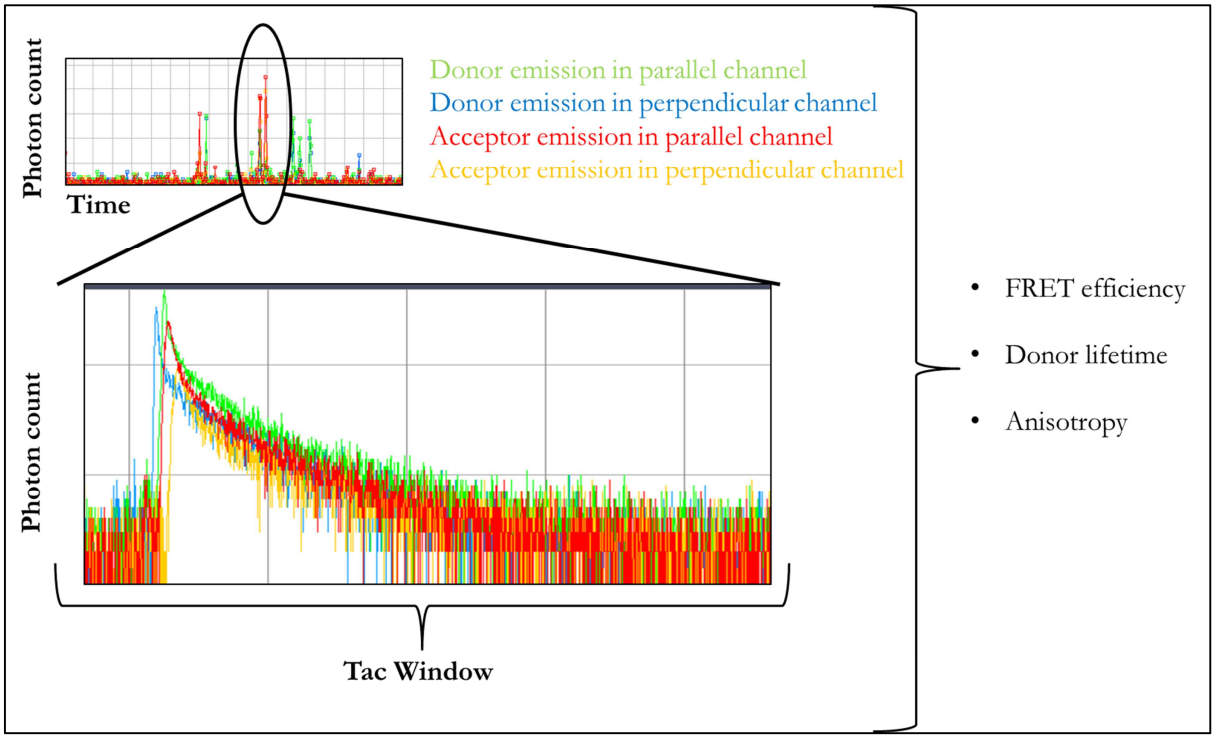

***Figure 3.20**. After reconstruction of the entire photon trace, a burst search algorithm based on a "maximum allowed interphoton time" is applied in order to extract the photons emitted from fluorescent single-molecules (bursts) from the background for each channel. For bursts containing more than 20 photons, the decay is reconstructed and the average excited state lifetime of the donor is estimated using a maximum likelihood estimator algorithm. In addition, the FRET and the anisotropy are calculated for each single molecule event. For the sake of clarity, it should be underlined that in this figure, the decay is in reality not created from a single molecule event but from an ensemble of events. The principle, nevertheless, remains identical.*

It will shortly be described how MFD data is analyzed and displayed but I would first like to stress a couple of very important points with regards to what has just been explained concerning the time-window analysis.

The time-window analyzing method described here should not be confounded with the other time-window based approach called photon (or probability) distribution analysis (PDA), which will be brought up in the chapter 3.3.4 "smFRET- Methods for analyzing fast dynamics". In the current example, the photons detected in a single time-window should be considered as representative of a single molecule, and each time-window will be analyzed and displayed in an identical manner as a single molecule event. Accordingly, by observing the 2D diagram (see next chapter), it is easy to verify if an investigated system is truly static, as the "burst integrated" result should be identical to the result of the time-window analysis with respect to all the investigated parameters (donor lifetime, FRET and anisotropy etc.).

In PDA, on the other hand, the entire photon stream is, indeed, also divided into time-windows of equal length which are analyzed individually, but only the FRET efficiency (or anisotropy) is calculated for each time-window, and displayed in a 1D histogram. Subsequently, PDA calculates the combination of photons that would give rise to the observed experimental FRET distribution, and thereby reveal whether several FRET states are involved (Antonik *et al.*, 2006). More details on how this is achieved will be provided in chapter 3.3.4.

Displaying MFD data on a 2D diagram

A MFD experiment brings about a substantial amount of data and it can, thus, be very challenging to extract and take advantage of all the information it contains. For that reason, I will now take on the question of describing how some of the most commonly used parameters are calculated and, once again, emphasize the usefulness of a 2D diagram.

Displaying a FRET indicator on a 2D diagram

In the chapter on μsALEX, it was pointed out how the 2D diagram allowed for the correct sorting of doubly labeled molecules engaged in FRET. Here, we will once more see how displaying the data in 2 dimensions assists in giving a general initial overlook of the data.

Figure 3.21 lists the main MFD parameters that can be plotted in the 2D diagram for single molecules. Consequently, by choosing the appropriate combination of factors, molecules of interest can be selected and represented based on the objectives of the study.

In general, the first steps consist of verifying that the "number of photons over time" (i.e. mean macro time) was constant throughout the experiment to verify, for instance, that the laser intensity was constant and that the sample did not contain any aggregations. The next step is to remove the molecules that photobleached by applying the criterion where the burst-averaged macroscopic arrival time has to be the same for the photons collected in the green channel and the photons collected in the red channel. Secondly, the FRET efficiency (E) (or another FRET indicator (FI)) or the steady state polarization anisotropy (r_D) is plotted against the lifetime of the donor.

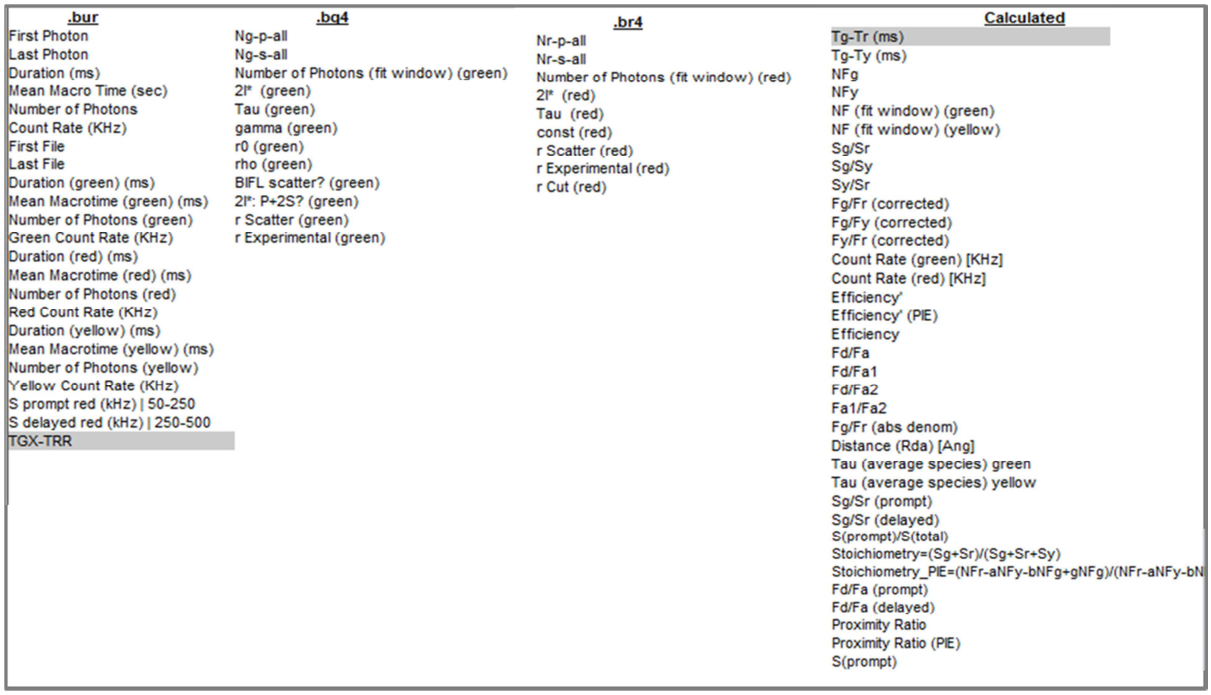

***Figure 3.21**. Illustration of the different parameters that can be represented either on the x- or on the y-axis of the 2D diagram displaying single molecule events. The .bur column represents the parameters for all channels; .bg4 shows the parameters in the green channel; .br4 represents the red channel and "calculated" shows the outcomes of everything that has been calculated. All parameters can be combined at will, which gives rise to a large number of possibilities. (Margarita software, Seidel group, Dusseldorf University)*

To display the commonly used FI, the fluorescence ratio $\frac{F_D}{F_A}$, the fluorescence from the donor (F_D) and the fluorescence from the acceptor (F_A) have to be calculated for each molecule.

The fluorescence of the donor (F_D) is calculated by using **equation 18**:

$$F_D = \frac{S_G - \langle B_G \rangle}{\delta_G}$$ **Equation 18**

where S_G is the total signal in the donor channel, B_G is the background in the donor channel and δ_G is the detection efficiency in the donor channel.

The signal detected in the acceptor channel corresponds both to acceptor emission via FRET but also by the small fraction of photons originating from the donor, due to the asymmetric emission profile (leakage), and by the direct excitation of the acceptor, as previously described in the chapter on μsALEX. Presently, these parameters are combined to define the crosstalk factor (α), which has to be taken into consideration while calculating the fluorescence of the acceptor F_A in **equation 19**.

$$F_A = \frac{S_R - \alpha F_G - \langle B_R \rangle}{\delta_R}$$ **Equation 19**

where α is the crosstalk pre-factor and S_R and B_R represent the total signal and the background in the acceptor channel, respectively.

It should be noted that other FRET indicators are commonly used to present MFD data. If the main goal of the study is to resolve exact distances the FRET efficiency (E) (see chapter on μsALEX) has to be employed. Otherwise, relative changes between different states can be expressed using for instance the $\frac{S_g}{S_r}$ ratio, or the proximity ratio ($PR = \frac{S_R}{S_R + S_G}$). (Sisamakis et al. 2010).

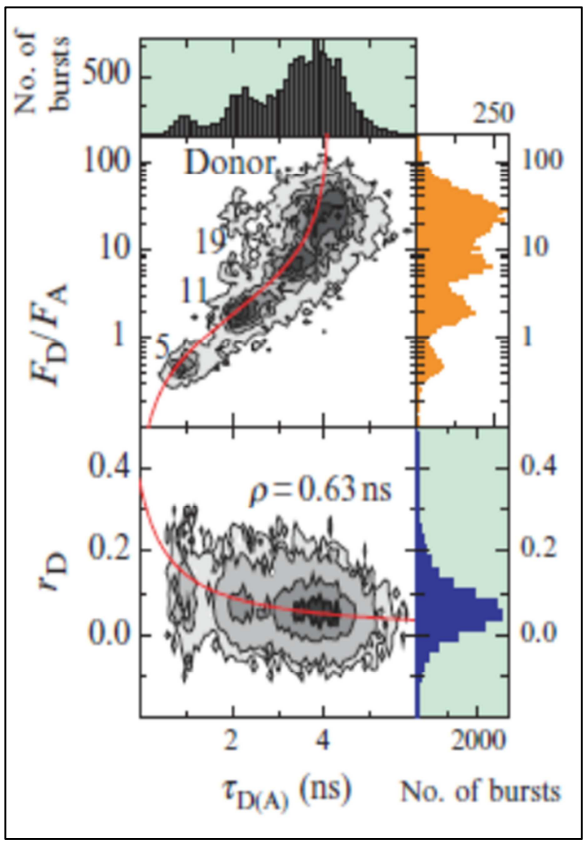

***Figure 3.22**. Examples of MFD 2D diagram. The FRET indicator F_D/F_A (upper) and the steady state anisotropy r_D (lower) are plotted as a function the lifetime of the donor in presence of an acceptor $\tau_{D(A)}$. This sample contains two DNA samples labeled with dyes either separated by 5 (high-FRET) or by 11 base pairs (low-FRET) and a donor only population. The F_D/F_A diagram clearly demonstrates that $\tau_{D(A)}$ decreases with an increase in FRET. The populations in the r_D vs. $\tau_{D(A)}$ are well overlaid with the theoretical perrin equation, which shows that the value for K^2 is constant. Ideally, variations in FRET should systematically be checked for a consistent shifts in $\tau_{D(A)}$ and r_D. In case of discrepancies, the observed FRET variation might be due to a photophysical phenomenon and not to a change in transfer efficiency. By projecting the populations along the axes, the resulting 1D histogram is a useful tool to represent and compare data between different measurements and experimental conditions. (Sisamakis et al. 2010)*

Displaying the polarization anisotropy on a 2D diagram

A shift in FRET also induces a variation in polarization anisotropy. At a high energy transfer rate, the excited state lifetime of the donor is shortened and, consequently, a lower amount of photons will be detected by the perpendicular detectors. Thus, according to the Perrin equation, adapted for FRET (**Equation 19**), the anisotropy should increase with an increase of FRET:

$$r_D = \frac{r_0}{1+\tau_{D(A)}/\theta_D} \qquad \textbf{Equation 19}$$

where r_0 is the fundamental anisotropy and θ_D is the rotational correlation time of the donor. For the calculation of the anisotropy for single molecules, detected using a high numerical aperture objective lens, **equation 20** is used:

$$r_D = \frac{GF_{D,\parallel} - F_{D,\perp}}{(1-3l_2)GF_{D\parallel} + (2-3l_1)F_{D,\perp}} \qquad \textbf{Equation 20}$$

where G represents the "G-factor", i.e. the ratio of detection efficiencies between the parallel and the perpendicular channel. ($G = \frac{\delta_{\perp}}{\delta_{\parallel}}$) and l_1 and l_2 are necessary to correct for polarization mixing by the objective (Koshioka *et al*, 1995).

Sometimes, the dye linker is constrained in space in one or several preferential positions and this might lead to the misinterpretation that there are several populations with different FRET values. To refute this hypothesis, the Perrin equation is used to draw a theoretical line, by which the different FRET populations represented on the 2D diagram should be overlaid. If this condition is not respected, it might indeed be caused by a difference in the rotational correlation time, which presumes that the K^2 value varies and that the calculated distances are not accurate, and it becomes indispensable to change for another linker or dye (Widengren *et al.*, 2006) (**Figure 3.22**).

The 2D diagram exposes donor and/or acceptor quenching

A visual inspection of the 2D diagram overlaid by the theoretical line for a static system (static FRET-line) (**Figure 3.23.a)**, also provides valuable information concerning possible artifacts due to donor or acceptor quenching that bias the observed FRET. Donor quenching in one of the sub-populations, for instance, results in a horizontal shift toward a lower $\tau_{D(A)}$ with respect to the static FRET-line (**Figure 3.23.b**). Acceptor quenching, on the other hand, leads to an underestimation of the FI which shifts the quenched subpopulation vertically. (**Figure 3.23.b**) A reliable approach to verify if the acceptor is quenched is to take advantage of the information provided by the additional acceptor excitation in the Pulsed Interleaved Excitation (PIE) mode, as will be described shortly.

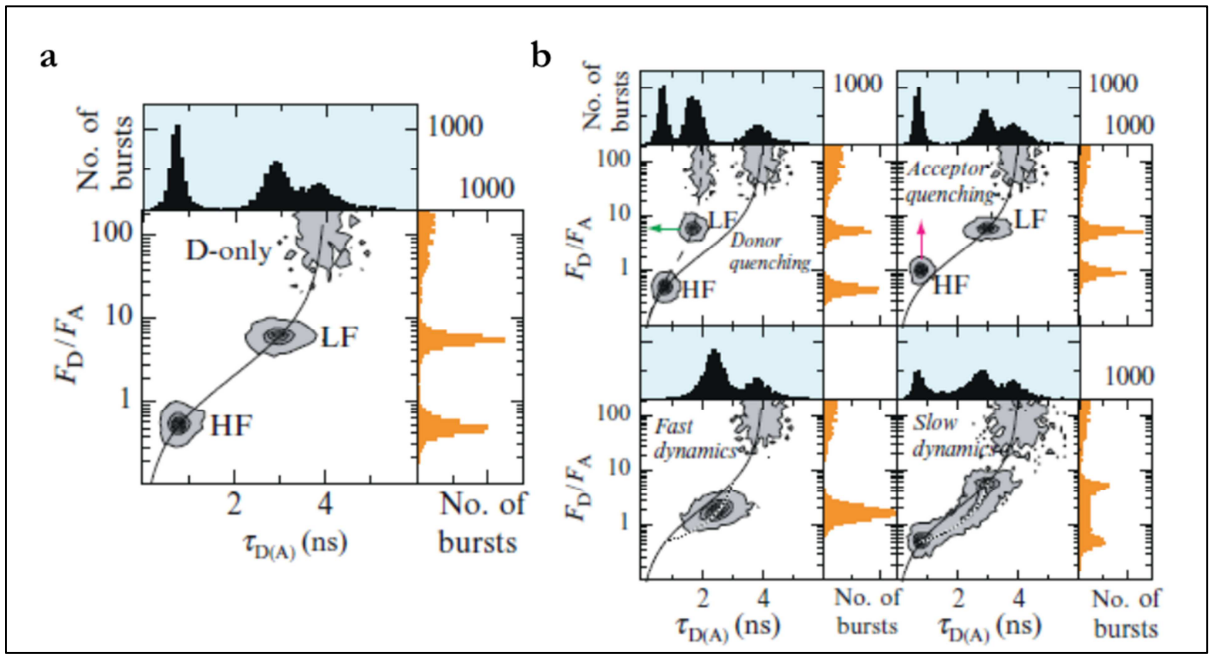

***Figure 3.23**. (**a**) Representation of simulated data of a static system containing a high-FRET population and a low-FRET population and donor-only molecules. The overlaid line corresponds to the theoretical line, on which two static states should be aligned. (**b**) Upper panel. In the case where the donor is quenched, the position of the low-FRET is shifted toward a shorter lifetime whereas acceptor quenching leads to a shift of the donor population toward a lower FRET efficiency. (**b**) Lower panel. 2D plots for a dynamic system interconverting either at a rate >> dwell time which results in the fusion of the two FRET populations around its mean value (N.B. the Gaussian distribution is wider than the one expected for a single static conformation), or at a rate =/> dwell time, which brings about a "smear" that interconnects the two distinguishable sub-populations, suggesting underlying dynamics.*

The 2D MFD diagram reveals underlying dynamics

Moreover, biological systems are rarely static, as the function of most macro-molecules is finely tuned by minor conformational changes seldom exceeding displacements of more than a couple of Ångströms. For this reason, the 2D MFD diagram is very advantageous as it gives a first indication to whether a system is dynamic or not. In fact, a two-state dynamic interconverting system gives rise to two FRET populations that are interconnected by a "smear" that is shifted horizontally toward a higher $\tau_{D(A)}$. It is crucial to underline that the same pattern is observed if the measurement is done at too high a concentration of molecules. Depending on the interconversion rate between the states, the 2D MFD diagram shows either all the involved states or provides important information for complementary quantitative methods (Sisamakis et al. 2010; Kalinin, Valeri, et al. 2010):

(**i**) If the transition rate between the states is slower than the residence time of the molecule in the focal volume (dwell time), the two states will be well separated as the molecule will appear static as it diffuses through. In this case, conformational changes are better studied on immobilized particles and TIRF

(**ii**) If the transition rate is much faster than the dwell time, only the mean FRET value will be observed. Even so, the Gaussian distribution is broader than the theoretical shot-noise distribution for a static system. The shot-noise contribution is due to the fact that the emission of a photon is a stochastic process which leads to a Gaussian emission profile around a mean with a calculable width. If the width is broader than the theoretical value, it suggests that more than one state is involved. In addition, this population will not be overlaid by the theoretical line for two static populations, thereby providing another argument for the importance of employing quantitative methods developed for the study of fast dynamics, such as fluorescence cross correlation based methods (**Figure 3.24.a**).

(**iii**) In the case where the transition rate is similar to the dwell time, the sub-populations will be somewhat fused but still to some extent discernable, and linked by a "smear". For this specific situation, a time-window analysis is an ideal tool to separate the different subpopulations (**Figure 3.24.a-b**).

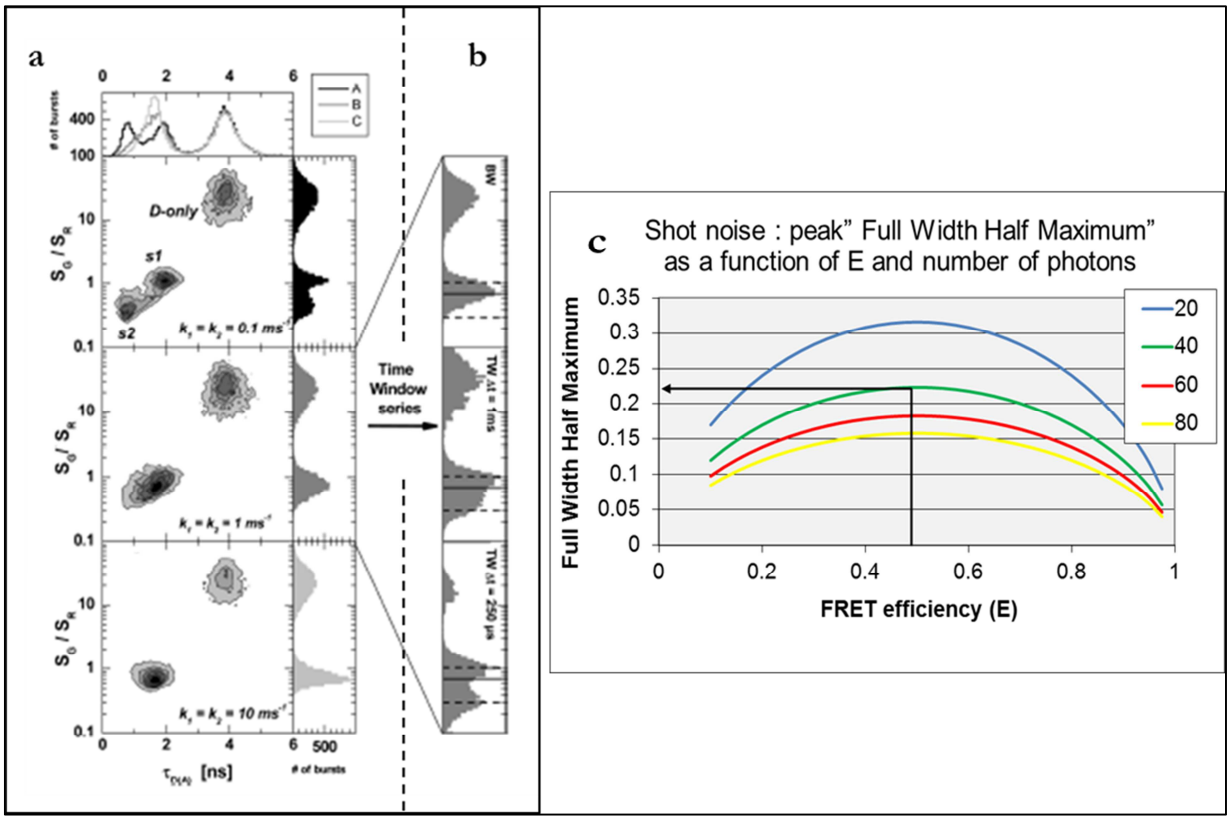

Figure 3.24. *(**a**) Influence of dynamics on the S_g/S_r vs. $\tau_{D(A)}$ distribution on the 2D diagram for a dynamic system interconverting between two states with varying rate constants: from top to bottom, $k_1=k_2=0.1ms^{-1}$, $k_1=k_2=1ms^{-1}$ and $k_1=k_2=10ms^{-1}$. At an interconverting rate slower than the dwell time of the molecules ($k_1=k_2=0.1ms^{-1}$), both states are clearly visible but somewhat interconnected by a smear. At an interconverting rate similar to the dwell time ($k_1=k_2=1ms^{-1}$), the two populations have fused, giving rise to one population with a very large Gaussian distribution that strongly suggest the existence of underlying dynamics. At an interconverting rate much faster than the dwell time ($k_1=k_2=10ms^{-1}$), only one population with a broad Gaussian distribution, and not overlaid by the static FRET line, is discernable. (**b**) Time window analysis (TW = 1ms or TW= 250µsec) on the sample interconverting at a rate similar to the dwell time (middle). By progressively decreasing the length of the time window, the two populations become well separated.* (Kalinin *et al.*, 2010a)*(**c**) Image representing the theoretical width of the Gaussian distribution as a function of E and the minimal number of photons criteria set for the burst search. A higher photon restriction narrows down the full width half maximum value. The black arrow indicates that for a state with a FRET value of 50% and a burst search criteria set to 40 photons, the theoretical shot-noise broadening should not exceed ~0.22. Any additional broadening suggests either dynamics, or possibly, photophysics.*

Chapter 3.3.4 is dedicated to some of the different techniques that might be utilized to precisely quantify the timescale of the dynamics revealed by the 2D diagram. However, to finish the chapter on MFD, I am first going to present the most useful extension of MFD called MFD with pulsed interleaved excitation (PIE), based on the implementation of a second laser to directly excite the acceptor.

MFD with Pulsed Interleaved Excitation (PIE)

Direct acceptor excitation with a second pulsed interleaved laser, undeniably, contributes valuable additional information (Kudryavtsev *et al.*, 2012). As previously described for μsALEX, an alternating excitation pattern allows for the sorting of molecules as a function of their stoichiometry. Therefore, in the case where the FRET efficiency for one of the subpopulations is low, it becomes possible to differentiate low-FRET and high-FRET molecules from donor- and acceptor-only labeled molecules.

Figure 3.25 illustrates the MFD-PIE setup that I have implemented at the CBS. Even though a thorough description of the different components is provided in chapter 4.1, a brief overview might be of assistance to understand how MFD-PIE data is acquired. Our setup differs from most other pulsed interleaved excitation setups by the use of a supercontinuum laser source emitting over the 450-800nm range. Therefore, instead of using two monochromatic lasers, the wavelengths are chosen by selecting the appropriate excitation bandpass filters right after having separated the output beam into two distinct paths with different length (prompt and delayed). The alternated excitation pattern is then created by recombining the beams again before the sample is excited, and the "green" pulse is coupled to the TAC synchronizer. With regard to the detection strategy, nothing has changed in comparison to what was earlier described for classical MFD.

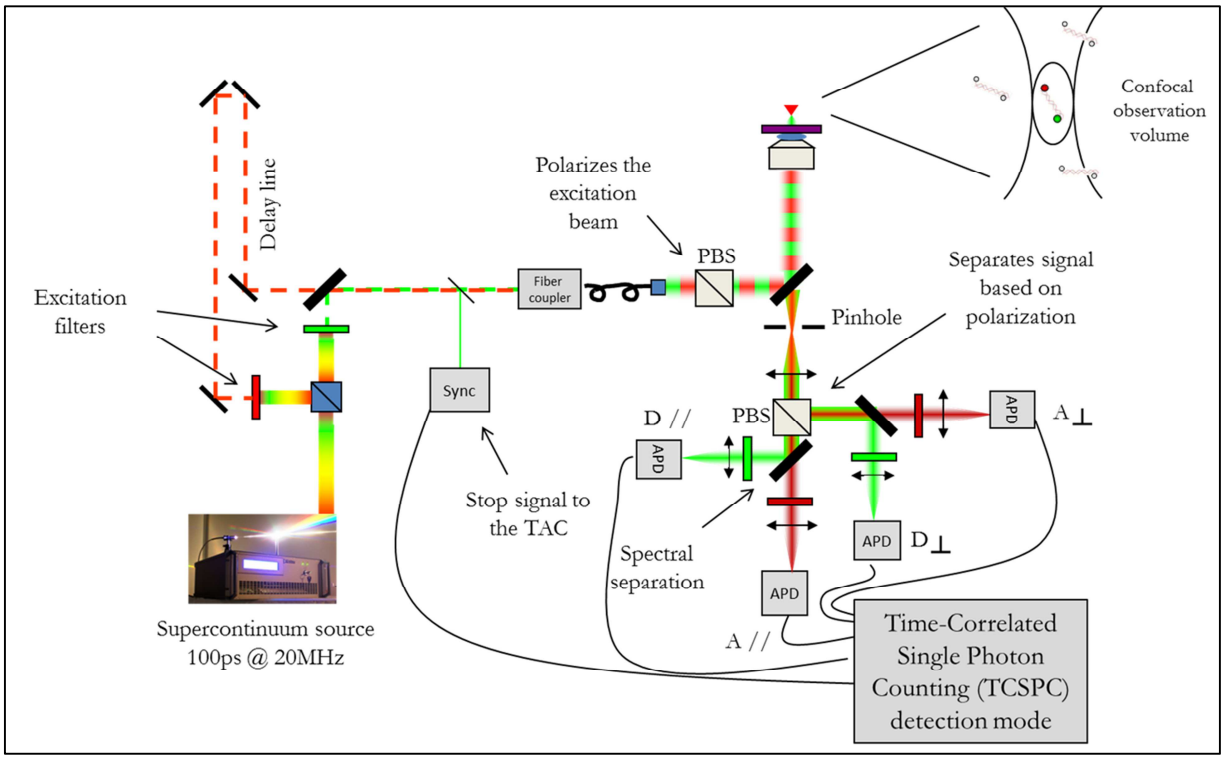

Figure 3.25. *Schematic illustration of our MFD-PIE setup. The excitation wavelengths are easily adjusted through the choice of appropriate excitation filters for the prompt and the delayed path. By subsequently recombining the beams, an alternated excitation pattern is generated. Importantly, only photons originating from the "green" pulses should be coupled to the synchronizer to maintain a TAC window of 50ns.*

As shown in **figure 3.26**, the second laser excites the sample long enough after the green laser to allow for the decay in the prompt part of the TAC window to be completed. The red laser then excites the acceptor, and its decay is generated in the delayed part of the TAC window. Altogether, three individual decays are created for each single molecule- a donor decay, an acceptor decay following donor excitation and an acceptor decay following acceptor excitation - and all three decays are fitted independently to estimate the mean excited state lifetimes.

To rule out the presence of photophysical artifacts in the FRET data, the quantum yields of both dyes have to be verified. Thanks to the direction excitation of the acceptor in PIE, the mean excited state lifetime of the acceptor is easily measured, in addition to that of the donor.

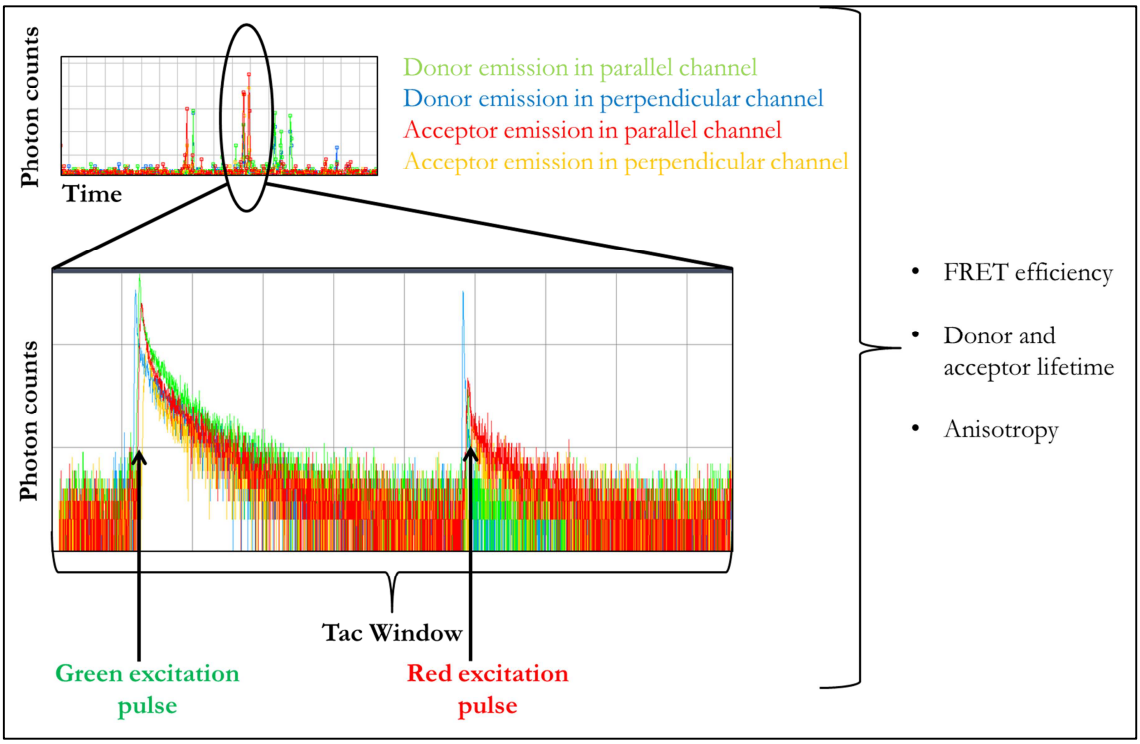

***Figure 3.26**. For bursts containing more than 20 photons, the decay histograms are reconstructed and the average lifetime of the donor and the acceptor are estimated using a maximum likelihood estimator algorithm applied to the prompt and the delayed window respectively. Moreover, the photons emitted in the delayed channel are used to calculate the stoichiometry value for each molecule as previously described for µsALEX.*

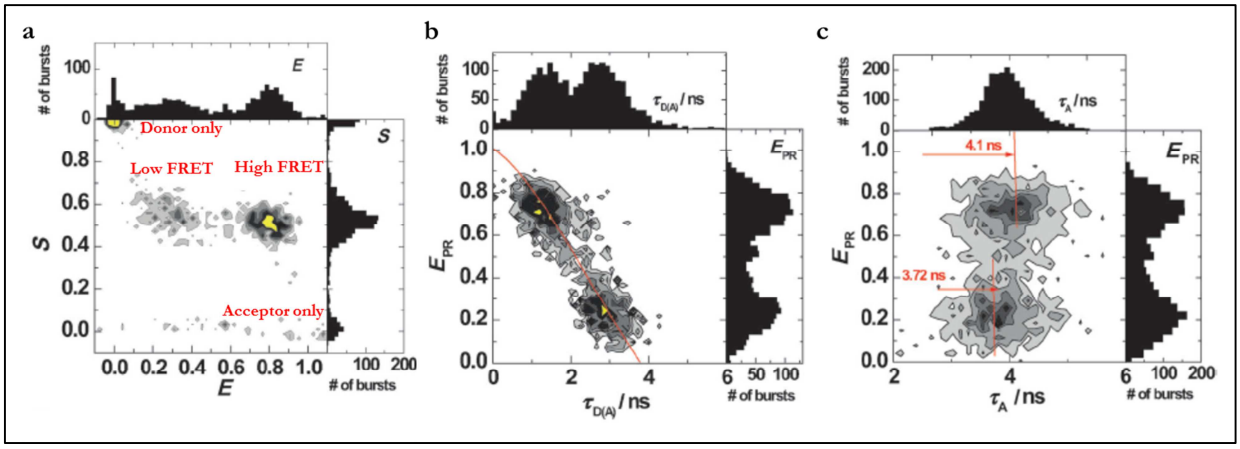

***Figure 3.27**. 2D representations of a sample containing a high-FRET and a low-FRET population acquired with PIE. (**a**) Stoichiometry vs. FRET efficiency 2D diagram. The donor only (S=1) and the acceptor only (S=0) molecules are well separated from the low-FRET and the high-FRET population (S=0.5), demonstrating the utility of the stoichiometry factor in the selection of the molecules of interest. (**b**) Proximity ratio vs. $\tau_{D(A)}$ 2D diagram. The lifetime distribution is in agreement with the calculated FRET, signifying that the existence of two separate populations is really the consequence of energy transfer. (**c**) By displaying the acceptor lifetime τ_A versus the proximity ratio, it is, however, unveiled that the acceptor is slightly quenched in the low-FRET state. The lower quantum yield of the acceptor, if not corrected for, would lead to an underestimation of the FRET efficiency for the low-FRET state, and it is only by performing PIE that this can be exposed and quantified* (Kudryavtsev *et al.*, 2012).

In addition to the stoichiometry (**Figure 3.27.a**), the mean excited state lifetimes for both dyes (**Figure 3.27.b-c**), the leakage, the direct excitation and the detection correction factor (γ) (see chapter μsALEX), MFD-PIE offers the possibility to detect acceptor blinking and sort out those molecules which have been photobleached during their residence time in the focal volume.

In fact, to eliminate the photobleached molecules from experimental data, only the single molecule events with similar burst-averaged macroscopic arrival times, following both donor and acceptor excitation are selected for further analysis on the 2D diagram by applying the criterion $|T_{GX}-T_{RR}|<0.7$ms with T_{GX} standing for "burst-averaged macroscopic arrival time" in any channel following donor excitation and T_{RR} for "burst-averaged macroscopic arrival time" in the red channel , following acceptor excitation (**Figure 3.28.a-e**) (Kudryavtsev *et al.*, 2012; Hendrix and Lamb, 2013).

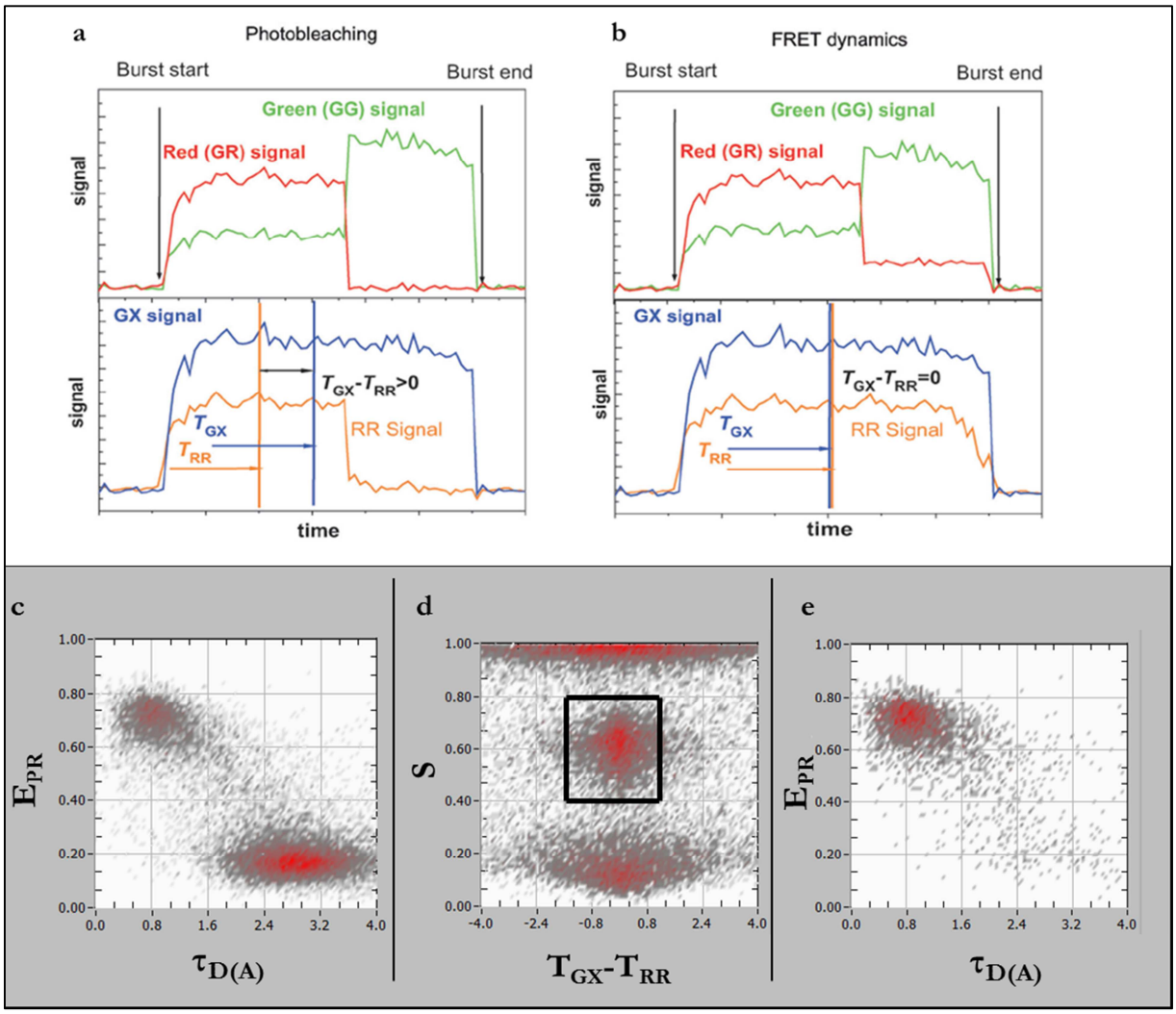

Figure 3.28. *Example of how PIE can assist in sorting out the molecules that have photobleached during their residence time in the focal volume. (**a**) and (**b**) represent the signal over time detected for one molecule (burst). In (a) the acceptor photobleaches before leaving the focal volume, which results in a value for T_{RR} much shorter than for T_{GX}, and consequently the value for T_{GX}-T_{RR} >0. In (b) on the other hand, the molecules change from a high-FRET state to a low FRET state during the stay in the focal volume. The total number of photons collected in the prompt channel is very similar in both (a) and (b). However, the direct excitation of the acceptor in the delayed channel attests that the acceptor is not bleached, as shown by the constant value for T_{RR} throughout the entire length of the burst (T_{GX}-T_{RR}=0)* (Kudryavtsev *et al.*, 2012). ***(c-e)*** *Example of a MFD-PIE experiment acquired with a doubly labeled DNA oligomer. (**c**) The FRET indicator "proximity ratio" (E_{PR}) for each molecule is shown as a function of $\tau_{D(A)}$ (**d**) By representing the stoichiometry of the molecules as a function of T_{GX}-T_{RR}, only doubly labeled molecules (S~0.6), spared of photobleaching (|TGX-TRR|<0.7ms), are selected for the representation shown in (**e**).*

Furthermore, the stoichiometry factor S provides valuable information with regards to the blinking behavior of the acceptor. If the acceptor occasionally enters the triplet dark state, it will not undergo FRET and consequently make appear a low-FRET state lacking real significance. This photophysical artifact cannot be identified just by observing the FRET distribution, as the apparent lifetime of the acceptor will not be affected by this phenomenon. However, acceptor blinking will broaden the Gaussian distribution of the stoichiometry factor, which is a good indication that another acceptor would be preferable.

In conclusion, PIE-MFD combines all the advantages of μsALEX and MFD, all the while overcoming their respective shortcomings. It has, to date, the most performing potential of all available smFRET analyzing procedures and has therefore been my method of choice throughout my Ph.D thesis.

Up until this point of the dissertation, I have several times insisted on how burst integrated data might suggest the existence of underlying fast dynamics, and I will now describe some of the analyzing methods that I have made use of to study the dynamics of mGluRs.

3.3.4 smFRET- Methods for analyzing fast dynamics

Depending on the timescale(s) of the biological and/or physical phenomena under investigation, it is critical to find which method is most appropriate. Moreover, often times, one single method is not sufficient to cover the entire range of timescales necessary to describe the complex behavior of most macromolecules. **Figure 3.29** suggests some of the analyzing methods that might be used to study dynamics. For the study of slow dynamics, diffusion based methods are not well suited because of the limited time during which the molecule is observed. Diffusion based methods for the studies of dynamics are therefore restricted to fast phenomena occurring on a sub-millisecond time-scale.

In view of this, an extensive overview of the techniques "photon distribution analysis" and "fluorescence correlation spectroscopy" will now be presented.

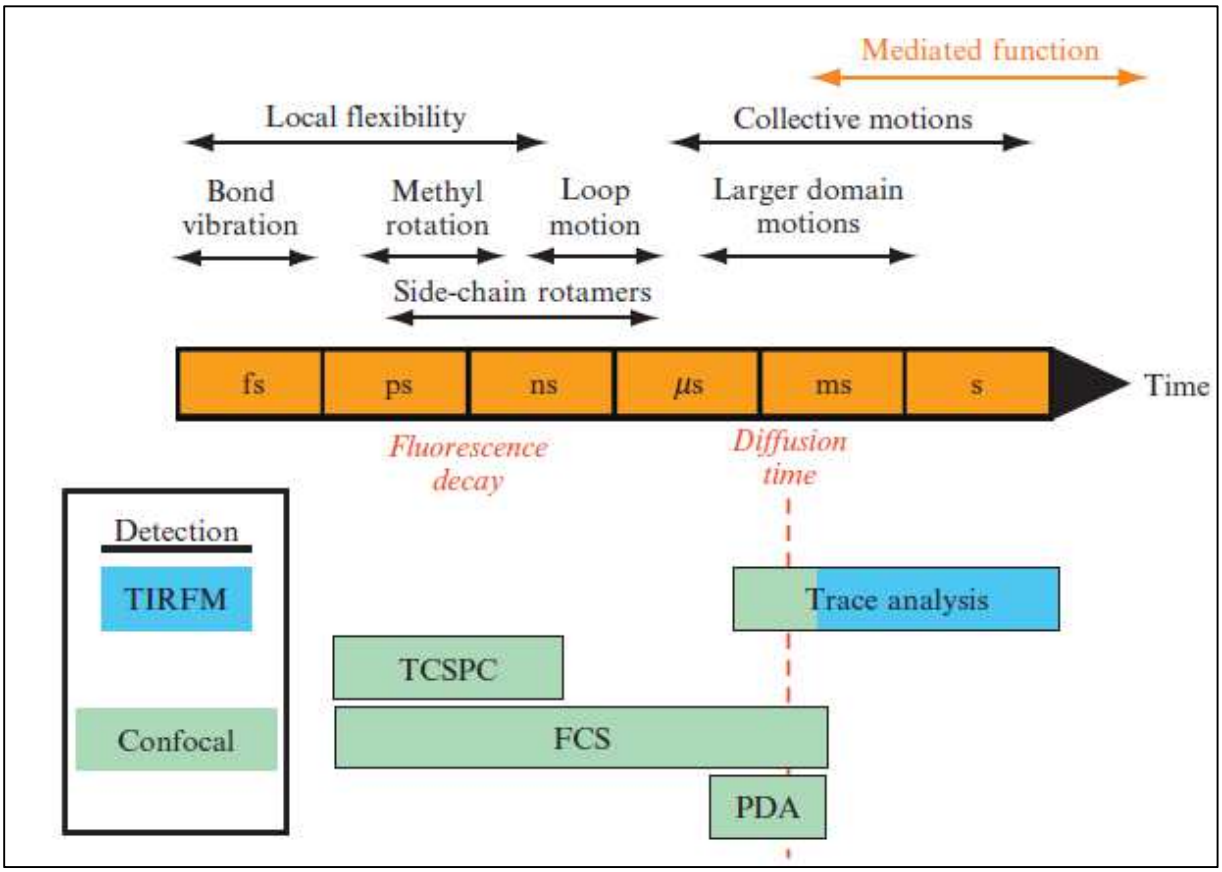

Figure 3.29. *Summary of the different techniques which either have or will be presented in this dissertation, and on which all the results in this thesis are based. Solution based methods are ideal for the studies of dynamics occurring on a timescale faster than the millisecond. PDA is an efficient method to quantify dynamics ranging from approximately 100μsec to a couple of milliseconds. If the dynamics are much faster, fluorescence correlation methods are better suited. (Sisamakis et al., 2010)*

Revealing dynamics through photon distribution analyses

smFRET data are most commonly displayed as a 1D histogram, distributed around its mean value and fitted with a Gaussian distribution. The width of the Gaussian distribution is due to the fact that fluorescence is a stochastic process, and this statistic broadening is generally referred to as "shot-noise". As a matter of fact, the theoretical distribution of a static state can be calculated (**figure 3.30.**), and any additional broadening of the Gaussian distribution might be caused by conformational dynamics but possibly also by the existence of several static overlapping states (or possibly photophysics). In order to determine the underlying cause of this additional widening, several methods have been instigated (Torella *et al.*, 2011; Tomov *et al.*, 2012). In this context,

however, I will mainly focus on the photon (or probability) distribution analysis approach conceived in the team of Pr. Seidel. (Kalinin, Valeri, et al. 2010; Gansen et al. 2009; Kalinin et al. 2007; Kalinin et al. 2008).

To perform a PDA analysis, the entire recorded photon-stream is first divided into time-frames of fixed and equal length for several different time-windows, generally 1, 2, 3 and 4ms and represented as a function of a chosen FRET indicator. PDA then makes use of a pre-determined "conditional detection probability" to calculate the combination of photons that would result in the experimentally obtained data distribution. As illustrated in **figure 3.31**, there are several possible outcomes following donor excitation, all of which are defined with a given probability. There is a certain probability that the acceptor is directly excited (p_{DE}). Therefore, the probability of the donor to be excited is (1- p_{DE}). If the donor is excited, there is the probability of having FRET (E), which of course depends on the distance that separates the donor and the acceptor. The donor and/or acceptor emission then depends on the quantum yield of each dye, Φ_{FD} and Φ_{FA} respectively. The fraction of these photons that are actually detected depend on the detection efficiencies δ_G and δ_R for the green and red channels as well as the cross-talk factor α (Sisamakis et al. 2010).

The high accuracy of PDA resides in part by the fact that the probabilities attributed to each step are estimated experimentally. For instance, the background is measured directly from a buffer sample, the leakage is determined from a donor only sample, the detection efficiencies are known from the MFD experiment and the quantum yields are measured separatelly.

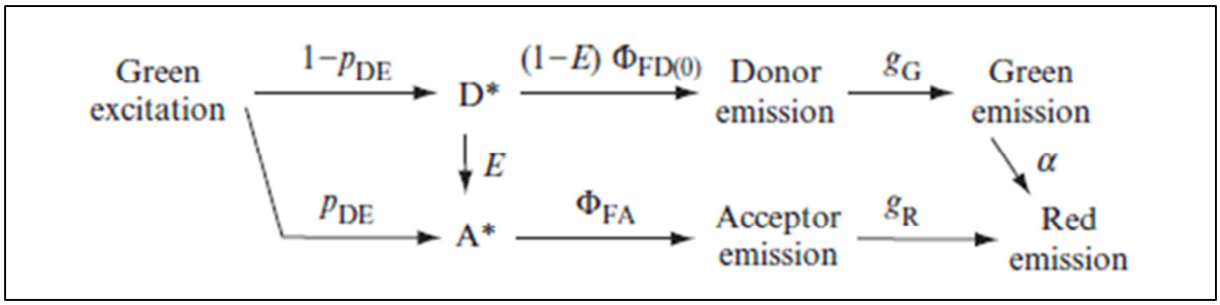

***Figure 3.31**. Flowchart giving an example of the probability calculus for detecting a photon following donor excitation. It becomes clear that upon donor excitation, there are several possible outcomes. The probability of directly exciting the acceptor p_{DE}, the probability of resonance energy transfer (E), the quantum yield of the dyes Φ, the detection efficiencies for the 4 channels respectively (δ) and the bleed-trough factor (α), all have to be considered (Sisamakis et al. 2010)*

If a system is strictly static, shortening the length of the time-windows will only enlarge the Gaussian distribution (see shot-noise contribution above) but no additional states should be visible and the mean FRET efficiency should not vary (**Figure 3.32**).

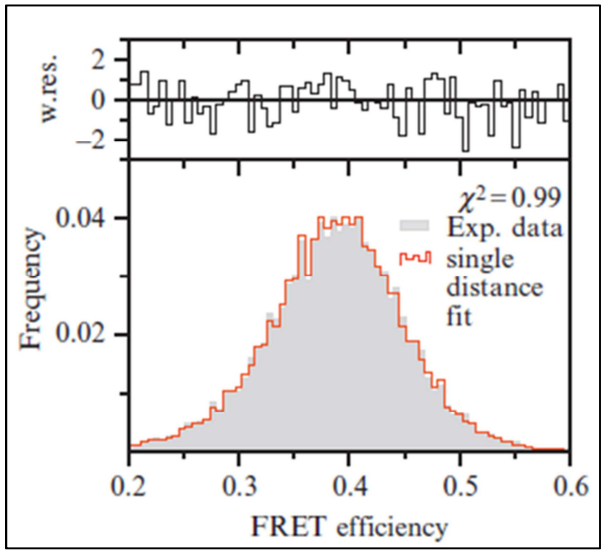

***Figure 3.32**. PDA fit of a single static FRET population. The experimental data is represented as a histogram of the FRET distribution and fitted with a single distance fit. The width of the Gaussian distribution is the consequence of shot-noise and partly also by the dynamics of the linkers through which the dyes are attached to the molecule. A single distribution is observed independently of the length of the time-window* (Sisamakis *et al.*, 2010).

On the other hand, if a molecule undergoes dynamic transitions at the same order of magnitude or shorter than the chosen time-window, E varies, resulting in a broadening of the green over red emission ratio. Therefore, if a visual inspection of the 2D diagram suggests underlying dynamics, a dynamic PDA model-function should be carefully chosen. By this approach, a static system can clearly be differentiated from a dynamic system. By varying the length of the time-windows, an approximation of the timescale of the dynamics can be evaluated (**Figure 3.33**).

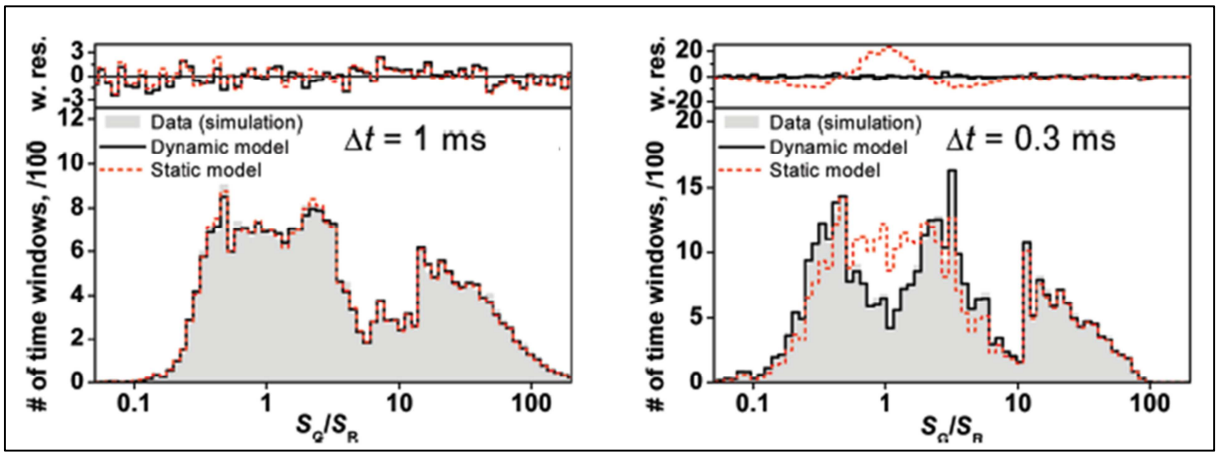

***Figure 3.33**. PDA fit of a simulated two-state dynamic system interconverting with rate constant of 0.5ms^{-1}, and donor only molecules, represented by means of the FI S_G/S_R. With a time-window of 1ms, the two states are well interleaved, and it is impossible to conclude whether the two populations are in reality two (or more) independent static, albeit overlapping states. By choosing a shorter time-window (0.3ms), the two populations are distinguishable and the static model does not accurately describe the data* (Kalinin *et al.*, 2010).

It is, however, essential to underline that prior knowledge of the system is indispensable in order to generate the right model-function, and that PDA is limited by the shortest length of the time-window that still offers a sufficient number of photons to be statistically significant, which normally imposes a limit at 250μs (Kalinin, Valeri, et al. 2010). PDA is therefore not ideal and entirely sufficient to characterize a rapidly interconverting dynamic system but remains an important tool to complement MFD and Fluorescence Cross Correlation analyses, which will be the topic of the upcoming section.

Quantifying FRET dynamics with fluorescence fluctuation based methods

In this chapter, the advantages and limits of a couple of fluorescence fluctuations based techniques will be detailed. I will begin by describing the basis of two commonly used techniques known as Fluorescence Correlation Spectroscopy (FCS) and Fluorescence Cross Correlation Spectroscopy (FCCS). After having introduced FCS and FCCS, I am going to bring up a technique called filtered FCS (fFCS), which is a relatively recent development in these techniques based on the implementation of probability filters to facilitate the study of fluorescence fluctuations, and FRET, at a single molecule level.

Fluorescence Correlation Spectroscopy as a mean to estimate the concentration of molecules and their diffusion-time

FCS is broadly used approach to determine the diffusion coefficient and concentration of labeled biomolecules (Schwille and Haustein, 2001). FCS is a fluctuation based method, which means that it takes advantage of variations in fluorescence intensity when labeled molecules diffuse through the focal volume, and is therefore achieved at a relatively low concentration of <1μM. In basic terms, the fluorescent signal (F) depends on both the number of emitting molecules and their brightness, in cpsm (counts per second par molecule), and can therefore be expressed as $F = \varepsilon . N$ with ε representing the molecular brightness and N the number of molecules. The autocorrelation function G(τ) reflects the probability that at a time t+τ, the detected photon originates from the same molecule that emitted a photon at time T, and is calculated by **equation 21**:

$$G(\tau) = \frac{\langle \delta F(t) \times \delta F(t+\tau) \rangle}{\langle F(t) \rangle^2} \qquad \textbf{Equation 21}$$

where $\delta F(t) = F(t) - \langle F(t) \rangle$ defines the fluorescence fluctuations as the difference between F(t), the fluorescent signal at a given time (t) and its mean. In other words, G(τ) is calculated by normalizing the fluctuations of fluorescence over time by the total signal (Schwille and Haustein, 2001; Haustein and Schwille, 2007).

A fitting of the autocorrelation function (G(τ)) enables the estimation of the average time a molecule spends in the focal volume (t_D) and consequently, if this volume is known, its diffusion coefficient. Additionally, the amplitude of the autocorrelation curve G(0) is inversely proportional to the average number of molecules $\langle N \rangle$ present in the focal volume: ($G(0) = \frac{1}{\langle N \rangle}$)

The relation between the G(0) value and the number of molecules is shown in **equation 22**:

$$G(0) = \frac{\langle \delta F(t)^2 \rangle}{\langle F \rangle^2} = \frac{\langle (F(t) - \langle F(t) \rangle)^2 \rangle}{\langle F \rangle^2} = \frac{\sigma_F^2}{\langle F \rangle^2} = \frac{\varepsilon^2 . \sigma_N^2}{\varepsilon^2 . \langle N \rangle^2} \qquad \textbf{Equation 22}$$

where σ_N^2 corresponds to the variance of the number of events, which, in the case of molecules diffusing in an open volume, can be described by a Poisson law. Thus, σ_N^2 is equal to the average number of molecules ($\sigma_N^2 = \langle N \rangle$), and consequently $G(0) = \frac{1}{\langle N \rangle}$.

It might seem somewhat counterintuitive at first, but an increase of the dye concentration will lower the amplitude of the correlation curve. This is, in reality, quite logical considering that the correlation function informs on the fluctuation of the fluorescent signal, and therefore, the variation is greater if not too many molecules are present at the same time.

The influence of the amplitude of G(τ) is given in **Figure 3.34**, where the concentration of a freely diffusing dye (Rhodamine 6G in 70% sucrose) was increased from approximately 0.5nM to 20nM (green curves). At too high a concentration, the amplitude of the correlation curve drops to almost zero. **Figure 3.34** also demonstrates that increasing the laser intensity gives rise to an additional correlation term at short times (red curve). This is due to fluorophore photoblinking, most commonly attributable to internal transitions leading to triplet state occupation, and which give rise to fluctuations at short times in the autocorrelation function.

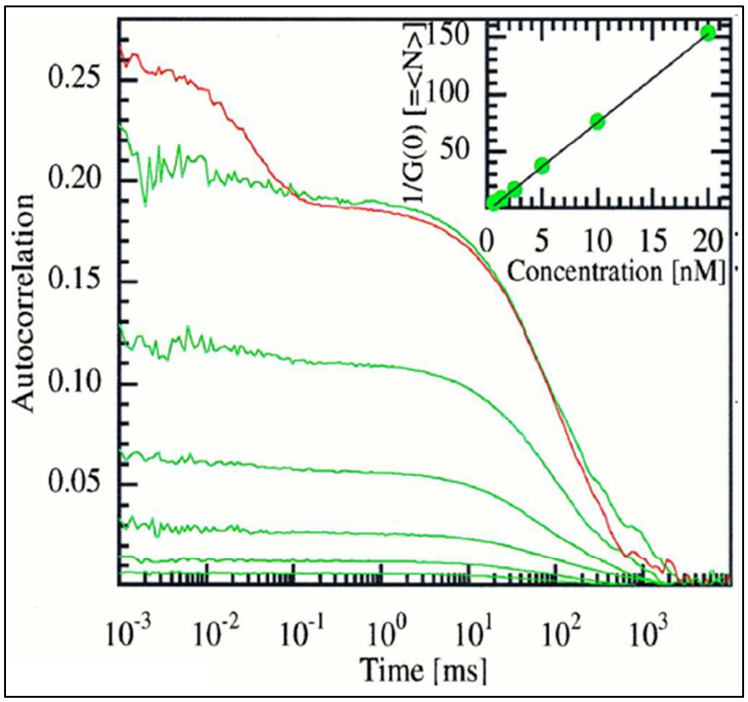

***Figure 3.34**. Autocorrelation curves for increasing concentrations of Rhodamine 6G. At a concentration of about 0.5nM, G(τ)has an amplitude of 0.2 whereas a concentration as high as 20nM, fluctuations in fluorescence are small and G(τ)is consequently very low. Following the increase of the laser power, an additional correlation term appears on a short timescale due to triplet formation.*

In simple terms, the diffusion time can be determined at the time by which G(τ) has reached 50% of its initial value. In practice, t_D is measured by fitting G(t) using an equation that describes the diffusion process, such as:

$$G(\tau) = \frac{\gamma}{N}\left(1 + \frac{4D\tau}{w_{3DG}^2}\right)^{-1}\left(1 + \frac{4D\tau}{z_{3DG}^2}\right)^{-\frac{1}{2}} \quad \textbf{Equation 23}$$

where w and z describe the shape of the confocal volume. In the case of a single species diffusing in a 3D Gaussian volume, however, this equation can be modified to take into account several species, or any additional photophysical phenomenon which leads to fluorescence emission fluctuations ((Schwille and Haustein, 2001))

The diffusion coefficient (D) can be derived from t_d if the observation volume has been estimated prior to the experiment. Thereupon, the molecular size of a spherical molecule can be calculated as the hydrodynamic radius of the molecule is linked to the diffusion coefficient via the Stokes-Einstein equation for spherical particules: $D = \frac{k_B T}{6\pi\eta_v R_H}$

where k_B is the Boltzmann constant, η stands for the viscosity of the medium and R_H stands for the hydrodynamic radius (Haustein and Schwille, 2007; Fitzpatrick and Lillemeier, 2011; Tian *et al.*, 2011).

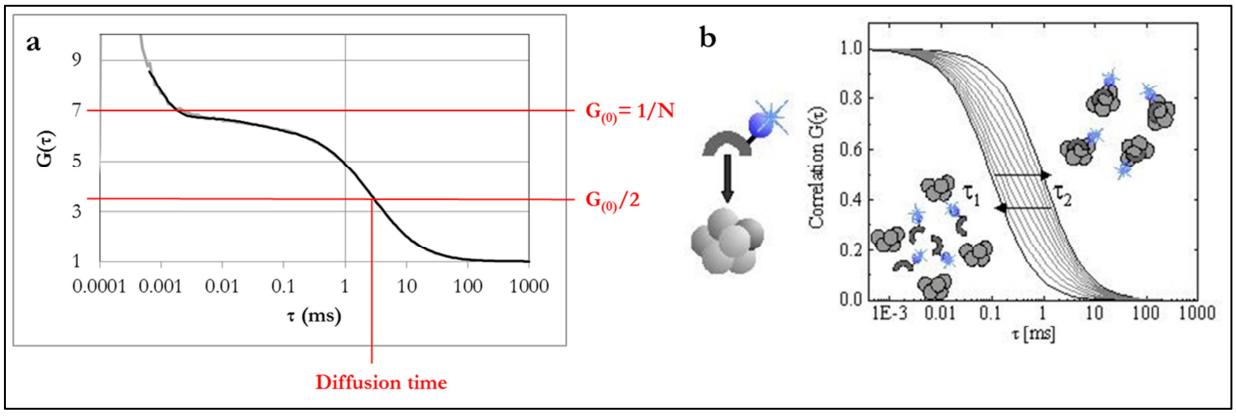

***Figure 3.35**. Representations of FCS curves. (**a**) Auto-correlation curve for a Cy3B labeled sample. The fit gives a value for 1/G(0)=<N>=0.14, and as the focal volume has been estimated to 15fl, the concentration is ~100pM. The fit also provides a diffusion time of 2.8ms. (**b**) Illustration of the effect of a change in size on the autocorrelation time in a FCS experiment. In this experiment, a small ligand is labeled and consequently, the binding of its large interaction partner increases the diffusion time, and induce a large shift of the autocorrelation curve toward longer times. (Schwille and Haustein, 2001)*

Fluorescence Cross Correlation Spectroscopy as a tool to reveal molecular interactions

FCCS is a useful tool to study macromolecular interactions by estimating the degree of co-diffusion of two presumed interaction partners (Schwille and Haustein, 2001). In order to investigate whether two molecules interact (for instance, protein-protein or protein-DNA interactions), they are labeled with spectrally distinct fluorescent dyes and the technical setup must be adapted to allow for a 2-color (simultaneous or alternated) excitation. If the molecules do interact, they simultaneously traverse the focal volume and spectrally distinct photons correlate, even in the absence of FRET (i.e. the photons detected in the green channel cross-correlate with the photons detected in the red channel).

The cross-correlation function derives from the correlation function, and is presented in **equation 24**.

$$G_{1,2}(\tau) = \frac{\langle \delta F_1(t) \times \delta F_2(t+\tau) \rangle}{\langle F_1(t) \rangle \langle F_2(t) \rangle} \qquad \textbf{Equation 24}$$

where F_1 and F_2 represent the fluorescence intensities for the two species, respectively. In this expression, $G_{1,2}(0)$ does not directly reflect the mean number of molecules in the focal volume. In FCCS, to extract the number of cross-correlating molecules, **equation 25** has to be applied.

$$G_{1,2}(0) = \frac{N_{1,2}}{(N_1+N_{1,2}).(N_2+N_{1,2})} \qquad \textbf{Equation 25}$$

where N_1 represents the average number of species 1 and N_2 stands for the average number of species 2. Thereupon the average number of complexes is defined as $N_{1,2}$.

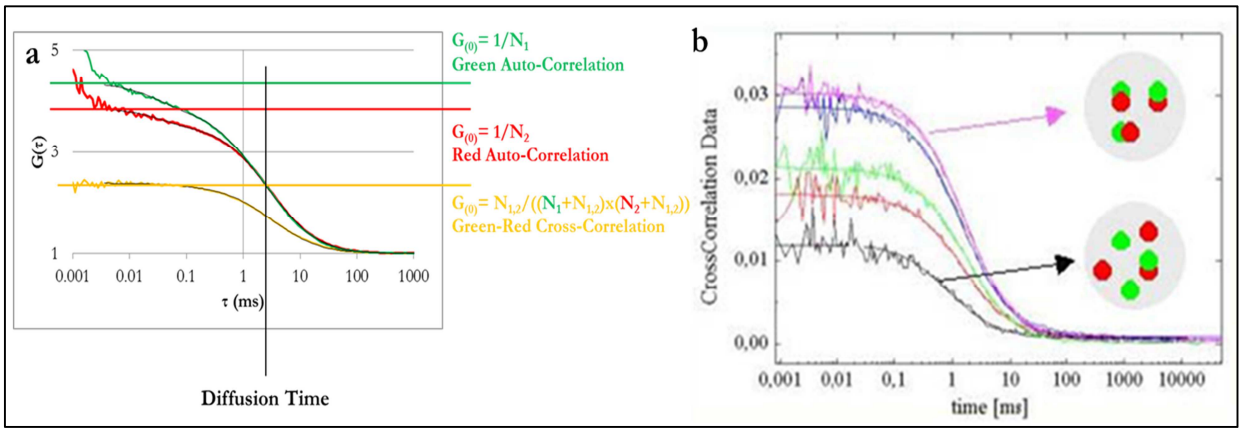

***Figure 3.36**. Representations of FCCS curves. (**a**) Auto (green and red) and Cross (yellow) correlation curves for a Cy3B – Cy5 labeled sample. A global fit gives the values <N_1>=0.24, <N_2>=0.27, <$N_{1,2}$>=0.55 and a diffusion time of 3.3ms. (**b**) Experimental curve illustrating the effect of a change in the degree of interaction (co-diffusion) on the amplitude of the cross-correlation curve in a FCCS experiment. The higher the number of interacting complexes, the higher the amplitude of G(τ). (Schwille and Haustein, 2001)*

FCCS as a means to quantify variations in FRET for dynamic systems

Generally, FCCS experiments are carried out with dyes as spectrally separated as possible to limit the contribution of FRET in the cross-correlation data, since it complicates the quantitation of the degree of interaction (Tian *et al.*, 2011). Nonetheless, in the presence of FRET, valuable information can be extracted from smFRET-FCCS data, notably for dynamic systems. If, for instance, a molecule undergoes conformational changes resulting in variations in FRET during its time in the focal volume, detected as variations in the emitted signal of both probes, it will introduce an anticorrelation in the cross-correlation curve on the timescale of the dynamic transition. A visualization of the concept of anti-correlation is given in **Figure 3.37.a**, where the entire length of the event corresponds to the diffusion time ($t_{D2cFCCS}$) and the rate-constant of the anti-correlation ($t_{R2cFCCS}$) indicates the dynamic transition time between the two FRET-states.

There are, however, several possible artifacts associated with this technique. For instance, most samples contain a considerable amount of donor only labeled molecules which pollute the total signal (Felekyan *et al.*, 2012). A possible solution to this problem consists in selecting only the molecules undergoing FRET from the 2D MFD diagram, and, subsequently, perform FCCS exclusively on them (**Figure 3.37.b**).

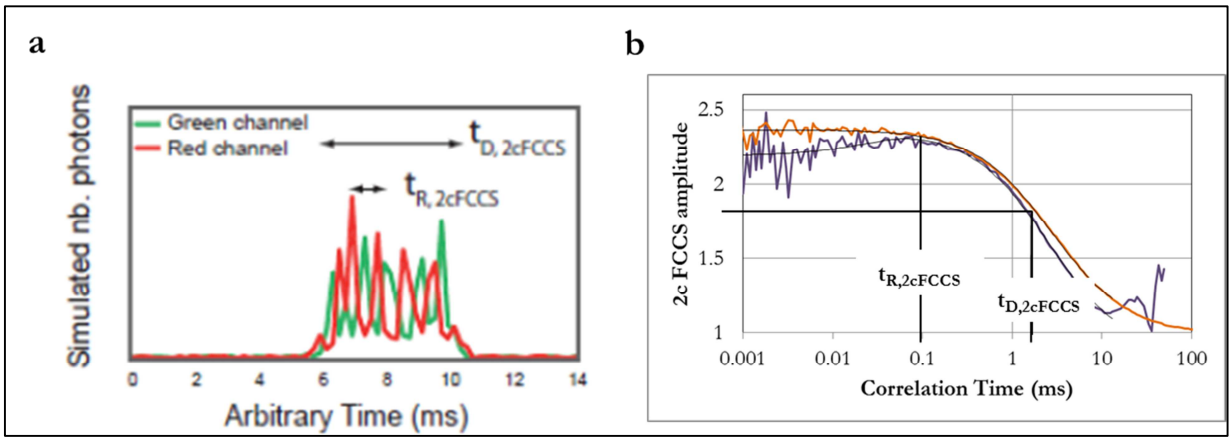

***Figure 3.37**. (**a**) Simulated photon trace of dynamic molecules undergoing rapid conformational transitions between two FRET states. The duration of the single molecule event, $t_{D2cFCCS}$, indicates the diffusion time of the molecule in the focal volume and the rate-constant of the oscillations is represented as $t_{R2cFCCS}$. This anti-correlation will generate an antibunching term in the FCCS-FRET curve. (**b**) Experimental FCCS-FRET curve of a dynamic system undergoing conformational changes on a timescale of ~100µsec. By cross-correlating all the green and all the red photons from the raw data (orange), no anticorrelation is detected, mainly because of the contribution of donor-only labeled molecules. If these donor only molecules are removed by means of the 2D MFD diagram, and a subsequent FCCS analysis is performed, a clear anticorrelation is detected on a timescale that corresponds to the rate-constant of the conformational transition.*

Combining PIE and FRET-FCCS offers the possibility to investigate data bias due to photophysical aberrations.

It is important to verify that the FRET efficiency is not biased by photoinduced dark states of the acceptor. To this aim, FCS/FCCS curves can be generated from PIE data, as well. An acceptor autocorrelation function of the photons detected following the direct excitation of the acceptor in the delayed channel, informs on the extent of blinking of the acceptor (due for example to triplet formation). In addition to the measurement of $\tau(A)$, this is very useful to verify that the quantum yield of the acceptor remains constant, and this result can be compared with the FCCS curve created from the photons detected in the prompt channel (Kudryavtsev *et al.*, 2012).

As a final remark to close the section on "classical" FCCS, it should be highlighted that this technique has been most valuable in elucidating and quantifying the structural dynamics of mGluRs as will be seen in our article "Specific regulation of transition rates between active and inactive states of metabotropic glutamate receptors determines agonist efficacy" presented in chapter 4.2. However, interpreting changes in FRET is a challenging mission at single molecule concentrations, especially if

these variations in FRET are small. One of the main reasons for this is the considerable number of detected photons arising from background noise due to Rayleigh and Raman scattering (Felekyan *et al.*, 2012). On top of that, two spectrally similar species differing only in terms of excited state lifetimes, or two different FRET species cannot be individually correlated, or cross-correlated, through the employment of classical FCS/FCCS. To overcome these limitations, a new method known as filtered FCS (fFCS) has been developed, and this will be the topic of discussion in the next couple of pages.

Accurately correlating subspecies at single molecule concentrations by filtered FCS (fFCS)

Introduction to the probability filter as a means to separate subspecies and exclude background noise in the correlation function

In the previous chapter, it was explained that an autocorrelation function generated in a classical FCS experiment is created by correlating the photons detected in the same channel. Therefore, in the case where two fluorescent dyes are spectrally similar but differ in terms of lifetime, they will still be autocorrelated. However, the methods that will now be detailed make it possible to auto- or cross-correlate different subspecies through the use of probability filters.

In this first attempt to explain the principle of fFCS (found in Kapusta *et al.*, 2007), let us consider a heterogeneous sample composed of two molecules referred to as A and B. They are spectrally close and consequently detected in the same channel but differ with respect to their excited state lifetime, with a shorter lifetime for A than for B. A TCSPC measurement of this sample gives the biexponential decay represented in **Figure 3.38.a** (black line). By reason of the shorter lifetime for A, approximately 60% of the photons detected in early TAC-channels have been emitted by this compound. The remaining 40% have been emitted by B. At longer microtimes, the probability steadily increases that the photons detected were emitted by B, and in very late TAC channels, this probability grows to reach 100%. By taking into account the species respective detection probabilities, each experimentally detected photon can be attributed a certain probability of belonging to either species A or species B, as represented in the probability filter in **Figure 3.38.b**. Subsequently, the photons attributed to the same state can be auto-correlated by correlating the probabilities.

Indeed, in classical FCS, all photons contribute equally to the correlation curve and, thus, the calculation is based on values of either zero or one. In fFCS, the filter value calculated from the photon's microtime is used instead. Consequently, the numbers used for the calculation of the correlation curve are fractions, and their absolute value can both exceed one and/or be negative. Nonetheless, the combined filter value for each channel (microtime) is always equal to one **Figure 3.38.b** (Kapusta *et al.*, 2007).

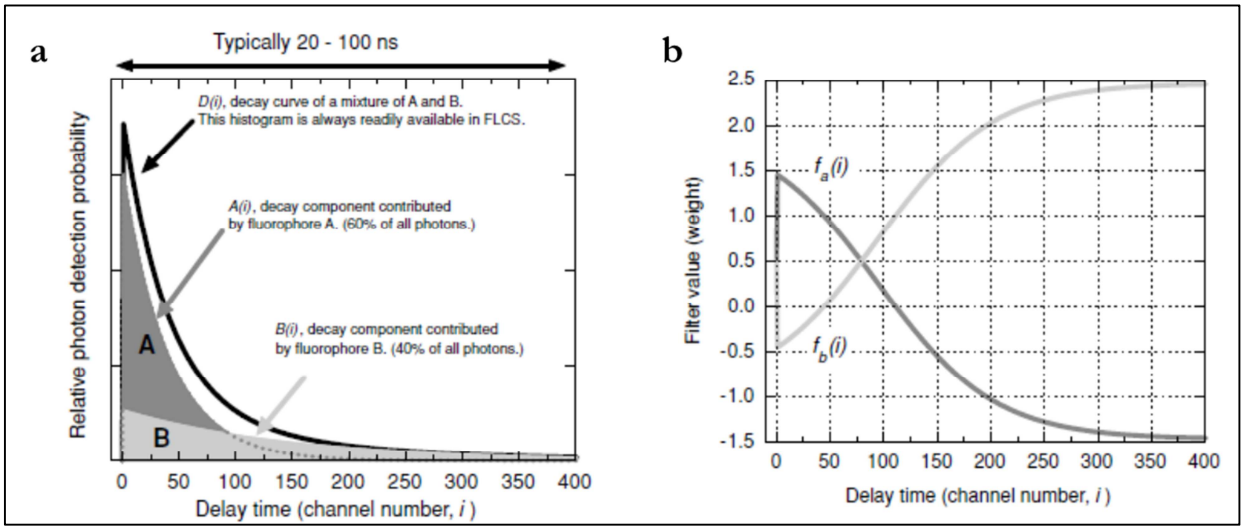
a
Typically 20 - 100 ns
D(i), decay curve of a mixture of A and B.
This histogram is always readily available in FLCS.
A(i), decay component contributed
by fluorophore A. (60% of all photons.)
B(i), decay component contributed
by fluorophore B. (40% of all photons.)
A
B
Relative photon detection probability
0 50 100 150 200 250 300 350 400
Delay time (channel number, i)
b
Filter value (weight)
2.5 2.0 1.5 1.0 0.5 0.0 -0.5 -1.0 -1.5
$f_a(i)$
$f_b(i)$
0 50 100 150 200 250 300 350 400
Delay time (channel number, i)

***Figure 3.38**. (**a**) Theoretical TCSPC biexponential decay for a heterogeneous sample composed of the molecules A and B. As a consequence of the shorter lifetime of A, 60% of all the photons detected in the first 100 TAC channels have been emitted by A and the remaining 40% of photons originate from B. Accordingly, at longer microtimes, most of the photons originate from B and the number of photons emitted by A decreases rapidly. (**b**) From the ratio of photons detected from A and B established in (a), a probability filter can be generated to attribute a certain probability to each detected photon to belong to either A or B. The probability filter represents $f_a(i)$ as the weighted fractional intensity of species A and $f_b(i)$ the weighted fractional intensity of species B.*(Kapusta *et al.*, 2007)

Elimination of background with fFCS

Classical FCS measurements are nearly impossible to implement at single-molecule concentrations due to Rayleigh and Raman scattered excitation light which influence the amplitude of the correlation curve and lead to an incorrect estimation of the number of molecules in the focal volume (Kapusta *et al.*, 2007; Felekyan *et al.*, 2012). Fortunately, by taking into consideration the contribution of these scattered photons in the probability filter creation, the influence of the

background on the correlation curve is minimized, as illustrated in **Figure 3.39**. In this example, found in (Kapusta *et al.*, 2007), a 10pM solution of freely diffusing Atto655 dyes is measured by TCSPC (**Figure 3.39.a** black decay). At this low a concentration, only about 60% of the detected photons actually originate from Atto655, whereas the remaining 40% of photons originate directly from the excitation laser (**Figure 3.39.a** light grey decay). The contribution of scattered photons in this example was estimated by subtracting the decay from a separate measurement on a sample containing Atto655 dyes at a concentration of 1nM for which the scatter contribution can be neglected (**Figure 3.39.a** dark grey decay). Alternatively, the contribution of scattered photons can be evaluated by performing a measurement on a water sample, referred to as the IRF in the chapter on MFD (Sisamakis *et al.*, 2010).

Hence, **Figure 3.39.b** represents the probability filter generated from the decays in **Figure 3.39.a** with the probability distribution for the specific Atto655 signal in dark grey and the probability distribution for scattered photons in light grey. Considering that the Rayleigh and Raman scattered photons originate directly from the laser pulse, they will be exclusively detected in very early TAC channels and result in a high initial probability filter value. At longer times (channel numbers) the contribution of scattered photon vanishes and all detected photons are attributed to the Atto655 specific signal. Applying the filter created in **Figure 3.39.b** generates the autocorrelation function (ACF) shown in **Figure 3.39.c**, where the unfiltered FCS curve is highlighted in black and the filtered FCS curve is represented in grey. The difference in ACF amplitude is significant, and it becomes evident that if no filter is applied, the exact number of molecules cannot be estimated.

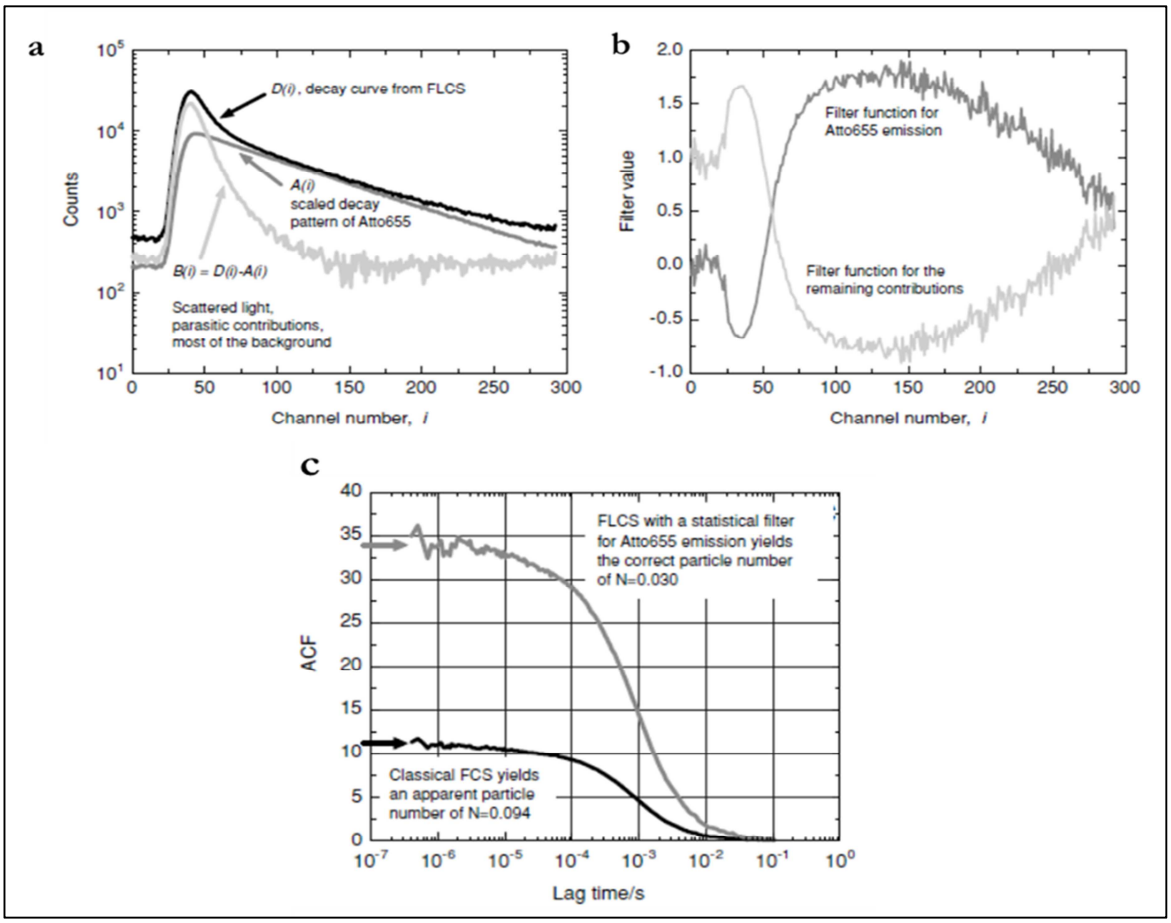

***Figure 3.39**. Principle of background removal through the use of probability filters. See text for details.*

fFCS as a tool to correlate FRET states and quantify dynamics

Although dynamic transitions between states with different FRET efficiencies give rise to an anti-correlation in the FCCS curve (see FRET-FCCS chapter), this anti-correlation is only observed if the FRET variations are large. Other factors such as non-optimal labeling efficiency, photophysical aberrations as well as the difficulty of removing the influence of scattered photons, also contribute in making FCCS-FRET an extremely challenging task. To overcome these limitations, the group of Pr. Seidel has extended fFCS to enable the correlation of species that differ either in terms of FRET (Felekyan *et al.*, 2013) and/or anisotropy (Felekyan *et al.*, 2012). These new methods are called "species filtered auto (or cross) correlation analysis" (SACF or SCCF).

The general idea of SACF and SCCF lies in the fact that two different FRET populations can be defined individually due to differences in the excited state lifetime, the FRET efficiency and/or

the anisotropy of each state. Consequently, by taking into account these three parameters in the probability filter creation, each detected photon is attributed a given probability of belonging to one of the different subspecies. Accordingly, **figure 3.40.a** illustrates the photon probability evolution for a dynamic FRET system interconverting between a high-FRET (red) and a low-FRET (green) state during the residence time of the molecule in the focal volume. Hence, the probability of the photons attributed to one state can either be auto-correlated (SACF) (**Figure 3.40.d**) or cross-correlated (SCCF) (**Figure 3.40.d**) with the photons attributed to the other state. The resulting correlation curve can then be analyzed in an identical manner as previously described earlier in this chapter. Just as in classical FCS/FCCS, the initial part of the curve at longer times gives the diffusion time, and in the case of a dynamic interconverting system, the SCCF curve anti-correlates at times representative of the timescale of the underlying dynamics. Therefore, by introducing an antibunching term in the cross-correlation fit, the transition rate between the two states can be determined. This is illustrated in **Figure 3.40**, which represents the ideal case where the different subspecies constituting the sample can be characterized directly by means of a 2D MFD diagram, as it allows for a visual separation of the subspecies (**Figure 3.40.b)**.

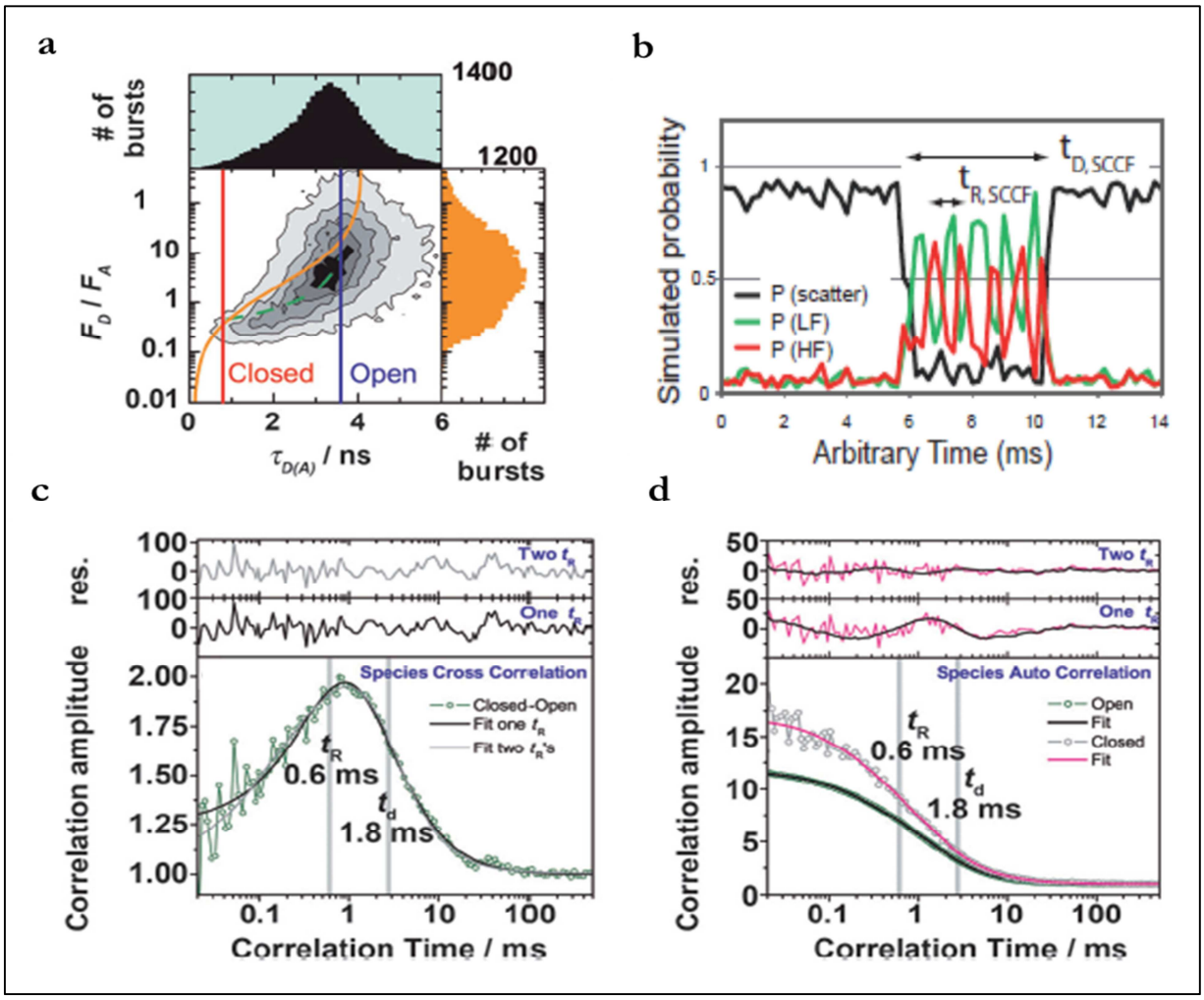

***Figure 3.40**. Overview of the principle of SACF and SCCF. (**a**) MFD 2D diagram representing the F_D/F_A distribution as a function of $\tau_{D(A)}$ for a protein that undergoes rapid conformational changes between a closed and an open state. The Gaussian distribution is very large, which suggest underlying dynamics.(**b**) By creating probability filters based on the characteristics in terms of lifetime, anisotropy and color (FRET) that represents the open and the closed state, respectively, each detected photon is attributed a certain probability of belonging to a specific state. (**c**) SCCF curve obtained by cross-correlating the probabilities of the photons attributed to the closed state with the probabilities of the photons attributed to the open state. The initial part of the SCCF curve at times >~1ms gives the diffusion time (t_d=1.8ms), similarly to a classical FCCS curve. At shorter times, the cross-correlation curves shows anti-correlation, and by introducing an antibunching term in the cross-correlation equation to fit this anti-correlation, the timescale of the conformational change (t_R) is estimated to 0.6ms. (**d**)The open or the closed state can alternatively be auto-correlated. The diffusion time is identical as in SCCF. The amplitudes of the autocorrelation functions indicate the fraction of molecules that remained in the same state over the entire time the molecules spent in the focal volume.* (Felekyan *et al.*, 2012)

The quality of the SACF and SCCF curves highly depends on the quality of the probability filters. for this reason, an explanation of the filter creation procedure, published in (Felekyan *et al.*, 2013), is illustrated in **Figure 3.41**.

Figure 3.41.a shows an example of a F_D/F_A versus $\tau_{D(A)}$ 2D diagram of a simulated FRET-sample rapidly interconverting between a high-FRET (closed) and a low-FRET (open) state and complemented with 20% donor-only molecules, with the blue and the red dotted lines indicating the lifetimes for the high-FRET and the low-FRET state, respectively. As the data is averaged over the residence time of the molecules in the focal volume, only one population with a broad F_D/F_A Gaussian distribution is visible. Moreover, the red line shows the theoretical line expected for a static system, and it is clear that it does not overlay well with the data, whereas the green line that represent the distribution expected for a dynamic system, agrees nicely with the data distribution. Therefore, despite the fact that no quantitative values can be extracted from the 2D diagram, its mere profile suggests fast dynamics.

Figure 3.41.b shows a diagram representing the likelihood of a photon belonging to a certain sub-species as a function of the stacked TCSPC channel number for all four detectors. Indeed, based on subtype specific characteristics, in terms of lifetime, FRET and anisotropy, each detected photon is attributed a certain probability of belonging to a given state, depending both on the photon's arrival time and in which channel it is detected (color and polarization).

Figure 3.41.c is a diagram that shows the filter value versus the stacked TCSPC channel number created from **Figure 3.41.b**

Figure 3.41.d gives an example of correlation curves with: the filtered autocorrelation function for donor only molecules in grey, the autocorrelation function for the low-FRET population in blue, the autocorrelation function for the high-FRET population in orange and the cross-correlation of the high-FRET state and the low-FRET state in green. The autocorrelation curves can be analyzed following the same procedure as in classical FCS to extract information concerning the diffusion time and the fraction of molecules belonging to each state. As already seen in **Figure 3.40**, the shape of the cross-correlation curve is strikingly different. The initial positive value of the cross-correlation curve proves the existence of inter-conversions between the states (N.B. if the system is not dynamic, the SCCF is flat). From this initial part of the curve, at times longer than 0.5ms, the diffusion time can be estimated, as in FCCS. In addition, there is a clear anticorrelation at shorter times corresponding to the timescale of the conformational change, and the

amplitude of the cross-correlation curve reflects the proportion of molecules undergoing dynamic transitions.

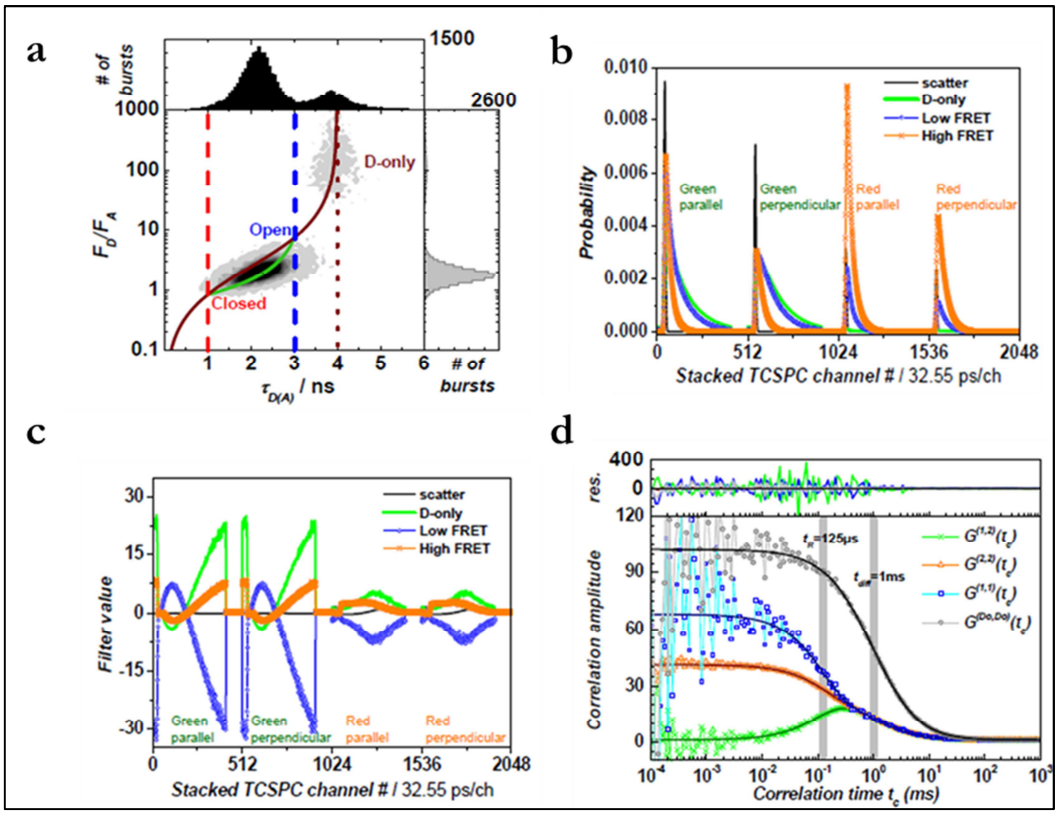

***Figure 3.41**. Illustration of the different steps involved in the creation of fFCS filters and generation of fFCS curves. See text for details.* (Felekyan *et al.*, 2013)

As a final remark regarding the filter creation procedure, it should be pointed out that there are several possible ways to design high-quality filters. Ideally, if some of the molecules in the sample are static, they can be selected from the 2D MFD diagram. If, however, no molecules stay in either one of these two states during the entire duration of the single molecule event, the procedure is slightly more complicated. The donor excited state decay is in that case reconstructed for the ensemble of dynamic molecules and subsequently fitted with a biexponential curve. The two lifetimes extracted from the biexponential fit, as well as the anisotropies, are then used to create specific filters for the two boundary states.

In conclusion SACF and SCCF offer the almost unique possibility to access dynamics on a nano- to microsecond timescale, which has proven extremely valuable in the elucidation of the dynamic behavior of the mGluR VFT.

To close the biological and technical introduction, I would like to point out that the aim of the present dissertation up until this point has been to give a global overview of both the biological aspect as well as the general principles of the techniques which have been used in the context of this Ph.D thesis. Hopefully, it has been underlined that the better understanding of the dynamics of GPCRs and notably the activation mechanism of mGluRs constitute important areas of investigation due to their importance in the process of synaptic transmission, and as targets for the pharmaceutical industry, and that smFRET acquisitions coupled to analyzing methods designed to probe the timescales of fast dynamics, represent exceptional techniques to address these questions.

Chapter 4. Results

In this chapter, I will provide some of the results engendered during my Ph.D. I will begin by describing the innovative experimental setup, based on a Supercontinuum laser to perform PIE, which I was in charge of building. This setup was the first of its kind and led to the first publication provided in this chapter. This publication details at length the advantages of using a Supercontinuum source to easily perform accurate FCCS measurements and MFD. I will then enter the more biological aspects of my project and present the main study of my Ph.D., focused on the dynamic behavior of the extracellular domain of mGluRs. The employment of the techniques, described in the introduction for the study of fast dynamics enabled to probe dynamics, on a timescale never before accessed for this family of receptors, and led us to propose a new inspiring activation model. This work will be submitted to *Nature Structural and Molecular Biology* and the submission manuscript is presented in chapter 4.2. In a final part, some of the projects that I have been carrying out in parallel to my main project will be briefly introduced. Even though they have not yet been published, preliminary data are encouraging and the methodology is interesting from a more general point of view.

4.1 Implementation of a supercontinuum source to perform FCCS-PIE

Single molecule time-resolved fluorescence spectroscopy methods require the use of high performance, very often home-built, optical microscopes. Over the three year period of my Ph.D. thesis, I have been directly involved in the construction of not less than three optical setups adapted for single-molecule measurements. Our most recent setup, implemented with a supercontinuum laser source, was constructed based on an entirely new concept and this achievement led to an article in *Optics Express*. (Olofsson and Margeat, 2013) Although the configuration of the setup is thoroughly described below in our publication, I would like to highlight some of the advantages related to its use.

Traditionally, a multicolor excitation scheme requires the use of several monochromatic independent lasers (B Müller *et al.*, 2005; Kudryavtsev *et al.*, 2012). To overcome this limitation, a broad spectrum supercontinuum source is an ideal alternative. In our original configuration, the output beam is divided into two distinct paths with different lengths (prompt and delayed) and the desired wavelength is chosen, for each of them, using bandpass filters. The alternated excitation pattern is then generated by recombining the two beams. In this new configuration, adding a new excitation color is cheap, as it only requires replacing the filter and adjusting the length of the delayed line, rather than buying an additional laser. Additionally, the assortment of available filters also opens for new combinations of excitation possibilities (**Figure 4.1**).

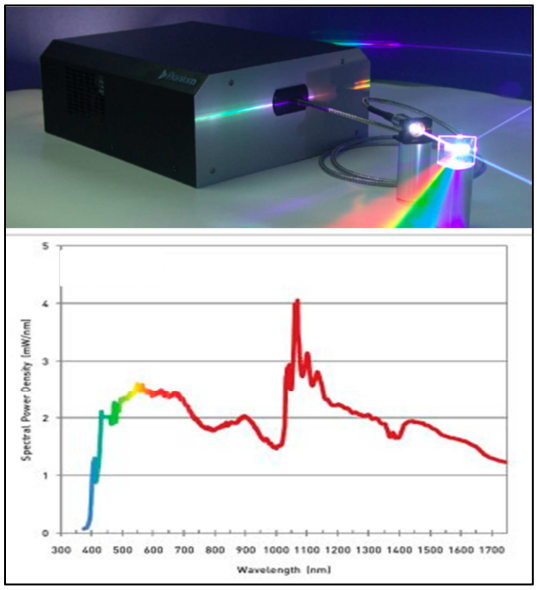

***Figure 4.1**. Diagram showing the spectral power density in mW/nm as a function of the wavelength. The broad emission spectrum of a supercontinuum source makes it possible to combine excitation wavelengths in multicolor experiments simply by changing the bandpass filters. (Fianium product datasheet)*

Moreover, in this paper, we propose a method to verify that the excitation volumes for the different colors are overlapping by acquiring data with a free dye that is excited at both wavelengths. As a matter of fact, by cross-correlating the photons emitted after the prompt pulse with the photons emitted after the delayed pulse, the degree of cross-correlation indicates whether the excitation volumes are correctly overlapping.

Additionally, the excitation frequency can be modified when a single excitation wavelength experiment is performed. In a TCSPC experiment, the optimal excitation frequency depends on the lifetime of the dye. For dyes with fairly long lifetimes (>3-4ns), a too high a frequency (>40MHz) results in an incomplete decay which might bias the data. In our configuration, however, by using the same bandpass filter for both paths, the excitation frequency can be either 20 or 40MHz, depending on the lifetime of dye.

Research article: Pulsed interleaved excitation fluorescence spectroscopy with a supercontinuum source,

(Olofsson and Margeat, 2013)

Pulsed interleaved excitation fluorescence spectroscopy with a supercontinuum source

Linnea Olofsson[1,2,3] and Emmanuel Margeat[1,2,3,*]

[1]*CNRS UMR5048, Centre de Biochimie Structurale, 29 rue de Navacelles, 34090 Montpellier, France*
[2]*INSERM U1054, Montpellier, France*
[3]*Universités Montpellier I et II, Montpellier, France*
[*]*margeat@cbs.cnrs.fr*

Abstract: Pulsed Interleaved Excitation (PIE) improves fluorescence cross-correlation spectroscopy (FCCS) and single pair Förster Resonance Energy Transfer (spFRET) measurements, by correlating each detected photon to the excitation source that generated it. It relies on the interleaving of two picosecond laser sources and time correlated single photon counting (TCSPC) detection. Here, we present an optical configuration based on a commercial supercontinuum laser, which generates multicoulour interleaved picosecond pulses with arbitrary spacing and wavelengths within the visible spectrum. This simple, yet robust configuration can be used as a versatile source for PIE experiments, as an alternative to an array of picosecond lasers and drivers.

©2012 Optical Society of America

OCIS codes: (170.2520) Fluorescence microscopy; (300.6500) Spectroscopy, time-resolved; (320.6629) Supercontinuum generation.

References and links

1. S. Weiss, "Fluorescence spectroscopy of single biomolecules," Science **283**(5408), 1676–1683 (1999).
2. X. S. Xie and J. K. Trautman, "Optical studies of single molecules at room temperature," Annu. Rev. Phys. Chem. **49**(1), 441–480 (1998).
3. T. Ha, T. Enderle, D. F. Ogletree, D. S. Chemla, P. R. Selvin, and S. Weiss, "Probing the interaction between two single molecules: fluorescence resonance energy transfer between a single donor and a single acceptor," Proc. Natl. Acad. Sci. U.S.A. **93**(13), 6264–6268 (1996).
4. D. Magde, E. L. Elson, and W. W. Webb, "Thermodynamic fluctuations in a reacting system : measurement by fluorescence correlation spectroscopy," Phys. Rev. Lett. **29**(11), 705–708 (1972).
5. E. L. Elson and D. Magde, "Fluorescence correlation spectroscopy. I. Conceptual basis and theory," Biopolymers **13**(1), 1–27 (1974).
6. P. Schwille and E. Haustein, "Fluorescence correlation spectroscopy. An introduction to its concepts and applications," Spectroscopy 1–33 (2009).
7. E. Haustein and P. Schwille, "Ultrasensitive investigations of biological systems by fluorescence correlation spectroscopy," Methods **29**(2), 153–166 (2003).
8. E. Margeat, A. N. Kapanidis, P. Tinnefeld, Y. Wang, J. Mukhopadhyay, R. H. Ebright, and S. Weiss, "Direct observation of abortive initiation and promoter escape within single immobilized transcription complexes," Biophys. J. **90**(4), 1419–1431 (2006).
9. A. N. Kapanidis, N.-K. Lee, T. A. Laurence, S. Doose, E. Margeat, and S. Weiss, "Fluorescence-aided molecule sorting: Analysis of structure and interactions by alternating-laser excitation of single molecules," Proc. Natl. Acad. Sci. U.S.A. **101**(24), 8936–8941 (2004).
10. T. A. Laurence, X. Kong, M. Jäger, and S. Weiss, "Probing structural heterogeneities and fluctuations of nucleic acids and denatured proteins," Proc. Natl. Acad. Sci. U.S.A. **102**(48), 17348–17353 (2005).
11. B. K. Müller, E. Zaychikov, C. Bräuchle, and D. C. Lamb, "Pulsed interleaved excitation," Biophys. J. **89**(5), 3508–3522 (2005).
12. E. Thews, M. Gerken, R. Eckert, J. Zäpfel, C. Tietz, and J. Wrachtrup, "Cross talk free fluorescence cross correlation spectroscopy in live cells," Biophys. J. **89**(3), 2069–2076 (2005).
13. P. Kapusta, M. Wahl, A. Benda, M. Hof, and J. Enderlein, "Fluorescence lifetime correlation spectroscopy," J. Fluoresc. **17**(1), 43–48 (2006).
14. M. Böhmer, M. Wahl, H. Rahn, R. Erdmann, and J. Enderlein, "Time-resolved fluorescence correlation spectroscopy," Chem. Phys. **353**, 439–445 (2002).
15. V. Kudryavtsev, M. Sikor, S. Kalinin, D. Mokranjac, C. A. M. Seidel, and D. C. Lamb, "Combining MFD and PIE for accurate single-pair Förster resonance energy transfer measurements," Chem Phys. Chem. **13**, 1060–1078 (2012).

#178826 - $15.00 USD Received 31 Oct 2012; revised 6 Dec 2012; accepted 7 Dec 2012; published 4 Feb 2013
(C) 2013 OSA

16. R. Fenske, D. Näther, M. Goossens, and S. D. Smith, "New light sources for time-correlated single-photon counting in commercially available spectrometers," Proc. SPIE **6372**, 63720H (2006).
17. D. Wildanger, E. Rittweger, L. Kastrup, and S. W. Hell, "STED microscopy with a supercontinuum laser source," Opt. Express **16**(13), 9614–9621 (2008).
18. E. Auksorius, B. R. Boruah, C. Dunsby, P. M. Lanigan, G. Kennedy, M. A. Neil, and P. M. French, "Stimulated emission depletion microscopy with a supercontinuum source and fluorescence lifetime imaging," Opt. Lett. **33**(2), 113–115 (2008).
19. R. Mercatelli, S. Soria, G. Molesini, F. Bianco, G. Righini, and F. Quercioli, "Supercontinuum source tuned by an on-axis monochromator for fluorescence lifetime imaging," Opt. Express **18**(19), 20505–20511 (2010).
20. H. N. Paulsen, K. M. Hilligsøe, J. Thøgersen, S. R. Keiding, and J. J. Larsen, "Coherent anti-Stokes Raman scattering microscopy with a photonic crystal fiber based light source," Opt. Lett. **28**(13), 1123–1125 (2003).
21. P. Blandin, S. Lévêque-Fort, S. Lécart, J. C. Cossec, M.-C. Potier, Z. Lenkei, F. Druon, and P. Georges, "Time-gated total internal reflection fluorescence microscopy with a supercontinuum excitation source," Appl. Opt. **48**(3), 553–559 (2009).
22. P. J. Rothwell, S. Berger, O. Kensch, S. Felekyan, M. Antonik, B. M. Wöhrl, T. Restle, R. S. Goody, and C. A. Seidel, "Multiparameter single-molecule fluorescence spectroscopy reveals heterogeneity of HIV-1 reverse transcriptase:primer/template complexes," Proc. Natl. Acad. Sci. U.S.A. **100**(4), 1655–1660 (2003).
23. O. Krichevsky and G. Bonnet, "Fluorescence correlation spectroscopy: the technique and its applications," Rep. Prog. Phys. **65**(2), 251–297 (2002).
24. J. R. Unruh, G. Gokulrangan, G. S. Wilson, and C. K. Johnson, "Fluorescence properties of fluorescein, tetramethylrhodamine and Texas Red linked to a DNA aptamer," Photochem. Photobiol. **81**(3), 682–690 (2005).
25. P. Schwille, F. J. Meyer-Almes, and R. Rigler, "Dual-color fluorescence cross-correlation spectroscopy for multicomponent diffusional analysis in solution," Biophys. J. **72**(4), 1878–1886 (1997).
26. K. Bacia, S. A. Kim, and P. Schwille, "Fluorescence cross-correlation spectroscopy in living cells," Nat. Methods **3**, 83–89 (2006).
27. M. Zhao, L. Jin, B. Chen, Y. Ding, H. Ma, and D. Chen, "Afterpulsing and its correction in fluorescence correlation spectroscopy experiments," Appl. Opt. **42**(19), 4031–4036 (2003).
28. E. Sisamakis, A. Valeri, S. Kalinin, P. J. Rothwell, and C. A. Seidel, "Accurate single-molecule FRET studies using multiparameter fluorescence detection," Methods Enzymol. **475**, 455–514 (2010).
29. J. Enderlein and I. Gregor, "Using fluorescence lifetime for discriminating detector afterpulsing in fluorescence-correlation spectroscopy," Rev. Sci. Instrum. **76**(3), 033102 (2005).
30. S. Felekyan, S. Kalinin, H. Sanabria, A. Valeri, and C. A. Seidel, "Filtered FCS: species auto- and cross-correlation functions highlight binding and dynamics in biomolecules," ChemPhysChem **13**(4), 1036–1053 (2012).
31. C. M. Pieper and J. Enderlein, "Fluorescence correlation spectroscopy as a tool for measuring the rotational diffusion of macromolecules," Chem. Phys. Lett. **516**(1-3), 1–11 (2011).

1. Introduction

Fluorescence spectroscopy is a powerful tool to investigate the structure and the dynamics of biological macromolecules. Thanks to the exquisite sensitivity of modern detection devices, useful information can be recovered from the fluorescence signal from single molecules [1,2]. Förster Resonance Energy Transfer (FRET) reports on the proximity between two complementary fluorophores through dipole-dipole interaction, and can be measured at a single molecule level [3]. FRET has thus become a method of choice to investigate macromolecular structural dynamics. Fluorescence Correlation Spectroscopy (FCS) and Cross-Correlation Spectroscopy (FCCS) [4–7] inform on the diffusion properties of fluorescent molecules as well as their interaction. For all these ultrasensitive methods, it is important to maximize the information extracted from each photon, in terms of arrival time relative to the laser pulse (reporting on the excited state lifetime of the fluorophore), polarization (reporting on the rotation of the fluorophore), and energy (reporting on the spectrum of the fluorophore). When multiple laser sources are used, it is important to assign each photon to the laser source that generated it. It is therefore not suitable to illuminate the sample with the various laser sources simultaneously. This assignment can be achieved by using alternating laser excitation schemes, that can be performed at various time scales: millisecond (msALEX [8]), microsecond (μsALEX [9]), or nanosecond (nsALEX [10] or Pulsed Interleaved Excitation, PIE [11,12]). Milli or microsecond alternation schemes are achieved using Electro-Optic modulators or Acousto-Optic Tunable filters and CW lasers; at these relatively slow timescales, it is straightforward to assign the detected photons (from an emCCD camera or a Single Photon Avalanche Diode) to the excitation laser. Nanosecond alternation is performed by interleaving the pulses of two pulsed lasers. It is necessary to use Time Correlated Single Photon Counting (TCSPC) detection to assign each individual photon

#178826 - $15.00 USD Received 31 Oct 2012; revised 6 Dec 2012; accepted 7 Dec 2012; published 4 Feb 2013
(C) 2013 OSA

to the laser pulse that generates it. In particular, nsALEX/PIE has proven to be a useful tool to perform FCS and FCCS quantitatively by removing spectral crosstalk [11,12]. By using a lifetime filtering algorithm, unwanted contributions from detector afterpulsing or scattered light to the correlation function can be discarded [13,14]. Additionally, as demonstrated recently, it is also possible to combine multiparametric fluorescence detection (MFD) and PIE to recover, in a single measurement, all the calibration factors needed to perform an accurate spFRET measurement [15].

Performing nsALEX/PIE requires the use of two pulsed lasers, and of a picosecond laser controller to drive them and generate the delay between the pulses. Ideally, this delay needs to be adjustable, in order to optimize it and obtain a full decay for each dye excited by each laser. When it is required to use another spectrally distinct dye (that needs to be excited at another laser wavelength) it is necessary to purchase and install a new laser head. Often, many excitation lasers will be needed, such as in a user facility, for example, where many different samples with different fluorophores are analyzed. Supercontinuum sources make use of optical nonlinear effects in photonic crystal optical fibers to create light with a wide spectrum, which can span the visible and near-infrared, typically from around 400 to 2000 nm. Commercially available, they achieve high power densities (several mW/nm in the visible), and have variable repetition rates (up to 80MHz typically). Recently, their usefulness has initiated the replacement of conventional lasers for various types of advanced microscopies and spectroscopies techniques, including TCSPC fluorescence spectroscopy [16], stimulated emission depletion (STED) fluorescence microscopy [17,18], FLIM (Fluorescence Lifetime Imaging Microscopy)-FRET microscopy [19], coherent anti-Stokes Raman scattering (CARS) microscopy [20], and total internal reflection microscopy [21].

Here we present a simple optical scheme, based on a commercial supercontinuum source, explaining how to perform nsALEX/PIE microscopies at any wavelength in the visible spectrum. In our experimental setup, the output beam of the supercontinuum source is divided in two paths, and each of them is spectrally filtered at the desired wavelength, using a simple bandpass filter. One beam path is much longer than the other, adjusted to the appropriate length (several meters), to generate the delay between the pulses. Recombination of the two beams leads to a pulsed interleaved excitation, with arbitrary wavelength (that depends on the filters), arbitrary delay (that depends on the path lengths), and perfect spatial overlap thanks to coupling into a single mode fiber. We present here the details of this realization, and demonstrate the use of this versatile setup for PIE / FCCS experiments.

2. Experimental setup

Our setup (Fig. 1) uses a SC450-4-20MhZ laser source (Fianium, Southampton, UK). It runs at 20MHz, and has a power density >2mW/nm over the 450-800nm range, with average pulse width of 100-150ps [16]. The collimated, unpolarized output of the source is divided by a 50:50 beamsplitter cube BS1 (BS016, Thorlabs, NJ, USA), thus generating two beams (the "*prompt*" and the "*delayed*"). Each beam is spectrally filtered using an excitation bandpass filter at the wavelength of choice (typically 10nm bandpass, 532/10 (BP1) and 635/10 (BP2) in the present example). Virtually any combination of filters compatible with the double band dichroic mirror in the microscope (DM2) can be used here. The *delayed* beam is reflected by a set of 9 mirrors, adding a beam path length of up to 8m relative to the *prompt* beam. Four mirrors are mounted on optical rails (Thorlabs, NJ, USA) to reduce this distance and fine adjustement of the delay if needed. Since the output of the supercontinuum source fiber is not perfectly collimated, this set of mirrors causes a divergence and diffusion of the beam, that is re-collimated using a telescopic system of lenses (f = 1000mm (L1) and f = 500mm (L2)). The two beam paths can then recombined using a dichroic mirror (DM1) reflecting only the prompt beam. However, we prefer using a 50:50 beamsplitter cube (BS016, Thorlabs, NJ, USA) resulting in a 50% power loss, but consistent with any wavelength combination (including when the two beam paths are at the same wavelength, in order to obtain a 40Mhz monochromatic pulse train (see Discussion)). This power loss is not detrimental since beam attenuation is required for most confocal experiments. The two beams are then focused using

#178826 - $15.00 USD Received 31 Oct 2012; revised 6 Dec 2012; accepted 7 Dec 2012; published 4 Feb 2013
(C) 2013 OSA

a 10x objective, and coupled into a single-mode fiber (SMF) (P1-460A-FC, Thorlabs, NJ, USA), by which the beams become spatially overlapped and filtered. At the exit of the fiber, using this setup, a power of up to 1mW is obtained for each wavelength. This power is reduced typically to 10-100µW for each beam by using neutral density filters.

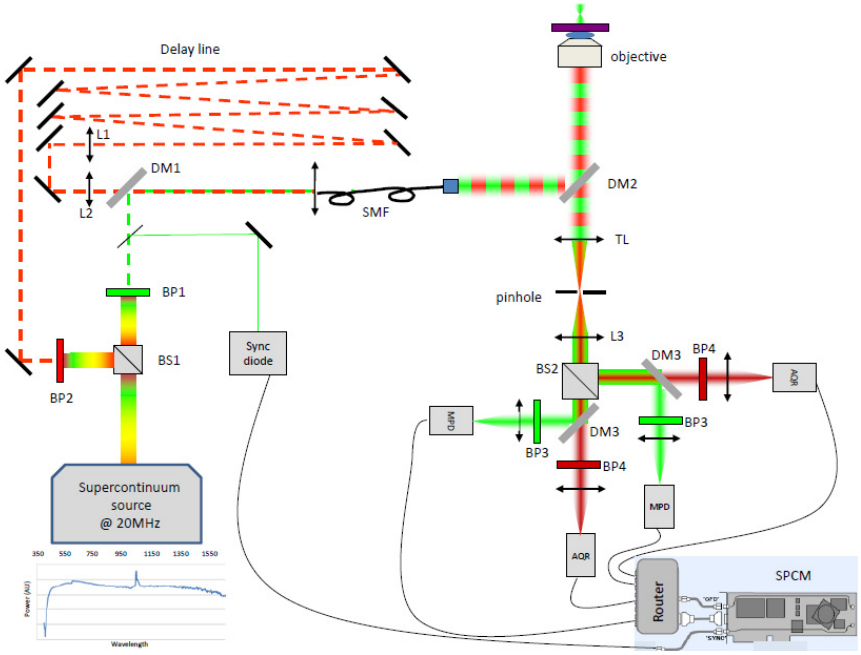

Fig. 1. Experimental setup (see text). Briefly, the output of the supercontinuum source is separated into two paths (the *prompt* and the *delayed*, the latter corresponding to a 8 meters long delay line) using a beamsplitter cube (BS1). The beams are recombined, thus interleaving the pulses, and coupled into a single mode fiber (SMF). The output of the fiber is then directed into a home-built confocal microscope, equipped with a 4-channels Single Photon Avalanche Diodes detection, and a Single Photon Counting Module (SPCM). L: lens; DM: dichroic mirror; TL: tube lens; BP: bandpass filter.

The output of the fiber is collimated using a 10x microscope objective lens (04OAS010; CVI Melles Griot, Albuquerque, NM, USA), and coupled into an inverted microscope (Axio observer D1, Carl Zeiss, Germany). The light is reflected by a dichroic mirror (DM2) that matches the excitation/emission wavelengths (FF545/650-Di01, Semrock, Rochester, NY, USA) and coupled into a Plan Apochromat 100x, NA1.4 objective (Carl Zeiss, Germany). Emitted photons are then collected by the objective and focused by the tube lens (TL) on a pinhole of desired width (typically 75µm for FCS and 150µm for spFRET). The detection part of our setup is a classical MFD/nsALEX configuration [10,22]. The photon stream is collimated (L3), and divided using a beamsplitter cube (BS2). In each created channel, the photons are spectrally separated using dichroic mirrors (DM3, here BS 649, Semrock, Rochester, NY, USA) and filtered using high quality emission bandpass filters (here ET BP 585/65 (BP3) and ET BP 700/75 (BP4), Chroma, Bellows Falls, VT, USA). Single photons are detected using Single Photon Avalanche Diodes. We use two MPD-1CTC (MPD, Bolzano, Italy) for the lowest wavelength channels (hereafter named the *green* channels) and two SPCM AQR-14 (Perkin Elmer, Fremont, CA, USA) for the highest wavelength channels (hereafter named the *red* channels). This choice is driven by the fact that MPD detectors have a better time resolution (which is important especially for spFRET experiments based on donor lifetime measurements), but have a lower quantum efficiency above 550nm than SPCM AQR detectors. Having two identical detection channels for each spectral range reduces the distortion of the autocorrelation functions by eliminating the effect of detector afterpulsing [23]. The output of the detectors is coupled into a TCSPC counting board (SPC-150,

#178826 - $15.00 USD Received 31 Oct 2012; revised 6 Dec 2012; accepted 7 Dec 2012; published 4 Feb 2013
(C) 2013 OSA

Becker&Hickl, Berlin, Germany), through a HRT41 router (B&H), using appropriate pulse inverters and attenuators. The *sync* signal that triggers the TCSPC board is provided by picking a small fraction of the light from the *prompt* path (reflected by a coverslip), and focusing it on an avalanche diode (APM-400, B&H). We note that when polarized emission and detection are needed (for MFD experiments for example), BS1 and BS2 can be replaced with polarizing beamsplitters (PBS ; PBS201, Thorlabs, NJ, USA). Control of the polarization can be performed on each of the *prompt* and *delayed* paths using ½ and ¼ waveplates.

3. Results

Detection of the emitted photons after prompted and delayed excitation

The detected fluorescence decays for the *green* and the *red* channels for a mixture of tetramethylrhodamine (TMR) and Atto655 fluorophores are presented on Fig. 2 (only one curve is represented / channel for clarity, using a linear or a logarithmic scale (inset)). The photons generated by the *prompt* beam (at 532nm, exciting mainly the TMR) appear in the 0-25 ns time window, while those generated by the *delayed* beam (at 635nm, exciting mainly Atto655) are detected in the 25-50ns window. The 25 ns delay between the pulses allows for a complete decay of the fluorescence intensities (Fig. 2, insets). As expected, excited state lifetimes τ of TMR and Atto655 were measured to be respectively 2.5 ns [24] and 1.8 ns (as provided by the manufacturer). Obtaining these complete decays justifies the use of a supercontinuum source running at 20MHz. Indeed, a source running at 40 MHz or higher would result in incomplete decays, and thus crosstalk between the *prompt* and *delayed* channels, while a source running at 10 MHz or lower would decrease the photon yield per molecule. Supercontinuum sources equipped with a pulse picker are also available, allowing an adjustment of the pulse frequency as needed. We note that if a fluorophore has a longer lifetime, it is possible to adjust the size of the *prompt* and *delayed* observation windows by changing the delay between the two laser pulses, simply by changing the length of the delay line.

The photons in the *delayed* decay appear only in the *red* channel, as expected. However, in the *prompt* decay, a significant fraction of photons appear in the *red* channel. The measured average decay time for these photons is 2.1 ns, indicating that they arise from two sources of cross-talk: the leakage of TMR emission (τ = 2.5 ns) in the *red* channel, due to its emission spectrum properties, and the emission of Atto655 (τ = 1.8 ns) directly excited by the *prompt* beam (at 532nm), due to its excitation spectrum properties (see below).

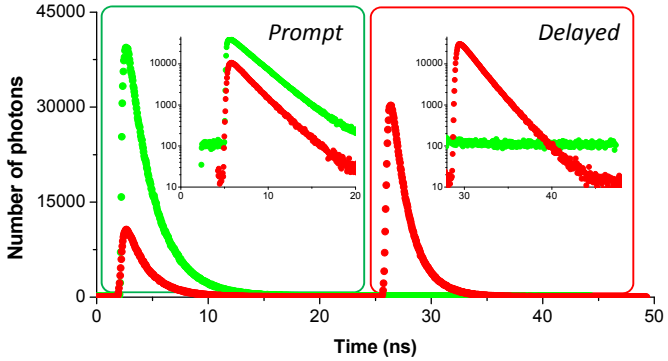

Fig. 2. Fluorescence decays obtained for a mixture of TMR and Atto655. Photons detected in the *green* channels appear in green, and are only observed upon excitation by the *prompt* pulses (at 532nm). Photons detected in the *red* channels appear in red. They are detected upon excitation by the *delayed* pulses (at 635nm) as expected, but also upon excitation by the *prompt* pulses, due to the leakage of the emission of TMR in the *red* channels, and due to direct excitation of Atto655 by the *prompt* pulses at 532nm. Insets represent the same decays on a logarithmic scale. The observed offset in the decays from the green channel arises from higher dark count rates in the *green* detectors than in the *red* detectors.

#178826 - $15.00 USD Received 31 Oct 2012; revised 6 Dec 2012; accepted 7 Dec 2012; published 4 Feb 2013
(C) 2013 OSA

Alignment of the emission detectors and the excitation lasers

It is possible to take advantage of these cross talk effects to verify the correct alignment of the detection channels and the correct overlap of the two excitation beams, by using FCS and FCCS. In an FCS experiment, the amplitude of the correlation function depends on the number of molecules in the observation volume [5]. In an FCCS experiment, the signal from two observation volumes is cross-correlated. The amplitude of the cross-correlation function relative to the correlation function for one of the volumes depends on the fraction of molecules detected in both channels relative to those detected in this specific volume [25,26]. Thus, if only one type of molecules that is able to emit photons in both channels is present, the amplitude of the cross correlation will reflect the overlap between the observation volumes.

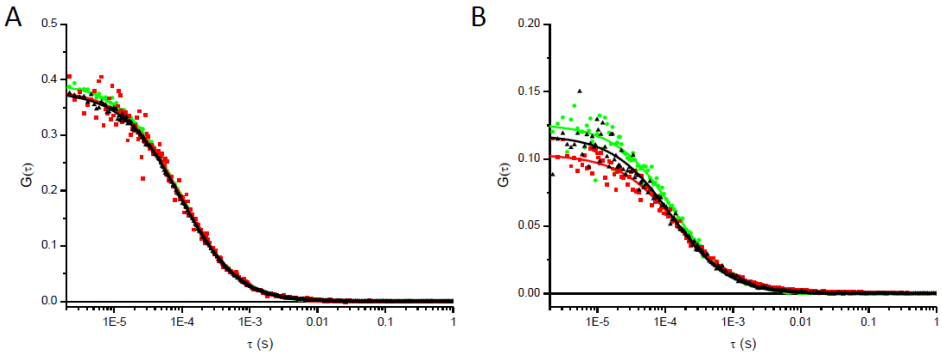

Fig. 3. A - Fluorescence autocorrelation (green and red) and cross-correlation (black) curves for a TMR solution. The cross-correlation amplitude represents 100% of the autocorrelation amplitudes of both channels, indicating a perfect overlap of the *green* and the *red* detection channels. B - Fluorescence autocorrelation and cross correlation (black) curves for an Atto655 solution upon excitation by the *prompt* and the *delayed* beams (green and red, respectively). The difference in correlation amplitudes indicate that the excitation volume generated by the *delayed* (red) beam is slightly larger than the other. However, the cross-correlation curves lie between the autocorrelation curves for both excitation beams, which indicates an excellent overlap between the two excitation volumes. Data were fit with a model taking into account one diffusion component and triplet blinking.

The observation volume results from the combination of the excitation volume defined by the excitation beam and the emission volume defined by the emission optics (pinhole + lenses + avalanche photodiodes). First, in order to verify the overlap of the emissions volumes, we use a solution of a fluorophore emitting photons in all detections channels (such as TMR), upon excitation by the *prompt* laser. In our setup, around 10 to 15% of the signal emitted by TMR in the *green* detection channels is detected in the *red* detection channels, due to TMR emission spectral properties. Figure 3(a) presents a correlation analysis of the fluorescence signal from a 1nM TMR solution, upon excitation by the *prompt* beam (the *delayed* beam is blocked). We observe equivalent correlation amplitudes (within error) for the autocorrelation curves for the photons detected in the *green* channels ($G(0)_{green} = 0.217 \pm 0.005$), the *red* channels ($G(0)_{red} = 0.212 \pm 0.004$), and the cross-correlation curve for the photons detected in both channels ($G(0)_{cross} = 0.215 \pm 0.004$). A similar, perfect overlap is also observed when cross correlating the two *green* channels together, or the two *red* channels (not shown). This shows that the TMR molecules emitting in all the channels are the same, and thus indicates a perfect overlap of the four emission volumes, upon excitation by a single beam. This type of control can be easily performed on any single color confocal microscope that can acquire FCS data.

Second, in order to verify the overlap of the excitation volumes by FCS, we need to make use of the ability offered by PIE to separate the photons generated by the two excitation beams. We use a solution of Atto655, excited by the *prompt* beam (at 532 nm) at about 10%

#178826 - $15.00 USD Received 31 Oct 2012; revised 6 Dec 2012; accepted 7 Dec 2012; published 4 Feb 2013
(C) 2013 OSA

of the level of excitation generated by the *delayed* beam (at 635 nm) (due to its excitation spectrum properties). By decreasing the power of the *delayed* beam by a factor of 10 compared to the *prompt* beam, a similar signal level is thus expected for the two beams, in the *red* detection channels. This is indeed the case, and enabled the calculation of the autocorrelation curves for the photons generated by the *prompt* beam based on their arrival time (Fig. 3(b), green, $G(0)_{prompt} = 0.126 \pm 0.003$), for those generated by the *delayed* beam (Fig. 3(b), red, $G(0)_{delayed} = 0.103 \pm 0.003$), and the cross-correlation between these photons streams (Fig. 3(b), black, $G(0)_{cross} = 0.118 \pm 0.003$). These data indicate a 22% difference in the autocorrelation amplitudes of the signals generated by the *prompt* (green) and the *delayed* (red) pulses. This indicates that the effective observation volume generated by the *delayed* (red) beams is 22% larger than the one generated by the *prompt* (green) beam, which is expected for diffraction limited volumes at 635nm vs. 532nm respectively. As expected theoretically [25], in such a case, for a single species emitting in both channels, the cross correlation curves lies between the two autocorrelation curves (Fig. 3(b)). Altogether, these data indicate that the two excitation volumes present an excellent overlap, and that the size of the observation volumes in our configuration is governed by the wavelength of the excitation light, and not the configuration of the emission module (equipped with a 75μm pinole).

Elimination of cross-talk effects in FCCS experiments

The crosstalk originating from the leakage of the emission of the *green* dye and the direct excitation of the *red* dye by the *green* laser is a well-known source of artifact in FCCS experiments [25], which can be minimized by choosing fluorophores whose spectral overlap is minimal. Using PIE, however, it is possible to eliminate this source of artifact by discarding these irrelevant photons based on their arrival time relative to the laser pulses, without loss in the signal to noise ratio of the correlation function [11]. This is demonstrated in Fig. 4. We used a mixture of two DNA fragments (labeled with Cy3 and Atto655), whose sequences are not complementary, and thus are not expected to hybridize. The correlation functions of all photons detected in the *green* and the *red* channels is presented in Fig. 4(a). A significant fraction of cross-correlation (A_{CC} = 14% of $A_{CC,\ green}$ (black curve vs. green curve)) is observed, due to spectral crosstalk. However, when the photons detected in the *green* channels only after *prompt* excitation are correlated with the photons detected in the *red* channels only after *delayed* excitation, the amplitude of the cross-correlation function drops to zero, demonstrating an efficient suppression of the crosstalk (Fig. 4(b)). On the contrary, when using a mixture of two DNA fragments (labeled with Cy3 and Atto655), for which the sequences are complementary and that have been hybridized, a significant cross correlation amplitude is observed (A_{CC} = 57%, Fig. 4(c)), that only slightly decreases after photon selection based on their arrival time (A_{CC} = 46%, Fig. 4(d))

#178826 - $15.00 USD Received 31 Oct 2012; revised 6 Dec 2012; accepted 7 Dec 2012; published 4 Feb 2013
(C) 2013 OSA

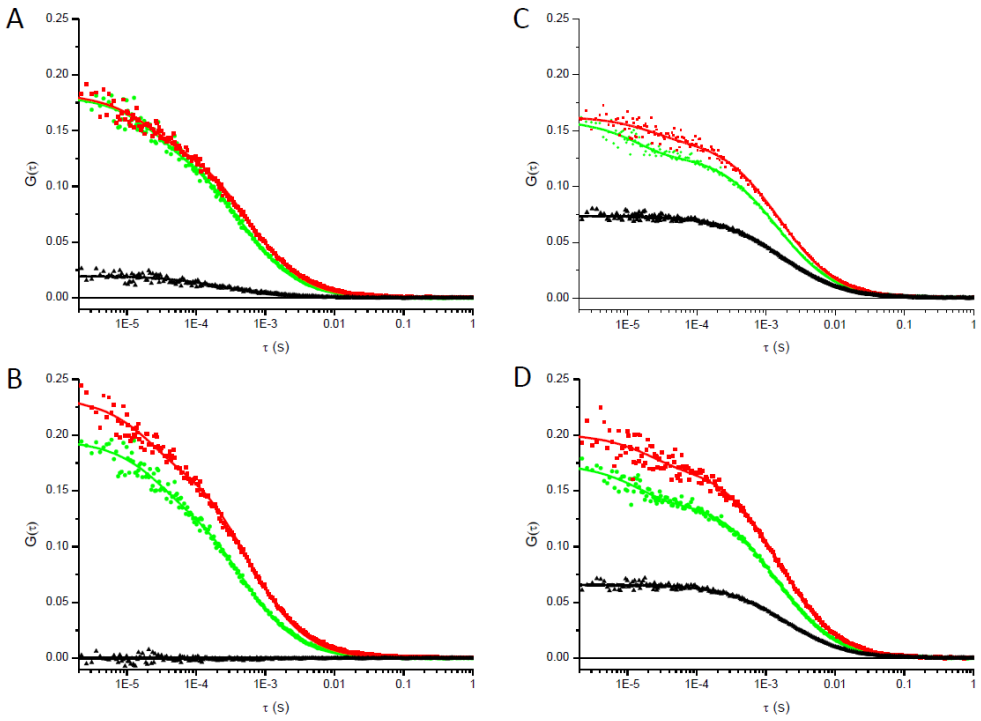

Fig. 4. Fluorescence autocorrelation (green and red) and cross correlation (black) curves for a 1:1 mixture of cy3 (green)- and Atto655 (red)- labeled DNA fragments either non complementary ((A) and (B)) or complementary and hybridized ((C) and (D)). A and C represent the correlation curves obtained for all photons, while B and D are obtained by selecting only the *green* photons generated by the *prompt* pulse and the *red* photons generated by the *delayed* pulse. For the non-complementary strands, the apparent cross-correlation amplitude that represents 14% of the *green* cross-correlation (A) is due to spectral cross-talk, and is completely removed by applying the PIE algorithm (B). For the complementary strands, the apparent cross-correlation amplitude represents 57% of the *green* cross-correlation (C). After removal of the cross-talk (D), this cross-correlation decreases to 46%, that represents the fraction of DNA molecules labeled with cy3 that are hybridized to DNA molecules labeled with Atto655. Data were fit with a model taking into account one diffusion component and triplet blinking (except for the cross correlation curves, where there is no triplet blinking).

3. Discussion and conclusion

We have presented here a simple optical configuration to perform nsALEX/PIE experiments at any wavelength combination within the visible spectrum, using a commercial supercontinuum source. Using this configuration, it becomes possible to benefit from the advantages offered by these alternating laser excitation technologies, such as: removing the cross-talk effects that complicate the interpretation of FCCS experiments, thus permitting the measurement of weaker interactions [11,12] ; removing spectral crosstalk in multicoulour fluorescence imaging [11]; separating in spFRET experiments the complexes that have a low FRET efficiency from those where the acceptor is inactive or absent [10,11].

In the setup presented here, four detection channels are used, but in principle only two channels are needed to perform PIE / FCCS experiments. However, using four channels offers several advantages. First, it allows a direct hardware-based correction for the spurious effects due to detector afterpulsing. Indeed, cross correlating the signals from two spectrally equivalent detectors removes the large autocorrelation signal observed at short time scales (typically <1μs) in the autocorrelation curves arising from detector afterpulsing [27]. Second, by using a polarizing beamsplitter in the detection module (BS2, Fig. 1) and polarization

#178826 - $15.00 USD Received 31 Oct 2012; revised 6 Dec 2012; accepted 7 Dec 2012; published 4 Feb 2013
(C) 2013 OSA

optics in the excitation module to polarize the excitation beam, it becomes possible to use this setup to perform multiparameter fluorescence detection (MFD [22,28],), and MFP combined with PIE [15]. These techniques enable accurate determination of FRET efficiencies on single diffusing molecules, and thereby a possible quantification of the structural dynamics of these biomolecules on a nanosecond to millisecond timescale. We would also like to point out that we have successfully modified the setup presented here in order to be able to perform single color excitation MFD experiments at twice the frequency of the supercontinuum source (i.e. 40MHz). This has been achieved by placing the 532/10 bandpass filter directly at the output of the supercontinuum source, and by adjusting the delayed path length so that the two pulses are interleaved with a delay of exactly 25ns. This configuration results in increasing the photon yield per molecule, or decreasing the photobleaching [11].

The optical setup presented here can also be used to perform Fluorescence Lifetime Correlation Spectroscopy (FLCS) [13,14], a method consisting in using the excited state lifetime information to separate the autocorrelation function of individual components of a mixture of fluorophores. This method also removes some parasitic contributions such as scattered light from the correlation curves (that typically lowers the amplitude of the correlation at low fluorophores concentrations). It allows as well efficient removal of detector afterpulsing when only one detector per channel is used [29]. Moreover the setup can be used to perform filtered FCS (fFCS) experiments, a technique that uses MFD data sets to create species-specific filters based on lifetime, spectral, and polarization information, and measure binding processes and fast conformational dynamics within diffusing molecules [30]. Finally, our setup can be modified to measure the rotational diffusion of macromolecules, by using the polarization-sensitive PIE-FCS method presented in [31]. It simply requires to generate two pulses streams (at the same wavelength), with orthogonal linear polarizations, instead of using two identical synchronized pulsed lasers with orthogonal polarizations, as previously described [31].

In conclusion, we show that it is possible to perform PIE-FCS and related techniques, using a supercontinuum laser source, for a cost equivalent to two pulsed picosecond sources and their drivers. However, the supercontinuum source configuration offers a much higher level of versatility, since changing the excitation wavelengths simply requires switching between interference filters, rather than require to purchase and install additional lasers and driver modules.

Acknowledgments

This work by supported by the GIS *«* IBiSA: Infrastructures en Biologie Sante et Agronomie *»,* a "Chercheur d'avenir" grant to E.M. from the Région Languedoc-Roussillon, and a doctoral grant from the Ministère de la Recherche to L.O. We thank Louis-Simon Rameau for his help in the initial phase of this project, and Ted Laurence (LLNL) and Antoine Le Gall (CBS) for their help with the FCS algorithm.

#178826 - $15.00 USD Received 31 Oct 2012; revised 6 Dec 2012; accepted 7 Dec 2012; published 4 Feb 2013
(C) 2013 OSA

4.2 Illuminating the activation mechanism of mGluRs with smFRET

Our article that summarizes the core and the main results of my research is joined later in this chapter. However, it seems appropriate to firstly give a short summary of the objectives of the study, and provide some additional information on the sample preparation, not included in the paper.

Short reminder of the objectives

In chapter 1.3, it was described that a reorientation and a stabilization of the active state of the VFT dimer is thought to be necessary for the activation of mGluRs in response to the binding of the full agonist glutamate. This hypothesized model derives both from experimental data showing, for instance, that cross-linking the receptor in the active state produces a constitutively active receptor (Huang *et al.*, 2011b), but also from crystal structures of the VFT (**Table 1.2**). The crystal structures are, however, not always in total agreement with the postulated activation model as the VFT has been crystallized both in a resting conformation despite the binding of an agonist, and inversely, in the active state in spite of the presence of an antagonist (**Figure 1.18**).

In order to investigate this activation model for mGluRs and attempt an explanation of the discrepancies observed between the biochemical and the structural data, a cell surface time resolved HTRF approach was established by our collaborators (Doumazane *et al.*, 2013). As described in chapter 2, the VFT dimer was labeled in its N-terminus with HTRF compatible dyes and variations in FRET were monitored in presence of various ligands. The outcome of this study indicated that a reorientation of the dimer toward the active state indeed follows the binding of an agonist, as detected by a decrease in FRET. In contrast, the FRET increases for an antagonist, which hence, suggests a stabilization of the resting state. In addition, they measured intermediate FRET values with partial agonists (Doumazane *et al.*, 2013).

Many questions remained, nonetheless, unanswered. For instance, it was impossible to conclude whether the FRET variations were really due to the full stabilization of the active and the resting state, or whether the averaged FRET values, in reality, represented a shift in equilibrium of the entire population toward a preferential conformation. The second hypothesis is in line with the

very popular conformational selection mechanism (Deupi and Kobilka, 2010; Changeux, 2012) presented in chapter 1.2.

Moreover, there are two possible theories to explain the intermediate FRET value measured with the partial agonists. Either the partial agonists induce a stable conformation that is slightly different from the one stabilized by the full agonist, or, it might be that the partial agonist less efficiently pushes the equilibrium of the receptor toward the active state.

To address these questions, I have carried out smFRET experiments on the isolated VFT domain. The utilization of the VFT domain as a model was justified by the observation that the VFT domain alone, either anchored to the cell-membrane via a GPI anchor, or cleaved and measured in solution, gave similar results in HTRF compared to the WT receptor (figure 1 in the article presented in chapter 4.2.).

All smFRET experiments were realized on the setup described in chapter 4.1 and analyzed with the methods described in chapter 3.

Sample preparation of soluble VFT-dimers

To enable the study of single VFTs in solution, I expressed the VFT dimer at the surface of HEK293cells via a GPI-anchor in position 499 (Flag-ST-hmGlu2-499GPI construct, provided by CisBio Bioassays, **figure 4.2**) using a standard lipofectamine 2000 transfection reagent protocol (life technologies™) (**Figure 4. 3:1**).

FLAG-SNAP-mGluR2(human)VFT-signal peptide

Translation 733 a.a. MW=79866.67000000004

MALPVTALLLPLALLLHAARPAAASGIDYKDDDDKAGIDAIMDKDCEMKRTTLDSPLGKLELSGCEQGLHEIKLLGKGTS
AADAVEVPAPAAVLGGPEPLMQATAWLNAYFHQPEAIEEFPVPALHHPVFQQESFTRQVLWKLLKVVKFGEVISYQQL
AALAGNPAATAAVKTALSGNPVPILIPCHRVVSSSGAVGGYEGGLAVKEWLLAHEGHRLGKPGLGDIEGPAKKVLTLEG
DLVLGGLFPVHQKGGPAEDCGPVNEHRGIQRLEAMLFALDRINRDPHLLPGVRLGAHILDSCSKDTHALEQALDFVRAS
LSRGADGSRHICPDGSYATHGDAPTAITGVIGGSYSDVSIQVANLLRLFQIPQISYASTSAKLSDKSRYDYFARTVPPDFFQ
AKAMAEILRFFNWTYVSTVASEGDYGETGIEAFELEARARNICVATSEKVGRAMSRAAFEGVVRALLQKPSARVAVLFTR
SEDARELLAASQRLNASFTWVASDGWGALESVVAGSEGAAEGAITIELASYPISDFASYFQSLDPWNNSRNPWFREFW
EQRFRCSFRQRDCAAHSLRAVPFEQESKIMFVVNAVYAMAHALHNMHRALCPNTTRLCDAMRPVNGRRLYKDFVLN
VKFDAPFRPADTHNEVRFDRFGDGIGRYNIFTYLRAGSGRYRYQKVGYWAEGLTLDTSLIPWASPSAGPLPASRRRSSST
VLFSSPPVILLISFLIFLIVG*

Full length human mGluR2 sequence, The VFT is represented in Green.

>sp|Q14416|GRM2_HUMAN Metabotropic glutamate receptor 2 OS=Homo sapiens
GN=GRM2 PE=2 SV=2
MGSLLALLALLLLWGAVAEGPAKKVLTLEGDLVLGGLFPVHQKGGPAEDCGPVNEHRGIQRLEAMLFALDRINRDPHL
LPGVRLGAHILDSCSKDTHALEQALDFVRASLSRGADGSRHICPDGSYATHGDAPTAITGVIGGSYSDVSIQVANLLR
LFQIPQISYASTSAKLSDKSRYDYFARTVPPDFFQAKAMAEILRFFNWTYVSTVASEGDYGETGIEAFELEARARNIC
VATSEKVGRAMSRAAFEGVVRALLQKPSARVAVLFTRSEDARELLAASQRLNASFTWVASDGWGALESVVAGSEGAAE
GAITIELASYPISDFASYFQSLDPWNNSRNPWFREFWEQRFRCSFRQRDCAAHSLRAVPFEQESKIMFVVNAVYAMAH
ALHNMHRALCPNTTRLCDAMRPVNGRRLYKDFVLNVKFDAPFRPADTHNEVRFDRFGDGIGRYNIFTYLRAGSGRYRY
QKVGYWAEGLTLDTSLIPWASPSAGPLPASRCSEPCLQNEVKSVQPGEVCCWLCIPCQPYEYRLDEFTCADCGLGYWP
NASLTGCFELPQEYIRWGDAWAVGPVTIACLGALATLFVLGVFVRHNATPVVKASGRELCYILLGGVFLCYCMTFIFI
AKPSTAVCTLRRLGLGTAFSVCYSALLTKTNRIARIFGGAREGAQRPRFISPASQVAICLALISGQLLIVVAWLVVEA
PGTGKETAPERREVVTLRCNHRDASMLGSLAYNVLLIALCTLYAFKTRKCPENFNEAKFIGFTMYTTCIIWLAFLPIF
YVTSSDYRVQTTTMCVSVSLSGSVVLGCLFAPKLHIILFQPQKNVVSHRAPTSRFGSAAARASSSLGQGSGSQFVPTV
CNGREVVDSTTSSL

***Figure 4.2**. Amino acid sequence for the Flag-ST-hmGlu2-499GPI construct, used throughout this study, and for the full length receptor. In the latter, the VFT is highlighted in green.*

After a 48h incubation period, I carried out the labeling with SNAP-tag® compatible Benzyl-Guanine (BG) dyes, at a ratio that depends both on the reactivity of the dyes and on whether the single-molecule FRET experiment that follows is performed using a classical MFD configuration or a MFD experiment coupled with PIE (**figure 4.3:2**). In fact, in classical MFD, it is fairly problematic to distinguish molecules labeled only with donor dyes from FRET molecules with very low efficiencies, similar or below the donor-leakage value. This has, therefore, to be taken into consideration already by the time of labeling by increasing the concentration of acceptor dyes compared to the donor dye concentration. For the FRET-couple M2BgCy3B (donor) - BgD2 (acceptor) employed throughout this study, I estimated that a donor:acceptor ratio of approximately

200 times more acceptors gave a satisfying result although the presence of donor-only labeled molecules could not be entirely avoided. For MFD-PIE experiments, a 50:50 labeling ratio is desired and to this aim, approximately 10 times more Bg-D2 than M2BgCy3B had to be added because of the better reactivity of the M2BgCy3B dye.

After incubation, the cells have to be washed extensively to ensure the removal of most excess dyes (**figure 4.3:3**) before the GPI anchor can be cleaved using a phosphatidylinositol specific phospholipase C enzyme, (**figure 4.3:4**) which releases the extracellular domain in the supernatant (**figure 4.3:5**). Despite repeated rinsing, it is necessary to desalt the supernatant to entirely eliminate the remaining free dye. Alternatively, the presence of a flag-tag in N-terminus can be exploited to purify the soluble VFT-dimers by affinity chromatography. However, due to the increased complexity of the purification protocol if this last step is implemented, I only performed flag-tag purification a handful of times for the sake of comparison with the non-purified receptors, for which I obtained similar results. As a matter of fact, the Phospholipase C cleaves all GPI-anchored protein at the cell-surface and it was for that reason critical to ascertain that none of these other proteins were non-specifically labeled or modified the behavior of the VFT.

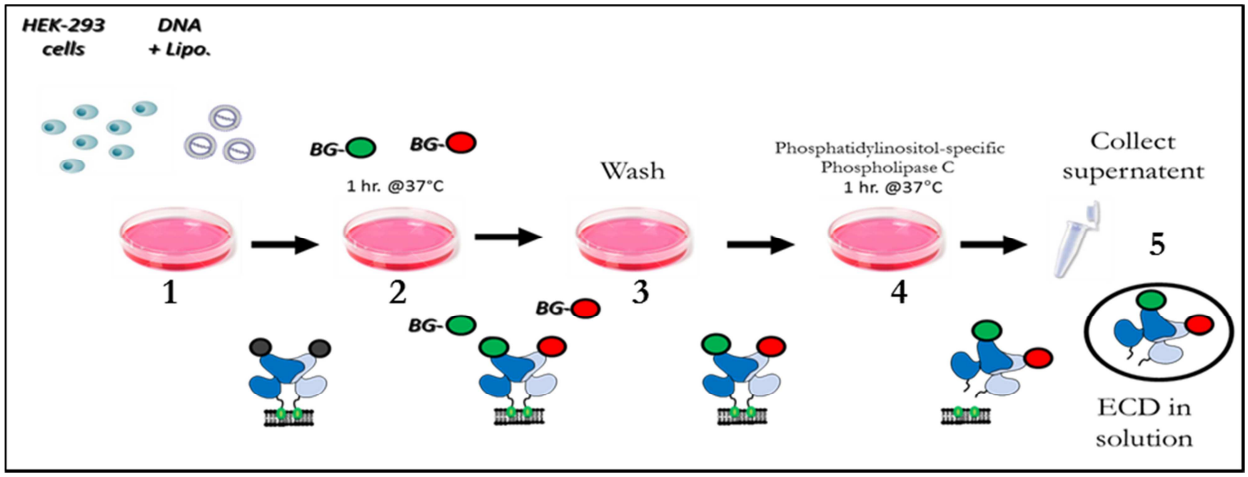

***Figure 4.3**. Schematic illustration of the different expression, labeling and isolation steps. The flag-ST-hmGlu2-499GPI construct is expressed at the cell surface by lipofectamine 2000 transfection. 48h after transfection, the SNAPs are randomly labeled with sm FRET compatible BG dyes for roughly 1h. A specific phospholipase C is then added to cut the GPI anchor and release the extracellular domain. smFRET experiments are directly performed on the supernatant after dilution.*

The labeling efficiency of the SNAP-tag® labeling approach is highly specific as can be concluded from the SDS-PAGE in **figure 4.4.** Three bands are observed for the VFT-dimer and the

ECD-dimer, and the incubation with β-mercaptoethanol that reduces the disulfide bond which maintains the dimeric structure also decreases the number of bands from three to two (**Figure 4.4.a**).

To verify if these three forms of the receptor arise from different degrees of glycosylation, I used a N-glycosidase to eradicate all possible N-glycosylated post-translational modifications, and the result shown in **figure 4.4.b** clearly suggests that this is, indeed, the case. Following N-glycosidase treatment, there is a noticeable shift toward a lighter form of the receptor and only one band is now visible, signifying that the initial statement was indeed valid. The biological significance of these differently glycosylated forms remain, nonetheless, unknown. In addition, it is noteworthy that no other bands except the ones that can be attributed to the SNAP-construct are visible, which attests the high labeling efficiency of the SNAP-tag.

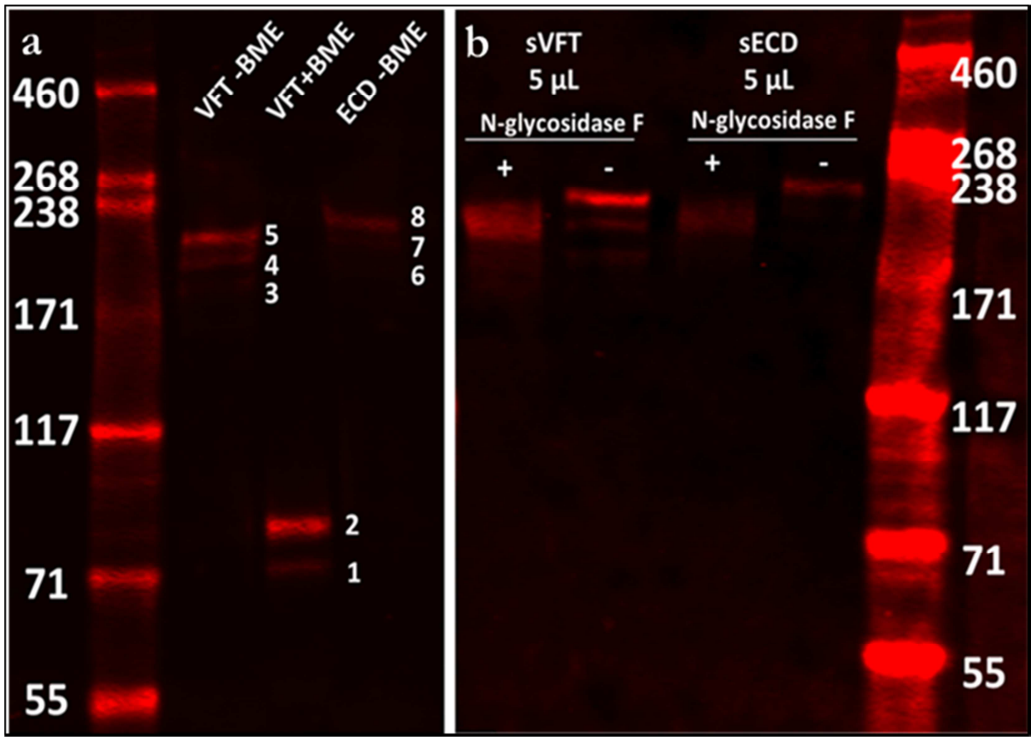

Figure 4.4. *SDS-PAGE of labeled VFT- or ECD-dimers. (**a**) The three lanes from left to right represent the non-reduced VFT, the reduced VFT with β-mercaptoethanol and the non-reduced ECD. For the non-reduced conditions, three bands are visible although the band corresponding to the heaviest form of the receptor is largely overrepresented. Interestingly, after the treatment with the reducing agent, only two bands remain suggesting that the monomer can exist in either in a form having undergone post-translational modifications or in a non-modified form. In addition, this first SDS-PAGE undeniably highlights the very high specificity of the SNAP-tag labeling as all bands can be attributed to the VFT, which is further proven by reducing the disulfide bond that maintain the dimeric structure of the VFT. (**b**) In order to verify the hypothesis proposing that the different forms are due to different degrees of post-translational modifications, I incubated the VFT (right lane) and the ECD (left lane) with an N-glycosidase that specifically removes all N-glycosylation introduced modifications. Following N-glycosidase treatment, there is a noticeable shift toward a lighter form of the receptor and only one band is now visible, signifying that the initial statement was indeed valid.*

Initial µSALEX smFRET experiments

After having optimized and confirmed the labeling specificity of the SNAP-VFT construct, some initial smFRET experiments using the µSALEX approach were realized with the purpose of validating the soluble VFT-dimer as a model for the study of conformational changes by smFRET. These experiments showed a clearly dominant population whose E_{PR} value varied depending on the nature of the ligand, in agreement with the HTRF results. In the presence of glutamate, a majority of molecules were centered on a fairly low E_{PR} value whereas in the presence of DCG-IV, the E_{PR} value slightly increased to reach an intermediate value and increased even further with the antagonist. Additionally, the FRET (E_{PR}) distribution of the main population was much broader than expected for a static population, which suggested underlying dynamics. Thereupon, it was concluded that the soluble VFT-dimer is both compatible with smFRET experiments and constitutes a valid model for the study of the fast conformational changes that occur following treatments with pharmacological compounds.

Altogether, these preliminary results motivated us to investigate the origin of the widening of the FRET distribution by MFD. Firstly, the MFD data was used to ascertain that the different FRET states are not due to acceptor quenching (**Supplementary figure 2 in the submission manuscript**) and that they are correctly overlaid by the Perrin equation, and thus not the result of variations in the K^2 value. After these initial control experiments, I performed a large number of acquisitions and explored various analyzing methods to reveal and quantify the behavior of mGluRs in the presence of various ligands. The outcome of this investigation is summarized in our article "*Specific regulation of transition rates between active and inactive states of metabotropic glutamate receptors determines agonist efficacy*", which will now be provided.

Research article: Specific regulation of transition rates between active and inactive states of metabotropic glutamate receptors determines agonist efficacy,

L.Olofsson *et al*, in preparation, 2014

Specific regulation of transition rates between active and inactive states of metabotropic glutamate receptors determines agonist efficacy

Linnea Olofsson [1,2,3], Suren Felekyan [4], Etienne Doumazane [3,5,6], Pauline Scholler [3,5,6,7], Ludovic Fabre [3,5,6,7], Jurriaan M. Zwier [7], Philippe Rondard [3,5,6], Claus A.M. Seidel [4], Jean-Philippe Pin* [3,5,6] and Emmanuel Margeat* [1, 2, 3]

[1] CNRS UMR5048, Centre de Biochimie Structurale, 29 rue de Navacelles, 34090 Montpellier, France

[2] INSERM U1054, Montpellier, France

[3] Universités Montpellier I et II, France

[4] Lehrstuhl für Molekulare Physikalische Chemie, Heinrich-Heine-Universität, Düsseldorf, Germany

[5] UMR 5203 CNRS, Institut de Génomique Fonctionnelle, Montpellier, France

[6] U661 INSERM, Montpellier, France

[7] Cisbio Bioassays, Codolet, France

* Correspondance to : Emmanuel Margeat, Centre de Biochimie Structurale, 29 rue de Navacelles 34090 Montpellier, France. Tél : +33 467.41.79.06. Fax : +33 467.41.79.13. E.mail : margeat@cbs.cnrs.fr or to Jean-Philippe Pin, Institut de Génomique Fonctionnelle, 141 rue de la Cardonille, 34094 Montpellier, France. Email : Jean-Philippe.Pin@igf.cnrs.fr

ABSTRACT

Efficient cell-to-cell communication relies on the accurate signaling of cell surface receptors. Understanding the molecular bases of their activation requires the characterization of the dynamic equilibrium between active and resting states. Here we monitored, using single molecule Förster resonance energy transfer, the kinetics of the reorientation of the extracellular ligand-binding domain of the metabotropic glutamate receptor (mGluR). We show that most of the receptors oscillate between a resting- and an active- state on a sub-millisecond timescale, while a small fraction remains locked in these states for longer periods, independently of ligand occupancy. Interestingly we demonstrate that differences in agonist efficacies stem from differing abilities to shift the conformational equilibrium toward the fully active state, rather than from the stabilization of alternative static conformations, which further highlights the dynamic nature of mGluRs and revises our understanding of receptor activation and allosteric modulation.

INTRODUCTION

Many cell-surface receptors are multimeric multidomain proteins and a better understanding of the underlying molecular mechanisms by which conformational changes regulate their activity is crucial for the development of new innovative drugs. X-ray crystallography, NMR, and other structural approaches have been proven useful to elucidate molecular structures of receptors in various states, but these techniques do not provide sufficient dynamic information on possible transitions between different states. It is therefore difficult to discriminate between the widely debated models that postulate that either (i) a receptor exists in an equilibrium of a few discrete states, independently of ligand structure and occupancy, and that these states might be differentially stabilized by ligands (conformational selection model), or that (ii) a conformational transition between static states only occurs after a ligand-induced change in shape of the protein (induced fit model)[1]. However, spectroscopic techniques performed at the single molecule level offer the possibility to distinguish between these models.

Metabotropic glutamate receptors (mGluR) are dimeric multidomain G-protein coupled receptors (GPCRs) (**Figure 1a**) whose activation mechanism depends on major conformational changes, modulated by the binding of ligands. Activated by glutamate, the major excitatory neurotransmitter in the central nervous system, they are essential in the regulation of synaptic activity[2], and represent promising targets in drug development[3]. The eight mGluR subtypes belong to the class C GPCR family, which also includes the receptors for GABA, calcium, and for the flavors sweet and umami [4,5]. These receptors are homo- or heterodimers[6], and share a large extra-cellular domain composed of a venus flytrap ligand binding domain (VFT), interconnected by a cysteine-rich domain (CRD) to a heptahelical transmembrane domain (7TM) activating G proteins (**Figure 1a**)[3,7–9]. Initial structural studies revealed that agonist binding in the orthosteric binding site of the VFT domain stabilizes an active (A) state, where the two VFTs have been reoriented by 70°, compared to the structure

obtained in the presence of antagonist (Resting (R) state) (**Figure 1b**) [10–12]. Yet, other crystal structures have, surprisingly, revealed that the VFT dimer can also adopt either a resting orientation with a bound agonist[9], or an active orientation in the presence of an antagonists, which raises a number of questions regarding the real activation mechanism of these receptors (**Figure 1b**).

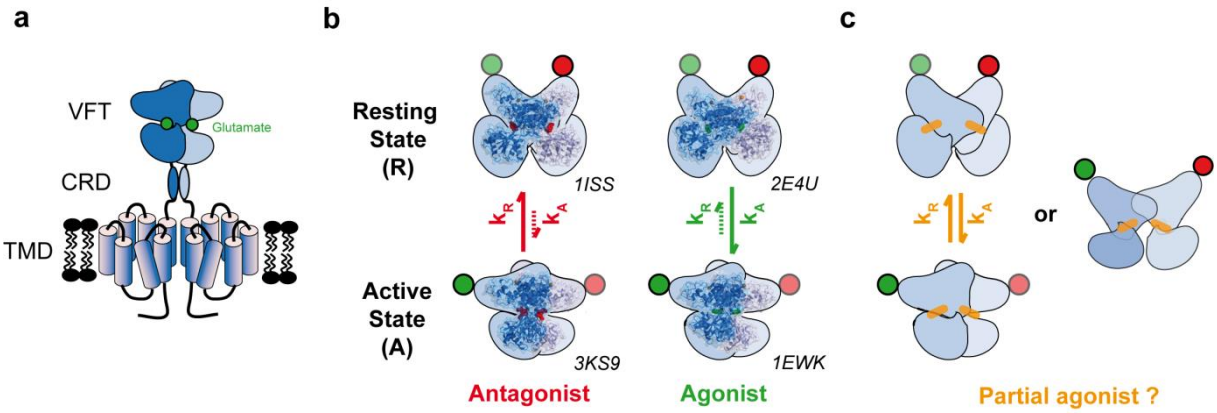

Figure 1. Schematic illustrations representing the full length metabotropic glutamate receptor and the VFT domain in the resting, the active, and the putative partially active state.
a - Cartoon representation of the full-length dimeric mGluR. Each subunit is composed of an extracellular bilobate Venus flytrap domain (VFT), forming an interlobe cleft shown to be the orthosteric binding site for ligands, and linked via a cysteine rich domain (CRD) to the transmembrane domain (TMD), responsible for transducing signals to the intracellular C-terminal domain.
b – Overlay of cartoon and molecular envelope representations of the VFT domain of mGluR, observed in the resting (R, top) and in the active (A, bottom) states. VFT domains of various mGluR have been crystallized in the resting state in the presence of antagonist (α-methyl-4-carboxyphenylglycine, PDB:1ISS), or in the active state in the presence of glutamate (PDB : 1EWK). Surprisingly, mGlu1R has also been crystallized in the active state in the presence of the antagonist LY341495 (PDB : 3KS9), and mGlu3R has been observed in the resting state despite the presence of glutamate (PDB : 2E4U). Conformational transitions between these states result in distance variations between the fluorescent labels (SNAP-tags at the N-terminus, green and red dots) [13]. We define k_A and k_R as the transition rate constants between these two states.
c– Schematic representation of the potential effect of a partial agonist that could either stabilize inefficiently the active state (left), or alternatively populate an intermediate conformation of the VFT dimer (right).

By labeling the N-terminus of each subunit with FRET compatible fluorophores attached to a SNAP-Tag[13], the R↔A conformational change has been validated in solution using a cell surface time-resolved luminescence resonance energy transfer (LRET or trFRET) assay. A decrease in the average LRET efficiency was observed in the presence of agonists, in agreement with a reorientation of the VFTs, while high affinity competitive antagonists

reversed this effect. This study also revealed that partial agonists lead to a partial change in LRET efficacy[13].

Altogether, these investigations established that the VFT dimer can adopt two main conformations, but failed to show how resting and active crystal structures have been observed with bound agonists and antagonists, respectively. Moreover, why do some agonists only generate partial receptor activation? This may well be explained by either the existence of a specific intermediate conformation, as observed for the AMPA receptor[14,15], or by a less efficient shift of the resting-to-active equilibrium with respect to the full agonists, as suggested for some NMDA receptor partial agonists[16] (**Figure 1c**).

In the present study, we addressed these issues by monitoring at the single molecule level the structural dynamics of the dimeric VFT of several mGluR subtypes. Using several advanced analysis procedures on single molecule FRET data, we show that a majority of receptor VFT dimers oscillate on a hundred microsecond timescale between two main conformations, attributed to the resting and the active state of the receptor, whether in their free form, or bound with agonists or antagonists. We show that the efficacy of these ligands does not result from a stabilization of specific conformations, but rather from the modulation of the equilibrium constant between the R and the A state. Additionally, a small fraction of VFT dimers appear locked in the R or the A state for periods exceeding several milliseconds. This mechanism seems to be conserved for all receptors subtypes, and therefore inspires for a new mGluR activation model.

RESULTS

Conformational changes linked to receptor activation are similar for isolated VFT dimers and full length mGlu receptors.

Prior to any single molecule analysis of isolated VFTs, we first verified that the conformational changes associated with the activation of isolated soluble VFT dimers were similar to those observed upon activation of the full length receptor, using a LRET based assay[13]. This assay reports on the distance between the SNAP-tagged N-termini using SNAP substrates carrying Lumi4®-Tb[17] and Green, and indicates on the R (high LRET efficacy) or A (low LRET efficacy) state of the VFT dimer[13]. We observed similar LRET changes following the activation of both full length mGlu2 receptors (**Figure 2a**), VFT dimers attached to the plasma membrane via a glycosyl phosphatidylinositol (GPI) anchor (mGlu2R-499GPI construct) (**Figure 2b**), or soluble VFT dimers obtained after cleavage of the GPI anchor with the phosphatidylinositol-specific phospholipase C (mGlu2 VFT, **Figure 2c**).

For all of these 3 constructs, glutamate triggered a significant decrease in LRET with similar potency, whereas the mGlu2R partial agonist (2S,2′R,3′R)-2-(2′,3′-Dicarboxycyclopropyl) glycine (DCG-IV) only triggered an intermediate LRET decrease (**Figure 2**). Interestingly, for all 3 constructs, the fit of the delayed emission decay of the acceptor' (whose emission is due only to energy transfer received from the long-lived donor) requires a triple exponential function, which might be an indication of the existence of several conformations[18,19]. Global fitting of these data finds a very short component (4µs, for a constant and negligible fraction of molecules, <5%), a short one (87µs), and a long one (810µs). The fraction of the short component (representing species with a high LRET efficiency) decreases similarly for all constructs upon addition of glutamate and, to a lesser extent, in the presence of DCG-IV (**Figure 2**, right axes). These data indicate that the receptor, whether in its full length or VFT form, is most certainly present in several conformations, with a relative abundance governed by the ligand. The data also validate the

use of soluble VFT dimers obtained after cleavage of GPI-anchored mGlu2 as a model to investigate the conformational dynamics of mGluR at the single molecule level.

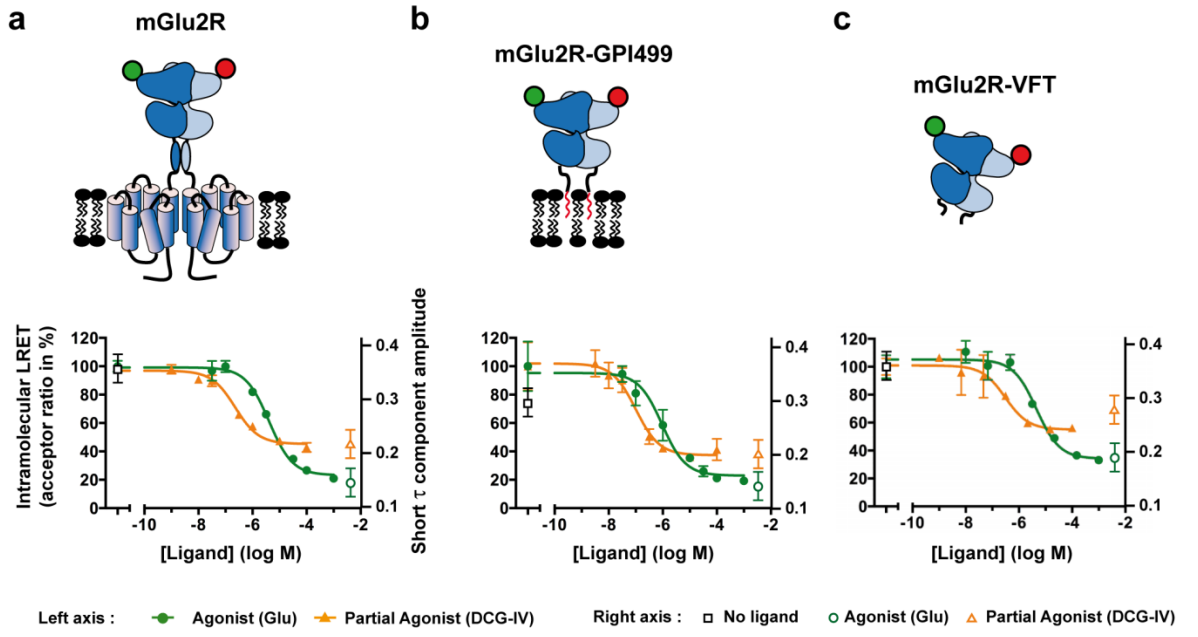

Figure 2. Ensemble LRET changes observed within the VFT dimer on SNAP-full length-mGlu2R expressing cells (a), GPI-VFT-mGlu2R expressing cells (b) or soluble VFT-mGlu2R after GPI cleavage (c) Receptors were labeled with the Lumi4-Tb donor and the Green fluorescent acceptor [13]. The LRET signal is represented on the left axis as the ratio of the acceptor-sensitized emissions (see Online Methods) and is normalized to the maximum signal. The right axis represents the fraction of the short component obtained by fitting the acceptor decay that represents the fraction of species with a high LRET efficiency. Binding of the full agonist glutamate leads to a decrease in LRET (●), and the fraction of the short lifetime component (○), as expected for a transition from the resting to the active state (**Figure 1b**). Binding of the partial agonist DCG-IV also decreases the LRET (▲) and the fraction of the short lifetime component (△) but to a lower extent, indicating a partial shift of the equilibrium toward the active state, or possibly a stabilization of a partially active intermediate state (see Text and **Figure 1c**). Binding constants are comparable for the cleaved VFT and the full length receptor (respectively 4.6µM and 4.1µM for glutamate and 0.31µM and 0.23µM for DCG-IV).

Single molecule analysis reveals a heterogeneous ensemble of mGlu2R VFT dimers

We thus characterized the behaviour of single mGlu2R-VFT dimers freely diffusing in solution, labelled with SNAP substrates carrying the organic fluorophores Cy3B (donor) and d2 (acceptor). We used single molecule FRET with pulsed interleaved excitation (PIE)[20,21] and multiparametric fluorescence detection (MFD) (**Figure 3a**)[22,23], a technique which provides for each single molecule: its apparent FRET efficiency (E_{PR}) calculated from the spectral information, its anisotropy (r) determined from the polarization of the photons, and

the average fluorescence lifetime of the donor dye in presence of the acceptor ($\tau_{D(A)}$). Thanks to the PIE scheme, the average excited lifetime of the acceptor dye (τ_A) is recovered as well, and only donor-acceptor (D-A) containing complexes are selected based on the stoichiometry factor S_{PR} (**Figure 3b)**[20,24].

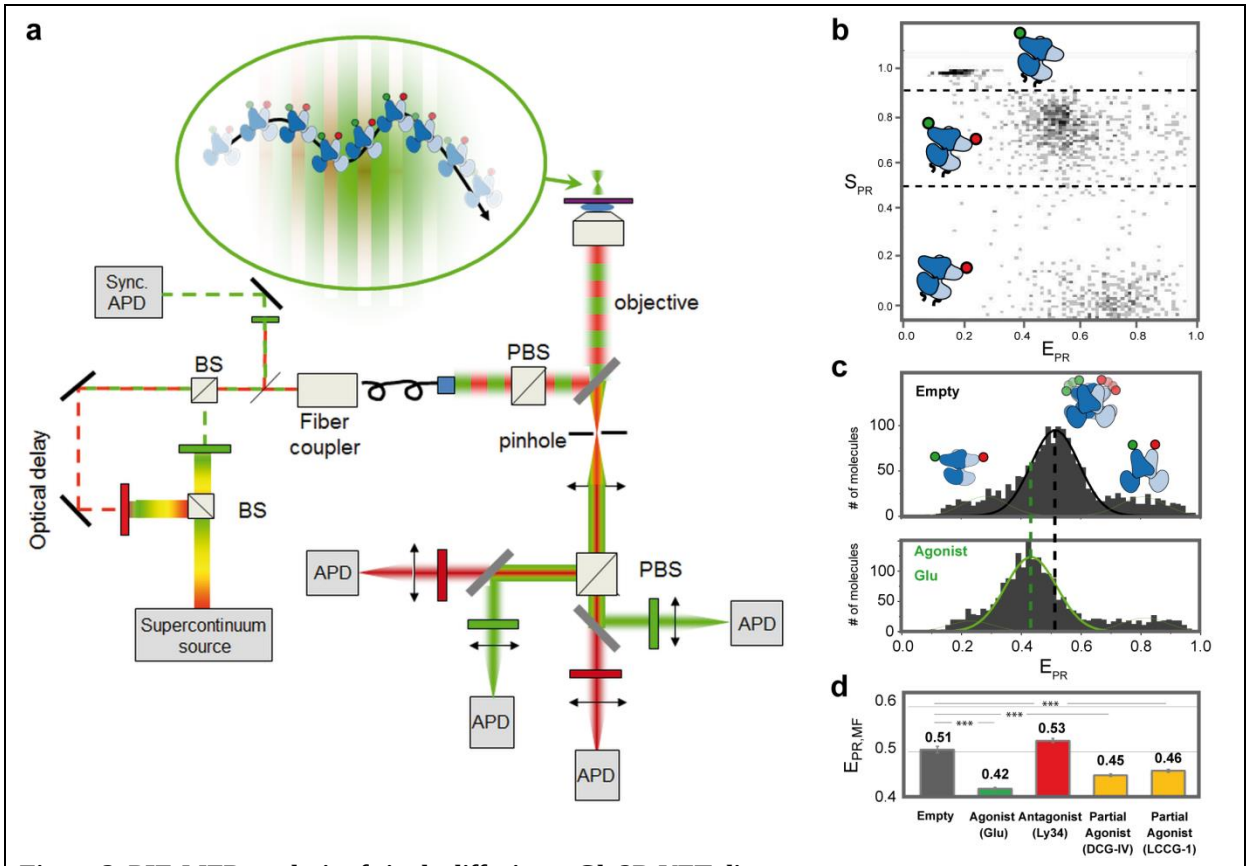

Figure 3. PIE-MFD analysis of single diffusing mGlu2R VFT dimers

a – Schematic illustration of the experimental setup (described in [20]). In brief, the output of a pulsed supercontinuum laser is divided into a prompt and a 8 meter long delayed line. Prior to entering the microscope, the beams are recombined and the pulses are interleaved, allowing for a multi-color alternating excitation scheme. For data acquisition, our confocal microscope is equipped with a 4-channel Single Photon Avalanche Diodes detection (APD), and a Single Photon Counting Module (SPCM) (BS : beamsplitter, PBS : polarizing BS)

b – 2D (E_{PR}-S_{PR}) histogram of detected single mGlu2R-VFT dimers in the absence of ligands. D-only and A-only labelled molecules appear with a S_{PR} value of ~1 and ~0 respectively, whilst the D-A complexes display an intermediate value (S_{PR} ~0.8). Only these D-A complexes are selected for further analysis.

c – The E_{PR} value distribution for the D-A mGlu2R-VFT complexes shows a main population centred around E_{PR}~0.51 in the absence of glutamate and two minor populations around E_{PR}~0.25 and E_{PR}~0.85 (top). In the presence of glutamate (bottom), the E_{PR} value of the main population is shifted toward a lower value (E_{PR}~0.42) (see text)

d – Histogram of the mean apparent E_{PR} values measured for the dynamic MF population, as a function of the pharmacological nature of the ligand. The E_{PR} value decreased for the agonist, marginally increased for the antagonist, and partially decreased for the partial agonists. Bars = s.e.m., N=10. (*** p<0.001)

The E_{PR} values observed for (D-A) containing complexes of mGlu2R-VFT show a wide distribution (**Figure 3c**), indicative of a co-existence of several conformational states, as inferred from the LRET data. In the absence of ligands, a main population is centred on E_{PR}~0.51 (hereafter designated as the Medium FRET population, MF), and two less well defined minor populations appear around E_{PR}~0.25 and E_{PR}~0.85 (hereafter referred to as the Low FRET, LF and the High FRET, HF populations respectively). The observation of these minor HF and LF populations does not arise from measurement noise as, for instance, they do not appear on a E_{PR} histogram obtained under similar conditions using a rigid, doubly labelled dsDNA construct (**Supp. Figure 1**). Moreover, the excited state lifetimes of the donor and the acceptor for these three observed populations match those expected theoretically for doubly labelled complexes engaged in energy transfer (**Supp. Figure 2**). In the presence of glutamate, the E_{PR} value of the MF population decreases significantly (E_{PR}~0.42, **Figure 3c,d**) as expected for a transition toward the A state of the receptor, while the antagonist Ly341495 (referred to as Ly34 from here onward) reversed this effect (E_{PR}~0.53, **Figure 3d**). Interestingly the E_{PR} values for the LF and the HF states do not appear significantly influenced by the presence of ligands, suggesting that these states remain identical on a macroscopic level.

mGlu2R VFT dimers oscillate between the resting and the active state on a sub-millisecond timescale.

In order to better define the conformational states from which these three apparent E_{PR} populations originate, we determined the excited-state lifetime of the donor dye for each for them. The decay representing the HF population can be described by a single exponential function ($\tau_{D(A),\ HF}$ = 0.5ns, **Figure 4a**), as can the decays of the LF complexes ($\tau_{D(A),\ LF}$ = 2.4ns, **Figure 4b**) and the donor only molecules (τ_D = 2.7ns, **Supp. Figure 3**). In constrast, the fit of the decay of the MF population requires a double exponential function, which

provides lifetimes identical to those recovered for the HF and LF state ($\tau_{D(A),\ MF1}$ = 0.5ns and $\tau_{D(A),\ MF2}$ = 2.4ns, **Figure 4c**). This indicates that the molecules that belong to this apparent MF population are not characterized by a fixed D-A distance (single $\tau_{D(A)}$ value), but probably oscillate between the HF and LF states, at a timescale faster than their diffusion in the observation volume (~ <4ms)[25].

The excited state lifetime measurement is a straightforward method to estimate the D-A distances for the LF and HF states. Assuming a Ro value of 54Å, we measured $R_{DA,LF,Lif}$ = 73 ± 4 Å and $R_{DA,HF,Lif}$ = 42 ± 2 Å respectively. To compare these values with what is theoretically expected for the active and the resting state, we simulated the fluorophores positions on a model of a SNAP-VFT dimer based on the crystal structures of mGlu1R. We found very broad distributions, differing significantly between the A and R conformations, in agreement with the LRET and smFRET measurements (**Supp. Figure 4)**. The difference in the mean theoretical inter-dye distance calculated between these two conformations (~10 Å) appears smaller than those measured experimentally (31 ± 6 Å), however, this theoretical mean value might be biased for the following reasons : first, the simulation was performed using the only receptor crystallized in the active and resting states (ie mGlu1R) while our measurement were carried out on mGlu2R ; second, the distribution of calculated distances is very wide (σ = 27-29 Å), which introduces a large uncertainty as to the real mean distance ; and third, the simulations rely only on excluded solvent volume, and it might be that the SNAP-tag adopts preferential orientations within the complex. Altogether we propose that the majority of mGluR VFT, belonging to the MF population, oscillate between two states representing conformations close to the A and R states observed by crystallography. In addition, at the timescale of our measurement (<4 ms), minor populations of the VFT-dimers appear blocked in a static LF active state (hereafter named A_S) or in a static HF resting state (named R_S).

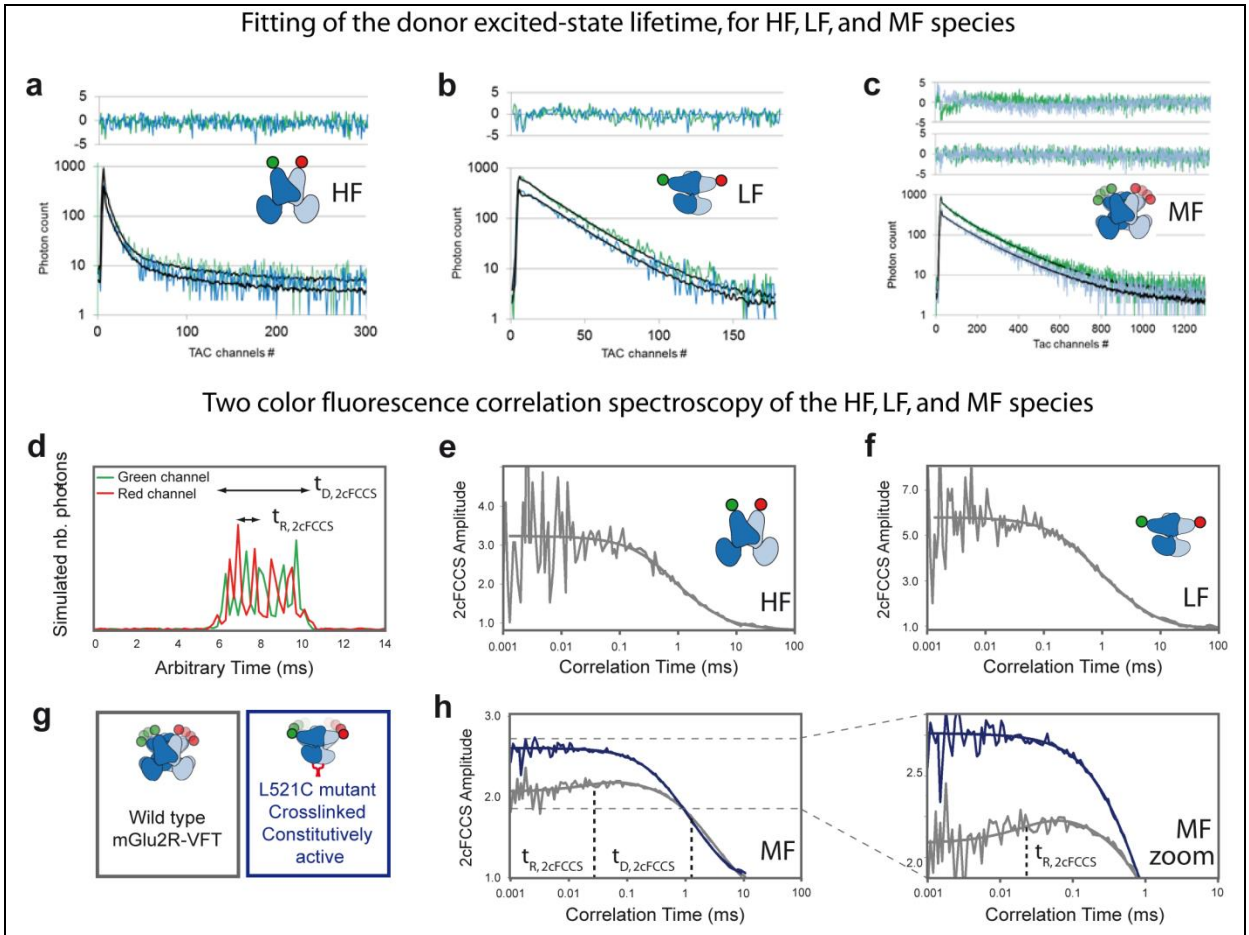

Figure 4. Excited-state lifetime and two color FCCS analysis of the HF, MF, and LF species. Effect of the L521C mutation

a, b – The excited-state lifetime of the donor dye is correctly fitted by a single exponential decay for the HF (**a**) and the LF (**b**) populations

c – The mono-exponential fit of the MF population (not shown) does not describe the data in a satisfying manner ($\chi 2 = 1.33$, see also weighed residuals above the decays curves, top), contrary to the bi-exponential fit (**c**) ($\chi 2 = 1.06$, see also weighed residuals above the decays curves, bottom). Moreover this unconstrained bi-exponential fit of the MF population provides the exact same excited states lifetimes ($\tau_1 = 0.5$ ns $\tau_2 = 2.4$ns) as the mono-exponential fits of the HF (**b**) and the LF (**c**) populations. This observation further highlights the dynamic character of the MF-population.

d – Principle of the two-color cross correlation spectroscopy (2cFCCS) analysis : when the molecule traverses the observation volume, the photons detected in the green and red emission channels are anticorrelated if the molecule undergo transitions between a high FRET and a lower FRET states at a timescale (t_R) faster than its diffusion (t_D). These two characteristic times will appear as negative and positive contributions respectively to a 2cFCCS curve.

e-h – 2cFCCS analysis. Anticorrelation between photons detected in the green and in the red channels is clearly observed for the MF population of the WT-VFT (**h**, grey) as expected for a LF↔HF transition, at the 50-100 µs timescale. This anticorrelation disappears for the L521C receptor (**g-h**, blue), indicating a reduction of its conformational dynamics as compared to the WT-VFT, and is not present for the staticHF (**e**) or LF (**f**) populations.

To confirm this hypothesis, we performed on these various subpopulations a two-color cross correlation spectroscopy analysis (2cFCCS)[26]. For a dynamic system undergoing FRET

changes at a faster-than-diffusion timescale, anti-cross-correlation, at short timescales, should theoretically be observed between photons detected in the green and in the red channels (see illustration on **Figure 4d**) although this effect is rarely observed experimentally. For the R_S and A_S subpopulations, this anticorrelation does not appear in the 2cFFCS curves (**Figure 4e-f**), while a slight but yet clearly visible anticorrelation effect is observed at short timescales for the MF species (**Figure 4h**). Similar curves were obtained for all investigated ligands (not shown), and were fitted with Eq 1 :

$$G_{diff}(t_c) = 1 + \frac{1}{N} \cdot \left(1 + \frac{t_c}{t_D}\right)^{-1} \cdot \left(1 + \left(\frac{\omega_0}{z_0}\right)^2 \cdot \frac{t_c}{t_D}\right)^{-\frac{1}{2}} \cdot \left(1 - A_{R,2cFCCS} \cdot e^{-\frac{t_c}{t_{R,2cFCCS}}}\right) \quad \text{(Eq.1)}$$

, where N is the average number of molecules in the observation volume, t_D is their diffusion time, ω_o and z_o are the $1/e^2$ radii of the laser focus volume perpendicular to and along the optical axis, respectively, $A_{R,2cFCCS}$ and $t_{R,2cFCCS}$ represent the amplitude and the relaxation time respectively of the dynamic transition observed in the case of the MF population. The exact $t_{R,2cFCCS}$ value could not be determined with high accuracy due to high noise levels in the 2cFCCS data, but it appeared to be in the ~100 µs range.

Our 2cFCCS data underline the dynamic nature of the MF population, which oscillates rapidly between two states. It is tempting to assign these two states to the HF (R) and the LF (A) state, based on the excited states lifetimes for the MF population. To verify this hypothesis, we employed filtered FCS (fFCS), a method used to separate the correlation functions of individual components of a mixture with different FRET-states[27] based on their differences in fluorescence lifetime, polarization, and spectral properties[28]. Three component fluorescence filters for fFCS were generated using decay patterns from scatter (buffer), and from HF and LF sub-populations selected from E_{PR} vs $\tau_{D(A)}$ 2D histograms. Generated filters were applied to the full photon stream to calculate the probability for each photon to belong to one of these three states (P(scatter), P(LF), P(HF), see **Figure 5a** for illustration).

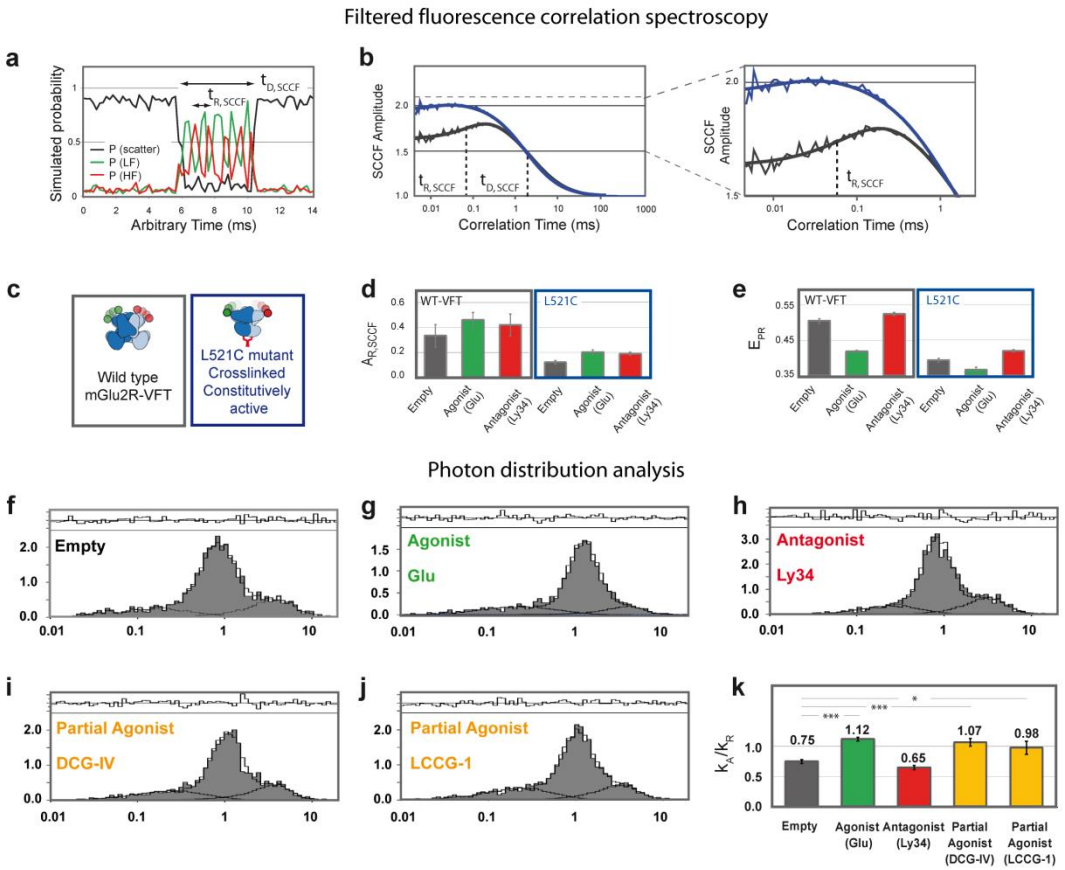

Figure 5. Filtered Fluorescence Correlation Spectroscopy (fFCS) and Photon Distribution Analysis (PDA) of the single molecule FRET data obtained with the wild type mGlu2R VFT. Effect of the L521C mutation

a – Principle of the filtered FCS (fFCS) analysis : a certain probability is assigned to each detected photon to belong to either the scattering signal (P(scatter)), to the low FRET state (P(LF)), or to the high FRET state (P(HF)). When a molecule is present in the observation volume (here at time 6 to 10ms), the probability of the photons to belong to the LF or the HF state are anticorrelated if the molecule undergoes transitions between these states, at a timescale (t_R) faster than its diffusion time through the focal volume (t_D). These two characteristic times will appear as negative and positive contributions respectively to a Species Cross Correlation Functions (SCCF) curve.

b – SCCF curves calculated using full photon streams for the WT-VFT (grey) and the constitutively active L521C (blue) receptor. SCCF curves were fitted applying a global model taking into account the molecular diffusion (positive cross correlation), and an anti-cross-correlation term representing the relaxation time $t_{R,SCCF}$ for the LF↔HF (and thus the A↔R) transition.

c,d - The amplitude of the anticorrelation term is strongly reduced for the L521C mutant (blue), indicating a reduction of its conformational dynamics as compared to the WT-VFT (grey)

e – Histogram of the mean apparent E_{PR} values measured for the dynamic species, as a function of the nature of the ligand, for the WT-VFT (grey, left) and the L521C mutant (blue, right). For all ligands, tested, the E_{PR} values for the L521C mutant are equal or lower than the ones observed for the WT-VFT activated by glutamate, in accordance with the constitutively active character of the L521C mutant.

f-j – PDA histograms (expressed as uncorrected S_G/S_R ratios) of single mGlu2R VFT dimers, in the presence of saturating concentrations of various ligands. Data were fitted (black lines) with a model that accounts for two static species (high FRET, S_G/S_R~0.2 and low FRET S_G/S_R~3), and dynamic species interconverting between these states (MF, S_G/S_R~0.8 to 1.2, depending on the ligand).

k – Histogram of the mean apparent k_A/k_R values calculated from the fit of the PDA histograms. Agonist binding leads to a strong increase of the k_A/k_R ratio compared to the empty receptor ($p<10^{-5}$), indicating that the equilibrium of the dynamic species shifts toward the Active (low FRET) state. Antagonist binding only marginally pushes the equilibrium in the opposite direction (Resting, high FRET state) ($p<0.07$). Interestingly, partial agonists push the equilibrium significantly toward the Active state, but with less efficiency than the full agonist glutamate ($p<10^{-3}$ for DCG-IV and $p<0.05$ for LCCG-1).

Species Cross Correlation Functions (SCCF) between HF and LF components display a positive cross-correlation diffusion term, indicating that a substantial fraction of molecules undergo LF↔HF transitions during their residence time in the observation volume. The clearly visible negative cross-correlation term at short timescales (~100µs) represents the relaxation time for the LF↔HF transition (**Figure 5**). SCCF curves were globally fitted applying Equation 1, where $A_{R,2cFCCS}$ and $t_{R,2cFCCS}$ are replaced by $A_{R,SCCF}$ and $t_{R,SCCF}$, that represent the amplitude and the relaxation time of the LF↔HF transition respectively. Similarly to the 2cFCCS measurements, the order of magnitude of these relaxation times is in the ~100µs range (for example $t_{R,SCCF}$ = 101 ± 29 µs for the empty receptor (see **Table**)). The amplitude of the $A_{R,SCCF}$ term, that reports on the fraction of molecules undergoing fast A↔R transition, is not significantly affected by the ligand (**Figure 5d** and **Table**).

Altogether, the data obtained using two independent correlation methods (fFCS and 2cFCCS) confirm that the molecules belonging to the MF population undergo fast (50-100 µs) transitions between the A and the R state. It should be noted that these fast relaxation events observed in the correlation analysis do not arise from fluorophore photophysics (blinking) for the following reasons. First, fluorophore blinking is not transferred into the fFCS function when it is independent of the kinetics under study[25] ; Second, 2cFCCS analysis on the isolated HF or LF populations does not show the anticorrelation behaviour (**Figure 4e-f**) ; Third, FCS analysis of the signal detected in the red channel for the MF population results in a positive correlation term at short timescales (~100µs) upon excitation of the donor, characteristic of FRET changes during HF↔LF transition, but not when the acceptor is directly excited (indicating that there is no acceptor blinking at these timescales) (**Supp. Figure 5**) ; And fourth, these anticorrelations are nearly suppressed in a constitutively active single point mutant (see below). Additionally, we verified that the various FRET distributions and FRET changes do not originate from artefacts due to our labelling strategy. We replaced

the SNAP-tag with the shorter Acyl Carrier Protein (ACP)-tag [29], and labelled with CoA-547 as the donor and CoA-647 as the acceptor. Similar E_{PR} distributions were obtained with this construct in the presence of the various ligands, even though the exact E_{PR} values differed due to a different geometry of the complex and spectroscopic properties (data not shown). Filtered FCS analysis on this construct also led to the characteristic negative cross-correlation term at short timescales (<100µs), representing the relaxation time for the LF↔HF transition (see **Supp. Figure 6**). Additionally, we labelled our SNAP-tag constructs with other couples of FRET pairs. For instance, Bg-Alexa488, Bg-Dy547, and Bg-TMR were used as donors and Bg-Cy5 and Bg-Dy649 were engaged as acceptors. Subsequent experiments led to similar results even though the exact E_{PR} values differed due to different spectroscopic properties (data not shown).

The A↔R equilibrium is biased toward the active state in a constitutively active receptor dimer.

We recently demonstrated that a specific crosslinking of the CRDs with an intersubunit disulfide bond (mGlu2R-L521C, **Figure 4g**) leads to a constitutively active receptor dimer[7]. The extracellular domain of this mutant shows an E_{PR} distribution qualitatively similar to the one observed for the glutamate-activated WT-VFT, indicating that the A↔R equilibrium is preferentially shifted toward the active form for the mutant. The apparent E_{PR} value of its dynamic MF peak is close to the value obtained with the fully activated WT-VFT construct (E_{PR}=0.393 ± 0.006 vs. E_{PR}=0.418 ± 0.003 respectively), while the antagonist (Ly34) or the agonist glutamate only marginally altered this E_{PR} value (**Figure 5e, Table**).

Correlation analyses also clearly show a reduction of the amplitude of the LF↔HF transition term for the mutant with respect to the WT-VFT, both in the filtered FCS analysis (**Figure 5b**, compare blue and grey curves respectively, and **Figure 5e**, compare the $A_{R,SCCF}$

values), and the 2cFCCS measurements (**Figure 4h**, compare blue and grey curves). Altogether, the E_{PR} values as well as the correlation curves clearly point toward a reduction of the conformational dynamics of the mGlu2R VFT, and a shift of the A↔R equilibrium toward the active state, as expected for this constitutively active receptor.

The binding of ligands influences the transition rates between the resting and the active state of the mGlu2R VFT dimer

In order to estimate the rates constants of the fast HF ↔ LF transition, we used Photon Distribution Analysis (PDA), a method that quantitatively and precisely describes the FRET signal distribution [30,31]. PDA has already been successfully implemented to discriminate between multiple species coexisting in solution and to highlight dynamic behavior of single molecules [31–33].

Figure 4f-j represents the signal intensity ratio distribution from the green and red detection channels (S_G and S_R respectively) for the mGlu2R-VFT dimers. The three populations appear at low, medium and high S_G/S_R ratios (for HF, MF, and LF respectively). By applying a simple PDA two-state dynamic model, taking into account two minor populations (HF and LF), presumably static at the measurement timescale (~4 ms), and a major MF population composed of molecules undergoing sub-millisecond interconversions between these two boundary states, the experimental distribution was accurately described (**Figures 4f-j** and **Supp. Figure 7**, black line). The choice of this dynamic PDA model (see **Supp. Figure 7**) is fully supported by the correlation analyses and the observation that fitting of the excited state lifetime of the donor in the MF population requires a double exponential function (**Figures 4 and 5**). In addition to the apparent FRET efficiency (E_{PR}) for these states, the PDA model also provides the fraction of molecules (A) for the LF, HF and apparent MF populations, and k_{LF} and k_{HF}, the rates constants of the transitions toward the LF and HF

states, respectively. The D-A distances measured by PDA for the LF and HF populations match those measured by analysing the excited-state lifetime of the donor. For the LF species, the agreement is perfect ($R_{DA,LF,PDA}$ = 76 ± 13 Å vs. $R_{DA,LF,Lif}$ = 73 ± 4 Å), while for the HF species, a slight difference is observed ($R_{DA,HF,PDA}$ = 31 ± 6 Å vs. $R_{DA,HF,Lif}$ = 42 ± 2 Å), possibly due to an overestimation of the donor lifetime at very high FRET efficiencies as a result of the small number of emitted photons.

The shift in equilibrium between R and A states for the MF population, which can be quantified by calculating the k_A/k_R ratio or the apparent E_{PR} value, is strongly influenced by the binding of ligands (**Figure 3d and 5k**, **Table)**. A saturating concentration of glutamate shifts the R↔A equilibrium toward the A state with respect to the empty receptor, as shown by an increase of the k_A/k_R ratio (from 0.75 ± 0.03 to 1.12 ± 0.03). The E_{PR} value of the MF population consistently decreased (E_{PR} = 0.505 ± 0.007 to E_{PR} = 0.418 ± 0.003), as observed in ensemble LRET analyses (**Figure 2c** and [13]). On the other hand, binding of the antagonist Ly34 did not lead to any significant changes, although a slight increase in the apparent E_{PR} of the dynamic MF population (E_{PR}=0.505 ± 0.007 to E_{PR}=0.525 ± 0.005), and a modest decrease of the k_A/k_R ratio (from 0.75 ± 0.03 to 0.65 ± 0.03) were observed. Interestingly, it appears that agonists potencies correlate with their ability to push the R↔A equilibrium toward the A state. Indeed, for the partial agonists DCG-IV and (2S,1′S,2′S)-2-(Carboxycyclopropyl)glycine (LCCG-1), the apparent E_{PR} value of the dynamic MF population decreased, and the k_A/k_R ratio increased, as with glutamate, but to a lesser extent (**Figures 3d**, **5k** and **Table**). This find highlights the partial character of these ligands, which seem to less efficiently shift the conformation equilibrium toward the A state, in comparison with the full agonist. It is not consistent with a model where the partial agonist stabilises an alternative conformation, different from the fully active one populated in the presence of a full agonist.

Submillisecond conformational dynamics of VFT dimers is conserved for all mGluR types.

Based on their sequence conservation and pharmacological properties, the eight mGluRs can be divided into three groups[2]: Group I is represented by mGlu1R and mGlu5R; group II comprises mGlu2R and mGlu3R; and all the other members belong to group III. mGluRs of the same group show about 70% sequence identity, whereas between groups this percentage decreases to about 45%. We found that the conformational dynamics linked to mGluR VFT dimer activation described here for mGlu2R is conserved for mGlu4R and mGlu5R, representing other receptors subtypes. E_{PR} distributions obtained with these receptors matched those obtained with mGlu2R, although the exact E_{PR} values differed, due to different structures of the complexes. Glutamate binding resulted in a decrease in the apparent E_{PR} value of the MF population (**Figure 6a**), and an increase of the k_A/k_R ratio (**Figure 6b**), and this effect is reversed by antagonist binding. Additionally, binding of the mGlu4R weak partial agonist γ-carboxy-L-glutamate (Gla)[34] leads to a slight decrease of the apparent E_{PR} value, whilst the increase of the k_A/k_R ratio is too weak to be considered significant. Finally, fFCS analyses also point to a fast (<1 ms) switching for both types of receptor dimers between the A and the R states (**Figure 6c**), as observed for mGlu2R.

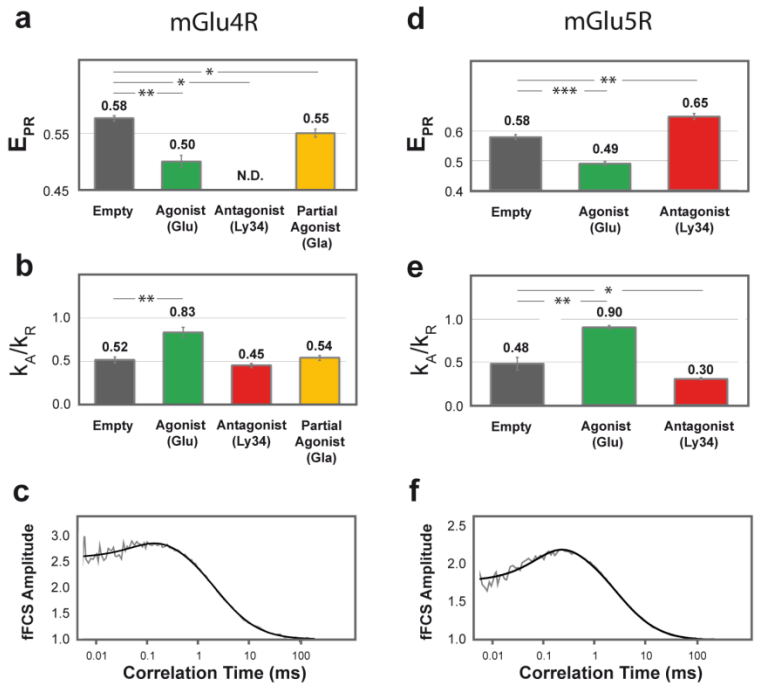

Figure 6 : MFD, PDA, and fFCS analyses of single diffusing mGlu4R (left) and mGlu5R (right) VFT dimers

a, d– Histogram of the mean apparent E_{PR} values measured for the dynamic MF species, as a function of the nature of the ligand, mGlu4R (a) and mGlu5R (d). For both receptors the E_{PR} values decrease upon agonist or partial agonist binding, and increase upon antagonist binding, although the exact E_{PR} value for mGlu4R in the presence of antagonist was too high to be determined (see text)

b, e – Accordingly, k_A/k_R values increase upon agonist binding, and decrease upon antagonist binding, reflecting the shift of the A↔R equilibrium induced by the ligands.

c, f– SCCF analysis shows a negative cross-correlation as sub milliseconds timescales term representing the LF↔HF (and thus the A↔R) transition. The order of magnitude of these relaxation times is similar to those found for mGlu2R.

DISCUSSION

Over the years, several models have emerged to account for the molecular mechanisms that govern receptor activation. In particular, two conflicting theories postulating either a conformational selection or an induced fit mechanism have drawn much attention and been widely debated. In addition, the molecular basis of the partial agonism observed for certain ligands remain obscure. Here, we presented a single-molecule FRET study revealing the characteristics of the structural dynamics, on a microsecond time-scale, of the ligand-binding domain of different mGluRs, all belonging to distinct sub-groups. The conclusions of this investigation motivated us to propose a new model for mGluR activation (**Figure 7**).

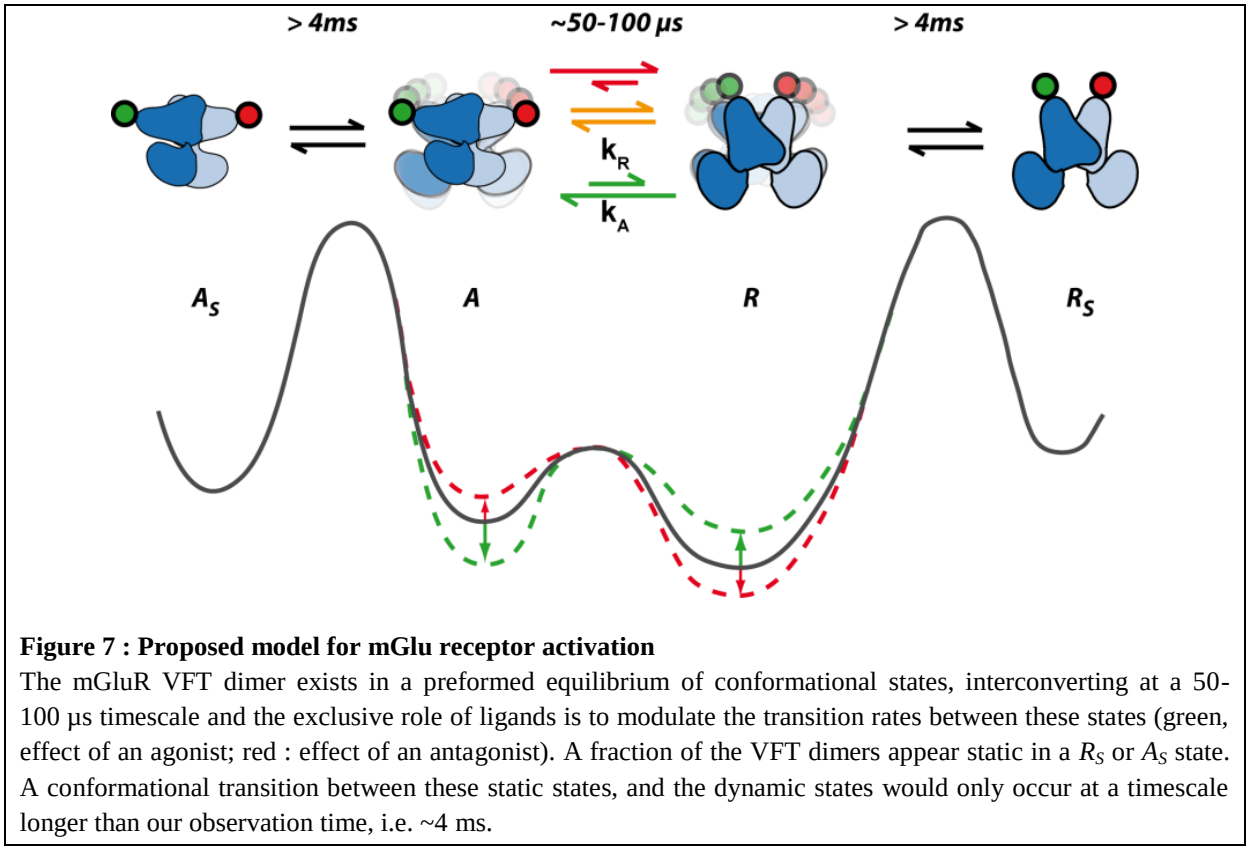

Figure 7 : Proposed model for mGlu receptor activation
The mGluR VFT dimer exists in a preformed equilibrium of conformational states, interconverting at a 50-100 µs timescale and the exclusive role of ligands is to modulate the transition rates between these states (green, effect of an agonist; red : effect of an antagonist). A fraction of the VFT dimers appear static in a R_S or A_S state. A conformational transition between these static states, and the dynamic states would only occur at a timescale longer than our observation time, i.e. ~4 ms.

Our data show that the mGluR VFT dimer is in a constant dynamic exchange between at least two states. Similar distances were obtained through the exponential fit of the excited state lifetime of the donor dye and from the PDA analysis.

Altogether, we propose that the LF and the HF state correspond to conformations where the receptor is preferentially either active or resting. The vast majority of molecules display an apparent intermediate (MF) E_{PR} value which is influenced by the pharmacological nature of the ligand. By means of several independent yet complementary methods, we show that this population does not correspond to a static state defined by an alternative conformation, essentially because (i) the exited state fluorescence lifetime of the donor dyes in the presence of an acceptor attributed to this MF population cannot be accurately fitted using a single exponential decay model, contrary to the HF, LF and the donor-only population (**Figure 4 a-c and supp Figure 3**). Moreover, a bi-exponential decay model applied to the MF population confirms the existence of two lifetimes that correspond exactly to those

measured for the HF (0.5ns) and the LF (2.4ns) populations. ; (ii) The E_{PR} distribution is better described by a PDA model considering two interconverting states than a model of three static states (both models incorporating Gaussian distributed distances) (**Supp. Figure 7**). ; (iii) 2cFCCS analyses of this MF population show a clear anticorrelation between the photons detected in the green and in the red channel (**Figure 4**); (iv) fFCS analyses demonstrate that the molecules undergo transitions between the LF and the HF state while diffusing across the observation volume (**Figure 5a,d**).

Our experimental results point to a model where a majority of receptors undergo conformational transitions between a resting (R) and an active (A) state on a ~100 µs timescale (**Figure 7**). The ligands influence the transition rates between these states, increasing thus the probability of the receptor to reside in one of them, although these effects are very subtle (see k_A/k_R analysis, **Figure 5k**). Additionally, the fact that some molecules appear static at high or low E_{PR} values implies that these molecules reside in a stabilized resting (R_S) or Active (A_S) state for a period of time exceeding the residence time in the observation volume, i.e. >4 ms (**Figure 7**). It cannot be excluded that these molecules are in reality in slow exchange with the population of dimers engaged in the fast A↔R exchange, even though this could not be examined in our study. To this aim, single receptor dimers would have to be immobilized and observed for an extended period of time, with the risk of having the immobilization method altering the conformational dynamics. Altogether, our data refute a simple static activation model, where the binding of a ligand triggers a conformational change of the receptor toward a static state. Our data also explain how a mGluR could be crystallized in an "active" conformation despite antagonist binding (PDB 3KS9, Structural Genomics Consortium, unpublished) or in a "resting" conformation in the presence of an agonist[9]. In fact, since these two states are exchanging at a fast rate and are energetically close even in the presence of ligands (**Figure 7**), crystallization of a receptor

dimer in any of these two states could easily be envisioned. This type of mechanism, characterized by the exploration of a conformational space, and where the ligand influences the probability of entering a given state has also been observed on the isolated monomeric glutamate binding domain of the GluA2 subunit of the AMPA receptor[35].

Our smFRET data are in very good agreement with the ensemble *in cellulo* LRET data regarding the general activation mechanism (**Figure 2**). Interestingly, the existence of several populations has been inferred from the LRET data, as an accurate fit of the delayed emission decay of the acceptor requires a triexponential function, which clearly favors the existence of at least three populations in cellulo (**Figure 2**). We cannot exclude that the presence of the trans-membrane domain in the full-length receptor influences the kinetics of the A↔R equilibrium. However, recent experiments[36] suggest that the dimeric VFT domain is the dominant element when it comes to regulating the conformational changes that occur within the 7TM domain and which lead to G-protein activation. Indeed, we showed that on a an isolated 7TM domain of mGlu2R and on a full length monomeric mGlu2R construct reconstituted in lipids nanodiscs, positive and negative allosteric modulators acted as full agonists and antagonists, while glutamate alone had no effect[36]. The activation of the G-protein by glutamate was recovered upon using of the full length dimeric receptor, underlying the key role of the VFT, as a dimer, in the activation process[36].

The proposed activation model also highlights the molecular mechanism of partial receptor activation by some ligands. *In vivo,* DCG-IV has a partial effect on mGlu2R estimated to be roughly 80% of that of glutamate, while that of LCCG-1 is slightly lower, about 70% [13]. Interestingly, the tendency of LCCG-1 to show a slightly lower effect than DCG-IV was detected in our smFRET experiments, highlighting the correlation between the k_A/k_R ratio of the various agonists determined by PDA and their potency for receptor activation. This effect is also observed for γ-carboxy-L-glutamate (Gla), a weak activator of

mGlu4R [34], whose effect on the k_A/k_R ratio is correspondingly very limited (**Figure 6b**). Our model proposes that partial agonists are able to push the A ↔ R equilibrium toward the fully activated state, but to a lesser extent than glutamate (**Figure 4b**). This finding is consistent with disulfide trapping experiment on the related GluA2 subunit of the AMPA receptor, for which a fully closed form of the LBD can be obtained in the presence of partial agonists [37]. It also explain the identical conformations observed by X-ray crystallography for mGlu3R both in the presence of glutamate and DCG-IV[9] even though the latter has been shown to behave like a partial agonist on mGlu3R in LRET experiments[13].

In summary, we clearly demonstrate that the receptor extracellular domain exists in a preformed equilibrium of conformational states and that the exclusive role of ligands is to modulate the transition rate between states rather than stabilizing individual conformations at the expense of others. Furthermore, these results were confirmed for receptors belonging to all three groups of receptors, and inspire for a new model describing the activation mechanism as a stochastic process where the probability of activation is intrinsically linked to the frequency of the conformational changes toward the activated state.

ONLINE METHODS

Materials

Glutamate was purchased from Sigma-Aldrich. LY341495 was acquired from Abcam Biochemicals (Cambridge, UK) and DCG-IV and L-CCG-1, from Tocris Bioscience (Bristol,UK). Lipofectamine 2000 was bought from Life Technologies (USA). CoA-547 and CoA-647 were purchased from NewEngland BioLabs. SNAP-Lumi4-Tb and SNAP-Green were obtained from Cisbio Bioassays.

Benzylguanine-Cy3B and Benzylguanine-d2

Benzylguanine-d2[38] was prepared according to the literature by Cisbio bioassays. Benzylguanine-cy3B was synthesized by adding aminomethylbenzamide-benzyl guanine (1 µmol) dissolved in anhydrous dimethylsulfoxide (100 µL) to *N*,*N*-diisopropylethylamine (1 µL – 5.7 µmol) and a solution of Cy3B-NHS (GE Healthcare Life Sciences, 1 µmol) in anhydrous dimethylsulfoxide (270 µL). The mixture was stirred at room temperature for 1 h. Purification was performed by preparative HPLC to give the desired conjugate evaluated by OD (355 nmol, 35%). HMRS (ESI^+) Calcd for $C_{52}H_{53}N_9O_7S$ $[M+H]^{2+}$: *m/z* 473.6891, found 473.6888.

Transfection, purification and labeling

pcDNA3 plasmids encoding the Flag-SNAP-tagged human mGlu2R-499GPI and human mGlu2R-561GPI were provided by Cisbio Bioassays (Codolet, France). The single point mutations generating the mGlu2R,L521C-561GPI constructs were generated using the QuikChange mutagenesis protocol (Agilent Technologies). HEK-293 cells were cultured in DMEM (Life Technologies) supplemented with 10% fetal calf serum (Lonza,Basel, Switzerland). HEK-293 cells were transfected by the reverse Lipofectamine 2000 protocol in 24 wells petri-dishes (Becton-Dickinson, USA) for 48h prior to incubation at 37°C for 1h with a solution containing 1µM Benzyl-Guanine-d2 and 10nM Benzyl-Guanine-Cy3B, and washed three times with filtered TK buffer, pH 7.4. (TrisHCl pH7.4, 20mM, NaCl 125mM,

KH_2PO_4 1,2mM, $MgSO_4$ 1.2mM, KCl 4.5mM, $CaCl_2$ 2mM) The GPI-anchor was cleaved by adding 0.25U/ml Bacillus cereus Phosphatidylinositol-specific Phospholipase C (Invitrogen P8804) and incubated for 45min at 37°C. The supernatant was desalted using ZebaTM desalt spin columns (Fisher Scientific) and stored at -20°C supplemented with 50% glycerol and 0.1mg/ml BSA. Occasionally, an anti-flag purification preceded desalting, in which case an ANTI-FLAG® M1 Agarose Affinity Gel was used (Sigma-Aldrich) following the provided standard protocol. For LRET measurements, cells were transfected and labeled as described in [13].

LRET experiments

The LRET measurements were performed in Greiner black 96-well plates on a PHERAstar FS microplate reader with the following setup: after excitation with a laser at 337 nm (40 flashes per well), the fluorescence was collected at 520 nm for a 50-µs reading after a 50-µs delay after excitation (window 1) or for a 400-µs reading after a 1,200-µs delay (window 2). The acceptor ratio was determined by dividing the signal measured in window 1 by the signal measured in window 2 and then was plotted on logarithmic scale. The intensity level of window 2 was above noise level by at least a factor of 5 to avoid erroneous divisions. We chose this representation because, in the range of acceptor ratio measured, the log of the ratio is correlated linearly with the distance between Lumi4Tb and Green. The delayed emission decays of the acceptor were fitted using the GLOBALS software (LFD, Irvine, CA) using a triple exponential decay function. The value of the excited state lifetimes were linked and fitted globally, while the amplitude of the various preexponential factors were allowed to vary freely. Molecular fractions presented in Figure 2 were calculated from the preexponential factors and the excited state lifetimes values as described in Heyduk & Heyduk[19].

Multiparameter Fluorescence Detection Setup and FRET-measurements

Single molecule FRET measurements were performed on our home-built confocal PIE-MFD microscope as described in Olofsson et al.[23], in 384-well plates with glass bottom (Sensoplate, Greiner Bio One) at a concentration of approximately 20-50 pM. All samples were prepared in filtered TK buffer, pH 7.4 and ligands were added at saturating concentrations. 40-60 million photons, corresponding to an acquisition time of roughly 2.5h, were collected per experiment and further analyzed with the Software Package for Multiparameter Fluorescence Spectroscopy, Full Correlation and Multiparameter Fluorescence Imaging developed in C.A.M. Seidel lab (http://www.mpc.uni-duesseldorf.de/seidel/). A single-molecule event was defined as a burst containing at least 40 photons with a maximum allowed interphoton time of 0.3 µs and a Lee-filter of 20. Molecules were selected for further analysis only if the following criteria were fulfilled: 0.6<Stoichiometry for the removal of acceptor only labeled molecules,1.5 ns<τ_A<2.5 ns for the removal of donor only labeled molecules and $|T_{GX}-T_{RR}|$<0.75 ms to eliminate photobleaching events as described in [22]. The VFT dimer was further purified using the Flag-tag inserted in N-terminus of the construct, and single molecule FRET results on this purified fraction were similar to those obtained on the supernatant, highlighting the excellent specificity of the Snap-tag labeling procedure (data not shown). Thus, for the remaining part of the study, measurements were conducted directly following PI-PLC cleavage without any further purification steps.

PDA analysis

In order to further resolve and quantify heterogeneities within the measured FRET distributions, PDA was employed (Fig. 4). For this analysis each burst is divided into time windows (t.w.) and then for each t.w. the fluorescence parameters are calculated. PDA is a powerful technique that allows for the determination of the minimum width of a FRET distribution arising from a single interdye distance. This minimum width is determined by the photon shot noise which arises from the fact that the number of photons detected per single

molecule burst is relatively small (typically a few hundreds photons). PDA has already been successfully implemented to discriminate between multiple species coexisting in solution and to highlight dynamic behavior of single molecules just by applying the model of static states to histograms of different t.w.'s. In fact, the static state model fails to fit the distribution histograms of larger t.w.'s due to more frequent transitions within dynamic systems.

A first attempt to fit the experimental S_G/S_R distribution histograms of the same data set for t.w.=2, 3, and 4 ms, with the model of three static populations of different FRET efficiencies (or distances) did not provide a satisfying result. Consequently we conclude that the molecules are dynamic on a time scale below 4 ms.

Then a model that accounts for two static species (high FRET (Resting) state, S_G/S_R~0.2 and low FRET (Active) state S_G/S_R~3), and dynamic species interconverting between these states (S_G/S_R~0.8 to 1.2, depending on the ligand) was applied, and allowed for an accurate description of the experimental S_G/S_R distribution.

In order to determine the reproducibility of the data, measurements were performed 10 times. The FRET derived mean distances and the standard deviations for the Resting and Active states are 28.4±0.8 Å, 56.1±0.8 Å, respectively. By, applying rigorous experimental calibration procedures, the average distances and errors obtained from different high precision-FRET measurements have only minimal variations and hence a high degree of statistical confidence in the discrimination between the states. It should be pointed out that the half-width fraction in dynamic model is by factor ~2 larger compare to static one. Therefore, even if the considered model overall relatively well describes the data histograms, the slower than 4 ms exchange within the populations of resting (R) and an active (A) states are possible, which we cannot identify in our experiments.

FCS, fFCS analysis

Table : Parameters extracted from the fit of the smFRET data obtained for mGlu2R (* see main text)

Receptor	WT-VFT	WT-VFT	WT-VFT	WT-VFT	WT-VFT	L521C	L521C	L521C
Ligand type	-	Agonist	Antagonist	Partial ago	Partial ago	-	Agonist	Antagonist
Ligand name	-	Glu	Ly34	DCG-IV	LCCG-1	-	Glu	Ly34
E_{PR} (x100)	50.5 ± 0.7	41.8 ± 0.3	52.5 ± 0.5	44.8 ± 0.3	45.8 ± 0.3	39.3 ± 0.6	36.7 ± 0.6	42 ± 0.3
k_A/k_R (PDA)	0.75 ± 0.03	1.12 ± 0.03	0.65 ± 0.03	1.07 ± 0.07	0.98 ± 0.11	ND*	ND*	ND*
$t_{R,PDA}$ (µs)	65 ± 10	61 ± 7	59 ± 8	100 ± 12	101 ± 18	ND*	ND*	ND*
$A_{R,SCCF}$	0.33 ± 0.09	0.46 ± 0.06	0.42 ± 0.09	0.31 ± 0.02	0.23 ± 0.04	0.12 ±0.02	0.20 ± 0.02	0.19 ± 0.01
$t_{R,SCCF}$ (µs)	101 ± 29	169 ± 38	128 ± 20	165 ± 19	70 ± 16	104 ± 37	188 ± 63	117 ± 40

Statistical analysis

Statistical analyses were performed on at least 6-10 individual data sets and the means ± s.e.m are shown as histograms. *represents p-value<0.05, **represents p-value<0.01 and ***represents p-value<0.001

AUTHORS CONTRIBUTIONS

LO, ED, JPP, PR, EM designed research ; LO, ED, PS, LF, JMZ provided reagents ; ED, PS, LF performed LRET experiments ; LO purified and labelled the proteins and acquired single molecule data ; LO and EM built the single molecule setup ; LO, SF, CS, EM analyzed and interpreted single molecule data; LO and EM wrote the manuscript with the help of all authors.

ACKNOWLEDGMENTS

We wish to thank: Driss El Moustaine (IGF) for his help in the initial phases of this project, , Thomas Peulen (U. Dusseldorf) for AV simulations of the SNAP-mGluR, Emmanuel Bourrier (Cisbio Bioassays) for the synthesis of Bg-Cy3B, and Eric Trinquet (Cisbio Bioassays), Alessandro Valeri, Catherine Royer, Soraya Ait-Bara and Gilles Labesse (CBS) for discussions.

This work was supported by *French National Research Agency (ANR)* grants to PR, EM and JPP (ANR-09-BIOT-018 and ANR-13-BSV5-0007), a "Chercheur d'Avenir" grant from the *Region Languedoc Roussillon* to EM, a doctoral grant from the *Ministère de la Recherche* to LO, and grants from the *Fondation pour la Recherche Médicale* and the *Fondation Bettencourt-Schueller* to JPP. We acknowledge France-BioImaging infrastructure supported by the *French National Research Agency* (ANR-10-INSB-04-01, « Investments for the future »), the GIS *« IBiSA : Infrastructures en Biologie Sante et Agronomie »*, and the *ARPEGE* platform.

REFERENCES

1. Changeux, J.-P. Allostery and the Monod-Wyman-Changeux model after 50 years. *Annu. Rev. Biophys.* **41,** 103–33 (2012).

2. Conn, P. J. & Pin, J. P. Pharmacology and functions of metabotropic glutamate receptors. *Annu. Rev. Pharmacol. Toxicol.* **37,** 205–37 (1997).

3. Niswender, C. M. & Conn, P. J. Metabotropic glutamate receptors: physiology, pharmacology, and disease. *Annu. Rev. Pharmacol. Toxicol.* **50,** 295–322 (2010).

4. Bräuner-Osborne, H., Wellendorph, P. & Jensen, A. a. Structure, pharmacology and therapeutic prospects of family C G-protein coupled receptors. *Curr. Drug Targets* **8,** 169–84 (2007).

5. Kniazeff, J., Prézeau, L., Rondard, P., Pin, J.-P. & Goudet, C. Dimers and beyond: The functional puzzles of class C GPCRs. *Pharmacol. Ther.* **130,** 9–25 (2011).

6. Doumazane, E. *et al.* A new approach to analyze cell surface protein complexes reveals specific heterodimeric metabotropic glutamate receptors. *Faseb J* **25,** 66–77 (2011).

7. Huang, S. *et al.* Interdomain movements in metabotropic glutamate receptor activation. *Proc Natl Acad Sci U S A* **108,** 15480–15485 (2011).

8. Rondard, P., Goudet, C., Kniazeff, J., Pin, J. P. & Prézeau, L. The complexity of their activation mechanism opens new possibilities for the modulation of mGlu and GABAB class C G protein-coupled receptors. *Neuropharmacology* **60,** 82–92 (2011).

9. Muto, T., Tsuchiya, D., Morikawa, K. & Jingami, H. Structures of the extracellular regions of the group II/III metabotropic glutamate receptors. *Proc. Natl. Acad. Sci. U. S. A.* **104,** 3759–64 (2007).

10. Kunishima, N. *et al.* Structural basis of glutamate recognition by a dimeric metabotropic glutamate receptor. *Nature* **407,** 971–977 (2000).

11. Tsuchiya, D., Kunishima, N., Kamiya, N., Jingami, H. & Morikawa, K. Structural views of the ligand-binding cores of a metabotropic glutamate receptor complexed with an antagonist and both glutamate and Gd3+. *Proc. Natl. Acad. Sci. U. S. A.* **99,** 2660–5 (2002).

12. Kniazeff, J. *et al.* Closed state of both binding domains of homodimeric mGlu receptors is required for full activity. *Nat. Struct. Mol. Biol.* **11,** 706–13 (2004).

13. Doumazane, E. *et al.* Illuminating the activation mechanisms and allosteric properties of metabotropic glutamate receptors. *Proc. Natl. Acad. Sci. U. S. A.* **110,** E1416–25 (2013).

14. Jin, R., Banke, T. G., Mayer, M. L., Traynelis, S. F. & Gouaux, E. Structural basis for partial agonist action at ionotropic glutamate receptors. *Nat. Neurosci.* **6,** 803–10 (2003).

15. Armstrong, N. & Gouaux, E. Mechanisms for activation and antagonism of an AMPA-sensitive glutamate receptor: crystal structures of the GluR2 ligand binding core. *Neuron* **28,** 165–81 (2000).

16. Inanobe, A., Furukawa, H. & Gouaux, E. Mechanism of partial agonist action at the NR1 subunit of NMDA receptors. *Neuron* **47,** 71–84 (2005).

17. Zwier, J. M., Bazin, H., Lamarque, L. & Mathis, G. Luminescent lanthanide cryptates: from the bench to the bedside. *Inorg. Chem.* **53,** 1854–66 (2014).

18. Selvin, P. R. Principles and biophysical applications of lanthanide-based probes. *Annu. Rev. Biophys. Biomol. Struct.* **31,** 275–302 (2002).

19. Heyduk, T. & Heyduk, E. Luminescence energy transfer with lanthanide chelates: interpretation of sensitized acceptor decay amplitudes. *Anal. Biochem.* **289,** 60–7 (2001).

20. Laurence, T. a, Kong, X., Jäger, M. & Weiss, S. Probing structural heterogeneities and fluctuations of nucleic acids and denatured proteins. *Proc. Natl. Acad. Sci. U. S. A.* **102,** 17348–53 (2005).

21. Müller, B. K. *et al.* Pulsed interleaved excitation. *Biophys. J.* **89,** 3508–22 (2005).

22. Kudryavtsev, V. *et al.* Combining MFD and PIE for Accurate Single-Pair Förster Resonance Energy Transfer Measurements. *Chemphyschem* **61801,** 1–20 (2012).

23. Olofsson, L. & Margeat, E. Pulsed interleaved excitation fluorescence spectroscopy with a supercontinuum source. *Opt. Express* **21,** 3370–8 (2013).

24. Kapanidis, A. *et al.* Fluorescence-aided molecule sorting. Analysis of structure and interactions by alternating laser excitation of single molecules. *Proc. Nat. Acad. Sci. USA* **101,** 8936–8941 (2004).

25. Felekyan, S., Sanabria, H., Kalinin, S., Kühnemuth, R. & Seidel, C. A. M. Analyzing förster resonance energy transfer with fluctuation algorithms. *Methods Enzymol.* **519,** 39–85 (2013).

26. Schwille, P. & Haustein, E. Fluorescence correlation spectroscopy An introduction to its concepts and applications. *Spectroscopy* 1–33 (2009).

27. Kapusta, P., Wahl, M., Benda, A., Hof, M. & Enderlein, J. Fluorescence lifetime correlation spectroscopy. *J. Fluoresc.* **17,** 43–8 (2007).

28. Felekyan, S., Kalinin, S., Sanabria, H., Valeri, A. & Seidel, C. A. M. Filtered FCS: Species Auto- and Cross-Correlation Functions Highlight Binding and Dynamics in Biomolecules. *ChemPhysChem* **13,** 1036–1053 (2012).

29. Yin, J. *et al.* Genetically encoded short peptide tag for versatile protein labeling by Sfp phosphopantetheinyl transferase. *Proc. Natl. Acad. Sci. U. S. A.* **102,** 15815–20 (2005).

30. Antonik, M., Felekyan, S., Gaiduk, A. & Seidel, C. A. M. Separating structural heterogeneities from stochastic variations in fluorescence resonance energy transfer distributions via photon distribution analysis. *J. Phys. Chem. B* **110,** 6970–8 (2006).

31. Kalinin, S., Felekyan, S., Antonik, M. & Seidel, C. A. M. Probability distribution analysis of single-molecule fluorescence anisotropy and resonance energy transfer. *J. Phys. Chem. B* **111,** 10253–62 (2007).

32. Kalinin, S., Felekyan, S., Valeri, A. & Seidel, C. A. M. Characterizing multiple molecular States in single-molecule multiparameter fluorescence detection by probability distribution analysis. *J. Phys. Chem. B* **112,** 8361–74 (2008).

33. Gansen, A. *et al.* Nucleosome disassembly intermediates characterized by single-molecule FRET. *Proc Natl Acad Sci U S A* (2009).

34. Brabet, I. *et al.* Comparative effect of L-CCG-I, DCG-IV and gamma-carboxy-L-glutamate on all cloned metabotropic glutamate receptor subtypes. *Neuropharmacology* **37,** 1043–51 (1998).

35. Landes, C. F., Rambhadran, A., Taylor, J. N., Salatan, F. & Jayaraman, V. Structural landscape of isolated agonist-binding domains from single AMPA receptors. *Nat. Chem. Biol.* **7,** 168–73 (2011).

36. El Moustaine, D. *et al.* Distinct roles of metabotropic glutamate receptor dimerization in agonist activation and G-protein coupling. *Proc. Natl. Acad. Sci. U. S. A.* **109,** 16342–7 (2012).

37. Ahmed, A. H., Wang, S., Chuang, H.-H. & Oswald, R. E. Mechanism of AMPA receptor activation by partial agonists: disulfide trapping of closed lobe conformations. *J. Biol. Chem.* **286,** 35257–66 (2011).

38. Maurel, D. *et al.* Cell-surface protein-protein interaction analysis with time-resolved FRET and snap-tag technologies: application to GPCR oligomerization. *Nat. Methods* **5,** 561–567 (2008).

Supplementary material

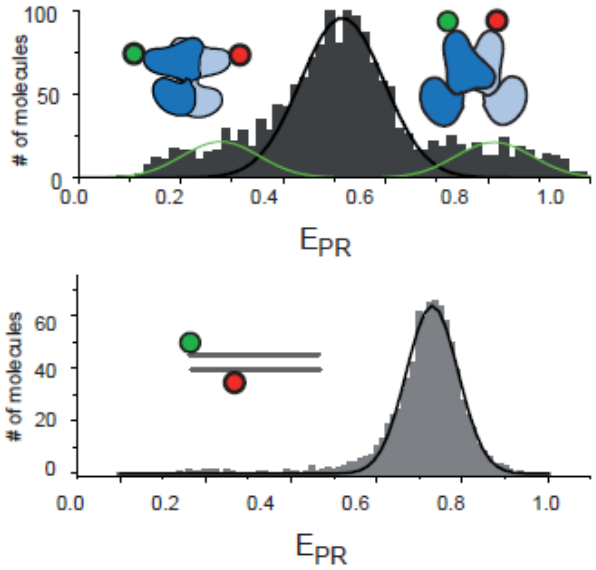

Supplementary Figure 1 : Comparison of the E_{PR} value distribution for a mGlu2R VFT dimer and a dsDNA sample
Top – The E_{PR} value distribution for the selected doubly labelled Donor-Acceptor mGlu2R-VFT **complexes shows a main population centred around E_{PR}~0.51 and two minor populations around E_{PR}~0.25 and E_{PR}~0.85**
Bottom – The E_{PR} value distribution for selected doubly labelled Donor-Acceptor complexes of a dsDNA shows a population around **E_{PR}~0.75 and no minor populations, indicating that in the case of a static system (dsDNA) a single** well defined population is observed in our experimental conditions **(see text)**

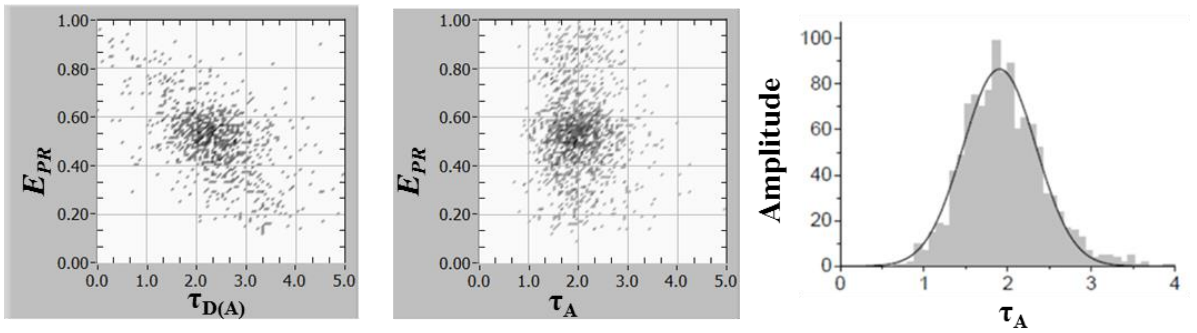

Supplementary Figure 2. (Left) 2-dimensional diagram of the proximity ratio represented as a function of the lifetime of the donor $\tau_{D(A)}$. The lifetime distribution of the donor decreases when the E_{PR} value increases, as expected for three populations with different FRET efficiencies. (Center) 2-dimensional diagram of the proximity ratio represented as a function of the lifetime of the acceptor τ_A. (Right) Histogram showing the 1D projection of the lifetime of the acceptor τ_A from the 2D-plot. Pulsed Interleaved Excitation offers the possibility to directly monitor the excited state lifetime of the acceptor, independently of FRET-induced sensitized emission. Here, we show that LF, MF, and HF species all contain an active acceptor, with an excited state lifetime of ~1.9ns, and thus that the different FRET efficiencies observed do not arise from variation in the photophysical properties of the acceptor.

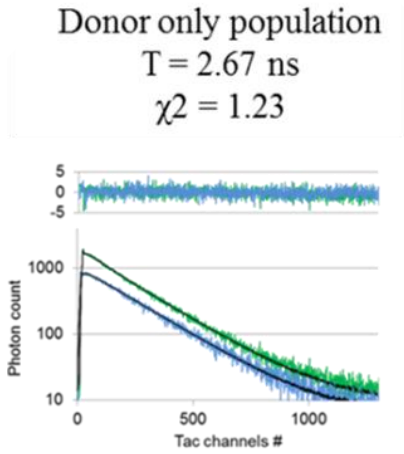

Supplementary Figure 3

Reconstructed excited state lifetimes decay for the donor only population. The dacay is correctly fitted by a single exponential function, with a lifetime similar to what is described in the literature for Cy3B alone (2.8 ns, (Cooper et al., 2004)).

Cooper, M., Ebner, A., Briggs, M., Burrows, M., Gardner, N., Richardson, R., & West, R. (2004). Cy3B: improving the performance of cyanine dyes. Journal of fluorescence, 14(2), 145–50.

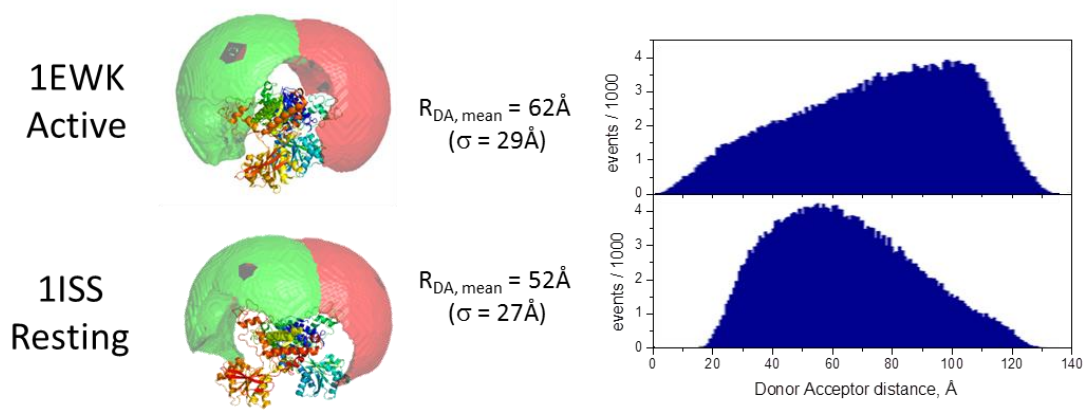

Supplementary Figure 4

Accessible volume (AV) simulations of the fluorophore positions (dye clouds) in the SNAP-VFT dimer based on the crystal structures of mGlu1R Left. Simulated molecular distribution of all possible SNAP-tag positions of either (upper) the active conformation of mGlu1R (PDB1EWK) or (lower) the resting conformation (PDB1ISS). Right. Distance distribution in Ångstroms for the active (upper) or the resting (lower) conformation, spanning the range 0-140 Å. The variation in distance following the reorientation of the VFT dimer is clearly compatible with FRET measurements as a significant shift in the predicted distribution toward lower FRET values is observed for the active conformation in comparison with the resting conformation.

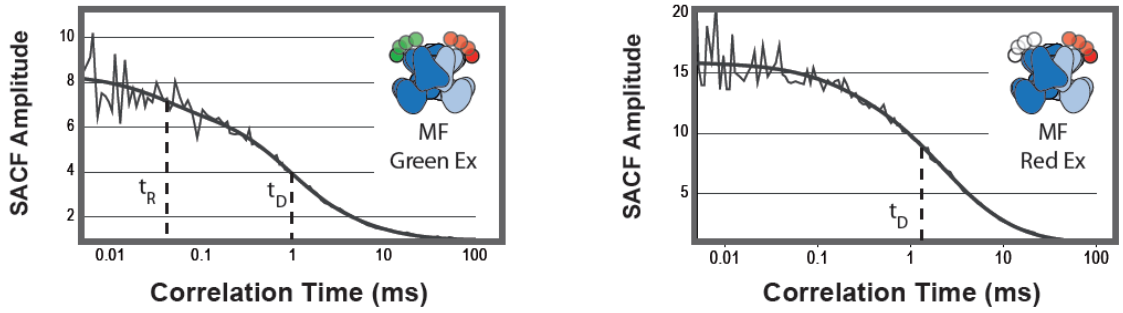

Supplementary Figure 5 : SACF analysis of the signal detected in the red emission channels for mGlu2R for the MF population. Upon excitation of the donor dye (left), a positive correlation term at short timescales (t_R~50µs) is observed, characteristic of FRET changes during HF↔LF transition. When the acceptor is directly excited, this positive correlation at short timescales is not apparent, indicating that there is no acceptor blinking at these timescales.

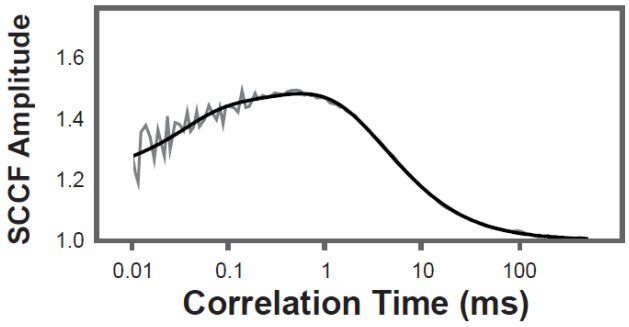

Supplementary Figure 6. An alternative labeling approach based on the acyl-carrier protein and subsequent SCCF analysis confirm that the reorientation occurs at a 100µs time-scale. To ascertain that the time-scale estimated for the reorientation of the VFT dimer is not influenced by the SNAP-tag, an alternative labeling method based on the acyl carrier protein (ACP) was implemented. smFRET measurements, with CoA-547 as a donor and CoA-647 as the acceptor, followed by a SCCF analysis between the HF state and the LF state resulted in time scales identical to those obtained with the SNAP-construct. (~100µs)

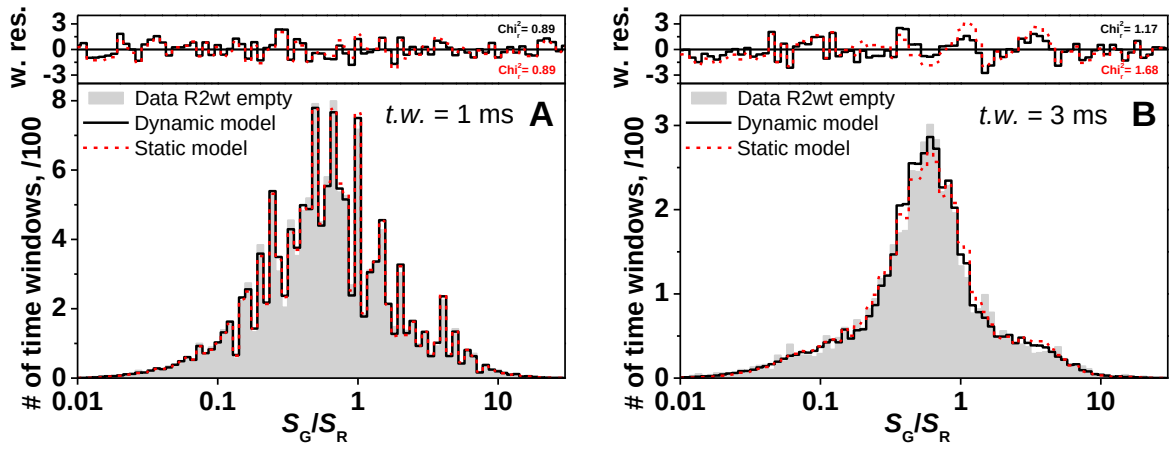

Supplementary Figure 7 : Comparison of the dynamic and the static PDA-model rules out the hypothesis of a static system

Global fit of S_G/S_R histograms (t.w. = 1ms (**A**), 2ms (not shown) and 3 ms (**B**)) for double labeled molecules (grey area) selected from the PIE measurement in absence of ligands, using the model of two interconverting states with Gaussian distributed distances (two-state dynamic) (solid black lines) and static three states with Gaussian distributed distances (dashed red lines) models. Weighted residuals plots are displayed above the main graphs.

For the static model, the reduced χ^2-values are: 0.89 (t.w. = 1 ms) and 1.68 (t.w. = 3ms), and the recovered parameter are $\langle R_{HF} \rangle$ = 35.3Å (19.3%), $\langle R_{MF} \rangle$ = 54.7 Å (77.2%), $\langle R_{LF} \rangle$ = 61.7 Å (3.5%).

For the two-state dynamic model, the reduced χ^2-values decrease to 0.89 (t.w. = 1 ms) and 1.17 (t.w. = 3ms), with $\langle R_{HF} \rangle$ = 30.9 Å (13.0 %), $\langle R_{LF} \rangle$ = 76.4 Å (20 %), dynamic fraction =66.8 %, k_{LF} = 17.3 ms^{-1}, and k_{HF} = 22.3 ms^{-1})

Half-widths of Gaussian distributions of distances are defined in the models as a fraction of corresponding mean inter-dye distance and global fit defined $\sigma_{R(DA)}$ / $\langle R_{DA} \rangle$ = 0.2 (dynamic model) and $\sigma_{R(DA)}$ / $\langle R_{DA} \rangle$ = 0.09 (static model), respectively.

Other parameters used for the fits: R_0 = 54 Å for the Förster radius of the chosen dye pair, crosstalk from donor to acceptor channel 0.1, quantum yields of donor and acceptor dyes 0.67 and 0.28, respectively. Background mean count rates in donor and acceptor channels: $\langle B_g \rangle$ = 0.948 kHz and $\langle B_r \rangle$ = 0.594 kHz, respectively.

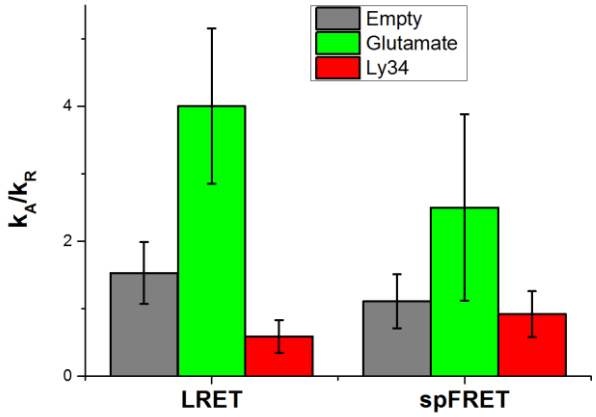

Supplementary Figure 8 : Comparison of the k_A/k_R ratios for LRET and spFRET experiments, for mGlu2R VFT dimers.

For LRET experiments, the ${}^{k_A}/_{k_R}$ ratio is calculated from the fractional amplitudes recovered from the fitting of the acceptor decays.

$$\left({}^{k_A}/_{k_R}\right)_{LRET} = {}^{A_{LF,LRET}}/_{A_{HF,LRET}}$$

, where the amplitude of the long lifetime component ($A_{LF,\,LRET}$) represents the active fraction, while the short lifetime component ($A_{LF,\,LRET}$) is assigned to the resting conformation.

For single molecule FRET experiments, the *kA/kR* ratio is calculated using the values recovered from PDA analyses. This ratio is corrected to take into account that a fraction of molecules x_{LF} that appear static in the LF state (As species) and a fraction x_{HF} that appear static in the HF state (Rs species)

$$\left({}^{k_A}/_{k_R}\right)_{spFRET} = \frac{x_{LF} + \left(1 - (x_{LF} + x_{HF})\right)\left({}^{k_A}/_{k_R}\right)_{PDA}}{x_{HF} + (x_{LF} + x_{HF})\left({}^{k_A}/_{k_R}\right)_{PDA}}$$

The error bars represent uncertainties calculated by propagation of the errors in the measurements. Note that the error in Figure 4b represent instead the standard error on the mean value of the ratio, for N=8-10 experiments.

4.3 mGlu3 – a good candidate to unveil the link between glutamate affinity and dynamic behavior

mGlu3 biology and project background

In addition to the results for mGlu2, mGlu4 and mGlu5, presented in the article "*Specific regulation of transition rates between active and inactive states of metabotropic glutamate receptors determines agonist efficacy*", I have also studied another member of the mGluR family, namely mGlu3. This project is realized in close collaboration with the group of Dr. PIN at the IGF (Amélie Tora, Pauline Scholler, Xin Li, Philippe Rondard, Emmanuel Margeat, Cyril Goudet and Jean-Philippe Pin)

mGlu3 belongs to subgroup II in the phylogenetic tree representing the eight different mGluR members (Conn and Pin, 1997) (**figure 1.12**). Up until now, the focus has mainly been on another member of the same sub-group, mGlu2, however, mGlu3 possesses some features with very intriguing differences with respect to mGlu2. The most striking divergence in behavior concerns the very high affinity that mGlu3 has for glutamate (**figure 4.5.a**), which is presumably a consequence of its localization in the synaptic periphery where the concentration of endogenous glutamate is lower (Niswender and Conn, 2010).

Because of this very high affinity for glutamate, it was difficult to interpret HTRF data for mGlu3. Interestingly, HTRF experiments gave almost the same FRET efficiency in the absence of ligands as with high concentrations of the high affinity full agonist Ly379268, which could be explained by either one of two just as likely hypotheses. Either the conformational equilibrium of the unbound VFT is shifted toward the active conformation, or the concentration of ambient glutamate is sufficient to activate the receptor and bias the data acquired on cells (**figure 4.5.b**) (unpublished data, Dr. Pauline Scholler, IGF). Moreover, inositol-phosphate accumulation assays (IP one) revealed a significant higher basal activity for mGlu3 than for mGlu2 (**figure 4.5.c**) (unpublished data, Dr. Pauline Scholler, IGF).

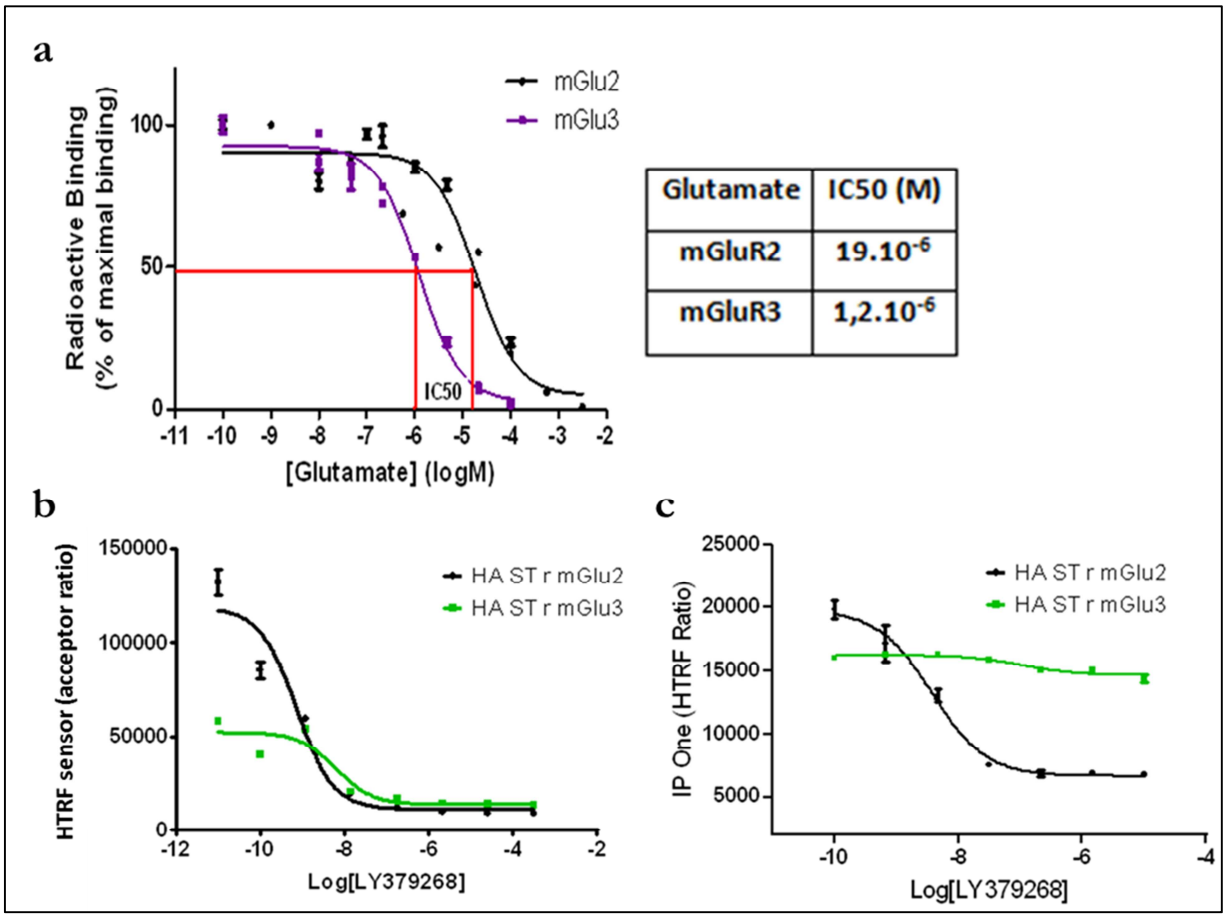

Figure 4.5 *(**a**) Radioactive binding assay for mGlu2 (black) and mGlu3 (purple), by competition with the antagonist [^{3}H]-LY341495. The IC_{50} (K_d) value is one order of magnitude lower for mGlu3. (**b**) In cellulo HTRF sensor experiments on the full-length constructs of mGlu2 (black) and mGlu3 (green), expressed as the acceptor ratio as a function of the concentration of the high affinity full agonist Ly379268. In the absence of ligands, the initial FRET value of mGlu3 is barely above that reached at a saturating concentration of the agonist. (**c**) Activation experiment of mGlu2 (black) and mGlu3 (green) expressed as the accumulation of inositol-phosphate as a function of the concentration in Ly379268. Contrary, to mGlu2, mGlu3 has a high basal activity and only a slight increase in IP is detected at high concentrations of agonist (revealed by the decrease in the HTRF ratio). (Unpublished data, Pauline Scholler, IGF)*

smFRET data reveal an inherent tendency for mGlu3 to favor the active state

To discriminate between these equally plausible hypotheses, I acquired smFRET-MFD-PIE data on the VFT-domain of mGlu3 in an identical manner as previously described in the submission manuscript, and calculated the E_{PR} value, the k_A/k_R ratio and performed SCCF.

The most straightforward difference between mGlu2 and mGlu3 is that the E_{PR} value in the absence of ligands is close to the value acquired with the glutamate bound VFT. These data, acquired in the total absence of glutamate, contrary to the HTRF experiments where ambient glutamate is unavoidable, favor a model where mGlu3 has an inherent tendency to favor the active conformation. Accordingly, in the presence of the antagonist Ly34, the E_{PR} value is strongly upshifted (**Figure 4.6**).

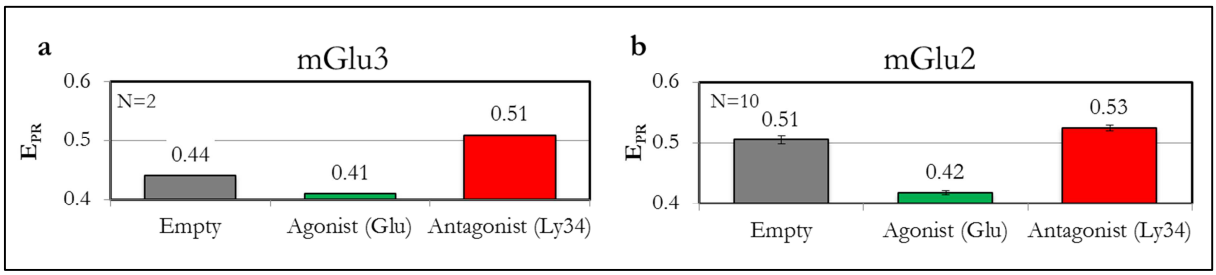

***Figure 4.6**. Comparison of the E_{PR} values for the MF population for mGlu3 (**a**) and mGlu2 (**b**). Interestingly, even in the total absence of glutamate, the E_{PR} value for mGlu3 is as low as 0.44 (0.51 for mGlu2) which is only slightly higher than with glutamate (E_{PR}=0.41). In contrast, the antagonist produces a strong upshift of the E_{PR} value to 0.51, which is fairly similar to the value of 0.53 observed with mGlu2. No error bars are shown in (a) because the values were strictly identical in both experiments. These data are consistent with the hypothesis suggesting that the preferential conformation of the VFT domain is the reoriented active state.*

Furthermore, these conclusion based on the E_{PR} distributions agree well with the k_A/k_R ratios, which demonstrate that even for the empty VFT, this ratio (0.91) is closer to that in presence of glutamate (1.2), than to the E_{PR} value measured upon antagonist binding (0.52), contrary the mGlu2R (**Figure 4.7**). Moreover, the PDA analysis points out an additional difference between mGlu3 and mGlu2 regarding the dynamic behavior, with a larger proportion of dynamic molecules for the former. In fact, it was estimated that about 60% of all molecules undergo constant oscillations in the case of mGlu2, whereas for mGlu3, this number is increased to reach almost 85%.

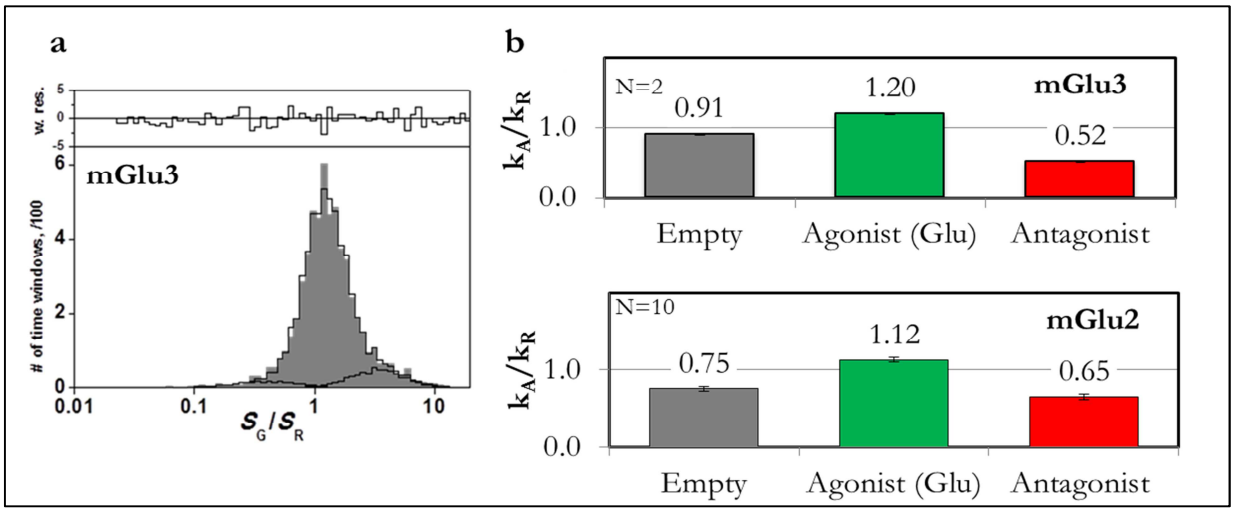

Figure 4.7. *(**a**) PDA S_G/S_R distribution and fit result for mGlu3 in the absence of ligands. The same PDA model as already described, considering two static states between which oscillate a significant fraction of dynamic molecules, was applied on all data. The static populations are barely visible, and the fit gives a dynamic fraction of almost 85% (~60% for mGlu2). (**b**) Comparison of the k_A/k_R ratio for mGlu3 and mGlu2. These results are in agreement with the previously shown E_{PR} values, with a k_A/k_R ratio for the empty receptor that is more similar to the value in presence of glutamate than with the antagonist, contrary to mGlu2.*

In addition, a SCCF analysis of the time-scale of the transitions between the active and the resting state, points toward slightly slower dynamics for mGlu3 (~200μsec) with respect to mGlu2 (~50-100μsec).

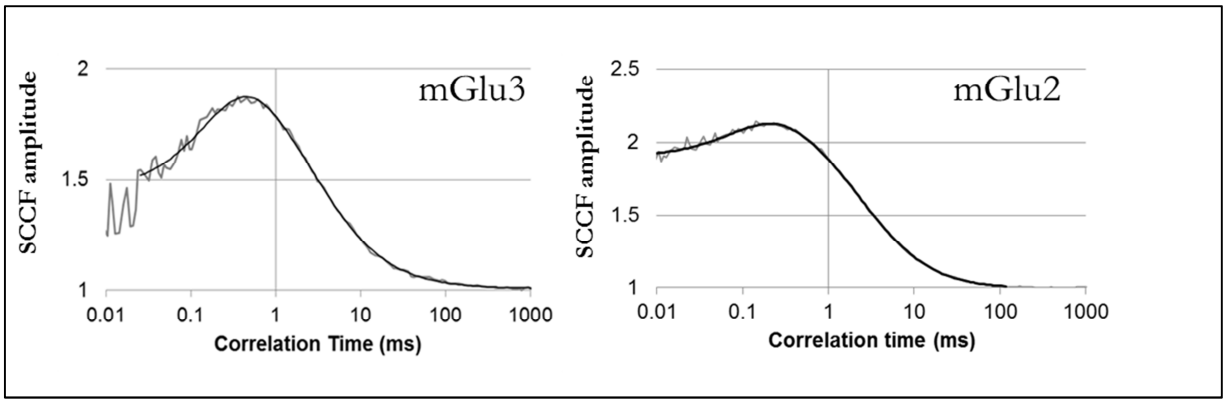

Figure 4.8*. SCCF curves for mGlu3 and mGlu2 in the absence of ligands. A global fit of the anti-bunching term in the SCCF curve for mGlu3 suggests fast dynamics with a specific relaxing time of approximately 200 μsec. It should be noted that nearly identical time-constants were estimated, independently of the pharmacological nature of the ligand. The anti-correlation occurs at longer times for mGlu3, indicative of a somewhat slower dynamic behavior than for mGlu2 (~50-100μsec).*

Concluding remarks on the dynamics of mGlu3

To summarize, a compilation of the preliminary data acquired with mGlu3 suggests that the general activation mechanism, as aforementioned for mGlu2, is conserved. Importantly, we conclude that the preferential conformation of the unbound mGlu3 VFT resembles the one in presence of glutamate. Additionally the two receptor subtypes also seem to deviate in terms of dynamics behavior. For instance, on the one hand, the fraction of molecules displaying constant transitions is higher for mGlu3 than for mGlu2, but on the other hand, the SCCF data seem to indicate slower relaxation-times.

Moreover, as illustrated in **figure 4.9**, there seems to be a correlation between the degree of basal activity and the affinity for glutamate for all mGluR subtypes (unpublished data from Dr. Xin Lin, IGF). Indeed, for mGluRs with a high basal activity, the affinity for glutamate also seems to be higher (this correlation is presumably to some extent amplified by ambient glutamate). Together with the smFRET results, this is very intriguing from a thermodynamic point of view as it reveals that the affinity for a given ligand is not only determined by the composition of amino acids in the binding cleft but also by the dynamic nature of the overall molecular structure and its predisposition to enter the active state. This hypothesis is favored by the fact that the orthosteric site is very similar for mGlu2 and mGlu3 (Conn and Pin, 1997), which suggest that the dissimilarities in terms of affinity and basal activity observed for this group of receptors are most probably due to the amino acid composition in the hinge region between the two lobes, which changes the energetic landscape.

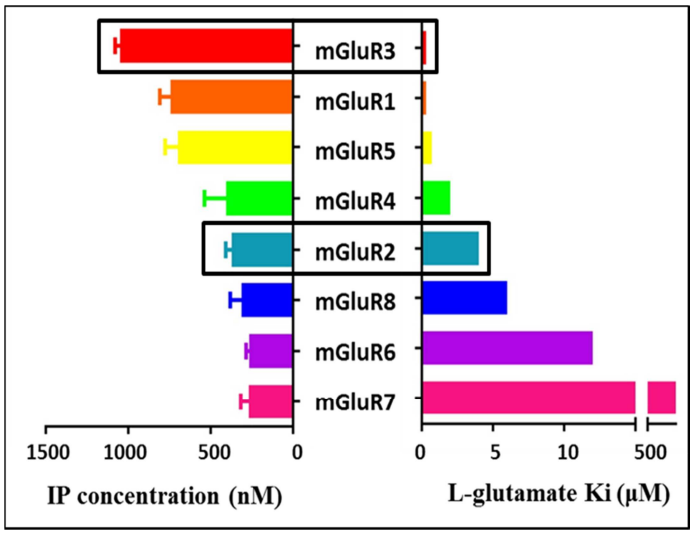

***Figure 4.9**. Diagram representing the degree of basal activity (IP concentration) on the left hand side and the affinity for glutamate on the right hand side, for all mGluR subtypes. Intriguingly, there is a clear correlation between the receptor's tendency to adopt the active conformation in the absence of ligands (NB. small amounts of ambient glutamate cannot be avoided in vivo.) and its affinity for glutamate. This is very interesting from a thermodynamic point of view, as it suggests that it is not only the specific residues within the orthosteric binding site that will control the affinity, but also the dynamic properties of the overall structure. (unpublished data from Dr. Xin Lin, IGF)*

Furthermore, it has been shown that the stronger basal activity for mGlu3 *in vivo* is attributable to the VFT domain. HTRF experiments showed that a chimeric structure composed of the VFT of mGlu3 and the 7TM of mGlu2 had a similar profile to WT mGlu3 and a higher basal activity than the WT mGlu2 receptor (**Figure 4.10**) (Dr. Pauline Scholler, unpublished data, IGF). In view of that, it is very appealing to put forward the VFT-domain as the dominant element in regulating the degree of activation.

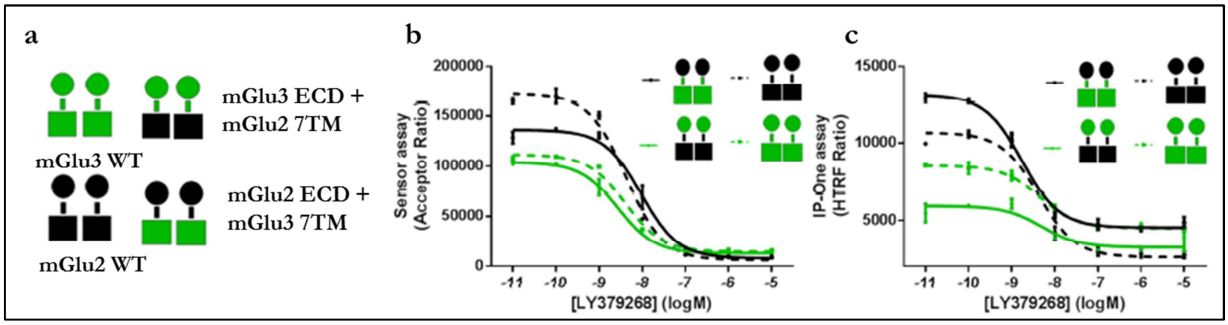

***Figure 4.10**. (**a**) Chimeric mGlu2/mGlu3 structures, with mGlu3 domains in green and mGlu2 domains in black. (**b**) HTRF sensor experiment showing that just by replacing the VFT domain of mGlu2 with the VFT domain of mGlu3, the FRET value resembles that of mGlu3 WT. Accordingly, the construct where the VFT domain of mGlu2 is coupled to the 7TM of mGlu3 gives rise to a dose-response FRET profile more similar the that of mGlu2 than mGlu3. (**b**) IP one activation assay performed with the chimeric structures. The basal activity for the chimeric structure where the VFT domain of mGlu3 is coupled to the 7TM of mGlu2 has a very high basal activity, higher than for the WT mGlu3. Interestingly for the chimeric structure where the VFT domain of mGlu2 is coupled to the 7TM of mGlu3, the basal activity decreases. (Unpublished data, Dr. Pauline Scholler, IGF)*

To conclude, altogether these results highlight striking differences between mGlu2 and mGlu3, regardless of their >70% sequence homology and conserved binding domain (Conn and Pin, 1997). *In cellulo* experiments have shown that the affinity for glutamate as well as the degree of basal activity is higher for mGlu3 than for mGlu2, and that these two parameters are correlated. Furthermore, it has been shown that the VFT- domain is the decisive element in this regulation (**Figure 4.10,** unpublished data).

In addition to the *in cellulo* data, smFRET experiments ascertained that the seemingly active conformation observed *in vivo* is not solely a consequence of ambient glutamate but that, indeed, mGlu3 has an inherent tendency to favor the active state. Single-molecule data also revealed a significant fraction of dynamic molecules, higher than for mGlu2. In my opinion, this could be explained by a postulation based on the argument that for the time being the A_S/R_S cannot be

distinguished from the A/R states just by comparing the FRET values. I suggest that the differences in energy levels toward the A_S and the R_S are greater for mGlu3 than for mGlu2, in which case only very few molecules would be found in these states for mGlu3. Nonetheless, to once and for all elucidate the origin of these two static populations, it would be interesting to assess the contribution of the 7TM to the overall stability of the receptor by studying the full-length construct by smFRET and then try to pinpoint, by means of specific mutations, the amino-acids that influence the different levels of the energetic landscape. Moreover, receptor immobilization might give access to the timescales (if any) of the A to A_S and the R to R_S transition.

4.4 The nanobody as a new mGluR subtype specific ligand

(The content of this chapter is strictly confidential for patent reasons)

In this chapter, I will describe the usefulness of nanobodies to specifically target mGluR subtypes and how smFRET can help to uncover their unique proprieties.

Project background

Our collaborators at the IGF, took on the challenging task of developing new mGluR subtype specific ligands with the idea that they might become valuable tools in a variety of conceptually different experiments aiming at the better understanding of the unique biological functions of each of the members of the mGluR-family (Scholler, Baty, Rondard, Pin, Trinquet, manuscript in preparation). In addition, ligands linked to the modulation of the degree of activation of their target molecules could be put forward as promising drug candidates for the selective treatment of the many neurological and psychiatric disorders that have been associated with various mGluRs subtypes.

In fact, up until now, very few subtype specific ligands have been found (Tocris Bioscience Scientific Review Series), mainly due to the relatively high sequence identity between the subgroups, not to mention, the almost 70% sequence identity shown for the different members belonging to the same subgroup. In this light, the group of Jean-Philippe Pin at the IGF, Cisbio bioassays and the group of Dr. Daniel Baty at the centre de recherche en cancérologie de Marseille decided to use an approach consisting in the employment of a particular kind of heavy-chain only IgG antibody (HcAb), exclusively found in camelids, to find subtype specific ligands for mGlu2 (Ph.D. thesis of Dr. Pauline Scholler). The isolated variable antigen recognition domain of a HcAb goes under the name "nanobody" or "single domain antibody" (Hamers-Casterman and Atarhouch, 1993) (**Figure 4.11**) and its usefulness in biology has only just begun to be unveiled (Rasmussen, Choi, *et al.*, 2011; Blanchetot *et al.*, 2013). In recent years, scientists have managed to invent methods to increase the stability, the affinity and the selectivity of the nanobody as well as making it possible to cheaply produce large quantities through the implementation of bacterial expression systems (Chames and Baty, 2009).

Nanobodies present the advantage of being highly stable as they maintain their antigen recognition capacity even after treatment with reducing agents, and they have been shown to rapidly refold after having been exposed to temperatures as high as 80-90°C (Dumoulin, 2002). Moreover, with a molecular weight of only 15kDa, and the possibility to be covalently coupled to organics fluorophores or fused to green fluorescent protein derivatives, nanobodies might turn out to be of high interest in super-resolution microscopy experiments where the mere size of classical antibodies might be larger than the localization resolution (van de Linde *et al.*, 2011).

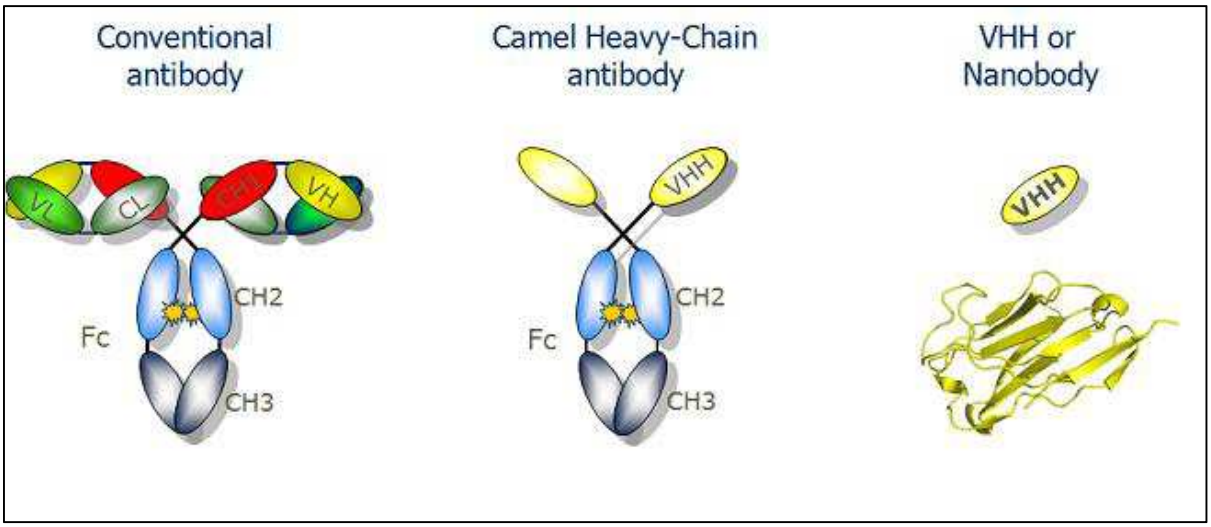

***Figure 4.11**. Illustration of the differences between a classical IgG antibody and the type of heavy chain only antibody exclusively found in camelids. The isolated variable domain of a camelids antibody is referred to as nanobody, still perfectly capable of recognizing the antigen. (Structural biology Brussels)*

The first step of the production procedure remains the same as in classical antibody production as it requires the immunization of the host. To this aim, llamas were injected with mGlu2 expressing HEK-293 cells combined with diverse adjuvants to trigger intense immune responses. Two weeks post-injection, RNA molecules were extracted from purified lymphocytes and the variable (V_H) was amplified by RT-PCR by means of appropriate primers. The amplified DNA molecules are then inserted into the genome of phages, which is a critical step to enable a first selection of mGlu2 antigens by ELISA. A more stringent sorting was then achieved on the nanodisc incorporated mGlu2 and resulted in the isolation of 10 different nanobodies. Finally, to obtain a large quantity of the selected nanobodies, all the anti-mGlu2 nanobody sequences were expressed in E.Coli and His-tag purified.

In order to determine both, qualitatively and quantitatively, the interaction of the purified nanobodies with mGlu2 *in cellulo*, Pauline Scholler measured by HTRF the binding of the nanobodies to mGlu2-GPI to verify that they specifically bound the receptor VFT in their experimental conditions.

Figure 4.12.a left, shows a HTRF experiment of the inositol phosphate accumulation as a function of the concentration in nanobodies, and thereby directly reflects the capacity of the nanobodies to trigger a cellular response. From this data, it is concluded that the three nanobodies that display the strongest tendency to activate the receptor are Dn7, Dn10 and Dn13 whereas for example Dn1 and Dn3 show no biological function. **Figure 4.12.b** represent a HTRF-sensor experiment, conducted to determine the apparent degree of reorientation of the VFT, and surprisingly, even Dn1 and Dn3 decrease the FRET efficiency, which suggests an unexpected and puzzling ability to promote the active state, despite their lack of positive effects in the cell-assay.

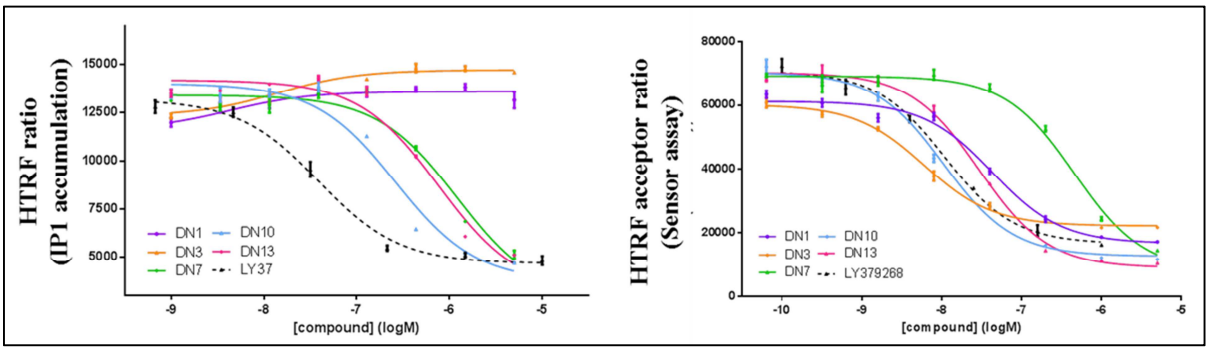

***Figure 4.12**. (**a**) HTRF experiment of inositol phosphate accumulation for increasing concentrations of nanobodies. Dn 7, 10 and 13 clearly trigger a cellular response whereas for instance dn 1 and 3 do not seem to have any visible effects on activation. (**b**). HTRF sensor data illustrating the apparent reorientation of the VFT-dimer toward the active state. The results for dn 7, 10 and 13 are in agreement with the cellular activation assay, however, both dn 1 and dn 3 also suggest that the VFT reaches the active state, which is in indisputable contradiction with the functional test.(Data kindly provided by Pauline Scholler, IGF)*

Nanobody characterization by smFRET

In order to decipher the underlying cause for the discrepancies between the HTRF-sensor experiment and the cell assay for Dn1 and Dn3, and to contribute with additional data that might provide new light to and help with the elucidation of the molecular mechanism by which Dn7, Dn10 and Dn13 activate the VFT, we decided to perform smFRET experiments.

smFRET validation of Dn 7 and Dn 13 as mGlu2 agonists

smFRET acquisitions on mGlu2 were carried out as previously described. For Dn7 and Dn13, in comparison with the empty receptor, the mean E_{PR} value decreased in presence of both of these nanobodies (**Figure 4.13**). Interestingly, for Dn13 the FRET efficiency is even slightly lower than what is observed in presence of glutamate alone and the Gaussian distribution is narrower. Thereupon, several major conclusions can be drawn: (**i**) the fact that the lowest measurable E_{PR} value is not reached with glutamate alone is in agreement with our previously hypothesized model arguing that the role of glutamate is to shift the equilibrium toward the closed state without being able to entirely induce its stabilization (**ii**) the FRET efficiency for Dn13 is comparable with the E_{PR} value obtained with the crosslinked mutant, which suggest that this nanobody is indeed capable of strongly shifting the equilibrium toward the active conformation.

In conclusion, for both Dn7 and Dn13, the results are consistent and conclusive. These two nanobodies are indeed perfectly capable of shifting the conformational equilibrium toward the active state. Consequently, they might, for instance, be employed in *in vivo* studies to better discriminate between the cellular responses initiated exclusively by mGlu2, without the influence of mGlu3 and other subtypes.

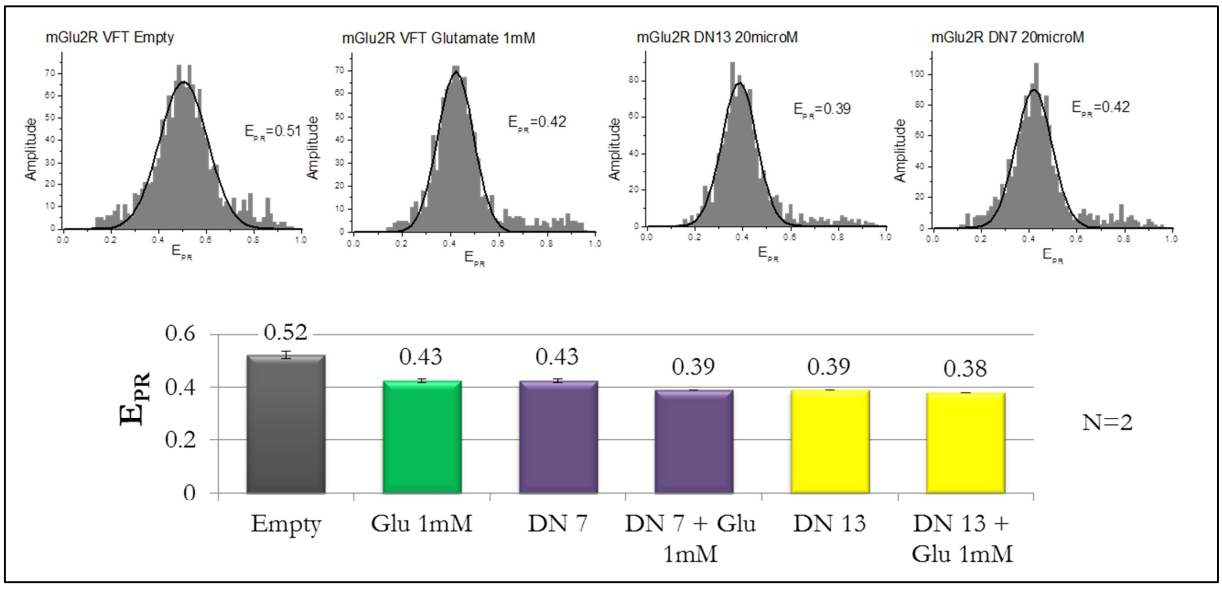

***Figure 4.13**. Upper panel. E_{PR} distributions for, from left to right, the empty VFT, at a saturating concentration of glutamate, with dn13 (20µM) and dn7 (20µM). Even in the absence of glutamate dn13 and dn7 are both capable of down-shifting the E_{PR} value. For dn13, the mean E_{PR} is even slightly lower than with glutamate alone, whereas for dn7, the same E_{PR} value as with glutamate is detected, highlighting a slightly higher efficacy for dn13 than for dn7. Lower. Histogram displaying the mean E_{PR} values for the different experimental conditions. The stabilization of reoriented conformation is enhanced in presence of glutamate for both dn7 and dn13.*

smFRET data reveal an unexpected behavior for Dn 10

The smFRET data for Dn10 were somewhat less easily interpreted. Indeed, it seems like dn10 in the absence of glutamate exerts only little effect on the conformation of the VFT with a E_{PR} value is similar to the E_{PR} of the empty receptor, which is in apparent contradiction with the HTRF sensor and activation data. To refute the hypothesis of constrained mobility induced by Dn10 as the underlying cause of these discrepancies, we verified that the anisotropy of both the donor and the acceptor dye correspond perfectly with the values measured for those of the empty VFT

In presence of a saturating concentration of glutamate, two populations are distinguishable, albeit overlapping, making a simple Gaussian fit difficult. Nonetheless, the two populations appear to take E_{PR} values of about 0.4 and 0.5, respectively. Intriguingly, the two populations, both in terms of anisotropies and lifetime distributions, present the expected profile for two populations with different FRET values. It, thus, seems that Dn10 stabilizes the resting conformation for a fraction of

receptors, acting as a competitive antagonist, which is much unexpected considering the strong positive response seen in HTRF.

A possible explanation to the differences between the *in vivo* and the *in vitro* data could be that although Dn10 has been shown to bind to the VFT, the 7TM is somehow necessary for this nanobody to exert it action as an agonist. It might be that Dn10 interact at the VFT-CRD interface, which might activate IP, and give a positive response in HTRF sensor experiments. Accordingly, the action of Dn10 on the isolated VFT would be reduced. Further investigations are therefore necessary to firmly conclude on the pharmacological proprieties of Dn10. It would be highly interesting to continue the investigation by performing smFRET experiments on the ECD-GPI construct or HTRF sensor experiments on the GPI-construct.

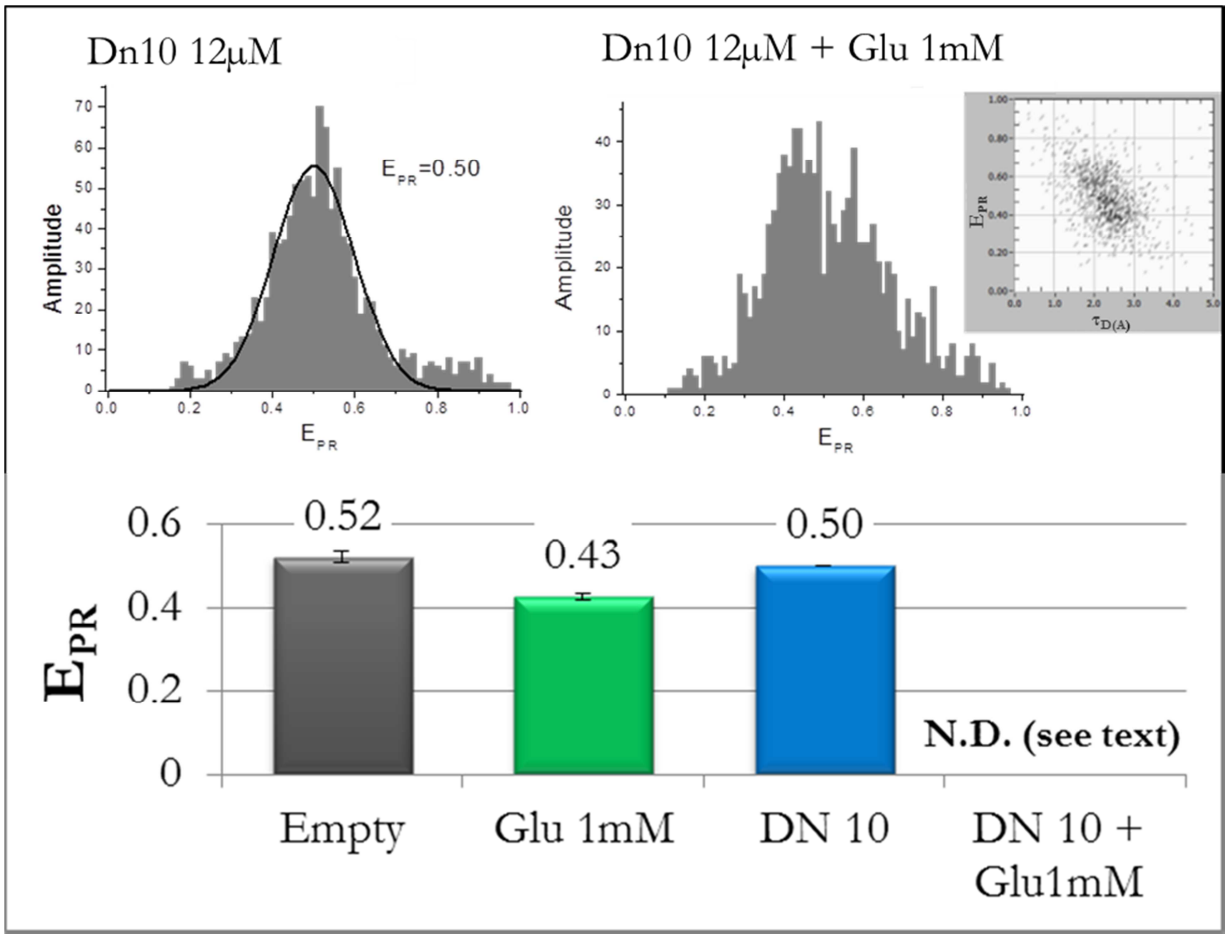

***Figure 4.14**. E_{PR} distributions for dn10 in the absence (left) and presence (right) of glutamate. It seems like Dn10 stabilizes the resting conformation and competes with glutamate, which makes it impossible to estimate a mean apparent E_{PR} value in its presence.*

A smFRET characterization of Dn 1 and Dn 3 gives leads to explain the discrepancies observed in HTRF for these nanobodies

smFRET data were also acquired for Dn1 and Dn3 in order to expose the origin of the discrepancies observed between the activation assay and the HTRF sensor experiment.

On the one hand, uncorrected smFRET data represented on the 2D E_{PR} versus $\tau_{D(A)}$ diagram for Dn1 and Dn3 show much dissimilarity between these two nanobodies and the other nanobodies and ligands previously described. As a matter of fact, two distinct populations with different lifetimes and anisotropies are clearly discernible, and neither Dn1 nor Dn3 show the typical E_{PR} Gaussian distribution profile observed in all other experimental conditions (**Figure 4.15.a**).

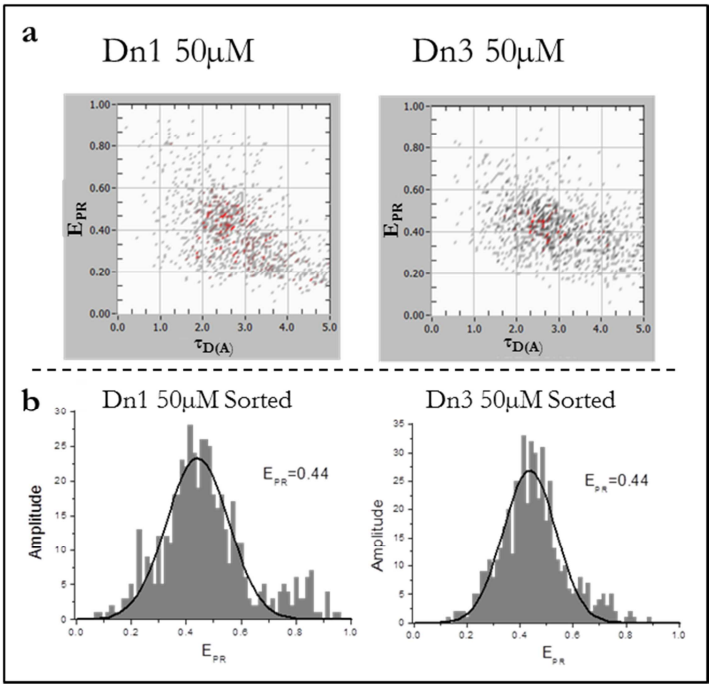

Figure 4.15. *(**a**) Uncorrected E_{PR} versus $\tau_{D(A)}$ 2D diagram for Dn1 and Dn3, clearly showing the existence of contaminating molecules with a lifetime exceeding that of the donor Cy3B. (**b**) E_{PR} distribution of the molecules that remain after sorting.*

On the other hand, by removing molecules with an excited state lifetime longer than 2.8ns and by correcting for photobleaching, the few molecules that remain display the usual E_{PR} Gaussian distribution with mean E_{PR} values of 0.44 for both Dn1 and Dn3 (**Figure 4.15.b**). Furthermore, it should be noted the anisotropies and the lifetime distribution for both the donor and the acceptor dyes of the remaining molecules correspond to the values of the control sample.

On these grounds, I performed measurements on samples containing only nanobodies and no labeled VFTs. The outcome of these experiments was that the nanobody only samples contained

molecules (nanobodies or impurities), emitting in the green channel with a lifetime of approximately 4ns and low anisotropy. Consequently, the presence of impurities explains the existence of the two populations in the raw data.

Moreover, if these impurities attach to the labeled VFT, the additional green photons will decrease the apparent E_{PR} value, without revealing an actual conformational change of the VFT (N.B. a mean E_{PR} values of 0.44, as observed with both Dn1 and Dn3 is very close to the E_{PR} value normally detected with glutamate). The fact that HTRF experiments might be biased by this contamination could explain why neither Dn1 nor Dn3 is capable of activating the receptor in the cell assay.

In conclusion, by performing an investigation at the single molecule level, clues to the underlying cause of the inconsistencies observed at the ensemble level were put forward, which once again highlights the strength of being able to discern the different subpopulations of a heterogeneous sample.

4.5 Nanodisc-incorporation as an approach to study the mobility of the C-terminus of the 7TM in solution

This project has been conducted in collaboration with the groups of Jean-Philippe Pin (Driss El-Moustaine, Philippe Rondard) IGF, Bernard Mouillac, IGF, Eric Trinquet, Cisbio and Jean-Louis Banères, Université Montpellier I.

Background – Role of the C-terminus in activation

Crystallization difficulties of transmembrane receptors limit the panoply of available structures of the heptahelical domain to a couple of class A (Okada *et al.*, 2000; Rasmussen *et al.*, 2007; Gautier *et al.*, 2010) and class B (Hollenstein, *et al.*, 2013; Siu *et al.*, 2013) GPCR members. Nonetheless, several recent studies (Pin *et al.*, 2003; Granier *et al.*, 2007; Wess *et al.*, 2008; Hlavackova *et al.*, 2012) have shown that the intracellular C-terminal is a key player in the G-protein activation regulation. As matter of fact, it is thought that in the inactive conformation, the C-terminal remains stuck against the 2nd intracellular loop due to the amphiphilic nature of the 8th helix (Bruno *et al.*, 2012), thereby, preventing the interaction with the G-protein. Consequently, upon activation the C-terminal is assumed to gain in mobility, which would expose the interaction surface to the G-protein.

Experimental approach – nanodisc-incorporation of the 7TM

In order to investigate this hypothesis, the isolated transmembrane domain of the mGlu2 was purified, incorporated into lipid nanodiscs and specifically labeled in the C-terminus domain for the purpose of conducting time-resolved anisotropy measurements. The general strategy is summarized in **Figure 4.16** and the different steps involved are described in upcoming paragraphs.

It was recently shown that a single heptahelical domain captured in a lipid nanodisc is capable of activating the G-protein in a similar manner as the full-length receptor, which justifies the use of a single 7TM as a minimal model to study G-protein activation (El Moustaine *et al.*, 2012). Interestingly, in the absence of the VFT-domain, positive allosteric modulators fully activate the G-protein, which once again highlights the supposed role of the VFT as a brake on the 7TM..

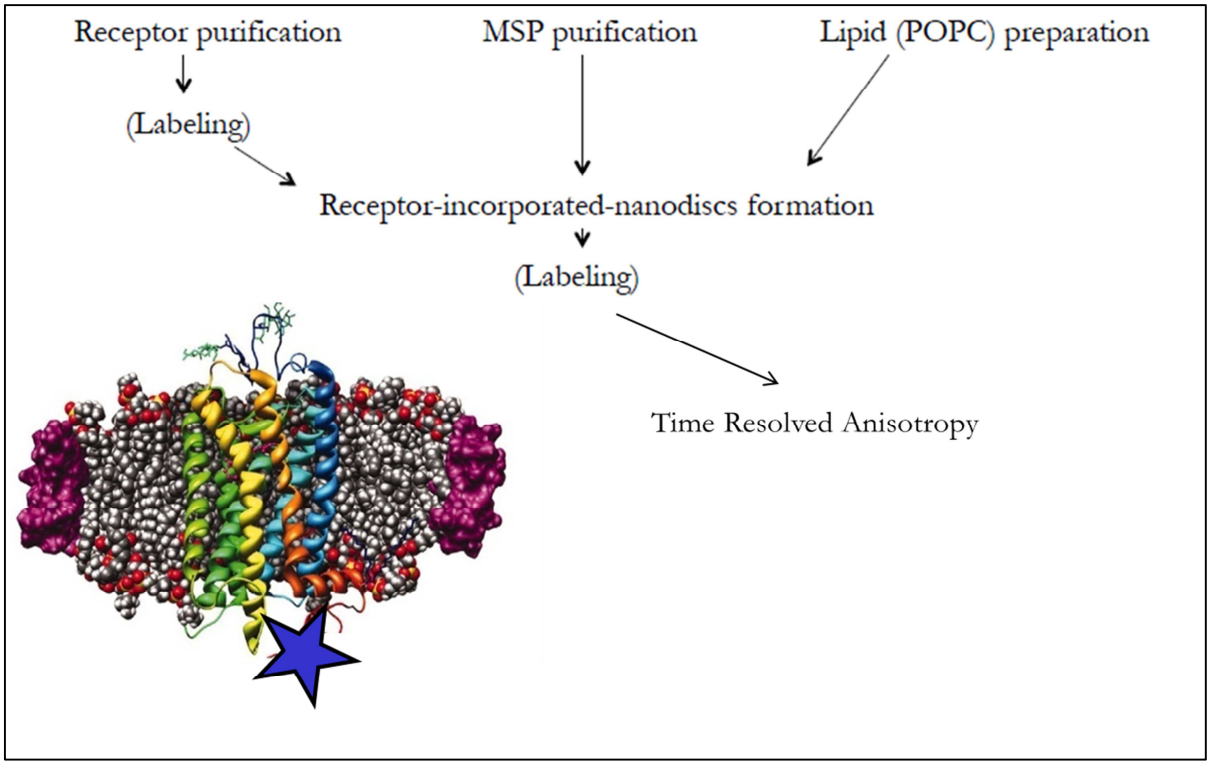

***Figure 4.16**. Illustration of the general experimental approach. The receptor and the MSP (Membrane Scaffold Protein) are purified separately and the lipids are modified with cholate. The different components are then incubated in a carefully estimated ratio in order to achieve an incorporation ratio of one 7TM per nanodisc. The C-terminus is labeled either before or after nanodisc incorporation depending on the hydrophobicity of dye employed.*

What is a nanodiscs?

A nanodisc is an assembly of one or several types of phospholipids held together by an amphipathic α-helix derived from the human apolipoprotein A1 sequence, named the "Membrane Scaffold Protein" (MSP). By adjusting the ratio lipids:MSP and the length in terms of amino acids of the MSP used, the size of the nanodisc can be varied between 9 and 13nm in diameter (**Figure 4.17)** (Bayburt and Sligar, 2010) The main interest of nanodiscs is that they offer the possibility to render soluble otherwise hydrophobic membrane proteins, and preserve them in a cell-membrane mimicking environment. In fact, membrane proteins are purified by means of detergents that disassemble the supporting membrane all the while maintaining the hydrophobic nature of the interactions. However, detergent solubilized proteins are not ideal for biochemical or biophysical assays since the function and behavior of the molecules might be altered and the optical proprieties

of detergents in terms of absorbance and light scattering are not as well suited for spectroscopic methods as aqueous solutions (Bayburt and Sligar, 2010).

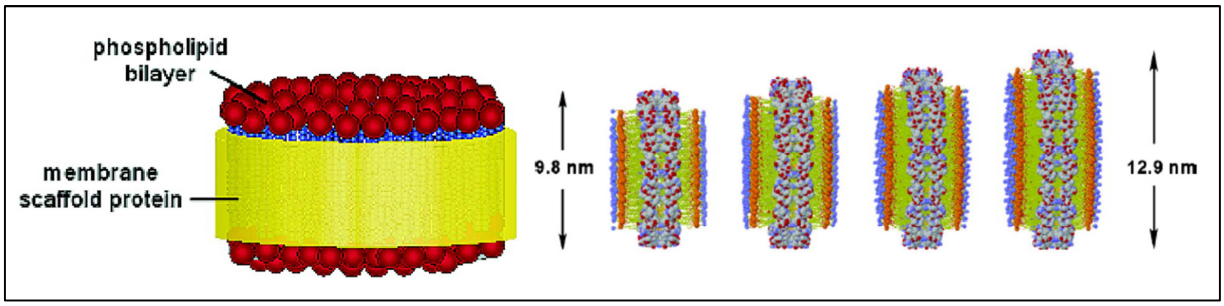

***Figure 4.17**. Schematic representation of nanodiscs. An amphipathic α-helix (MSP) wraps around an assembly of phospholipids with the hydrophilic side facing the aqueous solvent, allowing it to act as a belt maintaining a compact soluble otherwise hydrophilic structure. By varying the length of the MSP protein and the amount of lipids, the size of the nanodisc can span from 9-13nm in diameter.* (Bayburt *et al.*, 2002; Denisov *et al.*, 2004)

Purification, labeling and nanodisc incorporation protocol

The first step of the purification procedure is to lyse Sf9 cells expressing the 7TM domain of mGlu2 fused to a FLAG-tag in N-terminus (mGlu2-7TM-Tg3-flag construct), and harvest the membrane fraction by centrifugation. The membranes are solubilized and mechanically disrupted in detergents (20 mM HEPES pH 7.4, 0.5 % DDM, 0.2 % cholate, 0.03 % CHS, 500 mM NaCl and Protease inhibitors) and purified on an affinity anti-FLAG column after centrifugation. The elution of the protein of interest is achieved by competition with free peptide-FLAGs.

The mGlu2-7TM-Tg3-flag construct also contains a recognition site for the transglutaminase (Tgase) in C-terminus, which allows for site-specific enzymatic labeling (Sato *et al.*, 1996; Taki *et al.*, 2004; Jäger *et al.*, 2006). In fact, *in vivo*, the Tgase is an enzyme capable of catalyzing amide-bonds between glutamine and lysine side-chains. The enzyme is thought to be involved in various molecular processes requiring protein-protein cross-linking such as migration, apoptosis and wound-healing. Scientists have taken advantage of this feature to establish a site-specific labeling approach by appending the Tgase's substrate sequence "Pro-Lys-Pro-Gln-Gln-Phe" to the protein of interest. The Tgase then act by forming a covalent bond between the amino-group of the cadaverine-linked dye and the gamma-carboxamide group of the reactive glutamine within the specific substrate sequence (**Figure 4.18**.) (Sato *et al.*, 1996; Taki *et al.*, 2004; Jäger *et al.*, 2006).

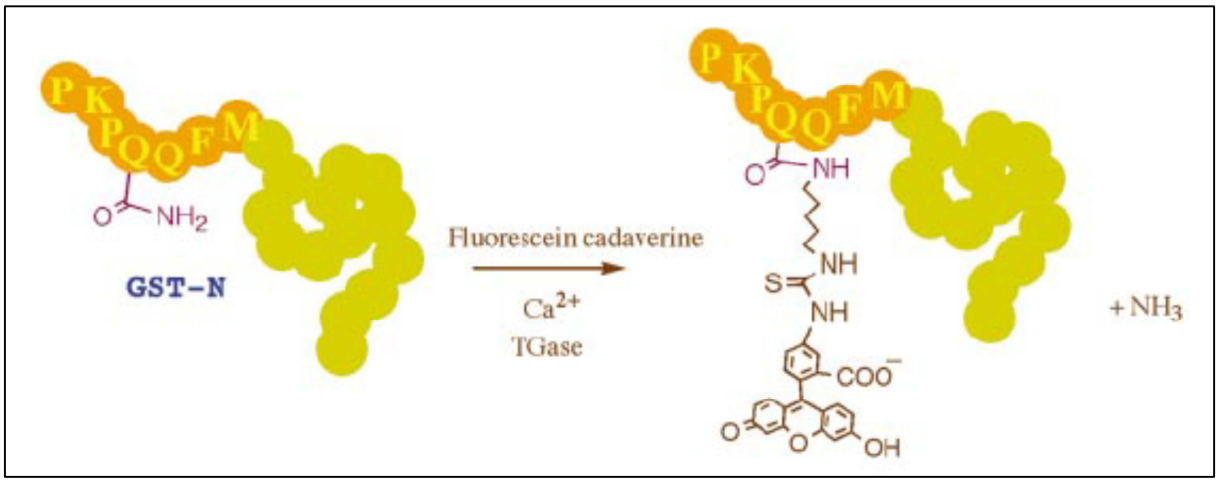

***Figure 4.18**. Schematic illustration of the Tgase specific labeling reaction. In this example, the glutamine adjacent to the proline residue in the peptide sequence "Pro-Lys-Pro-Gln-Gln-Phe" is coupled to cadaverine linked fluorescent dye (fluorescein) through the action of the Tgase.*

Following labeling, the receptor, the MSP and the cholate-modified 1-palmitoyl-2-oleoyl-sn-glycero-3-phosphocholine (POPC) are incubated at a ratio of 0.1:1:150 with 25mM cholate for 1h before being mixed with biobeads overnight. The biobeads serve to remove the detergents and, thereby, induce the formation of nanodiscs.) The final step consists of the removal of the biobeads by centrifugation and size-exclusion chromatography to separate the fraction of nanodiscs that has only incorporated one receptor from the empty nanodiscs and nanodiscs containing two or more receptors.

To verify that the incorporated monomeric 7TM was capable of activating the G-protein, a G-protein activation assay was carried out. The principle of the G_s test is based on the increased tryptophan emission in α-GDP than in α-GTP, which was, indeed, the case for the reconstructed 7TM. It was thereby concluded that the nanodisc incorporated 7TM was a valid model to study the dynamic behavior, responsible for G-protein activation.

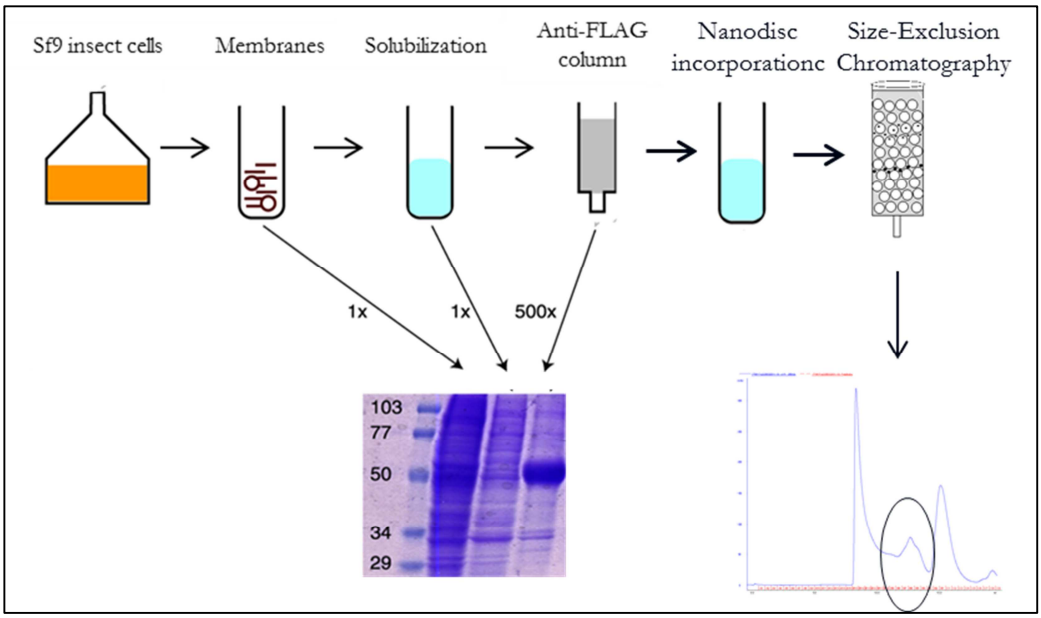

***Figure 4.19**. Illustration of the different steps leading up to the nanodisc-incorporated purified receptor. See text for details.*

Anisotropy measurements in the purpose of detecting changes in mobility following activation

Single molecule anisotropy measurements were carried out on the Alexa488-labeled mGlu2-7TM construct on our home-built MFD setup in presence of various PAMs and NAMs. If indeed the PAM-activation of the receptor leads to an increase in mobility of the C-terminus, a decrease in anisotropy and/or a variation in lifetime are expected. Unfortunately, both the PAMs and the NAMs gave similar results- increased lifetime and lower anisotropy, which prevented a thorough interpretation of the results (**Figure 4.20**).

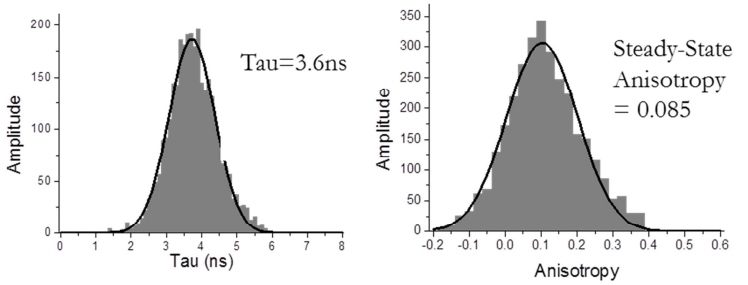

Drugs (10µM)	Tau (ns)	Anisotropy
Empty	3.6	0.085
CBiPES (PAM)	3.8	0.037
Ly487379 (PAM)	3.8	0.068
Ro-64 (NAM)	3.8	0.065

Figure 4.20 *Histograms showing the lifetime (left) and steady-state anisotropy (middle) of single mGlu2-7TM-Alexa-488 nanodiscs, in solution in the absence of drugs. (Right) Table displaying the lifetime and the anisotropy of the same mGlu2-7TM-Alexa-488 construct in presence of the PAMs CBiPES and Ly487379 and the NAM Ro-64. Both the lifetime and the anisotropy seem to increase in presence of drugs and this independently on their biological effects.*

Conclusions : Nanodisc-incorporation of the full-length receptor as a method to study the influence of the 7TM on the dynamics of the VFT.

Despite the somewhat disappointing anisotropy results, the nanodisc-incorporation protocol is now optimized and can easily be adapted for the incorporation of the full-length receptor. As a matter of fact, the continuation of the investigation of the structural dynamics of the VFT includes the nanodisc-incorporation of the entire dimeric receptor. In an initial step, the VFT will be labeled with N-terminus SNAP-tags and, thereby, the dynamic behavior of the VFT can be assessed in presence of the 7TM. This approach is further discussed in chapter 5.2 "future perspectives".

Chapter 5. Discussion and conclusions

In this last chapter, I will summarize the most essential findings of my main study and propose some future perspectives that might provide additional information to help decoding the complex interplay between the affinity, the efficacy and the dynamic behavior of mGluRs.

5.1 Result summary

Despite major technological improvements and extensive research in recent years, the underlying molecular mechanism of GPCR activation and regulation remains a controversial field of study, more than ever open to debate. In this light, I have undertaken a project aimed at the better understanding of the dynamic behavior of the extracellular ligand binding domain of metabotropic glutamate receptor with the purpose of determining how agonists with different efficacies exert their functions. To this aim, a thorough examination of all possible conformations of the receptor had to be achieved at the single molecule level to overcome the major shortcomings of ensemble studies that only report on the average behavior of many proteins simultaneously. Additionally, they also had to be performed with a sufficient time resolution to enable adequate probing of fast protein dynamics, which typically involves small changes in distance occurring on a nano- to milli-second timescale. Our method of choice which fulfills these criteria is the technique smFRET on diffusing molecules.

A first critical step to achieve high accuracy single-molecule FRET measurements with a sub-nanosecond time-resolution consisted of building the required optical setup. The implementation of a supercontinuum laser source to accomplish a interleaved multicolor excitation scheme coupled to a 4-channel Time-Correlated Single Photon Counting detection mode was published in *Optics Express* (Olofsson and Margeat, 2013).

After having established a functional labeling and purification protocol, enabling the specific N-terminus labeling of the soluble VFT domain and the subsequent acquisition of smFRET data, I employed several cutting-edge analysis procedures to quantify the degree and magnitude of dimer reorientation. I showed that the VFT constantly oscillates at the sub-millisecond time scale between two main conformations, attributed to the resting and the active states of the receptor, both in the absence of ligands as well as following the binding of ligands with different pharmacological proprieties- full agonists, partial agonists or antagonists. I also demonstrated that the efficacy of these ligands stems from their ability to modulate the equilibrium constant between the two main states of the receptor. Whereas full agonists strongly shift the conformational equilibrium toward the active

state, partial agonists display a less significant effect on this rate-constant. In contrast, antagonists act by pushing the equilibrium toward the inactive conformation. Interestingly, approximately 30-40% of the diffusing molecules remained static throughout their residency in the focal volume blocked in either the "active" or "resting" conformation. However, the biological functions of these two static states remain to be unveiled, and it might even be that these molecules are dynamic, as well, but on the timescale which is not compatible with the technique of smFRET on diffusing molecules.

With this report, which will shortly be submitted to *nature structural & molecular biology*, I provided the first ever insight into the highly complex structural dynamics of a G protein coupled receptor ligand binding domain and directly ascertained that the concept of conformational selection, rather than that of conformational induction, constitutes an essential mechanism to control ligand efficacy. Moreover, I have confirmed the existence of this mechanism on mGluRs from all subgroups, and by implementing this method for the study of nanobodies, I managed to clarify the discrepancies observed between the cellular activation and HTRF sensor assays. Altogether, these findings ground for several additional publication.

5.2 Future perspectives

Continuation of the study of the dynamics of the VFT on the full-length construct

It would be really interesting to extend the project to decipher the complex interplay between the dynamics of the mGluR VFT and the transmembrane domain. To this aim, a possible approach would be to incorporate the full-length receptor into lipid nanodiscs (Denisov *et al.*, 2004; Bayburt and Sligar, 2010). Not only would this construct better represent the *in vivo* functional entity but it would also expand the range of possible ligands and combination of ligands to include positive and negative allosteric modulators. It might be that the transmembrane domain through an upstream regulation lowers the energetic barrier of the transition between the dynamic population and the active and/or resting state (As and/or Rs), in which case the fraction of molecules in these states would be modified in the presence of ligands. In addition, *in vitro* smFRET experiments on the full-length nanodisc-incorporated construct could be carried out in presence of the G-protein whose role in stabilizing the active conformation has yet to be revealed for mGluRs. Presuming a similar

mechanism as previously described for β_2AR, where the G-protein is required to reach the fully active conformation (Nygaard *et al.*, 2013), it would be most interesting to determine how the dynamic behavior of the VFT is affected by this upstream regulation.

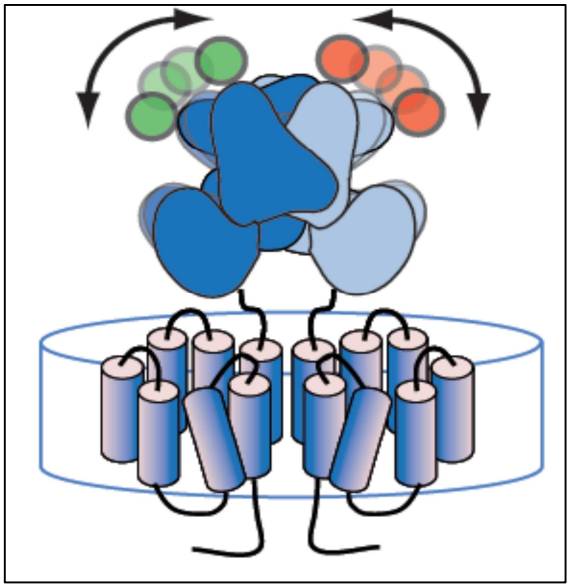

***Figure 5.1**. Pictogram illustrating the full length receptor incorporated into a lipid nanodisc. By incorporating the full-length construct into a lipid nanodisc, the otherwise hydrophobic receptor can now be investigated in solution, in vitro.*

Correlation between affinity and dynamic behavior

Not all mGluRs have been studied in the context of this thesis. Notably, mGlu7 warrant further investigations due to its very low affinity for glutamate (K_d in the mM range). In fact, mGlu7 is mostly expressed at the site of vesicle fusion and is believed to respond exclusively to very strong glutamate releases, and assumed to modulate the degree of neurotransmitter release (Ullmer *et al.*, 2012). An examination conducted to elucidate the dispersion of agonist affinities between the different members of the mGluR subgroup III identified, asparagine 74 in the mGlu7 sequence as responsible for its low affinity for glutamate (Rosemond *et al.*, 2004). By replacing this asparagine with a lysine, the affinity increased 12-fold. What is more is that if this N74K mutation was combined with mutations of residues 258-262, which lay outside the binding pocket, a 112-fold increase in affinity was observed (Rosemond *et al.*, 2004). On these grounds, it would be appealing to compare the dynamics of the different mutants of mGlu7 in an attempt to bring light on the true relation between conformational equilibrium, dynamics and affinity.

Furthermore, a comparison of the dynamic behavior of mGlu7 with that of a receptor with a strong affinity for glutamate such as mGlu3 might further inform on this complex interplay. In fact, several mGlu3 mutants with decreased affinities have been created in the lab (unpublished data) but they all involve amino acids exclusively localized in the orthosteric binding site. In my opinion, the generation of mutants where the modified amino acids are situated in the hinge region between the two lobes would be most valuable to pinpoint the relation between affinity and internal flexibility, as well as their respective contributions to the overall dynamic behavior. These two concepts are almost certainly closely intertwined.

Alternative labeling approaches

From a biochemical standpoint, the introduction of a smaller tag than the SNAP-tag, which could be specifically labeled, would enable a more precise measurement of the amplitude of the conformational changes. Moreover, other labeling sites than the N-terminus could be imagined. For instance, a comparison of the timescale estimated here with the ones measured following specific labeling in the 2nd lobe might provide a more global perspective. It has, however, turned out to be a very delicate task to design a tag that is both very reactive and specific for its substrate at the same time. One solution to this problem might be to implement the use of unnatural amino acids that can subsequently be specifically labeled (Chatterjee *et al.*, 2013). To my knowledge, the protocol for this fairly recent labeling approach has yet to be optimized for sf9 insect cells. However, a hybrid baculovirus vector was recently developed to enable the incorporation of unnatural amino acids in mammalian cells, even as complex as primary cell, stem cells and neurons (Chatterjee *et al.*, 2013). A purification and nanodisc-incorporation protocol conceived for mammalian cells would be optimal as it would only consume small amounts of reagents and still provide sufficient quantities for single-molecule experiments.

Other biological systems

To conclude on the smFRET aspect, the experimental approach presented here could also be applied on other completely unrelated proteins or on other class C GPCRs, for instance the $GABA_B$ receptor. The $GABA_B$ receptor constitutes a promising candidate for future investigations thanks to its ability to heterodimerize which offers the possibility to specifically label the two monomers that

form the functional receptor with distinct fluorophores by the use of different tags. Preliminary HTRF-sensor results are promising (Guillet *et al*, IGF, in preparation) and therefore, the conception of smFRET experiments could most certainly be envisioned for the near future.

In addition, iGluRs are ion channels, expressed in most excitatory synapses, where they are key players in neurotransmission regulation, following glutamate release (Kumar and Mayer, 2013). There are several iGluR subtypes, differing with respect to both ion permeability and kinetics, and they are therefore involved in as well rapid chemical signaling on the millisecond timescale as in the regulation of synaptic plasticity. The extracellular domain is 500 amino acids in length and interleaved with the three transmembrane α-helices that form the ion channel itself. The extracellular domain is composed of an amino-terminal domain (ATD) and a ligand-binding domain (LBD) on top of each other and they display structural similarities with the VFT of mGluRs (Kumar and Mayer, 2013). For this reason, the iGluRs represent potential receptors for the study of conformational dynamics by smFRET, and all the more so due to the existence of numerous partial agonists. In fact, recent studies have shown that iGluR activation is not a consequence of a static closed conformation, but depends on the probability that a given subunit enters a closed conformation (Landes *et al.*, 2011) and that the lower efficiency of gate opening observed with partial agonists is due to the lower stability of this fully closed conformation (Ahmed *et al.*, 2011).

smFRET for the study of protein dynamics *in cellulo*

Last but not least, I cannot help but mention the ultimate objective and "dream" of all scientists in the field of conformational dynamics, which consists in the establishment of reliant *in cellulo* smFRET experiments with high time-resolution. Presently, this remains a very arduous task for several reasons:

Firstly, the expression level of the proteins of interest has to be low enough to allow for the visualization of doubly-labeled proteins (FRET complexes) individually. This problem was addressed in two fairly recent papers where the authors either microinjected human BS-C-1 adherent cells (Sakon and Weninger, 2010) or electroporated bacterial *E.Coli* cells (Crawford *et al.*, 2013) to insert labeled proteins or DNA. The main advantage of these techniques resides in the fairly good control of the copy-number of molecules inserted per cells. In addition, the use of organic dyes, rather than fusion proteins, offers the advantages of better photostability and increased brightness (as a result of the slightly reducing environment of the cytoplasm) (Crawford *et al.*, 2013). However, it remains to

be explored whether these techniques are compatible with the study of membrane proteins, as their targeting to the membrane might be affected by the insertion procedure.

Secondly, in these two papers, the smFRET data was either acquired by means of total internal reflection fluorescence microscopy (TIRFM) (Sakon and Weninger, 2010; Crawford *et al.*, 2013) or wide-field microscopy (WF) (Crawford *et al.*, 2013) for the visualization of whole cells, or by a ALEX coupled confocal microscope equipped with APDs for the study of diffusing cytoplasmic proteins (Crawford *et al.*, 2013).

The advantages of using APDs and ALEX are the high time-resolution (~100μsec) and the possibility to sort molecules based on their stoichiometry. Unfortunately, this method can only be put into practice for the study of rapidly diffusing cytosolic proteins due to photobleaching issues (Crawford *et al.*, 2013).

The benefits of WF lie in the possibility of being able to observe larger areas of the cell. Yet, many cells show high levels of auto-fluorescence. This auto-fluorescent signal interferes with the specific signal, which complicates the data interpretation, and especially so if some of the investigated molecules display low FRET efficiencies.

To overcome the issue of high auto-fluorescence, TIRFM is a possible alternative to WF. In fact, the principle of TIRMF lies in the use of excitation beam that hits the sample above the critical angle (defined by the refractive indexes of the mediums) for which the beam is entirely reflected. Even so, the excitation beam creates an exponentially decreasing evanescent wave that only excites the sample at a depth of about 100nm, therefore, limiting the extent of auto-fluorescence (Jaiswal and Simon, 2007; Walter *et al.*, 2008). TIRFM is thus principally employed for the study of membrane proteins in eukaryotes but remains an option for the visualization of cytosolic proteins in bacteria.

Regardless, both WF and TIRFM are based on the use of cameras for data acquisition, and even the most sophisticated modern CMOS cameras have integration times of 0.5 to 1 milliseconds. This low time-resolution makes it impossible, for now, to probe dynamics on microsecond time-scales.

To conclude, only the future knows how far science will be able to push the boundaries of what is possible and what is not, and on this note, I would like to finish this dissertation, as it begun, with the citations of two great men,

"*Somewhere, something incredible is waiting to be known*" Carl Sagan

and

"*An expert is a person who has made all the mistakes that can be made in a very narrow field*" Niels Bohr

Bibliography

Acher FC (2012) Metabotropic Glutamate Receptors Molecular Pharmacology. *Tocris Biosci Sci Rev Ser*.

Ahmed AH, Wang S, Chuang H-H, and Oswald RE (2011) Mechanism of AMPA receptor activation by partial agonists: disulfide trapping of closed lobe conformations. *J Biol Chem* **286**:35257–66.

Antonik M, Felekyan S, Gaiduk A, and Seidel C a M (2006) Separating structural heterogeneities from stochastic variations in fluorescence resonance energy transfer distributions via photon distribution analysis. *J Phys Chem B* **110**:6970–8.

Audet M, and Bouvier M (2012) Restructuring g-protein-coupled receptor activation. *Cell* **151**:14–23, Elsevier Inc.

Bayburt TH, Grinkova Y V., and Sligar SG (2002) Self-Assembly of Discoidal Phospholipid Bilayer Nanoparticles with Membrane Scaffold Proteins. *Nano Lett* **2**:853–856.

Bayburt TH, and Sligar SG (2010) Membrane protein assembly into Nanodiscs. *FEBS Lett* **584**:1721–7, Federation of European Biochemical Societies.

Beqollari D, and Kammermeier PJ (2010) Venus fly trap domain of mGluR1 functions as a dominant negative against group I mGluR signaling. *J Neurophysiol* **104**:439–48.

Berberan-Santos M (2001) Pioneering contributions of Jean and Francis Perrin to molecular luminescence. *New Trends Fluoresc Spectrosc* Volume 1, pp 7–33.

Binet V, Duthey B, Lecaillon J, Vol C, Quoyer J, Labesse G, Pin J-P, and Prézeau L (2007) Common structural requirements for heptahelical domain function in class A and class C G protein-coupled receptors. *J Biol Chem* **282**:12154–63.

Blanchetot C, Verzijl D, Mujić-Delić A, Bosch L, Rem L, Leurs R, Verrips CT, Saunders M, de Haard H, and Smit MJ (2013) Neutralizing nanobodies targeting diverse chemokines effectively inhibit chemokine function. *J Biol Chem* **288**:25173–82.

Bockenhauer S, Fürstenberg A, Yao XJ, Kobilka BK, and Moerner WE (2011) Conformational dynamics of single G protein-coupled receptors in solution. *J Phys Chem B* **115**:13328–38.

Bräuner-Osborne H, Wellendorph P, and Jensen A a (2007) Structure, pharmacology and therapeutic prospects of family C G-protein coupled receptors. *Curr Drug Targets* **8**:169–84.

Brock C, Oueslati N, Soler S, Boudier L, Rondard P, and Pin J-P (2007) Activation of a dimeric metabotropic glutamate receptor by intersubunit rearrangement. *J Biol Chem* **282**:33000–8.

Bruno A, Costantino G, de Fabritiis G, Pastor M, and Selent J (2012) Membrane-sensitive conformational states of helix 8 in the metabotropic Glu2 receptor, a class C GPCR. *PLoS One* **7**:e42023.

Cao J, Huang S, Qian J, Huang J, Jin L, Su Z, Yang J, and Liu J (2009) Evolution of the class C GPCR Venus flytrap modules involved positive selected functional divergence. *BMC Evol Biol* **9**:67.

Chames P, and Baty D (2009) Fragments d'anticorps à domaine unique. *m/s médecins/science* **25**:1159–1162.

Changeux Jean-Pierre and Podleski Thomas (1968) On the excitability and cooperativity of the electroplax membrane. *Biochemistry* 944–950.

Changeux J-P (2012) Allostery and the Monod-Wyman-Changeux model after 50 years. *Annu Rev Biophys* **41**:103–33.

Changeux J-P, and Edelstein S (2011) Conformational selection or induced fit? 50 years of debate resolved. *F1000 Biol Rep* **3**:19.

Chatterjee A, Xiao H, Bollong M, Ai H-W, and Schultz PG (2013) Efficient viral delivery system for unnatural amino acid mutagenesis in mammalian cells. *Proc Natl Acad Sci U S A* **110**:11803–8.

Conn P, and Pin J (1997) Pharmacology and functions of metabotropic glutamate receptors. *Annu Rev Pharmacol …* **37**:205–37.

Craggs TD, and Kapanidis AN (2012) Six steps closer to FRET-driven structural biology. *Nat Methods* **9**:1157–8, Nature Publishing Group.

Crawford R, Torella JP, Aigrain L, Plochowietz A, Gryte K, Uphoff S, and Kapanidis AN (2013) Long-lived intracellular single-molecule fluorescence using electroporated molecules. *Biophys J* **105**:2439–50, Biophysical Society.

Davenport AP, Alexander SPH, Sharman JL, Pawson AJ, Benson HE, Monaghan AE, Liew WC, Mpamhanga CP, Bonner TI, Neubig RR, Pin JP, Spedding M, and Harmar AJ (2013) International Union of Basic and Clinical Pharmacology. LXXXVIII. G protein-coupled receptor list: recommendations for new pairings with cognate ligands. *Pharmacol Rev* **65**:967–86.

Degorce F, Card A, Soh S, Trinquet E, Knapik GP, and Xie B (2009) HTRF: A technology tailored for drug discovery - a review of theoretical aspects and recent applications. *Curr Chem Genomics* **3**:22–32.

Denis C, Saulière A, Galandrin S, Sénard J-M, and Galés C (2012) Probing heterotrimeric G protein activation: applications to biased ligands. *Curr Pharm Des* **18**:128–44.

Denisov IG, Grinkova Y V, Lazarides a a, and Sligar SG (2004) Directed self-assembly of monodisperse phospholipid bilayer Nanodiscs with controlled size. *J Am Chem Soc* **126**:3477–87.

Deupi X, and Kobilka BK (2010) Energy landscapes as a tool to integrate GPCR structure, dynamics, and function. *Physiology (Bethesda)* **25**:293–303.

Doumazane E, Scholler P, Fabre L, Zwier JM, Trinquet E, Pin J-P, and Rondard P (2013) Illuminating the activation mechanisms and allosteric properties of metabotropic glutamate receptors. *Proc Natl Acad Sci U S A* **110**:E1416–1425.

Dumoulin M et al (2002) Single-domain antibody fragments with high conformational stability. *Protein Sci* 500–515.

El Moustaine D, Granier S, Doumazane E, Scholler P, Rahmeh R, Bron P, Mouillac B, Banères J-L, Rondard P, and Pin J-P (2012) Distinct roles of metabotropic glutamate receptor dimerization in agonist activation and G-protein coupling. *Proc Natl Acad Sci U S A* **109**:16342–7.

Felekyan S, Kalinin S, Sanabria H, Valeri A, and Seidel C a M (2012) Filtered FCS: species auto- and cross-correlation functions highlight binding and dynamics in biomolecules. *Chemphyschem* **13**:1036–53.

Felekyan S, Sanabria H, Kalinin S, Kühnemuth R, and Seidel C a M (2013) Analyzing förster resonance energy transfer with fluctuation algorithms. *Methods Enzymol* **519**:39–85.

Fitzpatrick J a J, and Lillemeier BF (2011) Fluorescence correlation spectroscopy: linking molecular dynamics to biological function in vitro and in situ. *Curr Opin Struct Biol* **21**:650–60.

Foord SM, Bonner TOMI, Neubig RR, Rosser EM, Pin J, Davenport AP, Spedding M, and Harmar AJ (2005) International Union of Pharmacology . XLVI . G Protein-Coupled Receptor List. *Pharmacol Rev* **57**:279–288.

Francis perrin (1923) Polarisation de la lumière de fluorescence. Vie moyenne des molécules dans l'état excité. *J Phys* **10**.

Fredriksson R, Lagerström MC, Lundin L-G, and Schiöth HB (2003) The G-protein-coupled receptors in the human genome form five main families. Phylogenetic analysis, paralogon groups, and fingerprints. *Mol Pharmacol* **63**:1256–72.

Gansen A, Valeri A, Hauger F, Felekyan S, Kalinin S, Tóth K, Langowski J, and Seidel C a M (2009) Nucleosome disassembly intermediates characterized by single-molecule FRET. *Proc Natl Acad Sci U S A* **106**:15308–13.

Gautier A, Mott HR, Bostock MJ, Kirkpatrick JP, and Nietlispach D (2010) Structure determination of the seven-helix transmembrane receptor sensory rhodopsin II by solution NMR spectroscopy. *Nat Struct Mol Biol* **17**:768–74, Nature Publishing Group.

Ghanouni P, Gryczynski Z, Steenhuis JJ, Lee TW, Farrens DL, Lakowicz JR, and Kobilka BK (2001) Functionally different agonists induce distinct conformations in the G protein coupling domain of the beta 2 adrenergic receptor. *J Biol Chem* **276**:24433–6.

Granier S, Kim S, Shafer AM, Ratnala VRP, Fung JJ, Zare RN, and Kobilka B (2007) Structure and conformational changes in the C-terminal domain of the beta2-adrenoceptor: insights from fluorescence resonance energy transfer studies. *J Biol Chem* **282**:13895–905.

Granier S, and Kobilka B (2012) A new era of GPCR structural and chemical biology. *Nat Chem Biol* **8**:670–3, Nature Publishing Group.

Ha T, Enderle T, Ogletree DF, Chemla DS, Selvin PR, and Weiss S (1996) Probing the interaction between two single molecules: fluorescence resonance energy transfer between a single donor and a single acceptor. *Proc Natl Acad Sci* **93**:6264–6268.

Ha T, and Tinnefeld P (2012) Photophysics of fluorescent probes for single-molecule biophysics and super-resolution imaging. *Annu Rev Phys Chem* 595–617.

Hamers-Casterman C, and Atarhouch T (1993) Naturally occurring antibodies devoid of light chains. *Nature* **363**:446–448.

Hara MR, Kovacs JJ, Whalen EJ, Rajagopal S, Strachan RT, Grant W, Towers AJ, Williams B, Lam CM, Xiao K, Shenoy SK, Gregory SG, Ahn S, Duckett DR, and Lefkowitz RJ (2011) A stress response pathway regulates DNA damage through β2-adrenoreceptors and β-arrestin-1. *Nature* **477**:349–53, Nature Publishing Group.

Haustein E, and Schwille P (2007) Fluorescence correlation spectroscopy: novel variations of an established technique. *Annu Rev Biophys Biomol Struct* **36**:151–69.

Hendrix J, and Lamb DC (2013) Pulsed interleaved excitation: principles and applications. *Methods Enzymol* **518**:205–43, Elsevier Inc.

Hlavackova V, Zabel U, Frankova D, Bätz J, Hoffmann C, Prezeau L, Pin J-P, Blahos J, and Lohse MJ (2012) Sequential inter- and intrasubunit rearrangements during activation of dimeric metabotropic glutamate receptor 1. *Sci Signal* **5**.

Hollenstein, Kaspar et al (2013) Structure of class B GPCR corticotropin-releasing factor receptor 1. *Nature*.

Huang S, Cao J, and Jiang M (2011a) Interdomain movements in metabotropic glutamate receptor activation. *Proc Natl Acad Sci* **108**:15480–15485.

Huang S, Cao J, and Jiang M (2011b) Interdomain movements in metabotropic glutamate receptor activation. *Proc Natl Acad Sci* **108**:15480–15485.

Jäger M, Nir E, and Weiss S (2006) Site-specific labeling of proteins for single-molecule FRET by combining chemical and enzymatic modification. *Protein Sci* **15**:640–646.

Jaiswal JK, and Simon SM (2007) Imaging single events at the cell membrane. *Nat Chem Biol* **3**:92–8.

Juillerat A, Gronemeyer T, Keppler A, Gendreizig S, Pick H, Vogel H, and Johnsson K (2003) Directed Evolution of O6 -Alkylguanine-DNA Alkyltransferase for Efficient Labeling of Fusion Proteins with Small Molecules In Vivo. *Chem Biol* **10**:313–317.

Kalinin S, Felekyan S, Antonik M, and Seidel C a M (2007) Probability distribution analysis of single-molecule fluorescence anisotropy and resonance energy transfer. *J Phys Chem B* **111**:10253–62.

Kalinin S, Felekyan S, Valeri A, and Seidel C a M (2008) Characterizing multiple molecular States in single-molecule multiparameter fluorescence detection by probability distribution analysis. *J Phys Chem B* **112**:8361–74.

Kalinin S, Valeri A, Antonik M, Felekyan S, and Seidel C a M (2010a) Detection of structural dynamics by FRET: a photon distribution and fluorescence lifetime analysis of systems with multiple states. *J Phys Chem B* **114**:7983–95.

Kalinin S, Valeri A, Antonik M, Felekyan S, and Seidel C a M (2010b) Detection of structural dynamics by FRET: a photon distribution and fluorescence lifetime analysis of systems with multiple states. *J Phys Chem B* **114**:7983–95.

Kapanidis AN, Lee NK, Laurence T a, Doose S, Margeat E, and Weiss S (2004) Fluorescence-aided molecule sorting: analysis of structure and interactions by alternating-laser excitation of single molecules. *Proc Natl Acad Sci U S A* **101**:8936–41.

Kapusta P, Wahl M, Benda A, Hof M, and Enderlein J (2007) Fluorescence lifetime correlation spectroscopy. *J Fluoresc* **17**:43–8.

Katritch V, Cherezov V, and Stevens RC (2012) Structure-Function of the G Protein-Coupled Receptor Superfamily. *Annu Rev Pharmacol Toxicol* 1–25.

Kenakin T (2003) Ligand-selective receptor conformations revisited: the promise and the problem. *Trends Pharmacol Sci* **24**:346–54.

Khelashvili G, Albornoz PBC, Johner N, Mondal S, Caffrey M, and Weinstein H (2012) Why GPCRs behave differently in cubic and lamellar lipidic mesophases. *J Am Chem Soc* **134**:15858–68.

Kniazeff J, Bessis A-S, Maurel D, Ansanay H, Prézeau L, and Pin J-P (2004) Closed state of both binding domains of homodimeric mGlu receptors is required for full activity. *Nat Struct Mol Biol* **11**:706–13.

Kobilka BK, and Deupi X (2007) Conformational complexity of G-protein-coupled receptors. *Trends Pharmacol Sci* **28**:397–406.

Kudryavtsev V, Sikor M, Kalinin S, Mokranjac D, Seidel C a M, and Lamb DC (2012) Combining MFD and PIE for accurate single-pair Förster resonance energy transfer measurements. *Chemphyschem* **13**:1060–78.

Kumar J, and Mayer ML (2013) Functional insights from glutamate receptor ion channel structures. *Annu Rev Physiol* **75**:313–37.

Kunishima N, Shimada Y, Tsuji Y, Sato T, Yamamoto M, Kumasaka T, Nakanishi S, Jingami H, and Morikawa K (2000) Structural basis of glutamate recognition by a dimeric metabotropic glutamate receptor. *Nature* **407**:971–7.

Lagerström MC, and Schiöth HB (2008) Structural diversity of G protein-coupled receptors and significance for drug discovery. *Nat Rev Drug Discov* **7**:339–57.

Lakowicz J (n.d.) *Principles of fluorescence spectroscopy*.

Landes CF, Rambhadran A, Taylor JN, Salatan F, and Jayaraman V (2011) Structural landscape of isolated agonist-binding domains from single AMPA receptors. *Nat Chem Biol* **7**:168–73, Nature Publishing Group.

Lebon G, and Tate CG (2012) Les récepteurs couplés aux protéines G dans la lumière. *m/s médecins/science* **28**:876–882.

Lebon G, Warne T, Edwards PC, Bennett K, Christopher J, Leslie AGW, and Tate CG (2011) Agonist-bound adenosine A2A receptor structures reveal common features of GPCR activation. *Nature* **474**:521–525.

Lee NK, Kapanidis AN, Wang Y, Michalet X, Mukhopadhyay J, Ebright RH, and Weiss S (2005) Accurate FRET measurements within single diffusing biomolecules using alternating-laser excitation. *Biophys J* **88**:2939–53.

Lefkowitz RJ (2004) Historical review: a brief history and personal retrospective of seven-transmembrane receptors. *Trends Pharmacol Sci* **25**:413–22.

Lefkowitz RJ, and Shenoy SK (2005) Transduction of receptor signals by beta-arrestins. *Science* **308**:512–7.

Margeat E, Kapanidis AN, Tinnefeld P, Wang Y, Mukhopadhyay J, Ebright RH, and Weiss S (2006) Direct observation of abortive initiation and promoter escape within single immobilized transcription complexes. *Biophys J* **90**:1419–31.

Mary S (1998) A Cluster of Basic Residues in the Carboxyl-terminal Tail of the Short Metabotropic Glutamate Receptor 1 Variants Impairs Their Coupling to Phospholipase C. *J Biol Chem* **273**:425–432.

McIntire WE (2009) Structural determinants involved in the formation and activation of G protein betagamma dimers. *Neurosignals* **17**:82–99.

Michalet X, Weiss S, and Jäger M (2006) Single-molecule fluorescence studies of protein folding and conformational dynamics. *Chem Rev* **106**:1785–1813.

Milligan G, and Kostenis E (2006) Heterotrimeric G-proteins: a short history. *Br J Pharmacol* **147 Suppl** :S46–55.

Monod J, Changeux J-P, and Jacob F (1963) Allosteric proteins and cellular control systems. *J Mol Biol* **6**:306–329.

Müller B, Zaychikov E, Bräuchle C, and Lamb D (2005) Pulsed interleaved excitation. *Biophys J* **89**:3508–22.

Müller BK, Zaychikov E, Bräuchle C, and Lamb DC (2005) Pulsed interleaved excitation. *Biophys J* **89**:3508–22.

Muto T, Tsuchiya D, Morikawa K, and Jingami H (2007) Structures of the extracellular regions of the group II/III metabotropic glutamate receptors. *Proc Natl Acad Sci U S A* **104**:3759–64.

Neer EJ (1995) Heterotrimeric G proteins: organizers of transmembrane signals. *Cell* **80**:249–57.

Niswender CM, and Conn PJ (2010) Metabotropic glutamate receptors: physiology, pharmacology, and disease. *Annu Rev Pharmacol Toxicol* **50**:295–322.

Nordström KJ V, Sällman Almén M, Edstam MM, Fredriksson R, and Schiöth HB (2011) Independent HHsearch, Needleman--Wunsch-based, and motif analyses reveal the overall hierarchy for most of the G protein-coupled receptor families. *Mol Biol Evol* **28**:2471–80.

Nygaard R, Zou Y, Dror RO, Mildorf TJ, Arlow DH, Manglik A, Pan AC, Liu CW, Fung JJ, Bokoch MP, Thian FS, Kobilka TS, Shaw DE, Mueller L, Prosser RS, and Kobilka BK (2013) The dynamic process of β(2)-adrenergic receptor activation. *Cell* **152**:532–42.

Okada T, Le Trong I, Fox B a, Behnke C a, Stenkamp RE, and Palczewski K (2000) X-Ray diffraction analysis of three-dimensional crystals of bovine rhodopsin obtained from mixed micelles. *J Struct Biol* **130**:73–80.

Olofsson L, and Margeat E (2013) Pulsed interleaved excitation fluorescence spectroscopy with a supercontinuum source. *Opt Express* **21**:3370–8.

Padgett CL, and Slesinger P a (2010) GABAB receptor coupling to G-proteins and ion channels. *Adv Pharmacol* **58**:123–47.

Pankevych H, Korkhov V, Freissmuth M, and Nanoff C (2003) Truncation of the A1 adenosine receptor reveals distinct roles of the membrane-proximal carboxyl terminus in receptor folding and G protein coupling. *J Biol Chem* **278**:30283–93.

Pauling L (1940) A Theory of the Structure and Process of Formation of Antibodies. *J Am Chem Soc* **372**.

Peleg G, Ghanouni P, Kobilka BK, and Zare RN (2001) Single-molecule spectroscopy of the beta2 adrenergic receptor : Observation of conformational substates in a membrane protein. *Proc Natl Acad Sci* **98**.

Pin J-P, Galvez T, and Prézeau L (2003) Evolution, structure, and activation mechanism of family 3/C G-protein-coupled receptors. *Pharmacol Ther* **98**:325–354.

Rahmeh R, Damian M, Cottet M, Orcel H, Mendre C, Durroux T, Sharma KS, Durand G, Pucci B, Trinquet E, Zwier JM, Deupi X, Bron P, Banères J-L, Mouillac B, and Granier S (2012) Structural insights into biased G protein-coupled receptor signaling revealed by fluorescence spectroscopy. *Proc Natl Acad Sci U S A* **109**:6733–8.

Rajagopal S (2013) Quantifying biased agonism: understanding the links between affinity and efficacy. *Nat Rev Drug Discov* **12**:483, Nature Publishing Group.

Rasmussen SGF, Choi H-J, Fung JJ, Pardon E, Casarosa P, Chae PS, Devree BT, Rosenbaum DM, Thian FS, Kobilka TS, Schnapp A, Konetzki I, Sunahara RK, Gellman SH, Pautsch A, Steyaert J, Weis WI, and Kobilka BK (2011) Structure of a nanobody-stabilized active state of the β(2) adrenoceptor. *Nature* **469**:175–80, Nature Publishing Group.

Rasmussen SGF, Choi H-J, Rosenbaum DM, Kobilka TS, Thian FS, Edwards PC, Burghammer M, Ratnala VRP, Sanishvili R, Fischetti RF, Schertler GFX, Weis WI, and Kobilka BK (2007) Crystal structure of the human beta2 adrenergic G-protein-coupled receptor. *Nature* **450**:383–7.

Rasmussen SGF, DeVree BT, Zou Y, Kruse AC, Chung KY, Kobilka TS, Thian FS, Chae PS, Pardon E, Calinski D, Mathiesen JM, Shah ST a, Lyons J a, Caffrey M, Gellman SH, Steyaert J, Skiniotis G, Weis WI, Sunahara RK, and Kobilka BK (2011) Crystal structure of the β2 adrenergic receptor-Gs protein complex. *Nature* **477**:549–55, Nature Publishing Group.

Rasnik I, McKinney S, and Ha T (2006) Nonblinking and long-lasting single-molecule fluorescence imaging. *Nat Methods* **3**:891–893.

Rondard P, Goudet C, Kniazeff J, Pin JP, and Prézeau L (2011) The complexity of their activation mechanism opens new possibilities for the modulation of mGlu and GABAB class C G protein-coupled receptors. *Neuropharmacology* **60**:82–92.

Rondard Philippe, Goudet C, Kniazeff J, Pin J-P, and Prézeau L (2011) The complexity of their activation mechanism opens new possibilities for the modulation of mGlu and GABAB class C G protein-coupled receptors. *Neuropharmacology* **60**:82–92, Elsevier Ltd.

Rondard P, Liu J, Huang S, Malhaire F, Vol C, Pinault A, Labesse G, and Pin J-P (2006) Coupling of agonist binding to effector domain activation in metabotropic glutamate-like receptors. *J Biol Chem* **281**:24653–61.

Rosemond E, Wang M, and Yao Y (2004) Molecular basis for the differential agonist affinities of group III metabotropic glutamate receptors. *Mol Pharmacol* **66**:834–842.

Rosenbaum DM, Rasmussen SGF, and Kobilka BK (2009) The structure and function of G-protein-coupled receptors. *Nature* **459**:356–63.

Roy R, Hohng S, and Ha T (2008) A practical guide to single-molecule FRET. *Nat Methods* **5**:507–516.

Sakon JJ, and Weninger KR (2010) Detecting the conformation of individual proteins in live cells. *Nat Methods* **7**:203–5, Nature Publishing Group.

Santoso Y, Hwang LC, Le Reste L, and Kapanidis AN (2008) Red light, green light: probing single molecules using alternating-laser excitation. *Biochem Soc Trans* **36**:738–44.

Santoso Y, Torella JP, and Kapanidis AN (2010) Characterizing single-molecule FRET dynamics with probability distribution analysis. *Chemphyschem* **11**:2209–19.

Sato H, Ikeda M, Suzuki K, and Hirayama K (1996) Site-specific modification of interleukin-2 by the combined use of genetic engineering techniques and transglutaminase. *Biochemistry* **35**:13072–80.

Schwenk J, Metz M, Zolles G, Turecek R, Fritzius T, Bildl W, Tarusawa E, Kulik A, Unger A, Ivankova K, Seddik R, Tiao JY, Rajalu M, Trojanova J, Rohde V, Gassmann M, Schulte U, Fakler B, and Bettler B (2010) Native GABA(B) receptors are heteromultimers with a family of auxiliary subunits. *Nature* **465**:231–5, Nature Publishing Group.

Schwille P, and Haustein E (2001) Fluorescence correlation spectroscopy. An introduction to its concepts and applications. *doi:101002/lpor200910041* 1–33.

Sebag JA, and Pantel J (2012) Ciblage thérapeutique des récepteurs couplés aux protéines G. *m/s médecins/science* **28**:845–851.

Sindbert S, Kalinin S, Nguyen H, Kienzler A, Clima L, Bannwarth W, Appel B, Müller S, and Seidel C a M (2011) Accurate distance determination of nucleic acids via Förster resonance energy transfer: implications of dye linker length and rigidity. *J Am Chem Soc* **133**:2463–80.

Sisamakis E, Valeri A, Kalinin S, Rothwell PJ, and Seidel C a M (2010a) Accurate single-molecule FRET studies using multiparameter fluorescence detection. *Methods Enzymol* **475**:455–514, Elsevier Inc.

Sisamakis E, Valeri A, Kalinin S, Rothwell PJ, and Seidel C a M (2010b) Accurate single-molecule FRET studies using multiparameter fluorescence detection. *Methods Enzymol* **475**:455–514, Elsevier Inc.

Siu FY, He M, de Graaf C, Han GW, Yang D, Zhang Z, Zhou C, Xu Q, Wacker D, Joseph JS, Liu W, Lau J, Cherezov V, Katritch V, Wang M-W, and Stevens RC (2013) Structure of the human glucagon class B G-protein-coupled receptor. *Nature* **499**:444–9, Nature Publishing Group.

Stryer L (1978) Fluorescence energy transfer as a spectroscopic ruler. *Annu Rev Biochem* **47**:819–46.

Taki M, Shiota M, and Taira K (2004) Transglutaminase-mediated N- and C-terminal fluorescein labeling of a protein can support the native activity of the modified protein. *Protein Eng Des Sel* **17**:119–26.

Tateyama M, Abe H, Nakata H, Saito O, and Kubo Y (2004) Ligand-induced rearrangement of the dimeric metabotropic glutamate receptor 1 α. *Nat Struct Mol Biol* **11**:2–6.

Tesmer JJG (2010) The quest to understand heterotrimeric G protein signaling. *Nat Struct Mol Biol* **17**:650–2, Nature Publishing Group.

Tian Y, Martinez MM, and Pappas D (2011) Fluorescence correlation spectroscopy: a review of biochemical and microfluidic applications. *Appl Spectrosc* **65**:115A–124A.

Tomov TE, Tsukanov R, Masoud R, Liber M, Plavner N, and Nir E (2012) Disentangling subpopulations in single-molecule FRET and ALEX experiments with photon distribution analysis. *Biophys J* **102**:1163–73, Biophysical Society.

Torella JP, Holden SJ, Santoso Y, Hohlbein J, and Kapanidis AN (2011) Identifying molecular dynamics in single-molecule FRET experiments with burst variance analysis. *Biophys J* **100**:1568–77, Biophysical Society.

Ullmer C, Zoffmann S, Bohrmann B, Matile H, Lindemann L, Flor P, and Malherbe P (2012) Functional monoclonal antibody acts as a biased agonist by inducing internalization of metabotropic glutamate receptor 7. *Br J Pharmacol* **167**:1448–66.

Van de Linde S, Löschberger A, Klein T, Heidbreder M, Wolter S, Heilemann M, and Sauer M (2011) Direct stochastic optical reconstruction microscopy with standard fluorescent probes. *Nat Protoc* **6**:991–1009.

Walter N, Huang C, Manzo A, and Sobhy M (2008) Do-it-yourself guide: how to use the modern single-molecule toolkit. *Nat Methods* **5**:475–489.

Wellendorph P, and Bräuner-Osborne H (2009) Molecular basis for amino acid sensing by family C G-protein-coupled receptors. *Br J Pharmacol* **156**:869–84.

Wess J, Han S-J, Kim S-K, Jacobson K a, and Li JH (2008) Conformational changes involved in G-protein-coupled-receptor activation. *Trends Pharmacol Sci* **29**:616–25.

Whalen EJ, Rajagopal S, and Lefkowitz RJ (2011) Therapeutic potential of β-arrestin- and G protein-biased agonists. *Trends Mol Med* **17**:126–39, Elsevier Ltd.

Widengren J, Kudryavtsev V, Antonik M, Berger S, Gerken M, and Seidel C a M (2006) Single-molecule detection and identification of multiple species by multiparameter fluorescence detection. *Anal Chem* **78**:2039–50.

Yamashita T, Terakita a, and Shichida Y (2001) The second cytoplasmic loop of metabotropic glutamate receptor functions at the third loop position of rhodopsin. *J Biochem* **130**:149–55.

Yanagawa M, Yamashita T, and Shichida Y (2011) Comparative fluorescence resonance energy transfer analysis of metabotropic glutamate receptors: implications about the dimeric arrangement and rearrangement upon ligand bindings. *J Biol Chem* **286**:22971–81.

Yasuhara A, and Chaki S (2010) Metabotropic Glutamate Psychiatric Disorders Receptors : Potential Drug Targets for psychiatric disorders. *Open Med Chem J* **4**:20–36.

Yin J, and Straight P (2005) Genetically encoded short peptide tag for versatile protein labeling by Sfp phosphopantetheinyl transferase. *Proc Natl Acad Sci* **102**:15815–20.

Annex

Alternative labeling methods

The SNAP-tag® used to label single VFT-domains has the inconvenience of being a relatively large fusion protein of approximately 20kDa, which makes it difficult to extract exact distances. What is more is that measurements at an ensemble level of the fluorescence anisotropy result in a value of 0.2, which is a surprisingly high value indicating that the SNAP-tag® is not completely mobile in space. Consequently, the assumption of the parameter K^2 being equal to 2/3 in the Förster distance equation is not entirely accurate, which slightly alters the R0 value.

In order to evaluate the contribution of the SNAP to the measured distances, other labeling strategies have been attempted.

Transglutaminase labeling (Tg-hmGlu2-(561GPI))

The Tgase recognition tag was introduced in N-terminal of the hmGlu2-(561GPI) (VFT+CRD) construct, by replacing the FLAG and the SNAP sequences. This had to be done because one of the prerequisites to obtaining efficient labeling is that the tag should be as flexible and exposed to the solvent as possible. It is, therefore, desirable to put the tag at very beginning of the sequence.

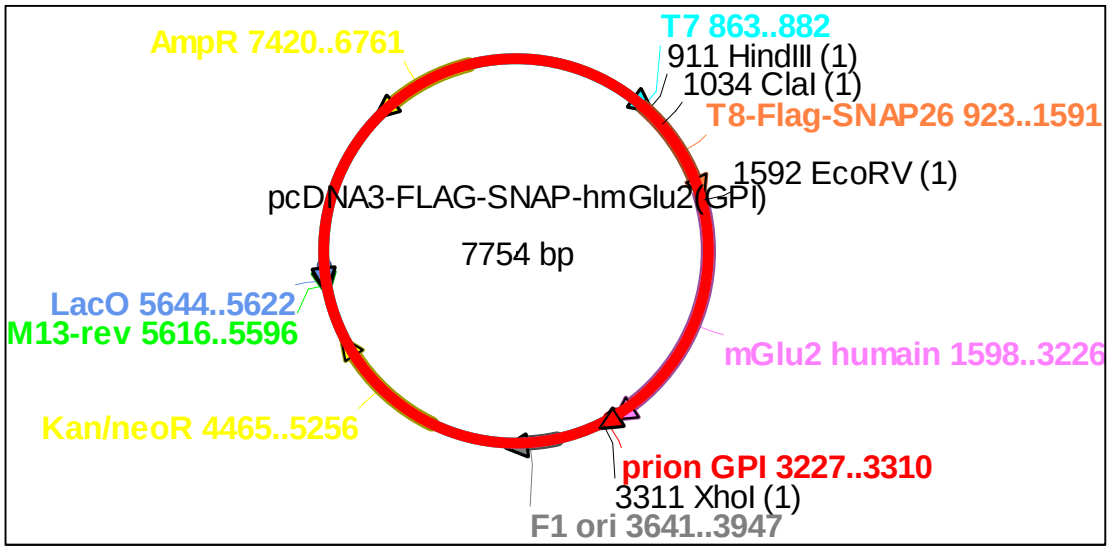

***Figure 4.21**. Cartography of pcDNA3 plasmid encoding hmGlu2-(561GPI)*

The Tg-hmGlu2-(561GPI) construct was created by amplifying the hmGlu2 gene between the

EcoRV and the Xho1 restriction sites by PCR (**figure 4.20**). The 3' probe was extended by the DNA sequence corresponding to the TGase recognition tag and a restriction site for HindIII. Both the vector and the PCR-fragment were then digested by HindIII and Xho1 and the large fragment was separated from the coding region in the case of the vector. After ligation of the PCR-fragment and the digested large fragment of the vector, the plasmid was amplified in bacteria, purified and sequenced.

The first test was performed by transfecting HEK-293 cells with the Tg-hmGlu2-(561GPI) construct, using the flag-snap-hmGlu2-5561GPI as a negative control. Labeling was performed at the cell-surface using the standard protocol described in chapter 4.2.

After several steps of protocol optimization, unspecific labeling was still unavoidable and it was concluded that the labeling efficiency was only approximately 5 times higher for the construct carrying the specific sequence than for the negative control. At a single-molecule concentration, no donor –acceptor complexes were detectable.

A thorough study of available literature (Sato *et al.*, 1996; Taki *et al.*, 2004) revealed that even though the aforementioned substrate sequence is considered to be specific, other semi-exposed Gln-residues might be labeled with a lower efficiency. It is also noteworthy that as the FLAG-tag is no longer present- the supernatant after cleavage cannot be purified. Hence any GPI-anchored protein, cleaved by the phospholipase C and carrying an exposed and subsequently labeled Gln-residue contribute to the unspecific signal.

No further work was done to establish a specific labeling approach based on the transglutaminase. The reintroduction of the flag-tag could have been a possible direction to explore but as the mGlu2-(561GPI) contains no less than 16 Gln residues, some of which possibly exposed, it was concluded that other labeling strategies were preferable.

Cysteine labeling (flag-hmGlu2(C4)-561GPI)

The extracellular domain of the mGlu2 monomer contains only one endogenous cysteine in the VFT involved in a disulfide bond with the corresponding cysteine in the other monomer, therefore, stabilizing the homodimeric structure of the receptor. There are, on the other hand, several cysteines in the CRD but they are all also involved in disulfide bonds. Therefore, the lack of endogenous reactive cysteines in the ECD makes it possible to attempt a labeling approach based on the introduction, by mutagenesis, of a cysteine that could be chemically labeled with a fluorescent dye.

The thiol group carried by the side-chain of the cysteine residue is reactive to a variety of chemical groups by nucleophilic substitution. Using a fluorescent dye functionalized with a maleimide group, the reaction is spontaneous and the highest yield is obtained at pH in the range 6-7.

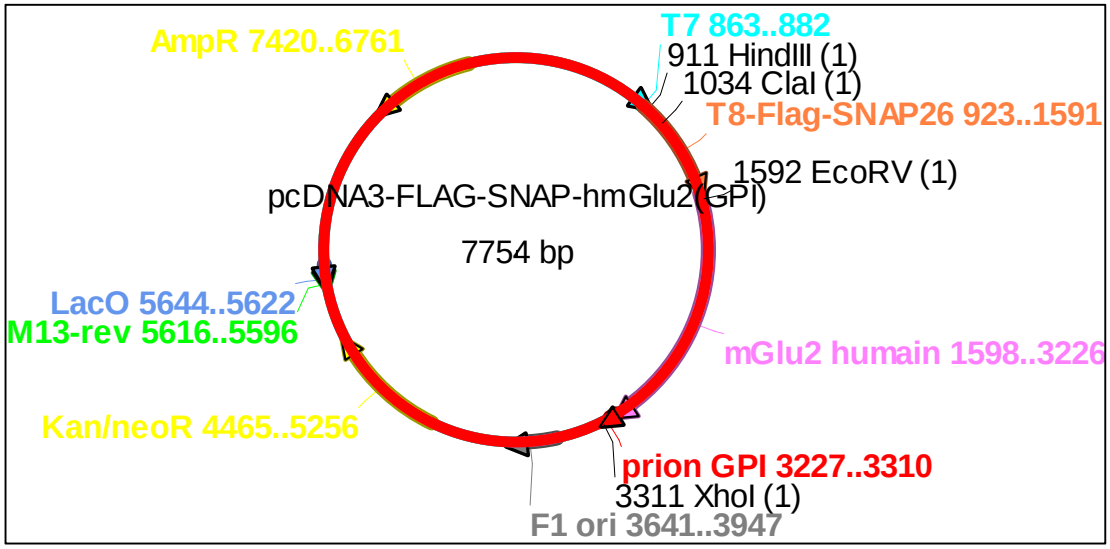

***Figure 4.22** Cartography of pcDNA3 plasmid encoding hmGlu2-(561GPI)*

For the sake of comparison with the SNAP-tagged labeled receptor, the cysteine was introduced in the N-terminal end of the receptor construct hmGlu2-(561GPI). Nevertheless, as many GPI-anchored proteins contain cysteines, a purification step after cleavage would be required. It was, thus, necessary to remove the SNAP-tag while keeping the FLAG-tag intact. This was achieved by amplifying the coding sequence between XhoI and EcoRV using a probe extended after the EcoRV restriction site by a recognition site for ClaI. To replace the alanine in position 4 by a cysteine, the probe was designed to be misaligned on one base (G-T). After digestion of the vector and the PCR fragment with XhoI and ClaI, the amplified sequence and the empty vector were ligated overnight before bacterial transformation and purification. Sequencing was then performed before further study.

In order to verify that the construction was sufficiently expressed in our HEK-293 cell-line, a fluoresceine labeled anti-flag antibody was used to detect the presence of the construct at the cell-surface. The flag-snap-hmGlu2-(561GPI) construct was used as a positive control and it was concluded that the expression level was similar for the two constructs.

Several labeling protocols were then tested in order to optimize the labeling efficiency. A classical cell surface labeling scheme or labeling after PI-PLC cleavage worked equally well and smFRET-PIE

measurements were performed. Unfortunately, from these experiences, the yield of doubly labeled receptors was estimated to be lower than 10%.

Following these observations, all further work to optimize the protocol was abandoned in favor of the acyl-carrier protein tag.

Acyl-Carrier-Protein tag (ACP-tag)

In the cell, the ACP Synthase (4´-phosphopantetheinyl transferase) is an enzyme that plays a key role in the biosynthesis of fatty acids. Its capacity to catalyze covalent bonds between specific sites has been applied by biotechnology companies to establish a method to label proteins both *in vivo* and *in vitro*.

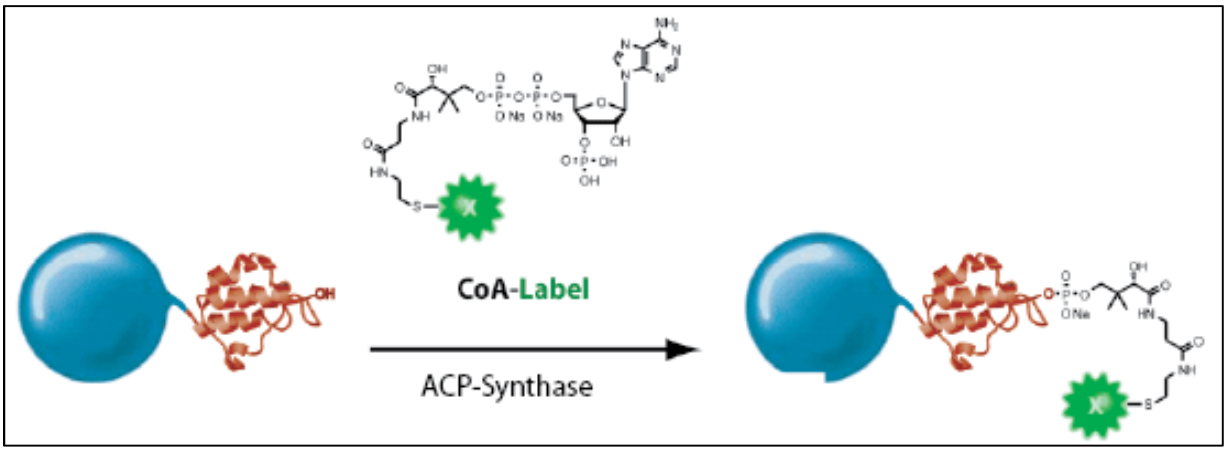

Figure 4.23. *Principle of ACP labeling*

Initially the ACP-tag was a relatively large polypeptide tag (8 kDa) having a conserved serine residue to which the ACP synthase covalently bound a Coenzyme A (CoA) linked dye. Since the first ACP-construct was introduced, several groups have tried to better characterize the tag in order to minimize its size by removing all non-necessary residues. In 2005, the group of Christopher T Walsh at Harvard University successfully managed to limit the number of required residues to only eleven without decreasing the labeling efficiency (Yin and Straight, 2005).

In this study, we chose to employ the short ACP-tag limited to 17residues described in the previously mentioned article published by C Walsh : GSQDVLDSLEFIASKLA

The construct was derived from the flag-hmGlu2(C4)-561GPI by first replacing the coding sequence carrying the Ala->Cys mutation by the WT hmGlu2-561GPI sequence. The complementary DNA oligos coding the sought peptide were hybridized using a standard protocol based on the heating of the sample to 95°C >Tm followed by a successive decrease in temperature (1°C/min) until the desired

temperature of 12°C was reached. As the DNA oligos had been designed with an extension corresponding to the recognition site for the restriction enzyme ClaI, an insertion into the previously ClaI digested vector was made possible. During the ligation with the DNA ligase, the first attempts resulted in the formation of catenates and in order to limit the number of inserted DNA hybrids to only one per vector, the insertion ratio had be decreased to 0.5 hybrids per vector. The sequence was then amplified, purified and sequenced.

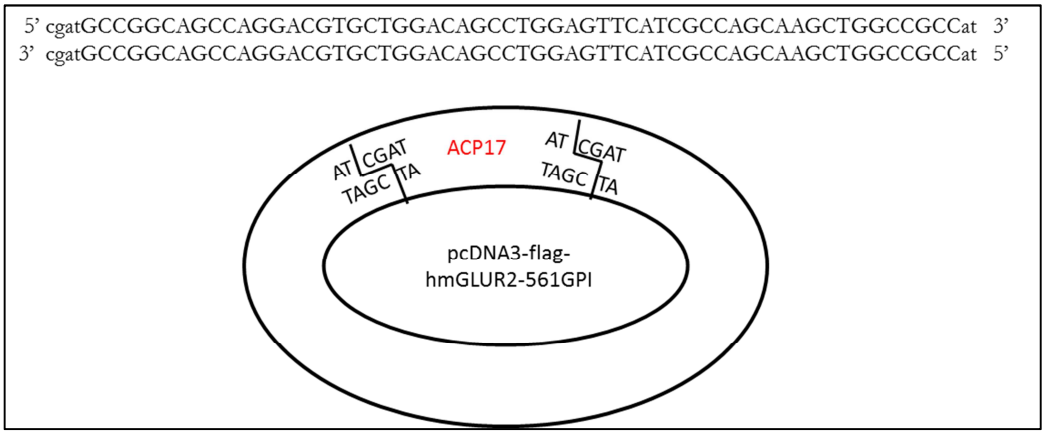

***Figure 4.24**. Principle of ACP17 insertion. See text for details.*

The expression level was determined as previously described, by the use of a fluorescein labeled anti-flag antibody at the cell surface and it was estimated to be similar to the degree of labeling observed for the SNAP-tag. Unfortunately, all subsequent attempts to specifically label the construct failed.

The exact same protocol was then employed to introduce the entire ACP-tag and this time, the outcome was a partial success. The labeling efficiency for the full-length ACP-tag is only about 25% and, thus, lower than for the SNAP-tag construct, for which the labeling efficiency is almost 90%. Nonetheless, smFRET experiments were carried out with this tag (**Supplementary figure 3 in chapter 4.2**). By using this construct, it could be verified that the timescale of the conformational changes occurring within the VFT, does not vary depending on the tag used for labeling.

Glossary and abbreviations

$\boldsymbol{B_R}$ - background in the acceptor channel

$\boldsymbol{F_A}$ – fluorescence from the acceptor (corrected for background)

$\boldsymbol{F_{Aexc}^{Aem}}$ - acceptor emission upon acceptor excitation

$\boldsymbol{F_D}$ – fluorescence from the donor (corrected for background)

$\boldsymbol{F_{Dexc}^{Aem}}$ - acceptor emission upon donor excitation

$\boldsymbol{F_{Dexc}^{Dem}}$ - donor emission upon donor excitation

$\langle \boldsymbol{N} \rangle$ - average number of molecules

$\boldsymbol{S_G}$ - total signal in the donor channel

$\boldsymbol{S_R}$ - total signal in the acceptor channel

$\boldsymbol{K^2}$ – the dipole orientation factor

$\boldsymbol{\delta_{\parallel}}$ - detection efficiency in the parallel detection channels

$\boldsymbol{\delta_{\perp}}$ - detection efficiency in the perpendicular detection channels

$\boldsymbol{\phi_D}$ - quantum yield of the donor

µsALEX - alternated excitation of single molecules for fluorescent aided molecule sorting

BG-substrate - benzylguanine group carrying a fluorescent dye for SNAP tag labeling

c - speed of light

Dir – direct excitation, excitation of the acceptor at the wavelength of the donor

E – FRET efficiency

$\mathbf{E_{hv}}$ - photon energy

FCCS –fluorescence cross correlation spectroscopy

FCS –fluorescence correlation spectroscopy

fFCS – filtered fluorescence correlation spectroscopy

FI – FRET indicator

FRET - Förster resonance energy transfer

G(τ) - autocorrelation function

h - Planck's constant

I - fluorescence intensity

$\mathbf{I_{//}}$ - fluorescence intensity in parallel detection channel

$\mathbf{I_{\perp}}$ - fluorescence intensity in perpendicular detection channel

J - the spectral overlap integral

$\mathbf{k_{,FRET}}$ – rate transfer FRET

$\mathbf{k_{nr}}$ - non-radiative de-excitation

$\mathbf{k_r}$ - radiative de-excitation

Lk – leakage, donor emission detected in the acceptor channel

Nanobody - heavy-chain only antibody produced by camelides

OD - optical density

Orthosteric binding site - primary binding site by opposition to an allosteric binding site

PAM - positive allosteric modulators - ligand potentiating the response of an orthosteric ligand

Partial agonist - a ligand that partially activate its target receptor

PNS - peripheral nervous system

R - perfect gas constant

r - steady state anisotropy

R_0 - Förster distance

r_0 - fundamental anisotropy

Resting conformation - the term given to specify the inactive conformation of mGluRs

SACF - species auto correlation function

SCCF - species cross correlation function

smFRET - single-molecule Förster resonance energy transfer

SNAP-tag - suicide enzyme covalently labeled with benzylguanine-derived fluorescent substrates

T - temperature in Kelvin

TIRFM – total internal reflection fluorescence microscopy

trFRET- time resolved FRET - also known as HTRF

VFT - Venus flytrap domain - ligand binding domain of mGluRs

α - crosstalk pre-factor

β_2AR - β_2 adrenergic receptor - a class A GPCR

ε - molecular brightness

θ - the rotational correlation time

λ - wavelength

τ - excited state lifetime

τ_A - excited state lifetime of the acceptor following acceptor excitation

τ_D - excited state lifetime of the donor

$\tau_{D(A)}$ - excited state lifetime of the donor in presence of an acceptor

Φ - quantum yield of a dye

γ - detection factor

δ - detection efficiency

η - viscosity or refractive index of the medium